Nanomaterials for Gas Sorption and Separation

Zur Erlangung des akademischen Grades eines

DOKTORS DER NATURWISSENSCHAFTEN

(Dr. rer. nat.)

der Fakultät für Chemie und Biowissenschaften

Karlsruher Institut für Technologie (KIT) - Universitätsbereich

genehmigte

DISSERTATION

von

M.Sc. Sara Simonato

aus

Padova, Italien

Dekan: Prof. Dr. Peter Roesky

Referent: Prof. Dr. Claus Feldmann

Korreferent: Prof. Dr. Reiner Staudt

Tag der mündlichen Prüfung: 20.12.2013

ad Alberto

Abstract

In this study, we investigate the feasibility of using different nanoscaled materials as sorption substrate: to capture atmospheric carbon dioxide, to capture oxygen, to transfer doxorubicin, to separate (S)-Ibuprofen from (R)-Ibuprofen.

The sorption and storage of CO_2 is high relevant as a means of combating the greenhouse effect and, consequently, the global warming. As potential gas sorbent material, we suggest AlO(OH) nanoscale hollow spheres first. This material has a high specific surface area and its hydroxyl groups, which are mildly basic, can interact with the acidic CO_2 molecules. The sorption of CO_2, investigated with a magnetic suspension balance, reveals an uptake of 260 mg g^{-1} at 50 °C and 90 bar, while the CO_2 uptake is 4.3-times higher as compared to pure N_2. To increase the uptake and selectivity of CO_2, a new amine-functionalized nanocompound is presented: magnesium aminoethyl phosphonate. Electron microscopy demonstrates a particle size of 20 nm, whereas the specific surface is 357 m^2 g^{-1}. The sorption of CO_2, measured up to 150 bar, shows an uptake of 150 mg g^{-1} at 80 °C and 110 bar. The nitrogen uptake, tested under similar conditions, is negligible (< 1 mg). The effect of the organic functionality is studied depending on the number of carbon atoms. Additionally, the magnesium is substituted by different cations (Ca, Ba, Fe, Co, Cu) and tested under similar conditions to asses the CO_2 capacity.

Furthermore, two novel nanomaterials are synthesised with regard to their future application as oxygen sorbents. Due to their relative high specific surface areas, according to the BET formalism, and the presence of a magnetic cation (Co^{2+} and Gd^{3+}), these materials could positively interact with O_2.

Moreover, nanoscale AlO(OH) hollow spheres are tested as nanocarriers for doxorubicin, one of the most common anti-cancer agents. The drug is encapsulated in the nanomaterial during the synthesis, resulting in a final concentration of 2% in weight. The activity of the final material is proven both *in vitro* and *in vivo*.

Finally, in view of the separation of the commercially available (S/R)-Ibuprofen, two inorganic-organic hybrids nanomaterials are proposed here, and are tested in the presence of supercritical CO_2 as solvent.

Zusammenfassung

Die in die Atmosphäre freigesetzt Menge an Kohlendioxid stieg in den letzten 150 Jahren erheblich. Im Hinblick hierauf haben Sorption und Lagerung von CO_2 große Bedeutung, um den Treibhauseffekt und somit auch die globale Erwärmung zu vermindern. Als mögliches Gassorptionsmittel werden zuerst nanoskalige AlO(OH) Hohlkugel vorgeschlagen. Aufgrund ihrer hohen spezifischen Oberfläche und der milden Basizität der Hydroxylgruppe, die mit den sauren CO_2 Molekülen wechselwirken können. Die Sorption von CO_2, untersucht mit einer Magnetschwebewaage, zeigt eine Aufnahme von 260 mg g^{-1} bei 50 °C und 90 bar während die CO_2-Aufnahme 4,3-fach höher liegt als im Vergleich zu reinem N_2.

Um Aufnahme und Selektivität von CO_2 zu erhöhen, wird ein neues aminfunktionalisiertes Nanomaterial vorgestellt: Magnesiumaminoäthylenphosphonat. Die Elektronenmikroskopie zeigt eine Partikelgröße von 20 nm, während die spezifische Oberfläche bei 357 m^2 g^{-1} liegt. Die Sorption von CO_2, gemessen bis zu einem Druck von 150 bar, zeigt eine Aufnahme von 150 mg g^{-1} bei 80 °C und 110 bar. Die Stickstoffaufnahme, die unter ähnlichen Bedingungen getestet wurden, ist vernachlässigbar (< 1 mg). Die Wirkung der organischen Funktionalität wird durch die Verkürzung und Verlängerung der Kohenstoffkette untersucht. Zusätzlich wird Magnesium durch verschiedenen Kationen (Ca, Ba, Fe, Co, Cu) substituiert und unter ähnlichen Bedingungen getestet, um die CO_2 Aufnahmefähigkeit nachzuweisen.

Weiterhin sind zwei neuartige Nanomaterialien mit dem Ziel einer späteren Anwendung als Sauerstoffsorptionsmittel aufgrund ihrer relativ hohen spezifischen Oberfläche gemäß der BET hergestellt worden, die aufgrund der Anwesenheit eines magnetischen Kations (Co^{2+} und Gd^{3+}), mit dem paramagnetischen Gas wechselwirken können.

Darüber hinaus werden nanoskalige AlO(OH) Hohlkugeln als Nanocontainer für Doxorubicin getestet, eines der häufigsten Antitumurmedikamente. Das Medikament wird im Nanomaterial, während der Synthese, eingekapselt, was zu einer Endkonzentration von 2 Gewichts-% führt. Die Wirkung des Nanocontainer wird sowohl in *in vitro* als auch *in vivo* untersucht.

Schließlich werden im Hinblick auf die Racemattrennung, der im Handel erhältlichen racemischen (S/R)-Ibuprofen Mischung, zwei anorganisch-organische Hybridennanomaterialien vorgeschlagen und deren Wirkung in Gegenwart von überkritischem CO_2 als Lösungsmittel getestet.

Table of contents

1 Introduction

"*There is plenty of room at the bottom*" was the title of an inspiring lecture given by the Nobel laureate Richard Feynmann in 1959.[1] Even if the term 'nanoparticles' appeared first in the 1980's,[2] we can consider him without doubt the Father of Nanoscience. The drastic change in the physicochemical properties of materials that occurs when the size in the nanometre region is varied (1 nm = 10^{-9} m) has opened up many new directions in several fields of current research and modern technology. Due to the special properties of nanomaterials, sustained efforts have established different applications.[2]

Nowadays, one of the most significant global challenges is the climate change: consequently, methods to efficiently and effectively capture, separate, store and convert greenhouse gases, especially CO_2,[3] have attracted notable attention. Current industrial CO_2 capture employs aqueous amine solutions[4] or chilled ammonia, which presents different negatives aspects: relatively low efficiency, equipment corrosion, solvent loss and toxicity. To avoid such disadvantages, different materials have been proposed; the most prominent ones are the so-called metal-organic frameworks (MOFs).[5] MOFs, also known as coordination polymers, are built up by metal ions linked together by multifunctional organic ligands.[6] They are characterised by large specific surface areas and wide structural and chemical tunability.[5] Three options for gas adsorption have been identified to operate in MOFs: low-pressure sorption based on the heat of adsorption (driven by functional groups in the material), medium-pressure adsorption based on the huge surface area of the sorbent, and high-pressure adsorption based on the accessible pore volume.[7] The research activities on MOFs can be used as a starting point to study new and, hopefully, improved sorbents for carbon sequestration, overcoming the disadvantages of metal-organic frameworks: high cost of production,[8] low selectivity toward CO_2 at high pressure[9] and instability toward water vapour.[8] The major challenge of CO_2 capture is to search for high performance and highly selective materials, easy to regenerate and, at the same time, inexpensive to produce. Since large CO_2 uptakes are mostly achieved with sorbents exhibiting large surface areas here porous nanomaterials are selected as sorbents.

Nanoparticles have been sparely addressed for sorption and separation of gases.[10] The most important characteristics of nanoparticles, concerning the applications in the field of gas adsorption, are their high specific surface area and their drastic influence in the chemical reactivity. The huge surface facilitates the diffusion and storage of gases into the porous material, whereas the higher

chemical response allows for chemical sorption. The specific surface of nanomaterials can be even more increased if an inner cavity is created inside the nanoparticles, achieving, at the same time, a low specific weight: nanoscale hollow spheres [11] can be then addressed to the sorption and storage of gases, due to their considerably high specific surface area compared to massive nanoparticles. Furthermore, the functionalization of the nanomaterials with basic nitrogen-containing groups is a strategy adopted in this work, also for sorbents suggested to work at higher than atmospheric pressure.

The aim of this work is to study the gas sorption behaviours of promising nanomaterials developed in the group of Prof. Feldmann of understanding their mechanism of interaction and improving it. The characterization is performed by use of a magnetic suspension balance (MSB), supplied by Rubotherm (Bochum, Germany), for gravimetric measurements of gas adsorption. As a potential CO_2 gas sorbent, nanoscale AlO(OH) hollow spheres, synthesized *via* the microemulsion approach,[12] is the first proposed. In order to improve the CO_2 capacity, basic molecules are attempted to be encapsulated.

As second class of nanomaterials, inorganic-organic hybrid nanomaterials are investigated for CO_2 capture and separation. The advantage of these materials is the possibility of functionalising them with different chemical groups. Magnesium aminoethyl phosphonate (Mg(2-AEP))[13] is here selected as a starting point. The effect of both the cation and the organic anion is analysed.

Moreover, sorption and storage of oxygen is studied. Oxygen is industrially separated from air by cryogenic distillation:[14] the research of new sorbents able to work at higher than liquid-nitrogen temperature could save a significant amount of money. As a potential O_2 sorbent, inorganic-organic hybrids containing magnetic cations are synthesised and characterised, owing to the favourable interaction between the magnetic feature of the porous materials and paramagnetic O_2.

Nanoscale hollow spheres show a large number of unique properties, allowing their use in a variety of additional interesting applications.[11a] In this work, AlO(OH) hollow spheres are additionally analysed as nanocarriers for a most widely applied anti-cancer agent: doxorubicin.[15] Moreover, in the field of medicine, nanomaterials can be applied not only as a delivery system, but, if containing a chiral information, they could be used to obtain optically pure compounds. In this context, two different hybrid nanomaterials are synthesised, aiming at the separation of (S/R)-ibuprofen mixture.

2 Gas sorption

2.1 Definitions

According to the definition given by the International Union of Pure and Applied Chemistry (IUPAC),[16] a**d**sorption is the enrichment of molecules of gases or liquids on a surface of a solid material. When the molecules of the fluid penetrate the surface layer and enter the structure of the solid material, the term a**b**sorption is used. Adsorption is a surface phenomenon, whereas absorption is a bulk or volume phenomenon. The difference between these effects can be visually understood with the help of the illustration in Figure 1: here the cake symbolises the molecule of the fluid, the person is the solid material. Absorption means eating the cake, whereas the cake splashed on the face of the person represents adsorption.[17]

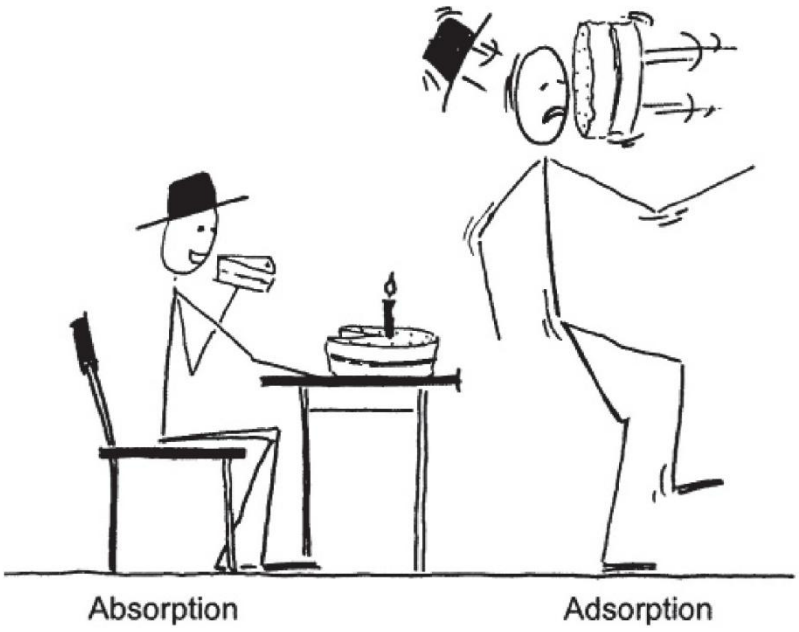

Figure 1: The difference between absorption and adsorption.[17]

The term adsorption describes the process in which molecules of a fluid accumulate in the interfacial layer. Its counterpart, desorption, denotes the opposite process, in which the adsorbed amount decreases. If the adsorption and desorption branches do not overlap, adsorption hysteresis appears. At a constant temperature, the relation between the amount adsorbed and the equilibrium pressure of the gas is known as the adsorption isotherm.[16] Figure 2 outlines the situation in an adsorption system. A list with the nomenclature used in this thesis is given, according to the references [16-18].

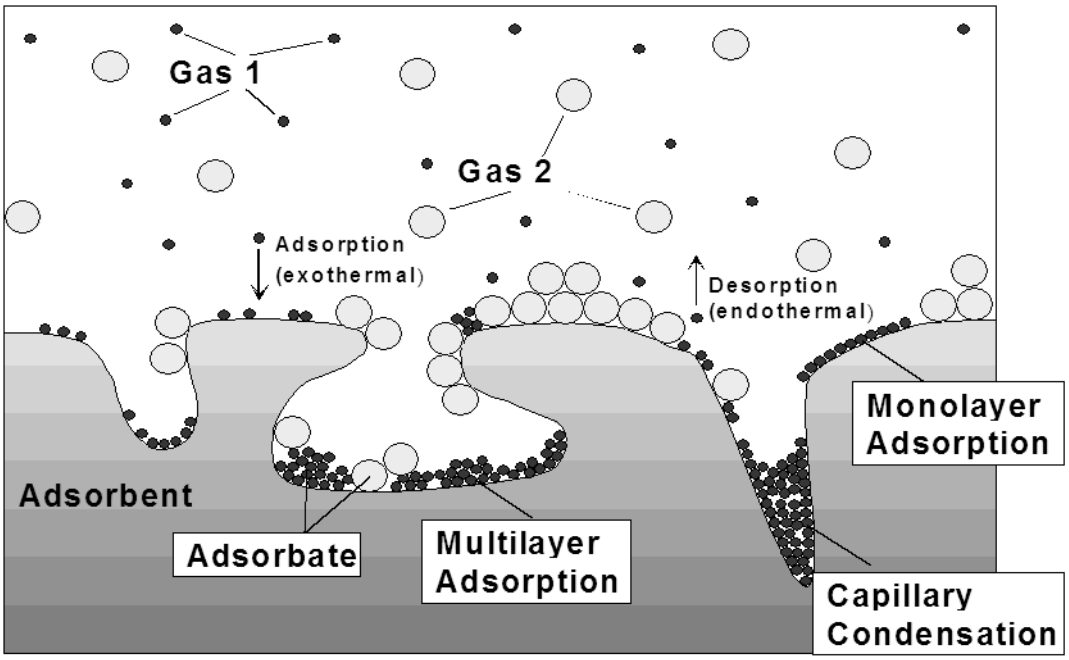

Figure 2: Definition of the different components in an adsorption system (modified from reference [17]).

- Adsorptive: gas or liquid whose molecules are interacting with the surface atoms of a solid phase;
- Adsorbent: solid phase with internal and external surfaces exposed to the molecules of gas or a liquid phase;
- Adsorbate: a set of molecules being adsorbed on the surface of an (often porous) solid material and forming a separate phase from the adsorptive;
- External surface of an adsorbent: area surrounding the discrete particles, taking into account their roughness, *i.e.* all cavities wider but not deeper than the surfaces of the pore walls;
- Internal surface of an adsorbent: area of the pore walls, excluding the external surface area.

Different phenomena can happen at the adsorbate surface. This is due to the varying possibilities of interaction of either the adsorbate molecules with the porous solid or with each other. Based on the strength of the interaction between the adsorbate molecules and the adsorbent's surface, it is possible to differenciate between physisorption and chemisorption. In physisorption, admolecules are weakly bounded, often by Van der Waals and/or dispersion forces due to induced dipole-dipole interactions; the adsorbate can be desorbed reversibly by lowering the adsorptive pressure or by working at a higher temperature. In the chemisorption process admolecules are usually strongly

bounded to the surface of the porous solid, and are subject to chemical reactions. Reversible physidesorption processes show a molar enthalpy of about 10 - 50 kJ mol^{-1}, whereas in chemisorption processes, 70 - 200 kJ mol^{-1} are necessary for desorption.[17] This suggests that chemisorption is associated with an appreciable activation energy and therefore it can be a relatively slow process. For this reason, chemisorption is often referred to activated adsorption. By contrast, Van der Waals adsorption does not require activation energy and occurs more rapidly than chemisorption.[19]

In the context of physisorption, the adsorbate molecules can exhibit many different structures:

- Micropore filling (not shown in Figure 2): adsorption only occurs in the micropores (pores with widths not exceeding 2 nm). It may be regarded as a primary physisorption process;
- Monolayer adsorption: all the adsorbed molecules are in contact with the surface layer of the adsorbent, *i.e.* the adsorbent offers many energetically nearly homogenous adsorption sites;
- Multilayer adsorption: the adsorption space accommodates more than one layer of molecules so that not all adsorbed molecules are in direct contact with the surface layer of the adsorbent;
- Capillary condensation: the residual pore space which remains after multilayer adsorption has occurred is filled with condensate separated from the gas phase by menisci. It is often accompanied by hysteresis of the isotherm. The term capillary condensation should not be used to describe micropore filling because this process does not involve the formation of liquid menisci.

It is sometimes difficult, impossible or irrelevant to distinguish between adsorption and absorption:[16] in this work, it is therefore preferred to use the more extensive term sorption, which embraces both phenomena, and its derivatives (sorbent, sorbate, sorbitive).

2.2 Adsorption isotherms

An adsorption isotherm is the thermal equation of state for the sorbed phase.[17] It depends on the temperature and pressure of the sorbitive, as well as on the mass of the sorbent (Equation (1) for single component systems, Equation (2) for a multicomponent system):

$$m^A = m^A(P,T,m^S) \quad (1)$$

m^A: mass of the sorbed phase, P: pressure of the system, T: temperature of the system, m^S: mass of the sorbent material

$$m_i^A = m_i^A(p_1 \ldots p_N, T, m^S) \quad (2)$$

m_i^A: masses of components sorbed (i = 1...N), p_i: partial pressure of component i in the gas phase, T: temperature of the system, m^S: mass of the sorbent material

The experimentally observed adsorption isotherms are classified according to IUPAC-recommendations into six different types I-VI, presented in Figure 3. Type I isotherms can be described by the Langmuir equation.[20] They have a horizontal plateau, *i.e.* the adsorbed mass approaches and maintains a constant value even at a higher pressure. Under the conditions of physical sorption, the type I isotherm represents the presence of micropores, showing micropores filling but not multilayer adsorption. When chemisorption is the main phenomenon, the Langmuir isotherm is the so-called ideal isotherm,[19] describing chemisorption on a perfectly smooth surface without interactions between adsorbed molecules.

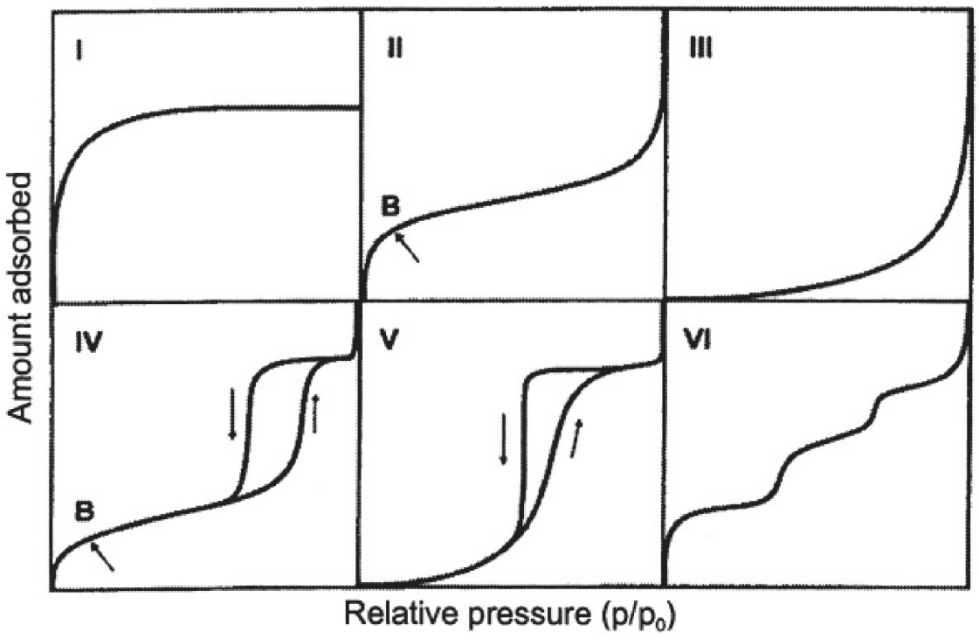

Figure 3: Main types of gas physisorption isotherms (IUPAC, 1985).[16]

Type II isotherms typically describe adsorption on mesoporous materials with monolayer adsorption at low pressure, multilayer adsorption near saturation and pore condensation, but do not involve a hysteresis.

Type III isotherms arise from nonporous or macroporous materials which interact very weakly with the sorbate , *i.e.* the sorbate-sorbate interaction is bigger than sorbate-sorbent interactions.

Type IV isotherms occur with mesoporous materials showing pore condensation together with hysteresis. Different types of hysteresis loops are observed depending on the shape of pores.

Type V isotherms deviate from type IV curves by nearly perpendicular middle portions of the adsorption and desorption branches, indicating the presence of mesopores in which phase change can occur.

Type VI isotherms are the stepped adsorption isotherm which come from layer-by-layer adsorption on a highly uniform surface. Typical examples are adsorptions on different faces of crystalline solids, or on breathing MOFs.[21]

2.3 Characterization of porous solid

A qualitative description of solid porous material can be found in Figure 4.[18]

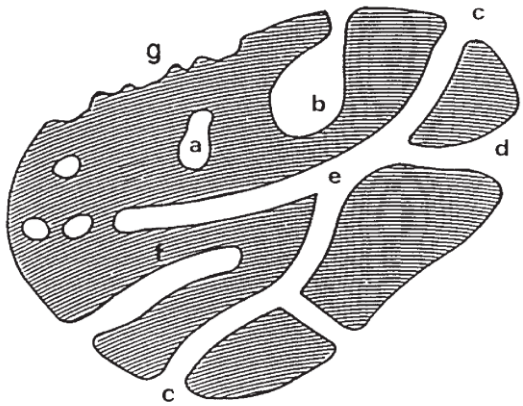

Figure 4: Schematic cross-section of a porous solid. Pores are classified according to their availability to an external fluid.[18]

a) Closed pores: pores totally isolated from their neighbours. They influence macroscopic proprieties such as density, mechanical strength, thermal conductivity, but are inactive in sorption of gases or liquids;
b) Ink-bottle shaped blind open pores: pores opened only at one end;
c) Cylindrical shaped open pores;
d) Funnel shaped open pores;
e) Through pores: pores opened at two ends;
f) Cylindrical shaped blind open pores;
g) Roughness: different from porosity, irregularities on the surface of the material that are deeper than wide.

The most common pore classification is made according to their size[16] (pore size is defined as the distance between two opposite walls of the pore):[18]

- Macropores: pores width exceeding 50 nm;
- Mesopores: pores of width between 2 and 50 nm;
- Micropores: pore width is not exceeding 2 nm.

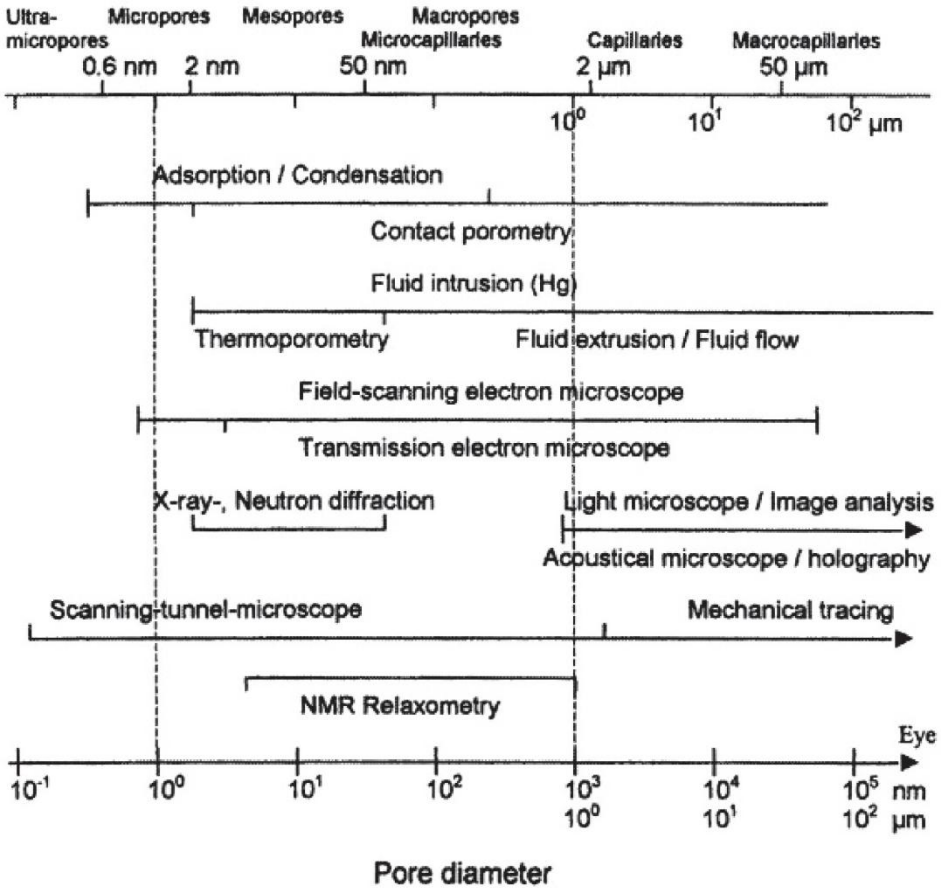

Figure 5: Physical methods for the characterization of porous materials.[17]

The determination of the porosity of a material can be performed with the use of different kinds of technologies. A summary of the most important physical methods and their range of applications are shown in Figure 5. Some methods have only access to the open pores (*i.e.* methods using a fluid), whereas other types of analysis can also detect the closed pores (*i.e.* methods using radiation). The specific surface area is defined as the accessible (or detectable) area of a solid surface per unit mass of material. Consequently it depends on the method and experimental conditions employed, and on the type of the probe used (*e.g.* adsorbate molecular size, wavelength of radiation, etc.). Since the analysis of these experimental data usually needs theoretical models to be interpreted, the recorded

values may additionally depend on the validity of the assumption inherent to these models. The pore size is even more susceptible to imprecise definition: the problems already explained for the specific surface area are complicated by the fact that pore shapes are normally highly irregular and variable. Moreover, pores usually consist of interconnected networks and the recorded results will often depend on the sequence in which pores are encountered with the used method.[18]

In the following paragraphs some methods for the characterisation of porous materials are outlined.

2.3.1 Helium measurements

This measurement can be performed either with a helium pycnometer or gravimetrically, by using a suspension balance. With the first technique, the sample is degassed at an elevated temperature and put in a vessel of known volume (V^{AC}) which, after evacuation, is filled with a known mass of helium gas (m^{He}). Assuming He is not sorbed on the surface of the material, the volume of the sorbent (V^{S}) which is impenetrable to the He molecules, the so-called helium volume ($V^{S,He}$) of the sample, can be calculated from a mass balance:

$$V^{S,He} = V^{AC} - m^{He}/\rho^{He} \qquad (3)$$

$V^{S,He}$: volume of the sample detected through He measurement, V^{AC}: volume of the vessel used to carried out the experiment, m^{He}: mass of helium used to perform the experiment, ρ^{He}: density of He

The helium measurement on the gravimetric suspension balance will be described in the paragraph 3.1, Gravimetric analysis for gas sorption – magnetic suspension balance.

2.3.2 Adsorption from gas phase

Similarly to the helium adsorption experiment described above, adsorption experiments with other gases can be taken into account for the characterisation of porous materials. Even if adsorption experiments, both volumetric (paragraph 3.2) and gravimetric (paragraph 3.1), became a standard technology, they present some limits.[17] First of all, measurements are quite sensitive to the experimental conditions, *i.e.* preparation of the porous sample, drying and outgassing, possible leaks in the gas connections, insufficient approach to equilibrium. Moreover, nowadays, there are different methods to calculate the pore size distribution from a measured gas adsorption isotherm and they often lead to different results. Gas analysis, in principle, does not allow the determination of the absolute mass of gas adsorbed (m^{A}) but only the so-called reduced mass (Ω).[22] In order to calculate

m^A from experimental data, a model assumption for the volume of the sorbent (V^S) and for the sorbed phase (V^A) should be used. Consequently, resulting m^A-data will depend on these assumptions.

In the next paragraph, different theories to calculate the surface area are expounded.

Theories for the determination of surface area and pore size distribution

Liquid nitrogen at -196°C is the recommended sorbitive for determining the surface area and the mesopore size distribution. For micropore size distribution it is necessary either to employ a range of different gases to obtain a reliable result, or more elaborated methods based on the non-local density functional theory (DFT). In the case of macropores, it is recommended to use an alternative technique to gas adsorption (*e.g.* mercury porosimetry, see paragraph 2.3.3).

The BET theory[23] (from the initials of the three researches, S. Brunauer, P.H. Emmett and E. Teller) is applied for the calculation of the specific surface area. It results in the so-called BET surface (see Volumetric analysis for gas sorption, paragraph 3.2). The BET theory, based on a simplified model of multilayer adsorption, is used as a kind of universal method for the determination of the specific surface area.[24] However, like the other models, it is based on several assumptions:

- The sample has an homogeneous flat surface consisting of equivalent adsorption sites;
- Only the uppermost molecules of a multilayered adsorbate are in dynamic equilibrium with the vapour;
- Heats of adsorptions for all layers except the first are equal to the heat of condensation;
- A molecule covered by another molecule cannot evaporate;
- At saturation ($p/p_0 = 1$) the number of layers becomes infinite;
- There are no lateral interactions between adsorbed molecules;
- Equilibrium is achieved when the rate of condensation is equal to the rate of evaporation.

The BET surface concept should only be used for non-porous, mesoporous and macroporous materials, not for microporous substances. Adsorption in micropores is governed by strong adsorbate-adsorbent interactions due to the overlapping adsorption potentials of opposing pore walls at very small distances to each other, resulting in a complete filling of the micropores at very low relative pressure. Furthermore multilayer adsorption, which is the basic assumption for the BET model, is not possible in narrow micropores.[24]

Today there are several adsorption theories in addition to the BET model mentioned above for the calculation of the surface and pore size distribution: this includes models according to Langmuir,[20, 25] Toth,[26] Dubinin and Radushkevich,[27] Kaganer,[28] Jura and Harkins[29]. However, none of them are able to describe an experimental adsorption isotherm over the complete range of pressure: they usually fail in the description of the upper range of the isotherm where capillary condensation occurs not only in the porous system, but also in the spaces between the particles. Due to the fact that physisorption normally comprises a hysteresis, Adolphs *et al.*[30] suggested to use a separate treatment for the first part of the isotherm prior to hysteresis (pure physical adsorption) compared to the second part, with hysteresis (changes in surface structures, transition to capillary condensation) therefore presenting a new method for the description of the complete isotherm.

Directly from the nitrogen desorption isotherm recorded at -196°C, the Barrett-Joyner-Halenda (BJH) method[31] for computing mesopore size distribution can be used. The theory is based on numerous assumptions:

- The system presents only cylindrical pores, thus all pores of equal radius can be regarded as behaving similarly with respect to changes of the relative pressure of the adsorbate;
- The equilibrium between the gas phase and the adsorbed phase during desorption is determined by two mechanisms, 1) physical adsorption occurs on the pore walls and 2) capillary condensation in the 'inner capillary volume'[32] (core of the fluid).

According to this theory, the radius of the pores can be described as the sum of the multilayer thickness of adsorbent on the solid surface (t, for a N_2 single adsorbent layer t = 0.354nm[33]) obtained from experimental data,[34] and the Kelvin radius r_K, achieved through application of the Kelvin equation (Equation (4)):[35]

$$r_K = -\frac{2\sigma M_v}{RT}\ ln\left(\frac{p_0}{p}\right) \qquad (4)$$

r_K: Kelvin radius (radius of curvature of hemispherical meniscus), σ: surface tension, M_V: molar volume of adsorbate liquid, R: universal gas constant, (8.314 J K^{-1} mol^{-1}), T: temperature, p_0: saturation pressure, p: equilibrium pressure

Absolute mass and reduced mass

As mentioned before, another limitation of the sorption experiments is that the entire experimental result refers to the reduced mass (Ω / mg g^{-1}), function of the sample mass, temperature, pressure/density and, of course, of the adsorption capacity of the material under

investigation. In order to explain this concept, a simplified sketch of the sorption mechanism is presented in Figure 6. The sorbent material has a mass m^S and volume V^S, with only one plane surface interacting with the fluid. The local density ρ of the sorbed molecules becomes a function of only one local coordinate (x), directed perpendicular to the plane surface of the sorbent. Taking into account that the surface forces of the sorbent are normally attractive to each other, the sorbate density ρ will be larger than the density of the sorptive gas which is far away from the sorbent (ρ^f).

The molecules of the fluid phase which are influenced by the solid sorbent surface are the sorbate or adsorbate of the fluid on the sorbent material. According to local thermodynamic equilibrium conditions, the absolute mass of the sorbate can be calculated as:[17]

$$m^A = \int_{V^A} \rho(x)\, dV \qquad (5)$$

m^A: mass of the sorbate fluid (*i.e.* all molecules of the fluid influenced by the surface forces of the sorbent material), V^A: volume of the sorbate fluid, ρ: density of the sorptive fluid (function of space coordinates (x))

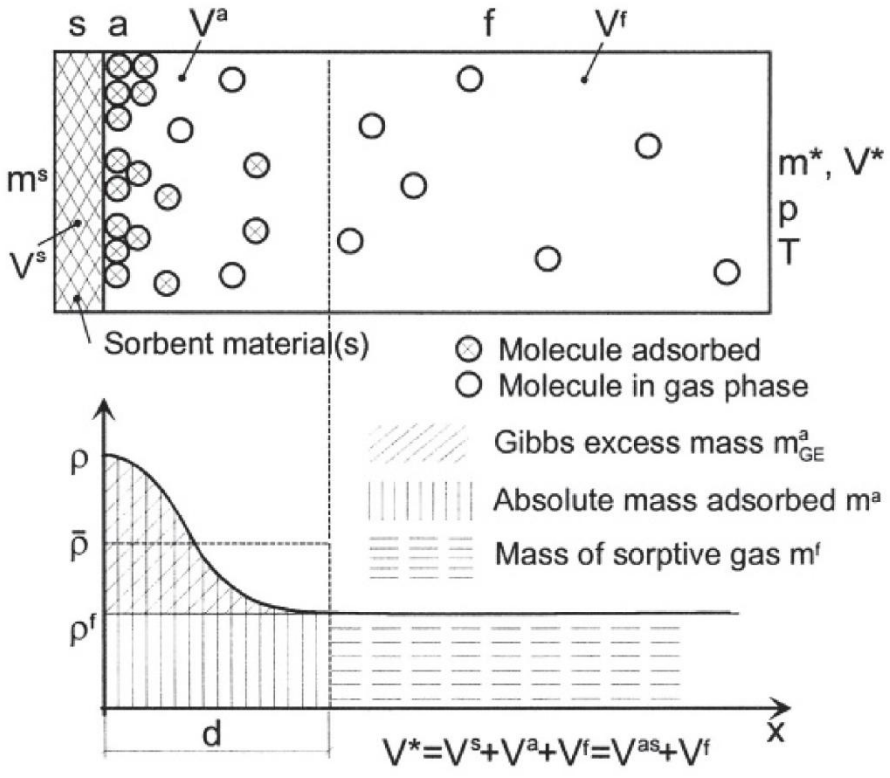

Figure 6: Plane surface sorption system in a box of total volume V* including a certain mass of sorptive gas (m*) part being sorbed on the surface of the solid, the sorbate having the absolute mass m^A (layer model) and the Gibbs surface excess mass[36] m^A_{GE}.[17]
m^a in the figure is replaced with m^A in the text for practical purpose.

Assuming that the sorptive fluid is far away from the sorbent solid material to reach an equilibrium state of constant density

$$\rho^f = \lim_{x \to \infty} \rho(x) \tag{6}$$

it is possible to define the so-called Gibbs excess mass[36] as

$$m^A_{GE} = \int_{V^A} \left(\rho(x) - \rho^f\right) dV = m^A - \rho^f V^A \tag{7}$$

m^A_{GE}: Gibbs excess mass, m^A: mass of the sorbate fluid, V^A: volume of the sorbate fluid, ρ: density of the sorptive fluid, ρ^f: density of the sorptive gas far away from the sorbent

The Gibbs excess mass is the difference between the mass of the fluid sorbed on the material and the mass of the sorptive fluid that would be included in the volume V^A if there were no attractive surface forces of the sorbent material. According to the definition of Gibbs excess mass, the experimental results corrected for the buoyancy acting on the solid sample are always underestimations of the 'real' amount of gas sorbed (or absolute mass sorbed). From a geometrical point of view, it is possible to write:

$$m^A_{GE} = \rho^f \left(V^* - V^S\right) \tag{8}$$

m^A_{GE}: Gibbs excess mass, ρ^f: density of the sorptive gas far away from the sorbent, V^*: total volume, V^S: volume of the solid sorbent

After the application of the mass balance and the introduction of the reference gas density ρ^{f*} as the density of the sorption gas would have if no sorbent surface forces were acting on its molecules, it results to:

$$m^A_{GE} = \left(\rho^{f*} - \rho^f\right)\left(V^* - V^S\right) \tag{9}$$

m^A_{GE}: Gibbs excess mass, ρ^{f*}: density of the sorption gas would have if no sorbent surface forces were acting on its molecules, ρ^f: density of the sorptive gas far away from the sorbent, V^*: total volume, V^S: volume of the solid sorbent

Equation (9) allows a calculation of the Gibbs surface excess from measured data if the volume of the sorbent material (V^S) is known. In summary, the Gibbs excess data are the experimental data corrected for the buoyancy effect acting on the solid sorbent: the corresponding isotherms are called excess sorption isotherms or surface excess isotherms.

The reduced mass (Ω) is the difference between the mass sorbed and the buoyancy related to the volume of sorbent/sorbate system in the sorptive gas density (ρ):[17]

$$\Omega = m^A - \rho\,(V^S + V^A) \qquad (10)$$

Ω: reduced mass, m^A: mass of the sorbate, ρ: density of the phase gas, V^S: volume of the solid sorbent, V^A: volume of the sorbate

The difference between the reduced mass and the surface excess amount is illustrated in Figure 7.

The calculation of the absolute mass sorbed (m^A) requires the application of models: two different models are presented below for the determination of m^A from excess isotherm data.[37]

1. The absolute amount of gas sorbed m^A can be described as the sum of the surface excess mass (m^A_{GE}, experimental result) and the product of the density of the gas phase and the volume of the sorbed phase (V^A):

$$m^A = m^A_{GE} + \rho\, V^A \qquad (11)$$

m^A: mass of the sorbate, m^A_{GE}: Gibbs excess mass, ρ: density of the phase gas, V^A: volume of the sorbate

The volume of the sorbate is unknown, but can be obtained from $V^A = m^A/\rho^A$, whit ρ^A as the density of the sorbate:

$$m^A_{GE} = m^A\left(1 - {}^{\rho}/_{\rho^A}\right) \qquad (12)$$

m^A_{GE}: Gibbs excess mass, m^A: mass of the sorbate, ρ: density of the phase gas, ρ^A: density of the sorbate

With the assumption that the sorbate is in a liquid-like state ($\rho^A = \rho_{liq}$), Equation (12) can be used for the calculation of the absolute amount, but only for fluids below their critical point. In the supercritical region, the mass of the sorbed gas can be substituted by $m^A = V^A\rho^A$. Thus the surface excess mass is:

$$m^A_{GE} = V^A\rho^A - V^A\rho \qquad (13)$$

m^A_{GE}: Gibbs excess mass, V^A: volume of the sorbate, ρ^A: density of the sorbate, ρ: density of the sorbtive

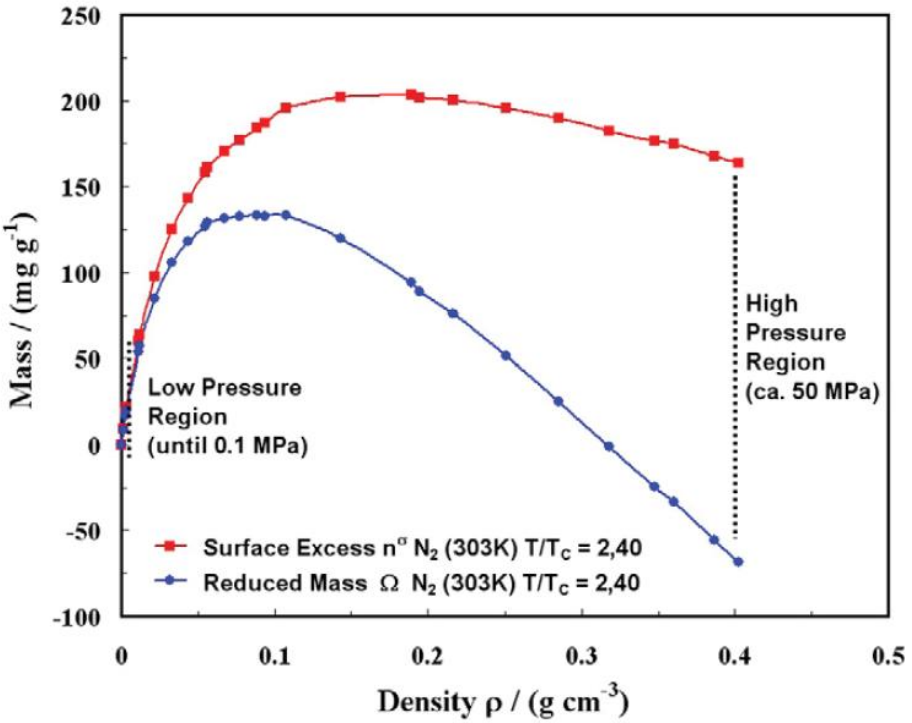

Figure 7: Nitrogen (30 °C) sorption isotherm using the reduced mass (circles) and the surface excess mass (squares) on the metal-organic framework HKUST-1. The increasing effect of buoyancy on the pressure is obvious.[37] Connecting lines are guides for eyes. (1 MPa = 10 bar).

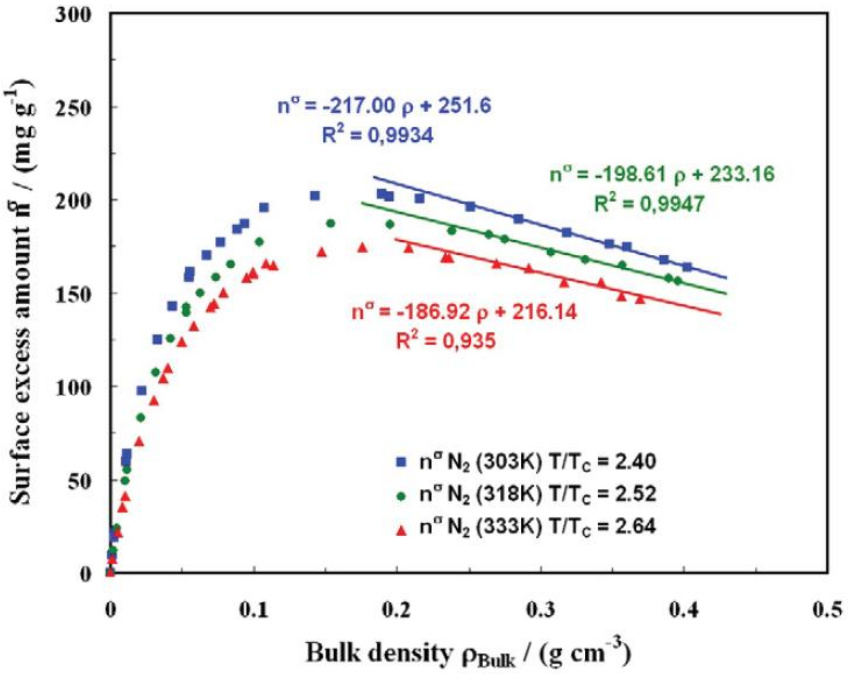

Figure 8: Nitrogen sorption isotherm in temperature range 30-60 °C on the metal-organic framework KUST-1. Each isotherm is fitted in the linear range above the maximum of the surface excess with Equation (13).[37]

The surface excess isotherm shows a maximum at the point where the difference between the density of the bulk phase and the density of the adsorbed phase is maximal; for high pressures, the bulk phase is more compressible than the adsorbed phase and the surface excess decreases.[37] By fitting the experimental surface excess masses against the density of the adsorptive in the linear range after the maximum, by using Equation (13), it is possible to obtain the adsorbed volume (V^A) and the density of the sorbate (ρ^A) by linear regression (Figure 8).

Equation (12) with $\rho^A = \rho_{liq}$ is then applied for the non critical conditions (*e.g.* for nitrogen, 0 bar < P < 40 bar, T = 30 °C), whereas equation (13) is used above the critical point (*e.g.* for N_2, P > 40 bar, T = 30 °C).[37]

2. A second model for the calculation of the absolute amount sorbed is based on the assumption that the specific pore volume obtained from the N_2 sorption isotherm at -196°C (BJH theory) is the volume of the sorbate. In this case, the total pore volume must be filled with the sorbate. By applying this approach, the resulting absolute amount can be explained as the maximum sorption capacity or as an overall limiting value.[37]

The result of the application of the two models here described is shown in Figure 9.

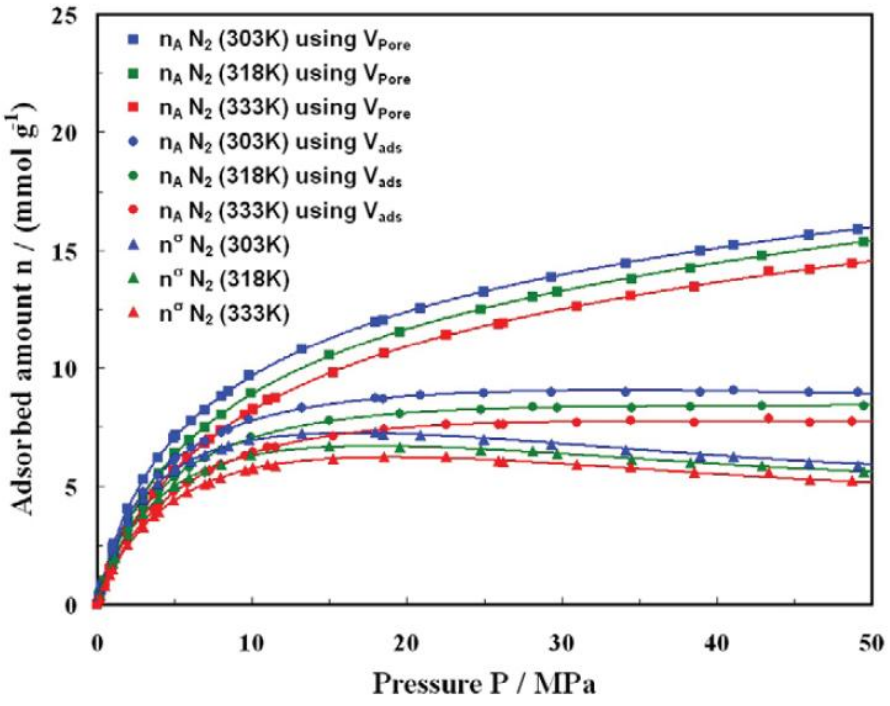

Figure 9: Nitrogen sorption isotherms in temperature range 30-60 °C on the metal-organic framework HKUST-1. Surface excess (triangles) *vs.* absolute amount sorbed using two different models: models 1 (circles) and model 2 (squares). Plotted lines are fitted with Padè equation.[37]

2.3.3 Other methods

It is impossible describe a porous material without a detailed explanation of the method employed to study it. There are several other methods, not used in this thesis, for the characterisation of porous solid such as stereology, thermoporometry, nuclear magnetic resonance (NMR), mercury intrusion porosity, only to cite some of them. A more detailed description of these analytical methods can be found in the literature.[17, 33]

2.4 Gas sorption for industrial applications

2.4.1 Carbon dioxide capture technology

One of the greatest environmental problems of our times is, without doubt, the rising level of atmospheric carbon dioxide (CO_2) concentration. These emissions, which stem mainly from the combustion of coal, oil and natural gas,[38] are not expected to stop in the future, due to the economic growth and industrial progress, particularly in developing countries.[3]

The prospect of an aggravation of the climatic situation due to global warming is a subject of widespread public concern and the urgent need for technologies to decrease Earth atmospheric concentrations of greenhouse gases, has encouraged programs from national and international governments and industries.[39] A modification of the existing infrastructures from carbon-based sources to a cleaner alternative would be ideal in this regard. Such a change, however, requires considerable modifications to the current energy production processes. Alternative technologies proposed up to now are not yet sufficiently developed to satisfy the large-scale industrial demand.[5] Thus, greenhouse gases, in particular carbon dioxide (Figure 10), capture and sequestration technologies will continue to play a vital role in the climatic situation until more significant modification to the energy infrastructure can be realised.[5]

The captured CO_2 can be subjected to permanent sequestration in geological formations: The Carbon Sequestration Regional Partnerships[40] has estimated so far that 1120 to 3400 billion tonnes of carbon dioxide can be sequestered in identified formations. In addition, with higher petroleum prices, there is an increased interest in using CO_2 flooding, as a means to enhance oil recovery (EOR).[41] The reusing of the captured CO_2 as a reactant in chemical transformations[42] is also an alternative option, although it would not be a viable long-term strategy because the tremendous scale of worldwide CO_2 emissions (ca. 30 Gt per year)[43] will rapidly saturate the market of

commodities prepared there from.[5] However, none of these activities will be possible unless CO_2 is first captured.

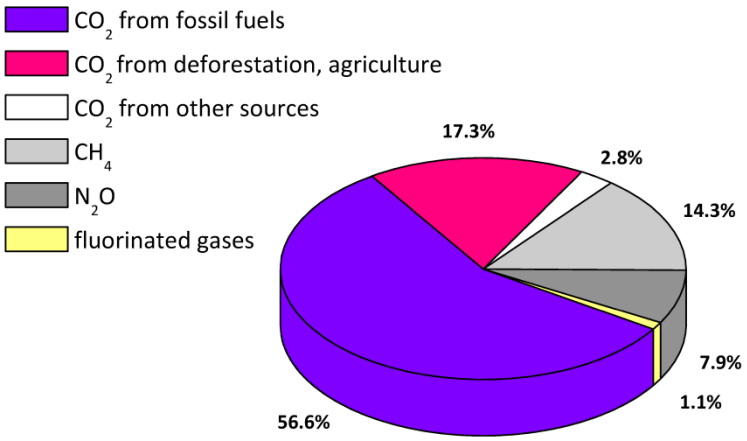

Figure 10: Global greenhouse gas emission sources in 2004 of which approximately 77% are represented by CO_2 emissions.[3]

None of the currently available CO_2 capture process are economically feasible to sequestrate the greenhouse gas, since they consume large amount of parasitic power and significantly increase the cost of electricity.[41]

Aqueous alkanolamine solutions have been extensively studied to date for CO_2 capture and are still considered state-of-the-art despite being known for many years.[4] The amino group interacts with the carbon in CO_2 through a nucleofilic attack to form a C–N bond and depending on the amine, this result in the production of a carbamate or bicarbonate species (Figure 11).

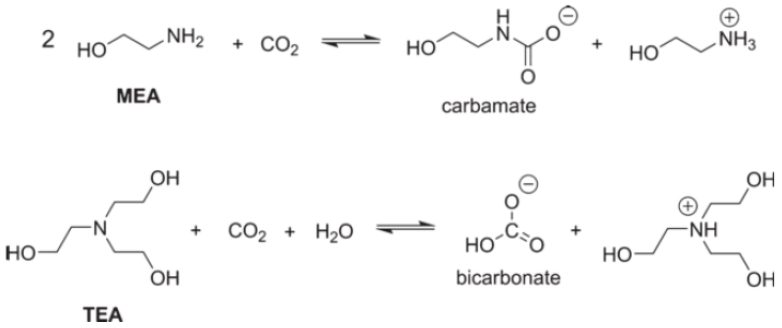

Figure 11: Reaction CO_2 with monoethanolamine (MEA) to give a carbamate product (upper) and the corresponding reaction with triethanolamine (TEA) resulting in a bicarbonate species.[5]

Monoethanolamine (MEA) is normally dissolved in water at a concentration of ca. 20 - 30% in weight. The reaction of two equivalents of MEA with CO_2 results in the formation of an anionic carbamate species and a corresponding ammonium cation. In the case of triethanolamine (TEA), the

steric obstacle allows the formation of a bicarbonate species instead of a carbamate with 1:1 ratio stoichiometry. Although amines have been used for many years, particularly in the removal of acidic gases from natural gas, they present several significant limitations as adsorbents for large-scale CO_2 capture. The solutions are unstable toward heating, which limits the temperature available for full regeneration of the sorbent. Decomposition of the amine results in a reduction of adsorption performances over time, diminishing the lifetime of the solutions. The amine solutions are also corrosive toward the vessels in which they are contained, although this is usually prevented by limiting the amine concentration, resulting in another disadvantages: the decrease of the reactant concentration and the increase of the amount of water to heat in order to regenerate the material. Effectively, the high heat capacity of water is the main contribution to the regeneration energy costs and this is the main reasons why solid porous adsorbents, which can have lower heat capacity, are promising materials to reduce the regeneration energy penalty.[5]

Zeolites[44], porous aluminosilicate materials with high chemical and thermal stability, have been largely studied in the context of CO_2 capture: zeolite 13X, for example, with its high surface area (A_{BET} =726 $m^2 g^{-1}$) shows 16.4 %wt CO_2 sorbed at room temperature and at 0.8 bar.[45] However, many of the zeolites studied to date have become readily saturated with the water vapour present in the flue gas stream, reducing the CO_2 adsorption capacity over time.[46]

Activated carbons have also attracted attention as CO_2 sorbents.[5] Activated carbons are amorphous forms of carbon than can be prepared by pyrolysis of various carbon-containing resins, fly ash or biomass.[47] Compared to zeolite, they show lower CO_2 capacities at low pressure, but greater adsorption capacities at higher pressure, due to their higher surface. Moreover, activate carbons present a hydrophobic nature eliminating the problem of the water presence. One advantage more over zeolites, they show lower heat of adsorption for CO_2, resulting in a lower temperature of complete regeneration,[48] remaining, nevertheless, an high energy required process.[8]

In addition to zeolites and activated carbons, other classes of porous materials are emerging as potential carbon dioxide adsorbents, including amine-grafted silicas, microporous organic polymers and covalent-organic frameworks.[5] However, the most studied materials for gas sorption and separation are the metal-organic frameworks (MOFs). MOFs are a class of hybrid materials built from metal ions with well-defined coordination geometry and organic bridging ligands forming crystalline one-, two- or three-dimensional coordination networks. In comparison with the other traditional adsorbent materials used in industry described above, MOFs possess many excellent features,

including large surface areas, high cristallinity with well-defined pore properties, easily tunable and tailorable structures and chemical functionalities.[9] However, engineering MOFs with incredibly high capacity and selectivity toward CO_2, while being at the same time not expensive to synthesize and stable toward water vapour, remains a challenge.

Wang *et al.*,[49] proposed a solid sorbents classification according to the temperature at which they work: low-temperature solid sorbents (< 200 °C) include zeolites, carbon-based sorbents, MOFs, several alkali metal-carbonate-based adsorbents and amine-based solid adsorbents. Hydrotalcite-like compounds have been classified as intermediate-temperature (200 - 400 °C) solid adsorbents. Finally, at high-temperatures (> 400 °C) are calcium-based adsorbents, lithium zirconate and several alkali ceramic-based adsorbents. Table 1 gives a summary of some CO_2 sorbent material, their range of application and their uptake recorder at 1 bar of pressure.

In consideration to how best to improve CO_2 capture, there are three main scenarios in which new materials could serve to reduce the energy requirements of capture from coal-derived power generation, as illustrated in Figure 12. In post-combustion capture, CO_2 is removed from the flue gas which results after combustion. Existing power plants use air for combustion, generating a flue gas that is at atmospheric pressure and typically has a CO_2 concentration of less than 15%. Thus, the thermodynamic driving force for CO_2 capture from flue gas is low (CO_2 partial pressure is normally less than 0.15 bar), creating a technical challenge for the development of cost effective advanced capture processes.[41] Alternatively, pre-combustion capture can be performed following gasification of the coal prior to combustion, producing a high-pressure flue gas containing H_2 and CO_2. This carries two advantages: first, CO_2/H_2 is an easier separation than the CO_2/N_2 separation required in post-combustion, owing to the greater difference in the polarizability and quadrupole moment of the molecules.[5] Secondly, the concentration and pressure of CO_2 containing stream is increased in comparison to post-combustion, reducing the size and cost of the capture facilities.[41] Another possible method of reducing CO_2 emissions would be the performing of oxy-fuel combustion, in which almost pure O_2 is utilised for the combustion of coal or natural gas, leading to a stream composition of almost pure CO_2, avoiding the necessity to selectively adsorb CO_2.

Each of the three process requires different gas separation, and, due to the different physical proprieties of the gases,[5] as listed in Table 2, there is a need for materials with different characteristics, depending on their applications.

Table 1: CO_2 sorbents with their uptake at 1bar.

Material	Temperature / °C	CO_2 uptake (at 1bar) / mg g^{-1}	Remarks	Ref.
Zeolite 13X	25	164	-Energy intensive regeneration	[45]
Activated carbon-MAXSORB	25	22	-Energy intensive regeneration	[50]
Lithium zirconate (Li_2ZrO_3)	500	100	-Long adsorption rates -Partially irreversible	[51]
Mg-MOF-74	25	365	-Active at T ≤ 25 °C	[52]

H. Furukawa in collaboration with O. Yaghi[53] achieved the record for CO_2 capacity: 2870 mg g^{-1} at 50 bar and 50 °C with MOF-200 and MOF-210 (Figure 13 and Figure 14) in 2010. It has to be underlined, however, that the uptakes reported are the absolute amounts estimated from the application of the second model as reported in paragraph 2.3.2. Furthermore, the authors, in view to pre-combustion applications, present a comparison between CO_2 isotherms collected at 25 °C and H_2 isotherms performed at -196 °C, and they do not report comparisons under the same conditions (same temperature, same range of pressures).

At low pressure, the best material to date is again a MOF, MOF-74 (Mg_2(dobdc), dobdc: 2,5-dioxido-1,4-benzenedicarboxylate),[52] with 36.5 %wt of CO_2 adsorbed at 1 bar of pressure at 25 °C. Table 3 summarizes high-pressure CO_2 adsorption capacities in selected metal-organic frameworks, whereas Table 4 reports CO_2 and N_2 uptakes (values estimated from single gas isotherms) in selected MOFs at pressure relevant to post-combustion CO_2 capture.

Table 2: Physical parameters of some gases.[54]

Molecule	Kinetic diameter / Å	Polarizability $x10^{-30}$ / m^3	Dipole moment / C m^2	Quadrupole moment $x10^{-40}$ / C m^2
CO_2	3.30	2.63	0	13.4
N_2	3.64	1.77	0	4.7
O_2	3.46	1.58	0	1.2
CH_4	3.82	2.60	0	0
Ar	3.70	1.66	0	0

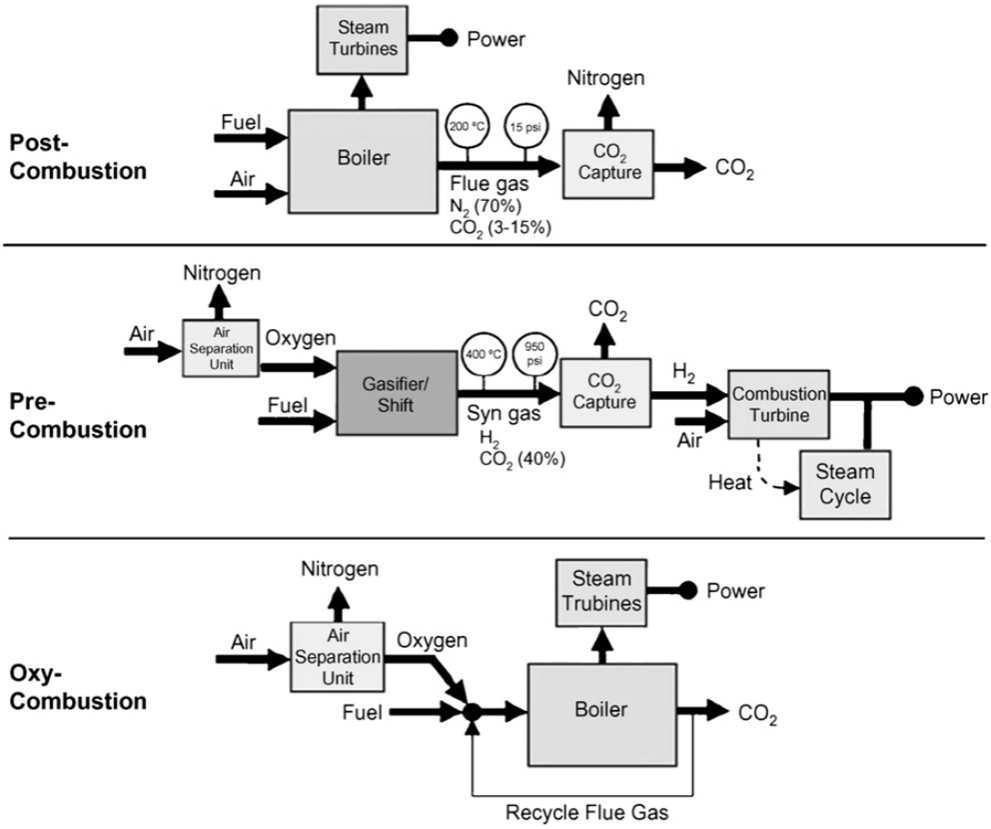

Figure 12: Block diagrams illustrating post-combustion, pre-combustion and oxy-combustion systems.[41] (15psi = 1bar).

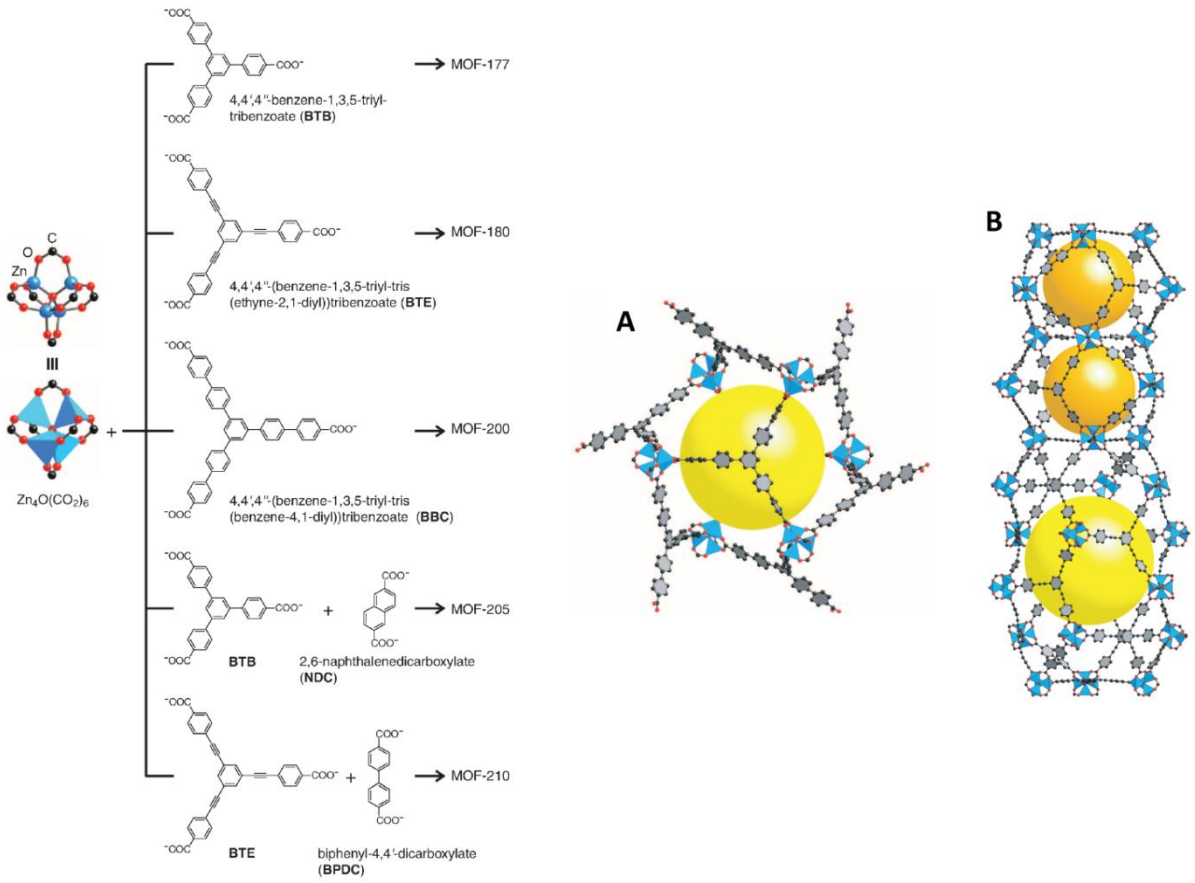

Figure 13: $Zn_4O(CO_2)_6$ unit (left) is connected with organic linkers (middle) to form MOFs. A) Crystal structure of MOFs-200 and B) MOF-210. The yellow and orange balls are placed in the structure for clarity and to indicate spaces in cages. Zn: blue tetrahedral, O: red, C: black. Hydrogen atoms are omitted for clarity.[53]

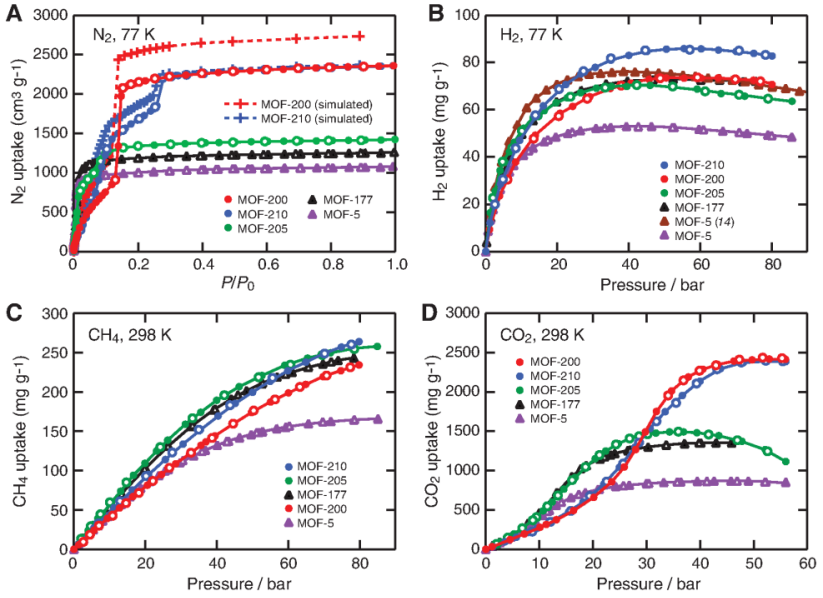

Figure 14: A) Low-pressure N_2 isotherms of MOF-5, -177, -200, -210 at -196°C. Simulated isotherms of MOF-200 and -210 were overlaid. High pressure H_2 isotherms measured at -196 °C (B). (C) CH_4 and (D) CO_2 isotherms were measured at 25 °C on the same MOFs.[53]

Table 3: High pressure CO_2 adsorption capacities in selected metal-organic frameworks.[5]

Material chemical formula [a]	Common names	A_{BET} / m^2g^{-1}	Capacity[b] / %wt	p / bar	T / °C	Ref.
$Zn_4O(BTE)_{4/3}$ (BPDC)	MOF-210	6240	74.2	50	25	[53]
$Zn_4O(BBC)_2$ $(H_2O)_3$	MOF-200	4530	73.9	50	25	[53]
Cu_3(TCEPEB)	NU-100	6143	69.8[d]	40	25	[55]
$Zn_4O(FMA)_3$		1120	69.0[d]	28	27	[56]
Mg_2(dobdc)	Mg-MOF-74	1542	68.9[c]	36	5	[57]
Ni_2(dobdc)	Ni-MOF-74	1218	54.2	22	5	[57]
$Be_{12}(OH)_{12}$ $(BTB)_4$	Be-BTB	4030	58.5	40	40	[58]
$Zn_4O(BTB)_2$	MOF-177	4500	60.8	50	25	[53]
$Cr_3O(H_2O)_2F$ $(BDC)_3$	MIL-101(Cr)	3360	50.2[d]	30	25	[59]

[a] See list of abbreviations. [b] Adsorption capacities are calculated from absolute adsorption isotherms unless otherwise noted and estimated from adsorption isotherms in case where the values were not specially reported. [c] Reported capacity was calculated from the excess adsorption isotherm. [d] It was not clear from the reference whether the reported isotherms were in absolute or excess adsorption.

Table 4: CO_2 and N_2 uptake in selected metal-organic frameworks at pressure relevant to post-combustion CO_2 capture.[5]

Material chemical formula [a]	Common names	CO_2 uptake at 0.15 bar /%wt [b]	N_2 uptake at 0.75 bar /%wt [b]	Selectivity [c]	T /°C	Ref.
Mg_2(dobdc)	Mg-MOF-74	20.6	1.83	44	30	[60]
Ni_2(dobdc)	Ni-MOF-74	16.9	2.14	30	25	[61]
Zn_2(dobdc)	Zn-MOF-74	7.6			23	[62]
$Cu_3(BTC)_2$	HKUST-1	11.6	0.41	101	20	[63]
Co_2(adenine$_2$) $(CO_2CH_3)_2$	bio-MOF-11	5.4	0.28	65	25	[64]
$Zn_4O(BTB)_2$	MOF-177	0.6	0.39	4	25	[60]

[a] See list of abbreviations. [b] When not directly reported, values were estimated from adsorption isotherms in the corresponding reference. [c] Selectivities were calculated from the pure components isotherms by dividing the mass of CO_2 adsorbed at 0.15 bar by the mass of N_2 adsorbed at 0.75 bar, according to the formula reported by Sumida *et al.*.[5]

The research of the best CO_2 capture material is still a challenge. The most crucial performance parameter is selectivity in regard to CO_2: a high selectivity is essential, such that the CO_2 component of the flue gas is completely removed. However, if the interaction is too strong, the desorption process will require high energy, raising the regeneration costs. Furthermore, the material should exhibit high stability under the power plant conditions, in order to present a long lifetime. It should also adsorb CO_2 at high density, so that the volume of the adsorbent bed can be minimised.[5] It is preferable that the adsorption rates are fast, an essential point for practical gas separation.[8] Other desirable characteristics are: presence of non-toxic constituents, good tolerance to contaminants, attrition resistance, low cost production[41] and an easy synthesis in view of industrial commercialisation.

2.4.2 Selective sorption of oxygen

Oxygen is one of the most commonly used commodity chemicals in the world with over 100 million tons produced every year.[65] The demand for pure O_2 could even grow in the near future, due to its potential in processes associated with the reduction of CO_2 emissions (see paragraph 2.4.1).[66]

Since the supply of air is almost infinite, the selective separation of O_2 is currently performed from air (O_2/N_2 separation), using an energy-intensive cryogenic distillation process. Moreover, the oxygen purity obtained is typically limited to 95%.[67] Furthermore, argon is present in the feed air with a concentration of ca. 1% and, due to similar adsorptive properties, O_2 and Ar exhibit closely related adsorption isotherms in many materials.[68] Currently, three methods are commercially used for O_2/Ar separation.[67] 1) Cryogenic distillation: high purity O_2 (99.5 %) and Ar (99.9 %) can be obtained, but, since the boiling points of the two pure gases are very close, a very high reflux ratio and a large number of theoretical stages are required, increasing the capital cost. 2) Catalytic hydrogenation: O_2 is removed as water by reaction with hydrogen. Consequently oxygen recovery is not possible. Moreover, the use of H_2 increases the operating cost and the method is only practical to remove traces of O_2 from a crude Ar stream. 3) Cryogenic adsorption: the adsorption equilibrium selectivity of oxygen to argon on the commercially available sorbent 4A zeolite becomes sufficiently large at very low temperature (-150 °C to -190 °C) to enable adsorption separation,[69] resulting in a very high energy intensive process.

By employing materials that selectively adsorb O_2 and can operate near ambient temperatures, a reduction of costs could be feasible. Oxygen is a paramagnetic gas with a relatively high magnetic susceptibly and can be attracted with a magnetizing force. Conversely, other gases are diamagnetic with low and negative magnetic susceptibly. The use of a magnetic sorbent could enhance the selectivity toward O_2, as was reported by Madeani *et al.*.[70] The selective separation of O_2 over N_2 was also demonstrated on Fe_2(dobdc) MOF by Bloch *et al. via* partial charge transfer from iron(II) to O_2.[66] In this case, unsaturated Fe(II) coordination sites show capacity to reversibly bind O_2 at -47 °C whereas, at higher temperature a thermal activation, barrier to the formation of iron(III)-peroxides is overcome and desorption of O_2 is no longer possible.

The search for a selective sorbent for O_2, which is able to work at room or higher temperatures, which is easy to regenerate and at the same time inexpensive, remains a difficult task.

2.4.3 Separation of light hydrocarbons

C_1 to C_3 light hydrocarbons CH_4, C_2H_2, C_2H_4, C_2H_6, C_3H_6 and C_3H_8 are very important energy sources and raw chemicals. Methane has been considered as the most promising alternative fuel for future vehicle transportation; ethylene and propylene are chemicals for the synthesis of polymers and it is essential to obtain high quality and purity of such commodity chemicals. Due to their similar sizes and low relative volatilities of the molecules, separations of olefin/paraffin mixtures has to be currently performed using highly energy-intensive cryogenic distillation.[71] Because these gas mixtures are produced by cracking long-chain hydrocarbons at elevated temperatures, a considerable energy penalty arises from cooling the gases to the low temperatures required for distillation. Consequently, tremendous energy savings could be made using materials enabling the efficient separation of olefins and paraffin's at higher temperatures.[72]

The most studied MOFs in this context are the metal organic frameworks of the family M_2(dobdc) (M = Mg, Mn, Fe, Co, Ni, Zn). Although different proprieties have been tested to adjust separation capacities, such as tuning the pore sizes, curvatures and porosities, it has been demonstrated that the open coordination sites at metals play the most important roles in differentiating interactions with light hydrocarbons.[73] Fe_2(dobdc), for example, displays a strong affinity for the unsaturated hydrocarbons acetylene, ethylene and propylene, resulting in ion-induced dipole interactions between coordinatively unsaturated metal cations and a hydrocarbon.[72]

The research in this particular field is still growing and the exploration of new porous materials will be strongly highly needed in the near future for the efficient separation of light hydrocarbons.

3 Analytical methods

3.1 Gravimetric analysis for gas sorption – magnetic suspension balance

The gravimetric technique for gas sorption determines the weight of gas sorbed on a solid material. The sample is exposed to an adsorptive gas by increasing the pressure stepwise at a constant temperature. The buoyancy effect correction is then applied and experimental data are interpreted. The final result is an isotherm, plotted as gas pressure (bar) *vs.* gas uptake (mg g^{-1}).

In the 1980's, researchers from the Ruhr-University Bochum invented a new type of magnetic suspension balance (MSB). The principal improvement introduced was the decoupling of the measuring cell from the weighing instruments, allowing measurements with highly corrosive fluids and in quite a broad range of pressure and temperature.

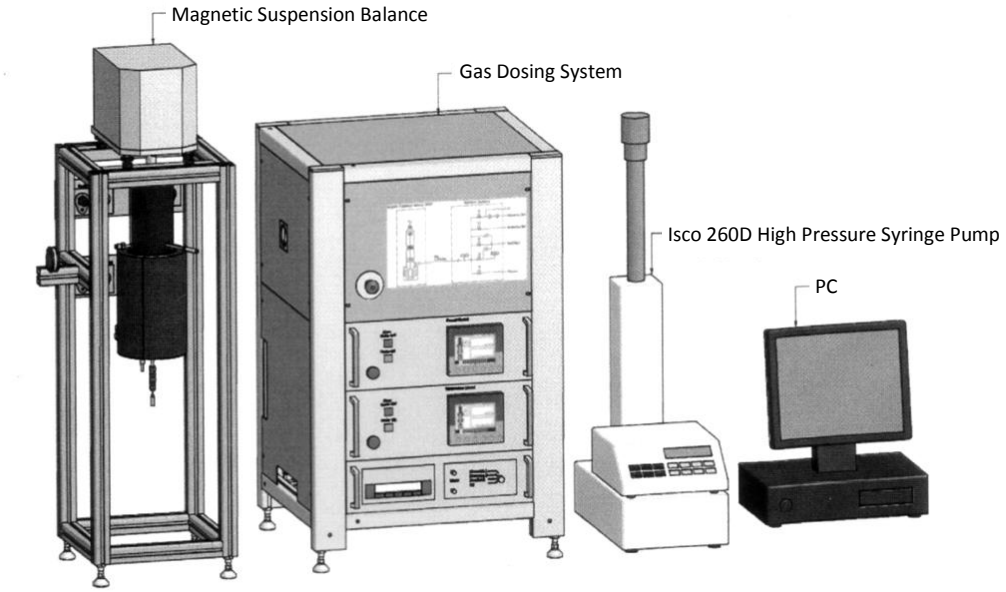

Figure 15: Magnetic Suspension Device, components.[74]

The components of the magnetic suspension balance are shown in Figure 15, whereas Figure 16 represents the MSB set-up. This device allows a detection of change in forces and mass acting on the sample with high accuracy. Its operating procedure is represented in Figure 17: the sample under investigation is linked to a suspension magnet which consists of a permanent magnet, a sensor core and a device decoupling the measuring load (sample). An electromagnet maintains a freely

suspended state of the suspension magnet *via* an electronic control unit. Using this magnet suspension coupling state, the measuring force is transmitted contactless from the measuring chamber to the microbalance that is located outside the chamber, under ambient atmospheric conditions. The controlled suspended state is achieved by means of a direct analogous control circle. This modulates the voltage on the electromagnet in such a way that the suspension magnet is constantly located in a vertical position.[74]

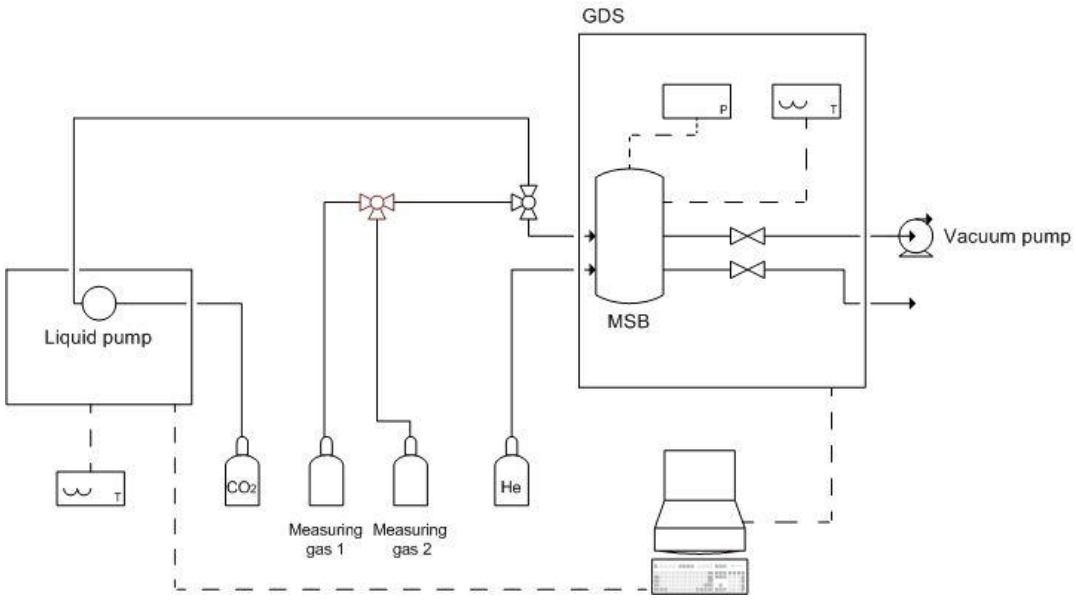

Figure 16: Magnetic suspension device, schematic view.

The second component of the instrument is the gas dosing system (GDS), with whom the gas pressure in the balance volume is adjusted. This is realised by dosing in (sorption) and dosing out (desorption) the gas into the measurement cell. In particular, the dosing of carbon dioxide is controlled by an external gas compressor pump (ISCO Syringe Pump, Lincoln, US): it compresses the gas and it enables working up to 200 bar of CO_2 pressure. Furthermore, a cooling jacket is used for removing the heat of compression as well as for liquefying the CO_2 before compression.

All the instruments are controlled by the MessPro software (Rubotherm, Bochum, Germany). Prior to measuring, the experiment is configured in segments; for each step, the pressure and the temperature are defined. Each segment can be stopped by a time switch or after reaching the equilibrium (Table 5). The measured mass change, pressure, sample temperature, and gas flow are displayed and saved.[74]

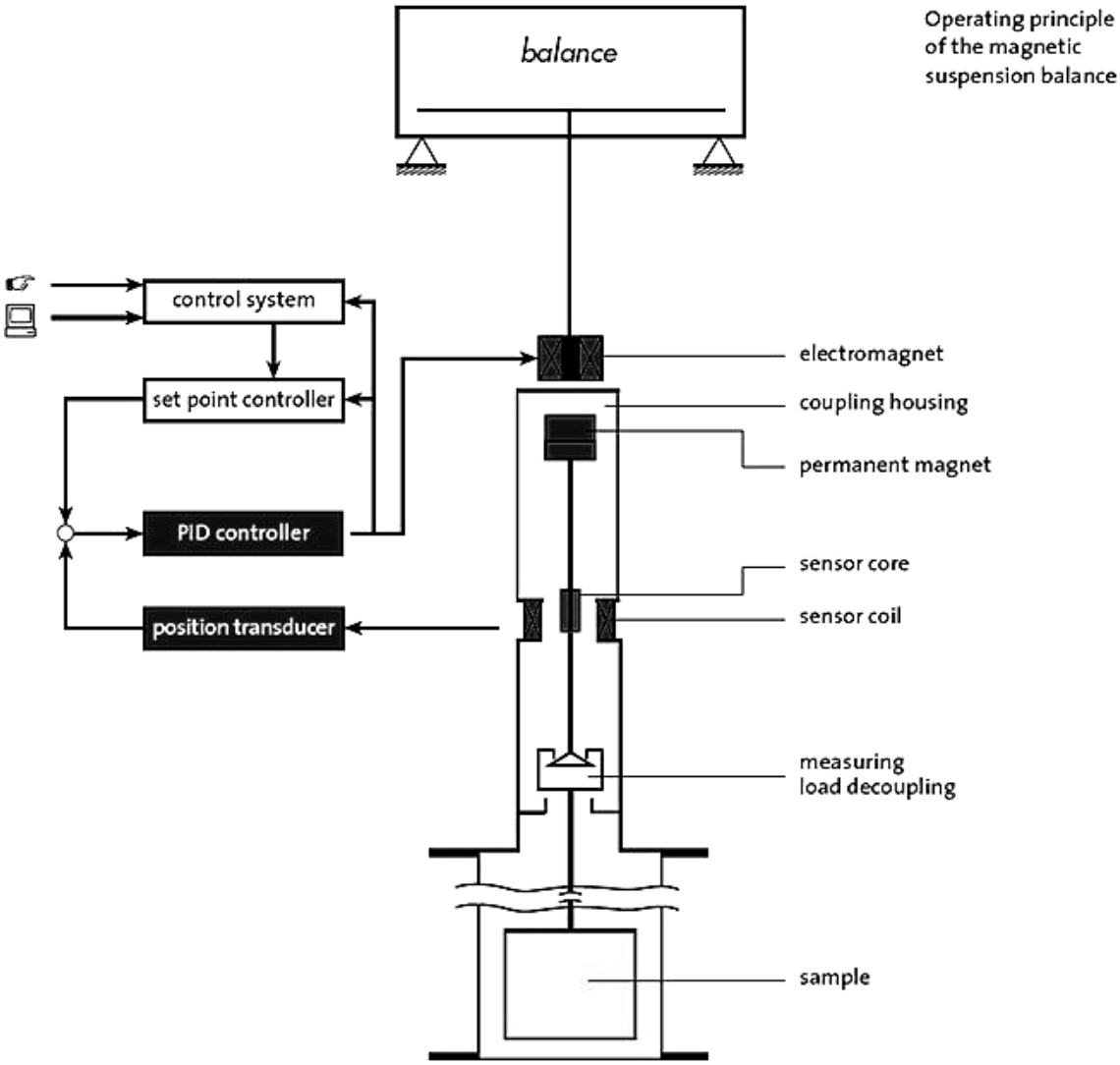

Figure 17: Operating principle of the magnetic suspension balance.[74]

The gravimetric method for the determination of the amount of gas sorbed on a solid, results in the direct measurement of the quantity of the sorbate. The main and only source of error is the determination of volumes and, as a consequence, the correction for buoyancy. For this purpose, helium is chosen for the measurement of volumes, even if in this context it can also be problematic, mainly for two reasons. On the one hand, at low temperatures, helium can indeed be sorbed in small amounts, so that the calculated sample volume is deceptive. On the other hand, the buoyancy effect is proportional to the adsorptive bulk density, but the density of helium is several times lower than the density of the gas measured under the same conditions[37] (with the exception of hydrogen): this means that the accuracy of the He buoyancy correction is low. For this reason, it is always recommended to perform buoyancy correction measurements at least in the same range of pressure of the sorption isotherm and at the same temperature.[75]

Table 5: Equilibrium conditions in a MSB measurement. (*) The average time is the period of time, over which an arithmetical mean will be calculated from the values of temperature, pressure and weight.

Parameter	Equilibrium conditions
Average time / min(*)	10
Weight – Bandwidth / ± µg	50
Temperature – Bandwidth / ± K	1.0
Absolute temperature / ± K	5
Pressure – Bandwidth / ± bar	0.90
Absolute pressure / ± bar	1

In this work, gravimetric analyses of powder samples were carried out with the metal version of magnetic suspension balance supplied by Rubotherm GmbH, Bochum, Germany, equipped with two different measurement positions. The device can work up to 200 bar of pressure and 200 °C with a resolution of 10 µg.[74] For the gravimetric results, no standard deviation errors were given: being a highly precise device, normally, no more than two measurements for each sample are performed. All the isotherms presented in this thesis are excess sorption isotherms ($V^A = 0$), whereas the volume of the solid sorbate is calculated from helium isotherms, assuming helium as not adsorbed on the surface of the material.[76] For sorption measurements of explosive gases, nitrogen as inert gas was flushed through the electrical parts of the device (GDS).

3.1.1 Procedure of performing a gravimetric sorption measurement

A gravimetric measurement consists of different steps. In the following paragraphs, the theory behind these measurements is explained.

Blank measurement

A blank measurement basically measures a sorption isotherm without a sample. Starting from reduced pressure (10^{-3} mbar), the pressure is increased step by step with any gas available. In this work, the same gas employed for the sorption analysis was used for the blank measurement and in the same pressure range. The experimental data recorded during this measurement are the balance reading, corrected for the zero point position (see Figure 19) (m^{BAL} / g), the temperature (T / °C), pressure (p / bar) of the gas and its density (ρ / g cm^{-3}). The decrease in masses of the empty sample container with increasing pressure (density) results from the effect of buoyancy acting on the sample

container. Buoyancy is an upward force exerted by a fluid that opposes the weight of an immersed object. The buoyancy effect is proportional to the density and can be described as the product of the density and the volume of the body. The balance reading is the difference between the downward gravity force and the upward buoyancy force:

$$m^{BAL} = \frac{F^{EXP}}{g} = m^{SC} - \left(V^{SC}\,\rho\right) \qquad (14)$$

m^{BAL}: balance reading, F^{EXP}: experimental force, g: gravitational force, m^{SC}: weight of the sample container, V^{SC}: volume of the sample container, ρ: density of the surrounding gas

Plotting the balance reading as a function of the gas density, a straight line with negative slope is obtained. A linear regression gives as result V^{SC} (the volume of the sample container) as slope and m^{SC} (its weight) as intercept (Figure 18).

A blank measurement was performed every four months or after a complete cleaning of the measurement cell.

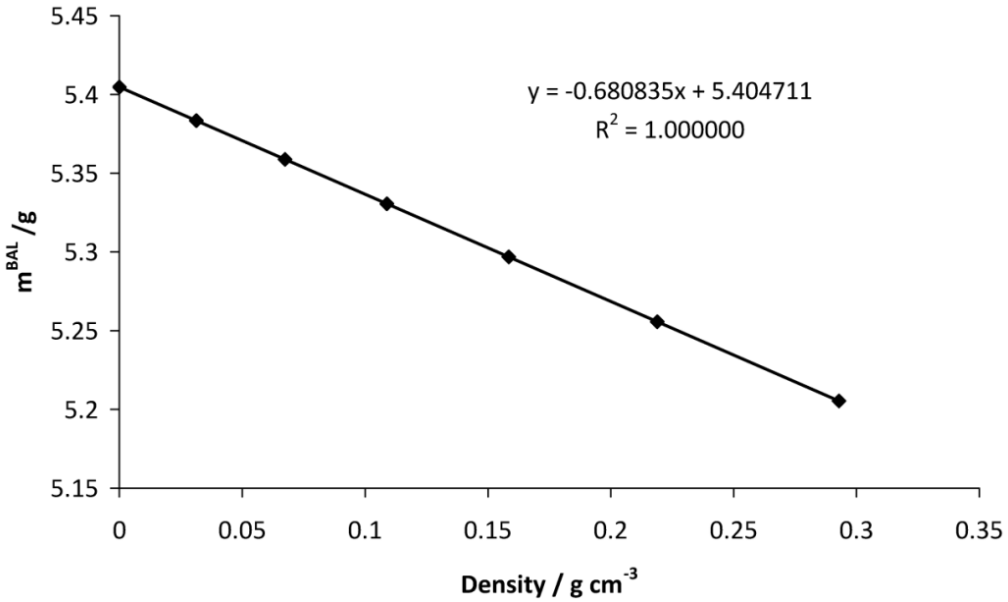

Figure 18: Graph (balance reading *vs.* density of the gas) used for blank measurement.
Gas atmosphere: carbon dioxide, T = 80 °C, 10^{-6} bar < p < 120 bar (10^{th} January 2013): m^{SC} = 5.404711 g, V^{SC} = 0.680835 g cm^{-3}.

Loading and reactivation of the sample

After the determination of the weight and volume of the sample container, the measurement cell was opened and the container loaded with the sample. After closing the cell, the sample must be reactivated to remove possible gases sorbed on its surface. For this procedure, the sample is evacuated at high temperature until no further mass change is recorded. In this work, the reactivation of different samples was performed between 50 °C and 150 °C for 12 hours in a reduced pressure environment ($p = 10^{-3}$ mbar).

Determination of sample mass and volume (m^S & V^S) – Density measurement with MSB

The mass of the sample weighed with the MSB during the sorption experiment needs to be corrected for the buoyancy effect; the volume of the sample is required for this calculation. For determination, a buoyancy measurement was performed. The measurement is again a stepwise increase of pressure by at a constant temperature. The gas used is helium: for most adsorbent materials, He is almost non-adsorbing, giving only generation of the buoyancy effect and any change in the mass of the sample.[76]

If the balance readings of He during the buoyancy measurement is plotted as a function of the density of the gas, again, a straight line with negative slope is the graphical result: here, m^{SC+S} is the intercept, whereas V^{SC+S} is the slope (m^{SC+S} is the weight sum of sample container and sample, whereas V^{SC+S} is its volume). By subtraction of the data collected with the blank measurement, the sample weight and volume (and consequently, its density) are determined.

The density (ρ) of the atmosphere surrounding the sample needs to be known for performing the buoyancy correction of the experimental data. It is directly measured with the magnetic suspension balance. This measuring principle is realised by establishing three different vertical positions of the permanent magnet, schematically shown in Figure 19. In the so-called 'zero point position', only the permanent magnet is freely suspended. If the MSB is compared to a normal balance, the zero point position corresponds to an empty balance, which allows for taring and calibrating. In the second position (sorption measurement) the sample container and the sample are picked up. In the third (density measurement) the vertical position of the permanent magnet is changed again in a way that a titanium cylinder with calibrated volume is lifted from its support. By weighing this calibrated volume in a gas or vapour atmosphere, the buoyancy effect acting on it is measured and the density is determined according to Archimedes's principle.[77]

In this thesis, the buoyancy correction is performed at the same temperature and in the same range of pressure of the sorption/desorption isotherm.[75] It has to be underlined that the density at 10^{-3} mbar is not exactly zero (usually, -0.00063($\pm$ 5x10^{-5}) g cm^{-3}). Therefore, the densities determined at different measurement pressures are corrected for this value. This offset is due to a wrong vacuum weight of the Ti-sinker used in the configuration file of the software.[75]

Sorption measurement

After the buoyancy measurement has been performed, the MSB and the sample are again evacuated. Successively, the sorption measurement can start. The data recorded are the balance readings, the temperature, the pressure and the density of the gas. The balance readings are again the difference between the downward gravity and the upward buoyancy force, which is calculated and resolved for the mass of adsorbate (m^A):

$$m^A = m^{BAL} - m^{SC} - m^S + \left[\left(V^{SC} + V^S + V^A\right)\rho\right] \qquad (15)$$

m^A: mass of adsorbate, m^{BAL}: balance reading, m^{SC}: weight of the sample container, m^S: weight of the sample, V^{SC}: volume of the sample container, V^S: volume of the sample, V^A: volume of the gas sorbed on the sample, ρ: density of the surrounding gas

In this work, all the isotherms are excess surface isotherms and the uptake is expressed in milligram of gas sorbed per gram of sample (mg g^{-1}).

Volume of adsorbate

In this thesis, the volume of the gas sorbed on the sample (V^A) was not calculated, with the exception reported in paragraph 5.1.1. Accordingly, the buoyancy acting on the gas sorbed on the sample was not taken into account and the data reported are excess sorption isotherms.[36] The experimental surface excess amount should be the starting point for the calculation of the absolute amount sorbed, because it is not possible to determine the absolute amount by experimental techniques.[37] This is of interest, when experimental data have to be compared with results from simulation experiments, where the absolute amount adsorbed can be obtained. Therefore, models have to be used for the determination of absolute isotherms from the experimentally available surface excess.[37]

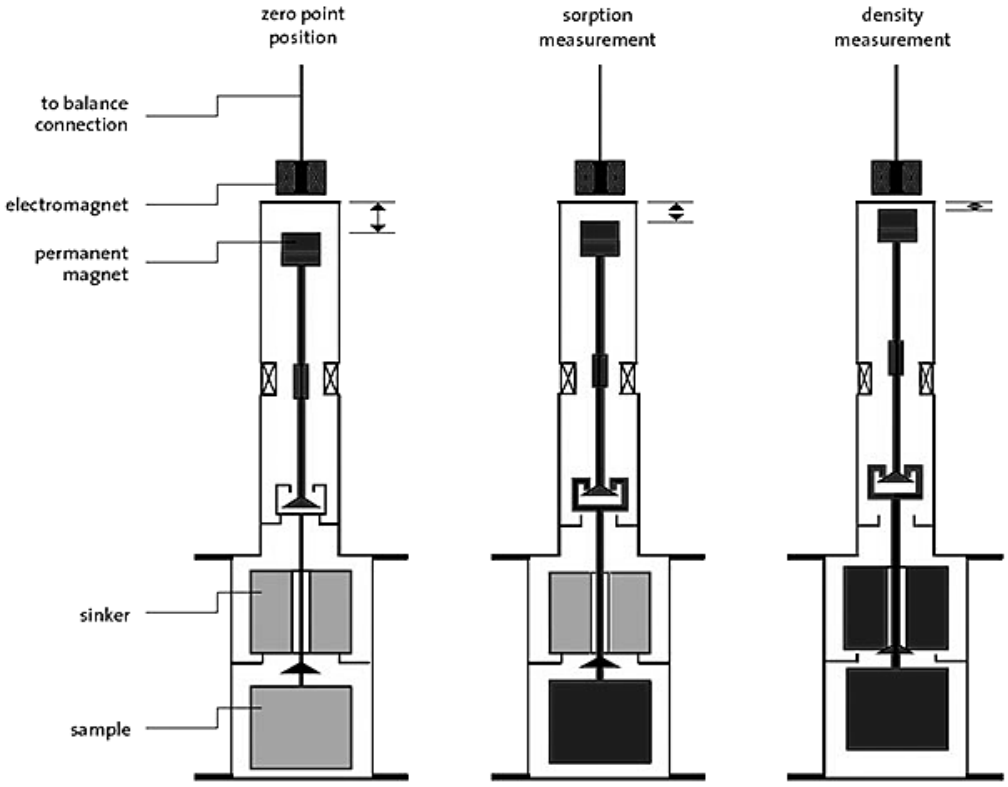

Figure 19: Magnetic suspension balance for the simultaneous measurement of sample mass and density of phase gas.[74]

3.2 Volumetric analysis for gas sorption

The volumetric measurement allows the determination of the specific surface area of powders as well as the pore size distribution of porous materials. Volumetry, or preferably manometry, is the oldest method for the investigation of gas sorbed on solid materials.[17]

An adsorption measurement starts with sample pretreatment, *i.e.* applying reduced pressure (10^{-3} mbar) at room temperature. Dead volume measurement (dead volume means the space inside the sample cell not occupied by the sample itself) is carried out and adsorption followed by desorption measurement is performed at the temperature of liquid nitrogen (-196 °C). In the volumetric method, the volume of gas sorbed (not its mass, as in the gravimetric method described above) is measured by calculating the difference between pressures before and after adsorption, corrected for dead volume values. In order to achieve highly reliable data, because of the evaporation of the liquid nitrogen, the dead volume of the sample cell and the dead volume of a reference cell are measured before each adsorption point.[78]

Having obtained the experimental data of the isotherm, the next task is to obtain the specific surface area. The most common used theory is the BET theory (see paragraph 2.3.2). The isotherm equation of the BET model in its linear form is:

$$\frac{p}{v(p_0 - p)} = \frac{1}{v_m c} + \frac{c - 1}{v_m c}\left(\frac{p}{p_0}\right) \qquad (16)$$

p: equilibrium pressure, p_0: saturation pressure of adsorbate, v: adsorbed gas quantity, v_m: monolayer adsorbed gas quantity, c: BET constant, p/p_0: relative pressure

The BET constant is expressed as:

$$c = exp\left(\frac{E_1 - E_L}{RT}\right) \qquad (17)$$

c: BET constant, E_1: heat of adsorption for the first layer, E_L: heat of adsorption for the second and higher layers and is equal to the heat of liquefaction

The plot of $p/\left(v\left(p_0 - p\right)\right)$ against p/p_0 (Equation (16)), in the correctly chosen pressure range, gives the values of v_m and c. The pressure range usually recommended is p/p_0 from 0.05 to about 0.35. One reason for the upper limit can be found in the fact that hysteresis might set somewhere about this value; the lower limit of 0.05 arises from the non-uniformity of the surface.[79] The specific surface area is then calculated with the help of the formula:

$$A_{BET} = \frac{v_m N_A A}{M} / m^S \qquad (18)$$

A_{BET}: specific surface area, v_m: monolayer adsorbed gas quantity, N_A: Avogadro's number (6.022×10^{23}), A: surface area that an adsorbate molecule occupies (for N_2, 0.162 nm^2), [78] M: molecular weight of the adsorbate, m^S: sample weight

The BET algorithm can be applied for the calculation of specific surface areas of nanoscopic materials. Nevertheless, the surface of a particle with a size of only a few nanometers is not flat, but strongly curved and the individual adsorption sites are not necessarily uniform and energies of adsorption may vary significantly from site to site.

Contrary to the gravimetric method, the volumetric experiment has the advantages of being easier and faster. On the other hand, the disadvantages of the volumetric analysis are:

- The volumetric unit measures the volumes of gases adsorbed by using an equation of state (the final data are not completely experimental data);
- The sources of errors are various: weight of the sample and determination of pressures, just to cite some of them;

- A relative large amount of sample (200 mg) is required;[78]
- The analysis gives no information about the kinetics of the process.

In this thesis, volumetric analyses of powder samples were carried out with a BELSORP-mini II instrument from BEL Japan (Osaka, Japan, software version 2.0.12). The applied adsorbate was N_2 and the isotherms were performed at the temperature of -196°C. Dead volume determinations were performed under helium. The BET plot and the BJH analysis (see paragraph 2.3.2) were carried out with the software BEL Analysis Software version 3.11.3, BEL Japan.

3.3 Fourier transform – infrared spectroscopy (FT–IR)

Infrared (IR) spectroscopy is a method for the detection of certain vibrations of chemical bonds. The vibrational frequencies are characteristic for particular functional groups in the sample, and they allow a qualitative and, with some expedients, quantitative analysis of the component.[54, 80]

Molecules can be excited from their ground vibrational states to higher vibrational states, through adsorption of energy; the energy of molecular vibrations of interest for analytical determination correspond to electromagnetic wavelengths in the range 2.5 - 25 μm, or expressed conventionally in terms of the wavenumber $\tilde{\nu}$, 4000 - 400 cm^{-1}. The IR spectrum can be divided into two regions: the first is the functional group region (4000 - 1000 cm^{-1}), where characteristic bands for the chemical functional groups appear. Vibrational frequencies of particular group of atoms in molecules tend to behave independently from the rest of the molecules. Consequently, the absorption frequencies for a particular chemical group are roughly constant and the adsorption appears approximately in the same region of the spectrum. This enables the classification of reference to standard correlations table. Between 1000 and 400 cm^{-1} (the fingerprint region) the spectra tend to be more complex and it is harder to assign single vibrations, but the patterns can be useful to confirm a structure by direct comparison with known spectra.

Vibrations are infrared active only when the electric dipole moment of the molecule changes during the movement of atoms. For a molecule consisting of *N* atoms, the number of vibrational degree of freedom (normal modes) is $3N - 6$, whereas for linear molecules, where two rotational modes are equivalent, it is $3N - 5$. There are two fundamental ways of vibrations, stretching (υ) and bending (δ). Vibrations with varying bond lengths are called stretching, whereas the bending motion involves the change of the bond angle, while the bond length stays mainly unchanged. It can happen

that two normal modes are simultaneously excited: in this case, a combination band is the result and its frequency is the sum of the two fundamental frequencies.

Nowadays, modern spectrometers use the Fourier–Transform (FT) technique. These instruments are equipped with a Michelson interferometer, shown in Figure 20. It parts the beam into two and introduces a varying path difference into one of them. When the two components recombine, they interfere either constructively or destructively depending on the different path length, b. The application of the mathematical transform, the Fourier Transform, allows the rearrangement of the intensity function of the path length $I(b)$ into intensity, a function of the wavenumber, $I(\tilde{\nu})$. The integration is carried out numerically by the software, which controls the spectrometer.

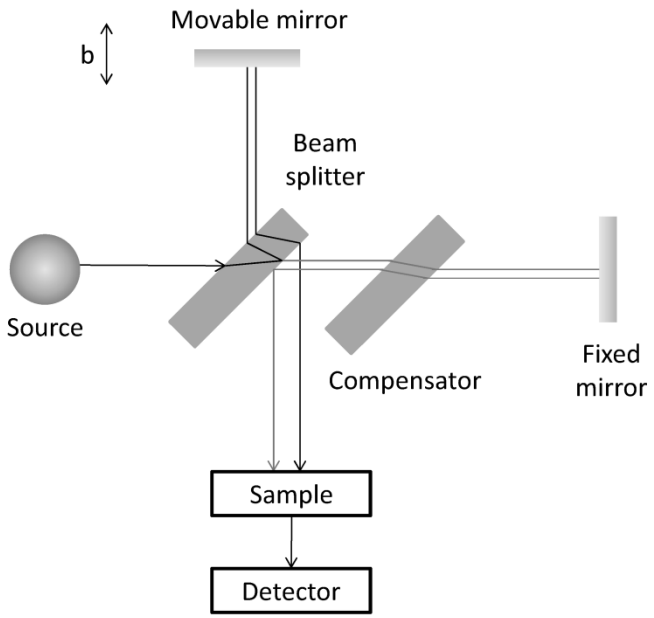

Figure 20: Schematic view of a FT–IR spectrometer. The beam-splitter divides the incident beam into two beams with a path difference that depends on the location of the movable mirror. The compensator ensures that both beams pass through the same thickness of material. (Modified reproduction of [54]).

In order to perform a quantitative analysis, the IR-spectra should be collected in absorbance rather than transmittance: the ratio of the transmitted intensity to the incident intensity at a given frequency is called transmittance of the sample, whereas absorbance is defined as the negative logarithm of transmittance. The Beer-Lambert law[54] is expressed as following:

$$Absorbance = \varepsilon\,[J]\,l \qquad (19)$$

ε: molar absorption coefficient, *[J]*: molar concentration of the sample, *l*: length of the sample

The spectrum in absorbance values allows the quantitative analysis of a sample, after adequate calibration of the instrument.[81]

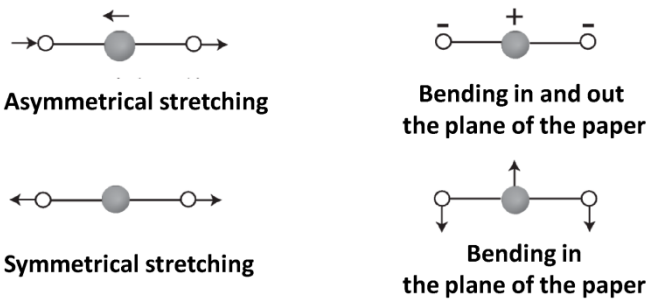

Figure 21: Stretching and bending vibrational modes of CO_2.

Carbon dioxide is a linear molecule; hence, it has four fundamental vibrational modes (Figure 21). The asymmetrical stretch of CO_2 gives a strong band in the IR spectrum at 2350 cm^{-1}. The two bending vibrations are equivalent and therefore, they have the same frequency and are said to be degenerate, appearing in an IR spectrum at 666 cm^{-1} (Figure 22). The symmetrical stretch of CO_2 is inactive in the IR because no change is produced in the dipole moment of the molecule.

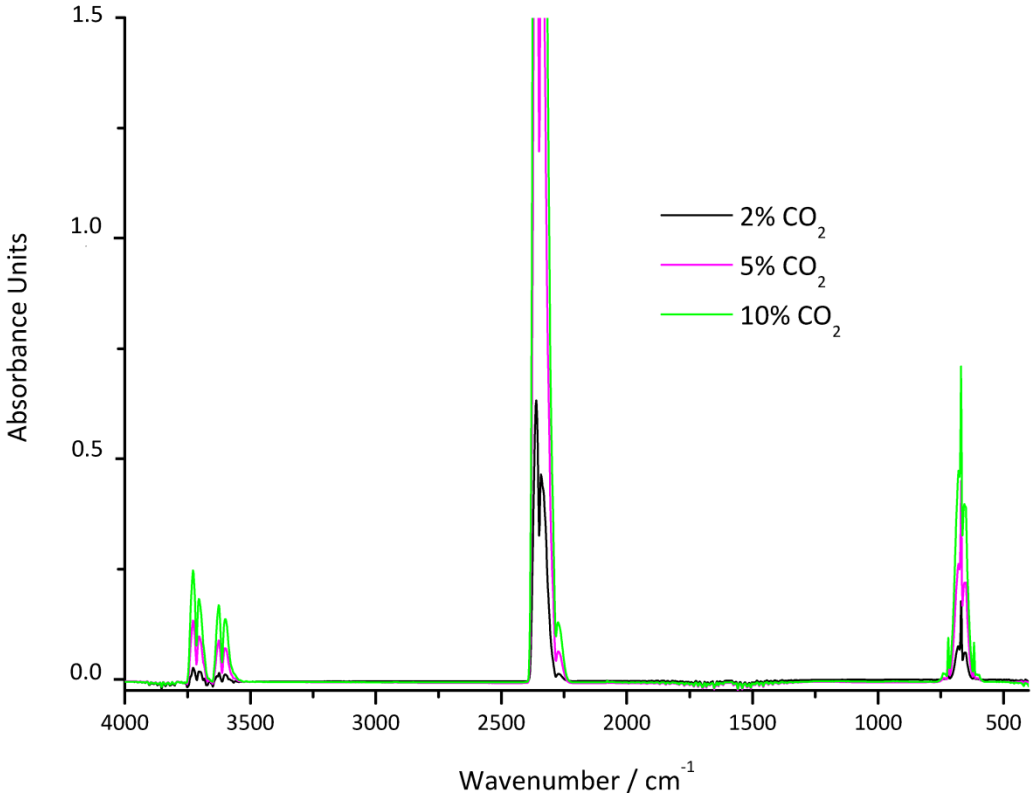

Figure 22: FT–IR spectra of 2%, 5% and 10% of CO_2 in N_2.

In this work, solid samples were measured in potassium bromide (KBr) tablets. For this purpose, 300 mg of dried KBr and 1 mg sample were carefully crushed and mixed together and finally pressed into a thin pellet, with a force of 50 kN using a special pressing device. FT–IR spectroscopy was

performed with a Vertex 70 FT–IR spectrometer from Bruker Optics (Ettlingen, Germany). The instrument applied a Globar (a silicon carbide rod) as radiation source and a pyroelectric detector. The measurement cell was under continuous flow of nitrogen during the analysis, in order to remove atmospheric signals (H_2O and CO_2). The final spectrum was corrected for the background signal (solid samples: empty measurement cell; gaseous samples, gas cell (Figure 23) filled with 1 bar of N_2). For the quantitative determination of CO_2 with a concentration up to 10% in N_2, a calibration of the instrument was performed with three different CO_2 concentrations, 2%, 5% and 10% (Figure 22). Dilutions from an initial concentration of 10% were performed inside an autoclave, error in the partial pressure of gases was ± 0.1 bar.

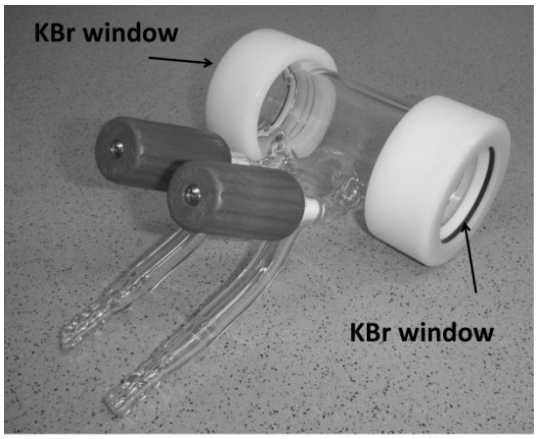

Figure 23: Gas cell for FT–IR analysis. Sample path 10 cm. Supplied by Bruker Optics (Ettlingen, Germany).

3.4 Ultraviolet – visible spectroscopy (UV–Vis)

Ultraviolet–Visible (UV–Vis) absorption spectroscopy allows the detection of electronic transitions within a material. The absorption or the reflectance in the visible range depends on the colour of the sample under investigation.[82]

The energy needed to change the electron distribution of molecules is of the order of several electronvolts (1 eV which is equivalent to about 8000 cm^{-1} or 100 kJ mol^{-1}). Consequently, photons involved when such a change occurs correspond to the visible and ultraviolet regions of the spectrum (Table 6). Sigma–electrons absorb high energy photons, whereas π–electrons absorb photons at lower energy (longer wavelength), often in the visible region.

In this work, optical spectra of powders in the UV–Vis range were recorded with a Cary 100 spectrometer from Varian (Darmstadt, Germany). The UV–light source is a deuterium lamp (from 180 to 360 nm) and the visible light source was a quartz halogen lamp (from 360 to 800 nm). As a

reference, pure dry barium sulphate was employed; 2 mg of dry samples were carefully crushed and mixed together with 200 mg of $BaSO_4$.

Table 6: Colour, wavenumber and energy of light.[54]

Colour of light	Wavelength / nm	Energy / kJ mol^{-1}
Infrared	>1000	<120
Red	750	170
Yellow	580	210
Blue	470	250
Ultraviolet	<300	>400

3.5 Fluorescence spectroscopy

Fluorescence spectroscopy detects electronic transitions within a material: the molecule examined undergoes a transition from a state of low energy to a state of high energy and from a state of high energy to low energy, enabling the characterization of photo-luminescent materials.[83]

The initial absorption takes the molecule to an excited electronic state (excitation spectrum). Afterwards, the excited molecule is subjected to collisions with the surrounding molecules, and as it gives up energy nonradiatively, it steps down the ladder of vibrational levels, to the lowest of the electronically excited molecular state. From here, radiative return to the ground electronic state can occur (emission spectrum).

In this work, excitation and emission spectra of nanoparticles in suspension were recorded with a Spex Fluorolog 3.2 from Horiba Jobin Yvon (Paris, France). The light source was a Xenon lamp working in the range between 240 and 600 nm for excitation (and between 290 and 850 nm for emission). SQ Quartz cuvettes, with a capacity of 3.5 ml, from Starna (Pfungstadt, Germany) were employed. The instability of the light source was taken into account.

3.6 Dynamic light scattering (DLS)

Dynamic Light Scattering (DLS), also known as photon correlation spectroscopy, is an experimental procedure, which yields a quantitative measure of scattering particle in suspensions.[84]

The method is based on the interaction of light with particles: the light is scattered in all directions, as long as the dimension of the particles is smaller than the wavelength of the incoming radiation. Particles in solution or suspension usually show a random motion (Brownian motion) caused by thermal density fluctuations of the solvent. As a consequence, the interference pattern and the resulting scattered intensity also change with the time, reflecting the motion of the scattering particles. To quantitatively analyse particles by light scattering, it is suitable to express the scattering intensity fluctuations in terms of correlation functions. If a signal, registered at one point in time t, is compared to the intensity signal obtained a very short time later ($t+\tau$), the two signal appear to be very similar, or strongly correlated. If the original signal is compared a little further ahead in time ($t+2\tau$), it will be a very good correlation between the two signals, but lower than at $t+\tau$. If the correlation is measured at $t+3\tau$, $t+4\tau$, $t+5\tau$, and so on, the correlation will approach zero. It is known that small particles move quickly in a liquid, whereas large particles move slowly: if small particles are detected, the intensity of the signal will also fluctuate quickly and if large particles are being measured, the signal will fluctuate slowly during the time. After the correlation function has been determined, the diffusion coefficient (D) can be calculated. D is inversely proportional to the hydrodynamic radius (R_H) of the nanoparticles according to the Stokes-Einstein equation:[84c]

$$D = \frac{k_B T}{6\pi\eta R_H} \qquad (20)$$

D: diffusion coefficient, k_B: Bolzmann constant (1.38×10^{-23} J K^{-1}), T: temperature, η: viscosity of the solvent, R_H: hydrodynamic radius

The DLS analysis has the advantage to be a fast and non-invasive method, which gives an approximate size distribution of a suspension within minutes. On the other hand, it cannot distinguish between particle agglomeration and single nanoparticles.

For determination of the size distribution of nanoparticles in suspension, the instrument Nanosizer ZS from Malvern Instruments (Herrenberg, Germany) was used. The light source was 4.0 mW He-Ne laser with wavelength of 633 nm. Samples were measured in suspension in disposable plastic cuvettes. For the elaboration of the experimental data the Dispersion Technology Software (Version 6.01) by Malvern Instruments was employed.

3.7 Scanning electron microscopy (SEM)

Scanning electron microscopy (SEM) is a type of electron microscope: it creates images of a sample by scanning it with a focused beam of electrons. It can be considered the most typical method for direct, high-resolution imaging of particles and solid surfaces.[85]

A primary electron (PE) beam is emitted from an electron source, normally a heated tungsten filament, and focused by different lenses to form a very fine probe a few nanometres in diameter. The electron probe is moved across the sample by means of deflections coils, scanning it point-by-point.

The incident beam of high energy electrons interacts with the sample producing different effects in the so-called 'interaction volume', the region of sample which is penetrated by the primary electrons (Figure 24, left). The most frequently signals used for creation of images are the secondary (SE, energy less than 50 eV) and backscattered (BSE, energy > 50 eV) electrons. SE signals are produced when an incident electron excites an electron in the sample causing its ejection. The excited electron moves towards the surface of the sample undergoing elastic and inelastic collisions, until it reaches the surface. Here it can escape, if its energy exceeds the energy needed to remove electrons from the surface of the material. One of the major reasons for coating a non-conductive specimen with a conductive material is to increase the number of secondary electrons that will be emitted from the sample. BSE are high energy primary electrons that suffer large angle (> 90°) scattering and re-emerge from the entry surface of a specimen. When the incident electron loses energy by dislodging out an electron from the sample, a vacancy is produced. If the dislodged electron is a valance electron, the vacancy is filled through a transition of electron from a higher energy level releasing energy in form of photon (CL, cathodoluminescence). If the dislodged electron is an inner shell electron, the release of excess energy can generate X-ray radiation (see paragraph 3.9) or the transition energy is imparted to an outer electron (Auger electron) which is emitted. Finally, the primary beam can pass through nanometers in size thin specimens (transmitted electrons, TE) and reaches the detector aligned with source and sample.

In this thesis, scanning electron microscopy was used to obtain images of nanoparticles and study their statistical particle size and degree of agglomeration. The device employed was a Supra 40 VP microscope from Zeiss (Oberkochen, Germany). Samples were prepared by depositing suspensions in ethanol on silicon wafers and letting the solvent evaporate. The Si wafers are supported by aluminium sample carriers. The acceleration voltage of the primary electron beam used

was in the range of 1 and 20 kV. Detection of the scattered electrons was performed with a secondary electron detector placed within the lens system (perpendicular to the specimen under evaluation, InLens detector).

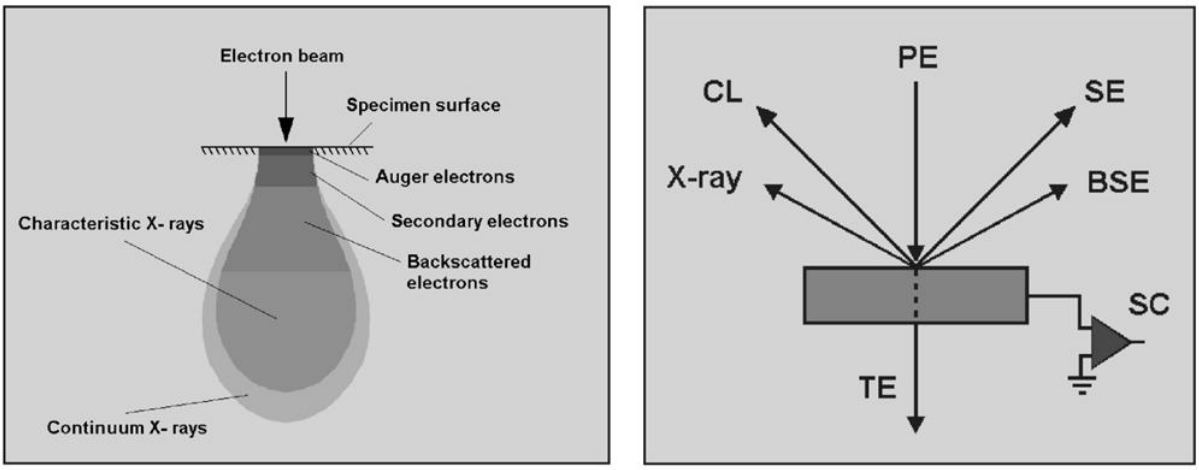

Figure 24: (Left) the interaction volume and the regions from which secondary, backscattered, Auger electrons and X-rays may be detected. (Right) Interaction processes between the primary beam of high energy electrons hits a specimen.[85a]
PE: primary beam, CL: cathodoluminescence, SE: secondary electrons, BSE: backscattered electrons, TE: transmitted electrons, SC: specimen current.

3.8 Transmission electron microscopy (TEM)

In a transmission electron microscope (TEM), electrons are accelerated to a voltage of typically 100 to 300 kV and sent through the sample. Sample thickness should be less than 200 nm to avoid complete absorption.

In this work, TEM was utilized to obtain high resolution images of nanoscale hollow spheres. TEM samples were prepared by depositing sample suspensions in ethanol on holey carbon-film Cu grids. The TEM images presented in this thesis were taken by Dr. R. Popescu in the research group of Prof. Dr. D. Gerthsen, Laboratory for Electron Microscopy, Karlsruhe Institute of Technology (LEM, KIT) with a Philips CM 200 FEG/ST transmission microscope, operating at 200 kV.

3.9 Energy dispersive X – ray analysis (EDX)

Energy Dispersive X-Rays (EDX) investigation is an analytical tool for the qualitative and quantitative (with some restrictions) determination of the elemental composition of a sample.[86]

When an electron is dislodged from an atom, the atom is in an excited state; a single outer electron jumps into the inner shell vacancy and the energy difference, characteristic of the particular atomic species, is compensated by emission of X-radiation. The transitions are named K-series, L-series, etc. after the shell of the knocked out electron (Figure 25). Since the samples are analysed inside a SEM equipped with an EDX detector, where electron energies with a maximum of 30 kV are available, X-rays which are more easily excited should be analysed, while taking also into account that the most efficient production of characteristic X-rays generally occurs when the primary electron beam has an energy two or three times higher than the generated X-rays radiation.

EDX detection for quantification purposes shows some restrictions. Characteristic X-rays are generated isotropically, but only those emitted in the small angle seen by the EDX detector are eligible for detection. Moreover, different elements generate and adsorb X-rays with different efficiencies. If elements with similar atomic numbers are present in the same compound, it may occur that primary X-radiation, generated by the electron beam, will partially be adsorbed in the sample generating secondary or fluorescence emission. The software carries out the correction (the so-called ZAF correction: Z, atomic number; A, absorption; F, fluorescence) automatically, but the magnitude of the error depends on the specimen thickness, density and surface roughness, as well as on the take-off angle, which is the angle between the sample surface and the detector axis. Straightforward correction requires the knowledge of parameters which are uncertain, unless the sample is perfectly flat and horizontal at zero tilt.[86a]

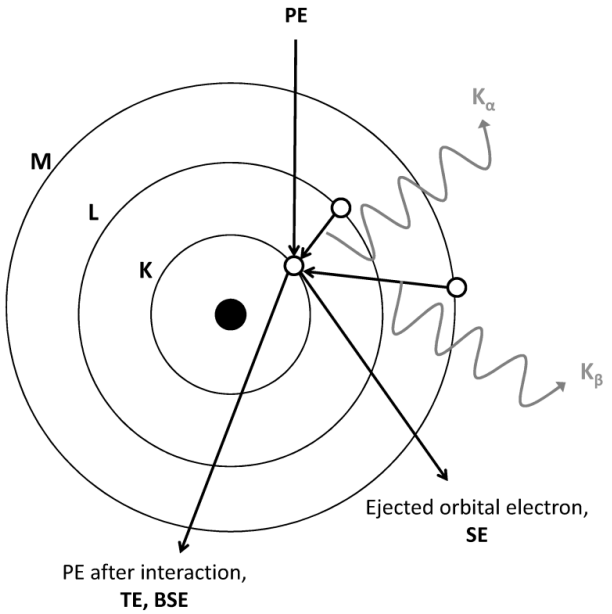

Figure 25: Production of X-rays in one atom.

EDX was performed with a Supra 40 VP microscope equipped with a Sapphire Si(Li) detector (Zeiss, Oberkochen, Germany). Between 30 and 50 mg of sample were pressed in order to obtain a tablet, which was later glued on aluminium sample carriers. The take-off angle used was 35°. For the quantitative analysis the software Genesis-EDX version 4.52 was employed.

3.10 Thermogravimetric analysis (TGA)

Thermogravimetric analysis (TGA) is an analytical method in which the weight of the sample is continuously recorded during heating, allowing the investigation of sample chemical degradation, its dehydration, sublimation and/or oxidation.[87]

The thermogravimetric curve obtained (weight change *vs.* temperature), can be used to estimate the sample composition, its thermal stability and, when coupled with other analytical methods (*e.g.* mass spectrometry or infrared spectroscopy) the products of decomposition. The shape of the resulting curve and the validity of its interpretation depend on different factors, divided into three main groups (a,b and c):

a) Effects arising from the nature of the apparatus:
    i) Reactions of the specimen with the crucible (porosity, catalytic effects, previous history of the crucible);
    ii) Shape, size and material of the crucible;
b) Effects resulting from construction and method used:
    i) Heating rate and heating transfer;
    ii) Rate of recording the curve;
    iii) Composition of the atmosphere in the reaction chamber;
    iv) Effect of buoyancy;
    v) Sensitivity of the balance and the recording system;
    vi) Method of temperature measurement;
c) Effects of physical and chemical proprieties of the sample:
    i) Amount of the sample;
    ii) Particle size;
    iii) Heat of reaction and thermal conductivity of the sample;
    iv) Nature of the sample and type of changes taking place.

According to what reported above, the interpretation of TGA measurements should be done according to the sample analysed and the conditions adopted.

TGA were performed with a Netzsch STA 449F Jupiter from Netzsch (Selb, Germany), TGA resolution 0.00001%. Al_2O_3 was used as crucible material. The samples were heated in air atmosphere up to maximum 800 or 1000 °C with a heating rate of 1 or 10 K min^{-1}.

3.11 X – Ray diffraction (XRD)

X–Ray Diffraction (XRD) analysis is the traditional method for studying crystal structures. Powder diffraction techniques are mostly used to identify samples by comparison of the position of the reflexes and their intensities with diffraction patterns stored in a data bank. Powder XRD could also be used to determine the relative amounts of each crystalline phase present in a mixture. Amorphous samples cannot be studied with this analytical tool.[88]

If translatory symmetry exists in a sample, diffraction occurs when the dimensions of the diffracting material are comparable to the wavelength of the incident radiation. X-rays are electromagnetic radiation with wavelengths of the order of 10^{-10} m, the same order of magnitude of the distance between the planes in the atomic lattice. Constructive interference, necessary to obtain a detectable signal, is observed when the relation formulated by Bragg (Equation (21)) is fulfilled. If the phase lag is not an integral of the wavelength (*e.g.* 0.5λ), destructive interference will occur and the diffraction intensities are cancelled out.

$$2d \sin\theta = n\lambda \qquad (21)$$

d: interplanar spacing between two parallel planes, θ: incident angle, *n*: integer number (1,2,3…), λ: wavelength

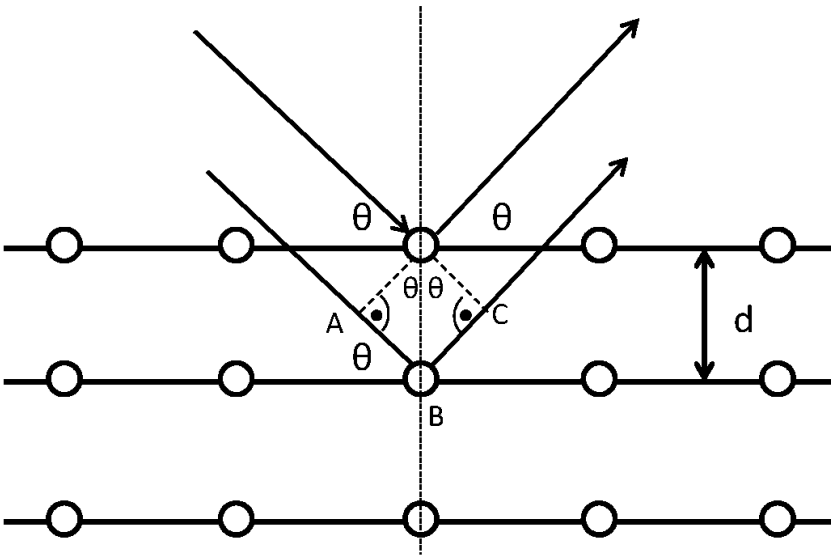

Figure 26: The conventional derivation of Bragg's law. The path length differ by AB+BC (AB = BC = sin θ); constructive interference occurs when AB + BC is equal to an integer number of the wavelength. Although scattering of X-rays occurs primarily by interaction with electrons within the sample, the atomic (nuclear) positions can be treated as the scattering centres. (Modified reproduction of [54]).

In large crystals, the number of lattice defects is very small compared to the defect concentrations presents in small crystals: therefore, the distance between the lattice planes in nanocrystals has a wider variety which results in broader reflections. The broadening of the line increases with the decrease of the crystallite size: thus, X–ray powder diffraction can be often used to estimate the size of the nanocrystals, according to the Scherrer formula:[89]

$$L = \frac{k\lambda}{\beta \cos\theta} \qquad (22)$$

L: volume average crystallite size, *k*: Scherrer constant, depends on crystallite shape, the way in which *L* and β are defined and on the size distribution (the constant is the ratio by which the apparent size must be multiplied to give the true size), λ: wavelength, β: integral breadth, θ: diffraction angle

The limit of the application of the Scherrer equation can be realized in the case of a crystal coated with a layer of amorphous phase: the amorphous phase is not detected from the X-ray diffraction patterns. Consequently, the size of the crystalline domain, as determined by XRD, and that of the whole particle, as determined by electron microscopy or DLS, are different.[24]

In this work, X–ray powder diffraction analyses were carried out with a STADI–P diffractometer from STOE & CIE (Darmstadt, Germany) operating with curved Germanium(111) monochromatized Cu-$K_{\alpha 1}$ radiation, the Debye-Scherrer geometry was applied and a position sensitive image plate detector was used. The measured diffraction patterns were evaluated with the software Win-XPOW and compared with the International Center for Diffraction Data (ICDD, release 2005) database.

Samples were prepared by applying a thin film of powder on a piece of adhesive tape. The obtained diffraction pattern was plotted as intensity *vs.* 2θ, with 2θ as the diffraction angle.

3.12 Elemental Analysis (EA)

Elemental analysis (EA) of the elements H, C, N and S allows the qualitative and quantitative determination of the above four cited elements. It is a destructive method, since the sample is lost after its detection.

The sample is heated in the presence of oxygen-containing atmosphere at temperatures above 1150 °C. The gases produced upon burning the sample (CO_2, H_2O, SO_2, NO_x after reduction to N_2) are analysed and quantified by a thermal conductivity detector.

The elemental analyses of dried samples (between 1 and 8 mg) presented in this work were performed by Ms. Sabine Lude and Ms. Nicole Klaassen (Prof. Feldmann group, KIT) with a Vario Micro Cube device (Elementar, Hanau, Germany).

4 Experimental

4.1 Nanoparticles

In this work, the process of nanoparticles synthesis was performed in solution, through two strategies of synthesis: the microemulsion (described in paragraph 4.1.1) and the hot-injection technique (see paragraph 4.1.2).

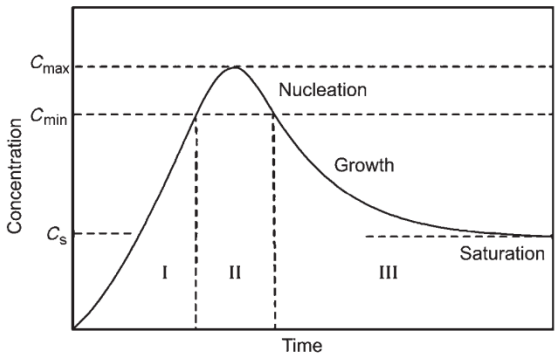

Figure 27: LaMer and Dinegar's model to describe nucleation and nucleus growth (modified reproduction of [90]).

According to the model of LaMer and Dinegar, the synthesis of nanoparticles in solution involves two different steps: nucleation and growth.[90] The mechanism was developed for the preparation of a monodisperse sulphur hydrosol by slow decomposition of acidic aqueous solution of sodium thiosulfate. The diagram in Figure 27 illustrates the development of the sulphur concentration during the time. In the first step, the concentration increases continuously with advancing time; as the concentration reaches the critical supersaturation value, nucleation occurs. Later, the decrease of concentration is due to the growth of the particles by diffusion, until the concentration reaches the solubility value. To ensure nearly monodisperse particles, the key idea of separating the nucleation stage from the growth process is often used (see paragraph 4.1.2).

In order to control the growth of nanoparticles, their surfaces can be saturated by steric stabilization,[2] similarly for the synthesis in microemulsion as described in the following paragraph.

4.1.1 Microemulsion synthesis

Microemulsions are thermodynamically stable and optical isotropic systems composed of two immiscible liquids (water and oil) and a surfactant. Surfactants are molecules with a polar hydrophilic

head (cationic, anionic or non-ionic) and a hydrophobic hydrocarbon chain (attached to oil); droplets of water-in-oil (*w/o*) (Figure 28) or oil-in-water (*o/w*) are stabilised by surfactants, if small amounts of water or oil are used, respectively.[91] A co-surfactant (often, a low molecular weight alcohol) can also be included in the synthesis: it helps the formation and stabilisation of the micelles, influences the curvature of the interface between the polar and non-polar phase, and therefore, the interface energy,[92] lowering the electrostatic repulsion of the surfactant charge.

Usually, micelles have dimensions in the order of magnitude of some tenth of nanometers and can be used as nanoreactors to perform chemical reactions.[91]

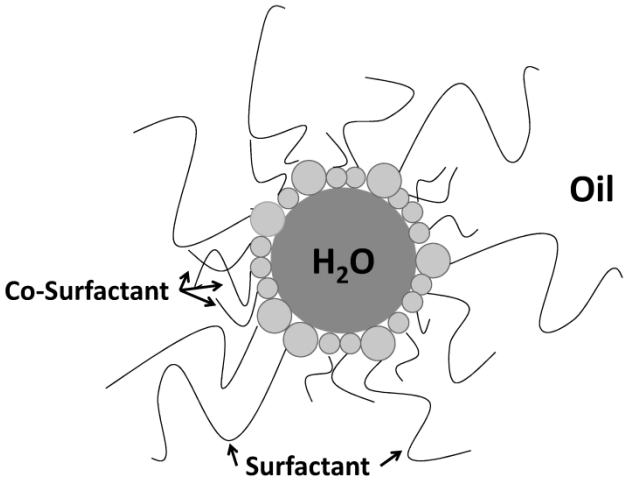

Figure 28: Schematic representation of a reverse micelle, *w/o* microemulsion.

Substantially, there are two basic mechanisms to perform reactions in microemulsions: the first one (Figure 29) is based on the mixture of two *w/o*-microemulsions, each containing one of the reactants. Upon mixing, the reverse micelles collide with one another as a result of the Brownian motion. In theory, successful collisions lead to coalescence, fusion, and efficient mixing of the reactants, followed by nucleation and growth of the favoured product.[93]

The second mechanism is called single microemulsion reaction (Figure 30): here, the formation of nanoparticles involves the introduction of two reactants to the water pools of the micelles at two different times. Such a mechanism promotes intramicellar nucleation and growth, not encountered in the mixing of two microemulsions, where intermicellar mechanism is preferred.[93] The second reactant, added after stabilisation of the microemulsion, can, on the one hand, be soluble in the polar phase. In this case the final amount of the polar phase is the addition of the water which is used to dissolve both precursors and the reaction takes place inside the micelles, both through intra- and intermicellar mechanisms. On the other hand, when the second reagent is only soluble in the oil-

phase, depending on the reaction rate control, the resultant products are again massive nanoparticles or, otherwise, nanoparticles with a water-filled cavity (Figure 31).

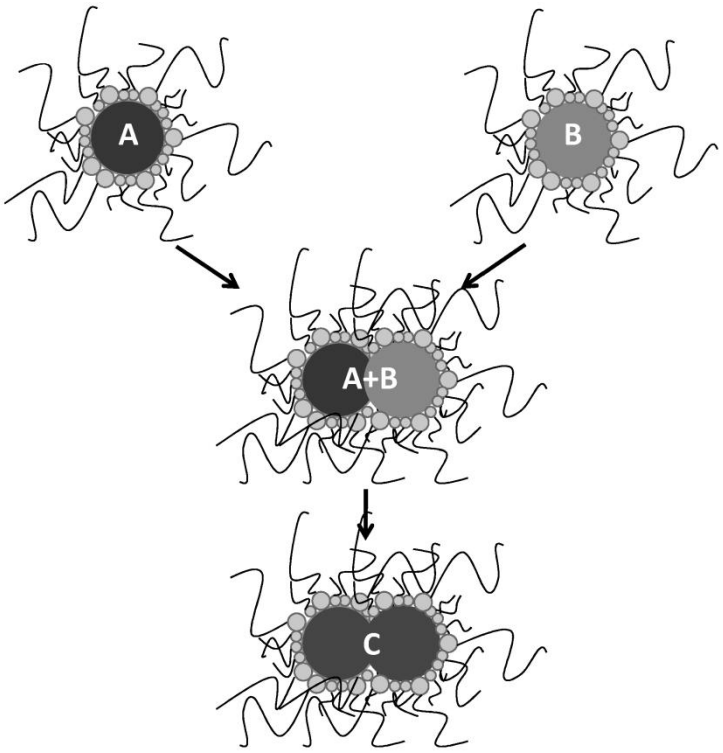

Figure 29: Schematic representation of mixing two microemulsions reactant addition (modified reproduction of [93]).

In contrast to common strategies, in the last case outlined above, the reaction is not performed inside a micelle, but at its phase boundary.[11b] To perform a reaction controlled by diffusion and to limit the formation of massive nanoparticles, appropriate experimental conditions are prerequisite. This includes suitable types and concentrations of reagents, as well as optimal values of solubility/non-solubility of the start and final materials. In order to control the diffusion and reaction rate, the experimental conditions are normally kept at room temperature. Moreover, reactions are performed over a long period of time (12 hours) without stirring.[11a] The microemulsion approach is only one route for the synthesis of nanoscale hollow spheres: instead, hard-template based techniques[94] are most often employed. Nevertheless, the template dissolution out of the shell (future sphere wall) without destroying it can result complicated. Moreover, in view of container-type functionalities, hard-templates are disadvantageous, due to the fact that the transported agent would have to be introduced inside the hollow spheres after removing the template.[11a]

It can be outlined that the size of the nanomaterial prepared *via* microemulsion approach has a similar dimension as the droplet used as a template: unfortunately, the template is not the key parameter in the shape control.[95] The contact of one reactant with the second is only possible if a channel through the surfactant layers is opened. The permeation rate through this channel is highly material-depending (a spacious and highly charged ion will barely pass the channel, whereas a non-voluminous and neutral molecule will cross it easily). The reaction rate depends on the film flexibility (type of surfactant and co-surfactant), concentration of reagents, and water-surfactant molar ratio.[91]

Another restriction of the microemulsion techniques is the limitation of the temperature: conventional micellar systems turn out to be stable only under certain temperature limits, namely up to 50 - 60 °C, giving as products amorphous materials.[96]

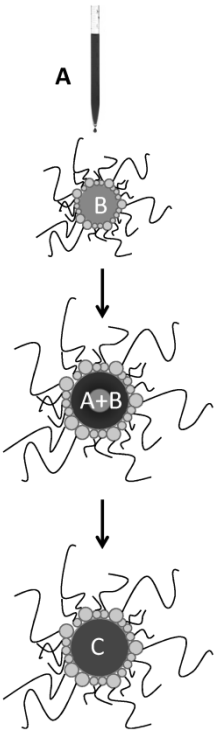

Figure 30: Schematic representation of single-microemulsions reactant addition (modified reproduction of [93]).

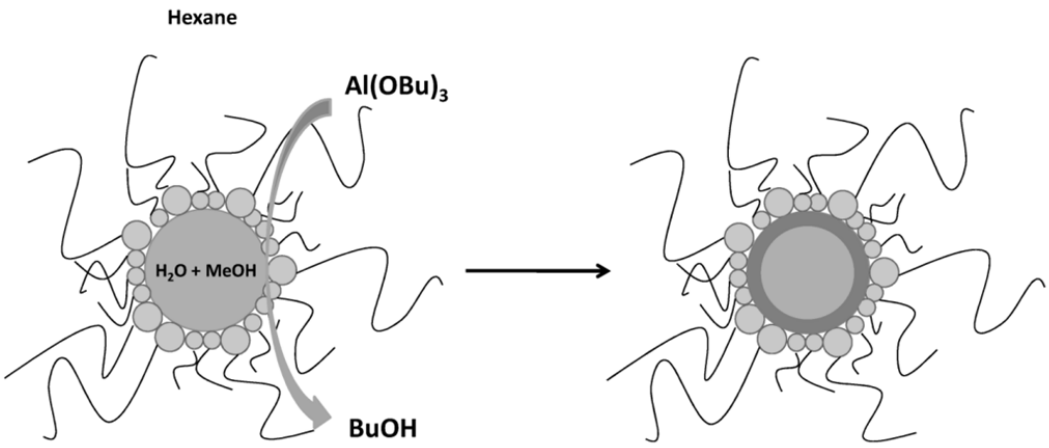

Figure 31: Schematic representation of the synthesis of hollow spheres: reaction takes place at the phase boundary (modified reproduction of [12]).

4.1.2 Hot injection technique

Following the model proposed by LaMer and Dinegar (see paragraph 4.1), nucleation is an endothermic process, whereas particle growth is exothermic.[2] In order to avoid premature particle growth, the increase of the reaction temperature before adding the second precursor can be a successful strategy. Hot injection leads to instantaneous nucleation by injecting the second reagent into the first one at high temperature, quenched by fast cooling of the reaction mixture. Further growth of the nuclei into nanoparticles occurs at a lower temperature, avoiding new nucleation events.[97]

4.2 Working under inert gas conditions

In order to work with air sensitive reagents and to dry the final products, a standard Schlenk line was employed. The device was equipped with an evacuation and an inert gas line. The inert gas was nitrogen, which was dried with the use of four different essicator materials: silica gel, potassium hydroxide, molecular sieve (4 Å), and phosphorus pentoxide. A vacuum up to 10^{-3} mbar was produced by a rotary vane vacuum pump from Vacuubrand (Wertheim, Germany). A cold trap, cooled with liquid nitrogen, was inserted between the vacuum pump and the evacuation line, to avoid the presence of volatiles into the rotary pump. The pressure was measured with a digital manometer VAP5 from Vacuubrand.

4.3 Washing and drying of nanoparticles

The resultant suspension of nanoparticles after the synthesis were normally washed, centrifugated (Sigma Centrifuges, Osterode am Harz, Germany) and re-dispersed several times in order to remove surfactant and non-reacted precursors. Depending on the synthesis, ethanol, isopropanol or water were used as solvent and an ultrasonic bath (for massive nanoparticles) from Bandelin Sonorex (Berlin, Germany) or magnetic stirring (for nanoscale hollow spheres) were used to re-suspend. After washing, final products were dried under reduced pressure (10^{-3} mbar) at 60 °C in an oven.

4.4 Chemicals used

The following chemicals were used in the syntheses presented in this thesis (Table 7).

Table 7: Chemicals used in this thesis: empirical formula, purity and distributors.

Chemicals	Empirical formula	Purity	Distributor
Aminomethyl phosphonic acid (H_2AMP)	CH_6NO_3P	99%	Acros Organics
Aluminium tri-*sec*-butoxide	$C_{12}H_{27}AlO_3$	97%	Sigma-Aldrich
Argon	Ar	N50, > 99.999%	Air Liquid
DL-1-(Aminoethyl) phosphonic acid (1-H_2AEP)	$C_2H_8NO_3P$	97%	Acros Organics
2-Aminoethyl phosphonic acid (2-H_2AEP)	$C_2H_8NO_3P$	99%	Acros Organics
3-Aminopropyl phosphonic acid (H_2APP)	$C_3H_{10}NO_3P$	97%	Acros Organics
4-Aminobutyl phosphonic acid (H_2ABP)	$C_4H_{12}NO_3P$	≥ 99%	Sigma-Aldrich
1R(+)(1-Amino-2-methylpropyl) phosphonic acid	$C_4H_{12}NO_3P$	98%	Sigma-Aldrich
Barium 2-ethylhexanoate	$C_{16}H_{30}BaO_4$	98%	Sigma-Aldrich
β-alanine	$C_3H_7NO_2$	99%	Sigma-Aldrich
Calcium-2-ethylhexanoate	$C_{16}H_{30}CaO_4$	98%	ABCR
Carbon dioxide	CO_2	N45, > 99.995%	Air Liquid
Cobalt(II) acetate tetrahydrate	$C_4H_6CoO_4 \cdot 4H_2O$	for analysis	Merk
Copper(II) acetate hydrate	$C_4H_6CuO_4 \cdot H_2O$	≥ 98%	Fluka
Copper(II) nitrate trihydrate	$CuN_2O_6 \cdot 3H_2O$	> 98%	Sigma-Aldrich
(L)-Cysteine	$C_3H_7NO_2S$	97%	Sigma-Aldrich

Meso-2,3-diaminosuccinic acid	$C_4H_8N_2O_4$	-	Sigma-Aldrich
Di-*n*-butylmagnesium, 0.5 M in heptane	$C_8H_{18}Mg$	-	Acros Organics
Doxorubicin hydrochloride	$C_{27}H_{29}NO_{11}$ HCl	100 ± 2% (HPLC)	Sigma-Aldrich
Ethanol	C_2H_6O	Techn.	Seulberger
Ethylenediamine-N,N'-diacetic acid	$C_6H_{12}N_2O_4$	≥ 98%	Sigma-Aldrich
Gadolinium(III) chloride hexahydrate	Cl_3Gd $6H_2O$	99.999%	Sigma-Aldrich
Guanidine hydrochloride	CH_5N_3 HCl	≥ 99%	Sigma-Aldrich
(1-Hexadecyl)trimethylammonium bromide (CTAB)	$C_{19}H_{42}BrN$	98%	ABCR
Helium	He	N50, > 99.999%	Air Liquid
n-Hexane	C_6H_{14}	Techn.	Seulberger
1-Hexanol	$C_6H_{14}O$	98%	Sigma-Aldrich
Iron(II) chloride tetrahydrate	Cl_2Fe	≥ 98%	AppliChem
Lanthanum(III) chloride heptahydrate	$LaCl_3 \cdot 7H_2O$	99.99%	Sigma-Aldrich
(L)-Malic acid	$C_4H_6O_5$	97%	Sigma-Aldrich
Melamine	$C_3H_6N_6$	-	Sigma-Aldrich
Methanol	CH_4O	99%	Seulberger
Nitrogen	N_2	N50, > 99.999%	Air Liquid
Oxygen	O_2	99.5%	Air Liquid
2-Propanol (Isopropanol)	C_3H_8O	Techn.	Seulberger
Propyl phosphonic acid (H_2PP)	$C_3H_9O_3P$	95%	Sigma-Aldrich
Riboflavin 5'-monophosphate sodium salt hydrate (FMNHNa)	$C_{17}H_{20}N_4NaO_9P$	73-79% fluorometric	Sigma-Aldrich
Sodium Hydroxyde	NaOH	≥ 99%	Riedel de Haën
Toluene	C_7H_8	Techn.	Seulberger
Urea	CH_4N_2O	99.5%	ABCR

5 Results and Discussion

5.1 Application of nanoscale γ-AlO(OH) hollow spheres

The discharge of CO_2 into the atmosphere has increased considerably in the last few years: in this respect the sorption and storage of CO_2 attract more and more attention particularly in the area of greenhouse gas emission and, consequently, global warming. As potential gas sorbents, nanoscale AlO(OH) hollow spheres are proposed here for several reasons: their high specific surface area, the mild base character of the hydroxyl groups which can interact with the acidic CO_2 molecules, their low weight, chemical stability and relatively low cost.[98]

Moreover, the presence of the inner cavity is capable of loading different molecules, drugs for example. This, as well as the low toxicity of the material, suggest the use of nanoscale AlO(OH) hollow spheres also for medical purpose, as presented in paragraph 5.1.2.

Nanoscale AlO(OH) hollow spheres were firstly synthesized and characterized by Buchold *et al.*.[12] Transmission electron microscopy is shown in Figure 32: it reveals an outer diameter of 30 - 35 nm, a cavity size of 20 - 25 nm and a wall thickness of 4 - 7 nm.

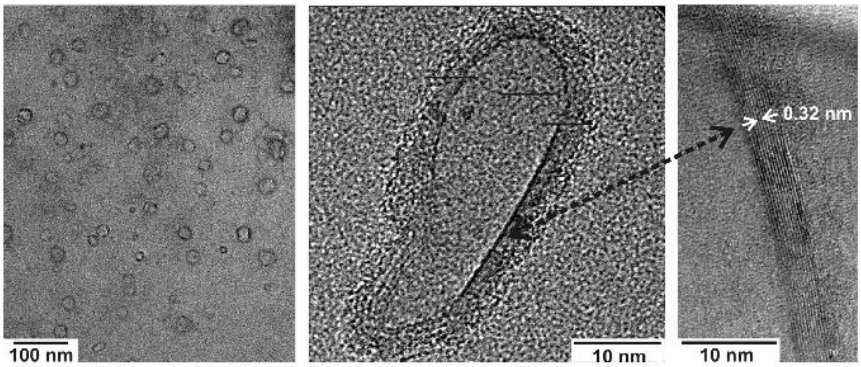

Figure 32: TEM of the as-prepared AlO(OH) hollow spheres.[12]

5.1.1 CO_2 sorption with nanoparticles γ-AlO(OH)

Nanoscale hollow spheres as an alternative for sorption and storage of CO_2 have been yet barely addressed for CO_2 capture as well as for gas sorption at all.[94] First studies are limited to hydrogen storage on carbon shells[99] and various precious metal clusters-containing SiO_2 hollow spheres.[100]

The synthesis of the AlO(OH) hollow spheres was performed according to the literature[12] and as described in paragraph 8.1. After careful drying and removal of water from the inner cavity, the AlO(OH) hollow spheres were first subjected to volumetric nitrogen sorption analysis (Figure 33). According to the BET formalism, a specific surface area of 545(±24) m^2 g^{-1} was deduced. The observed significant hysteresis of the N_2 sorption/desorption isotherms at -196 °C can be explained when assuming a kinetically hindered gas transport through the sphere wall. With regard to the pore volume, BJH analysis results in 0.6 - 0.8 cm^3 g^{-1} and a broad pore size distribution ranging from 1 nm to 20 nm, pointing out the inner cavity of the hollow spheres as well as much smaller pores across the sphere wall.

The presence of a sphere wall suggests a certain activation energy for CO_2 molecules to be stored in the inner cavity of the hollow spheres. On the other hand, the pretreatment temperature, necessary to remove eventually gas sorbed prior to the CO_2 sorption measurement, should not be too high in order to avoid any modification due to dehydration and/or aggregation of the nanoscale hollow spheres. Consequently, the pretreatment temperature was chosen in the range between 50 and 150 °C, subsequently followed by CO_2 sorption performed at 50 and at 100 °C (Figure 34). A maximal CO_2 uptake of 260 mg g^{-1} was observed at 90 bar and 50 °C. If all water inside of the hollow sphere cavity was removed, the pretreatment is only with minor influence on the CO_2 sorption isotherms (Figure 35).

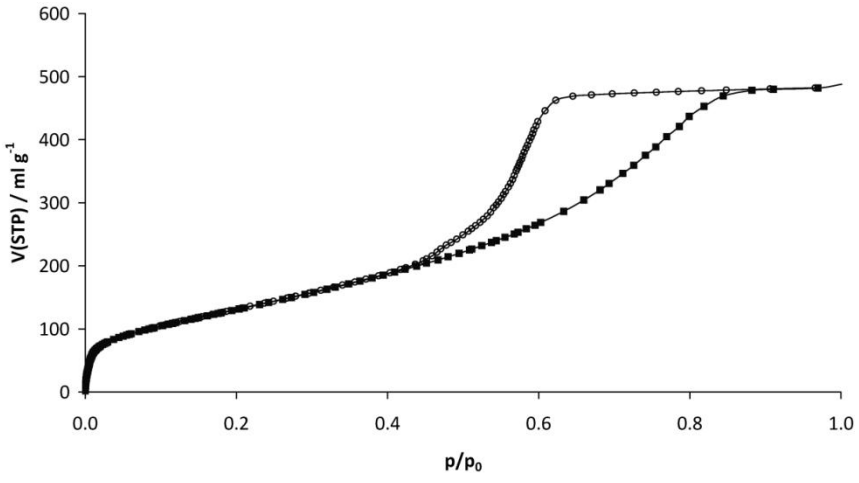

Figure 33: Volumetric analysis on AlO(OH) hollow spheres: N_2 sorption (squares) and desorption (circles) isotherms at -196 °C.[98]

In view of future industrial application, the material should be reusable for more than one time. In this context, a second and a third sorption cycle of gravimetric sorption analysis was performed on the same sample, after re-activation at 150 °C: the result is presented in Figure 36. The material is stable and does not show inactivity after three cycles of sorption/desorption, confirming a reversibility of the process up to three cycles.

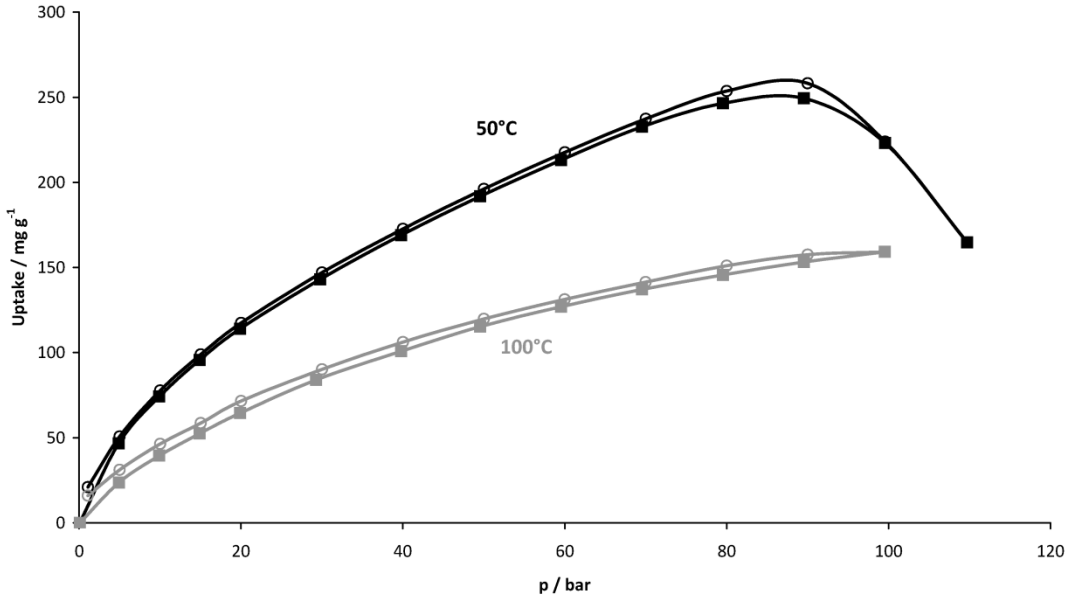

Figure 34: Gravimetric analysis on AlO(OH) hollow spheres: pretreatment at 150 °C with CO_2 sorption analysis at 50 °C and 100 °C.[98]

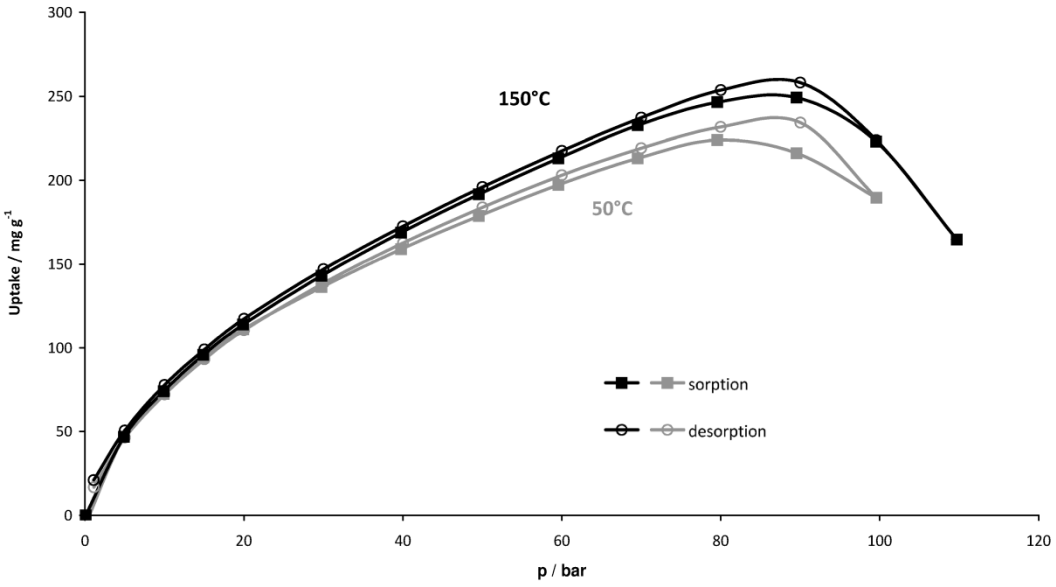

Figure 35: Gravimetric analysis on AlO(OH) hollow spheres: pretreatment at 50 °C and 150 °C with sorption analysis at 50 °C.[98]

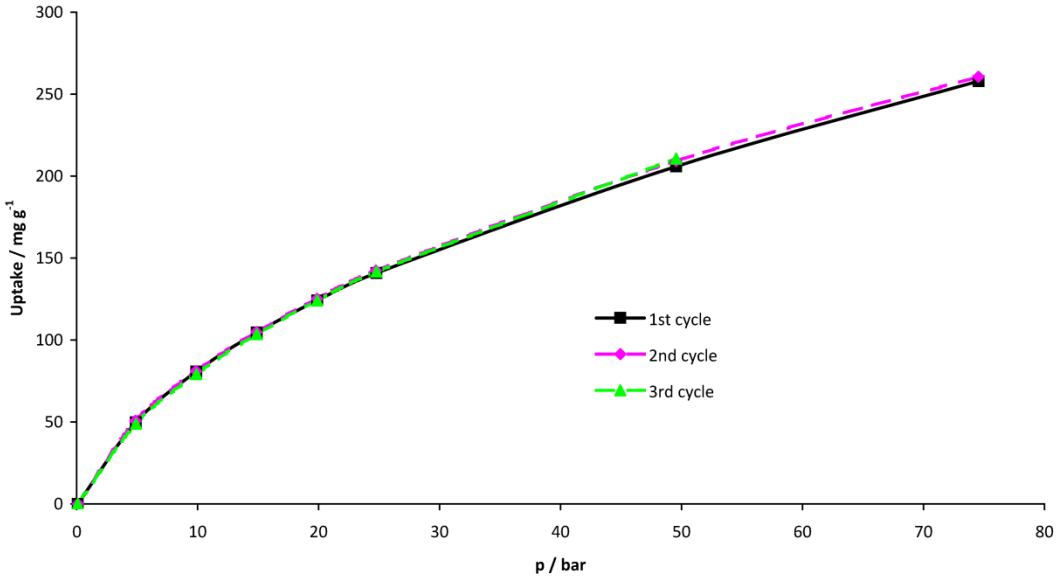

Figure 36: CO_2 isotherms (sorption branches) on AlO(OH) hollow spheres at 50 °C, repeatability test. Between each cycle the sample was reactivated (T = 150 °C, P = 10^{-3} mbar).

As an example, only for the gravimetric sorption/desorption CO_2 analysis performed on this material, the difference between reduced mass and surface excess is shown in Figure 37. Moreover, the application of the two models for the calculation of the absolute amount of gas sorbed (Figure 38 model 1, Figure 39 model 2) described in theoretical section (paragraph 2.3.2) is shown. Note the significant difference in the uptake expressed as reduced mass (-150 mg g^{-1} at 30 bar) and as surface excess (145 mg g^{-1} at 30 bar), as well as the dissimilarity of the CO_2 capacity obtained by applying model 1 (357 mg g^{-1} at 90 bar) or model 2 (480 mg g^{-1} at 90 bar). The seemingly decrease in the CO_2 uptake at pressure ≥ 90 bar in the surface excess is due to a less precise buoyancy correction at high pressure,[101] whereas applications of different models for the calculation of the absolute amount sorbed result in the saturation (model 1) or even increase (model 2) of the gas uptake at higher pressure (carbon dioxide at the temperature of 50 °C becomes supercritical at 80 bar)[102]. As a consequence, it appears obvious the impossibility to describe an isotherm without a detailed explanation of the theory employed to analyse it.

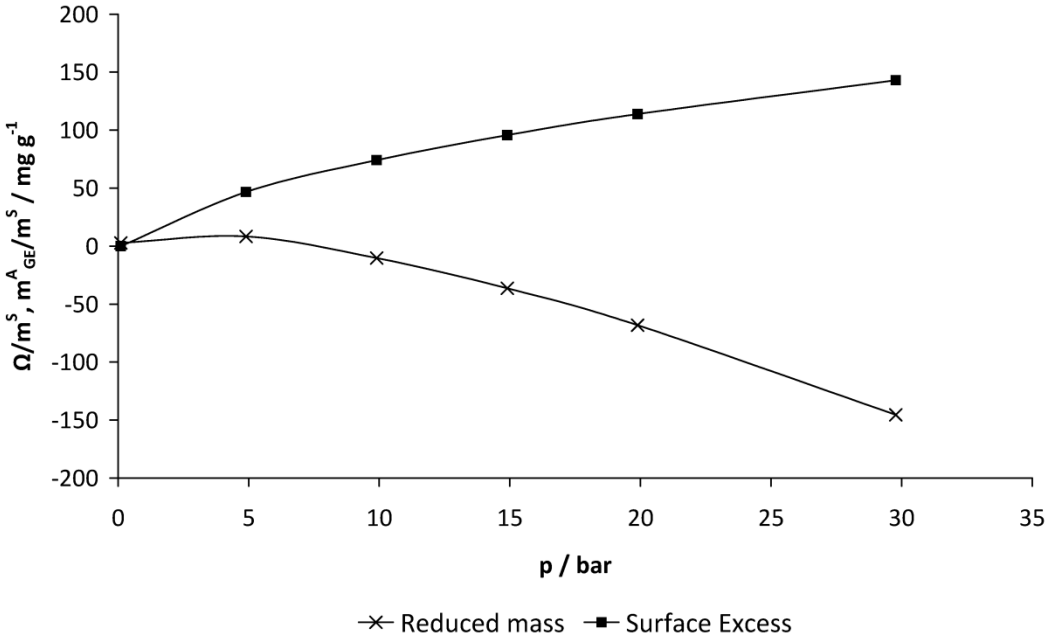

Figure 37: Carbon dioxide (50 °C) sorption isotherm on AlO(OH) hollow spheres using the reduced mass (crosses) and the surface excess mass (squares).

The assumption of a certain activation energy for CO_2 to pass the sphere wall suggests the possibility to store CO_2 on AlO(OH) hollow spheres. To this concern, the hollow spheres were first loaded 100 °C and 50 bar, allowing the gas to enter the hollow sphere at high activation energy. The result is a CO_2 uptake of about 100 mg g^{-1} (Figure 40). Next, the CO_2-loaded hollow spheres were cooled to 45 °C, directly inside the MSB. With about 190 mg g^{-1} at 38 bar the CO_2 uptake is now almost doubled. And finally, the pressure was reduced up to 1 bar at the temperature of 45 °C. The CO_2 uptake remains at a more-or-less doubled value as compared to the isotherm at 100 °C. Altogether, the above course of temperature and pressure and the observed sorption/desorption hysteresis afford a reversible storage of CO_2.

Analogous to the procedure with CO_2, the same experiment was performed for N_2 (Figure 40). Here, the maximal N_2 uptake (30 mg g^{-1}) on the nanoscale AlO(OH) hollow spheres turned out to be four times lower as compared to CO_2 (190 mg g^{-1}). In addition, the sorption/desorption hysteresis is much less pronounced for N_2. Adsorption enthalpies of 25.5 kJ mol^{-1} (CO_2) and 10.2 kJ mol^{-1} (N_2), resulting from Langmuir isotherm models calculated by co-workers in the group of Prof. Staudt, (Institut für Nichtklassische Chemie, Leipzig), confirm the stronger interaction of the AlO(OH) hollow spheres with CO_2. These findings might allow the application of nanoscale AlO(OH) hollow spheres for post-combustion gas separation. This is supported by the fact that the activity of the material is tested at temperatures higher than room temperature.

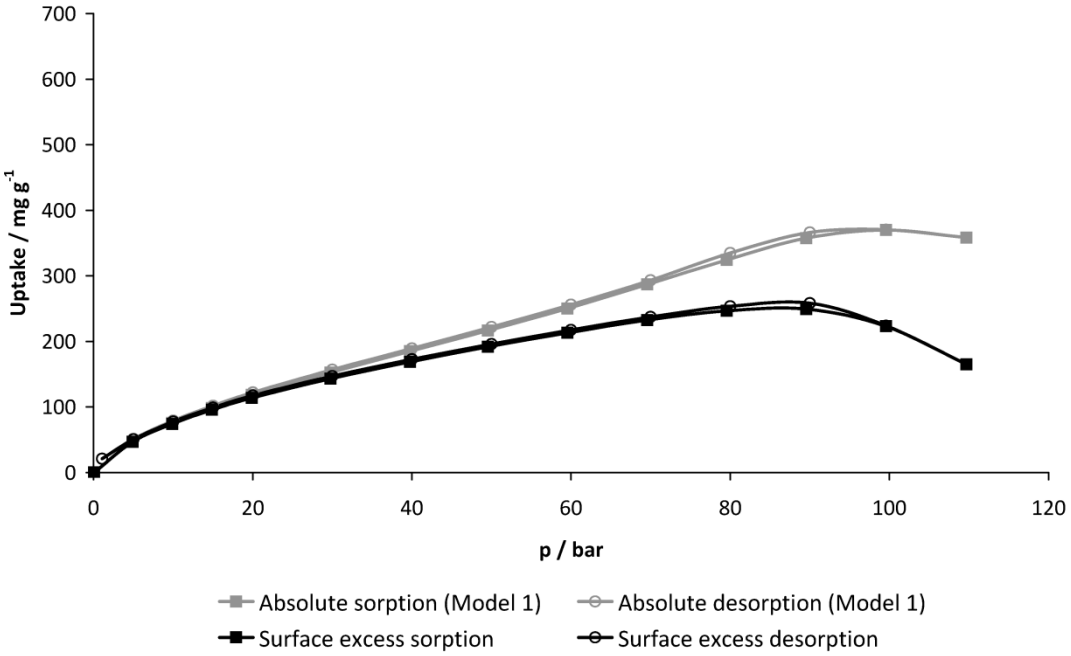

Figure 38: Isotherms for CO_2 sorption and desorption at 50 °C on AlO(OH) hollow spheres, surface excess (blank) *vs.* absolute amount (gray) using model 1, ρ_{liq} = 0.89 g cm^{-3}.

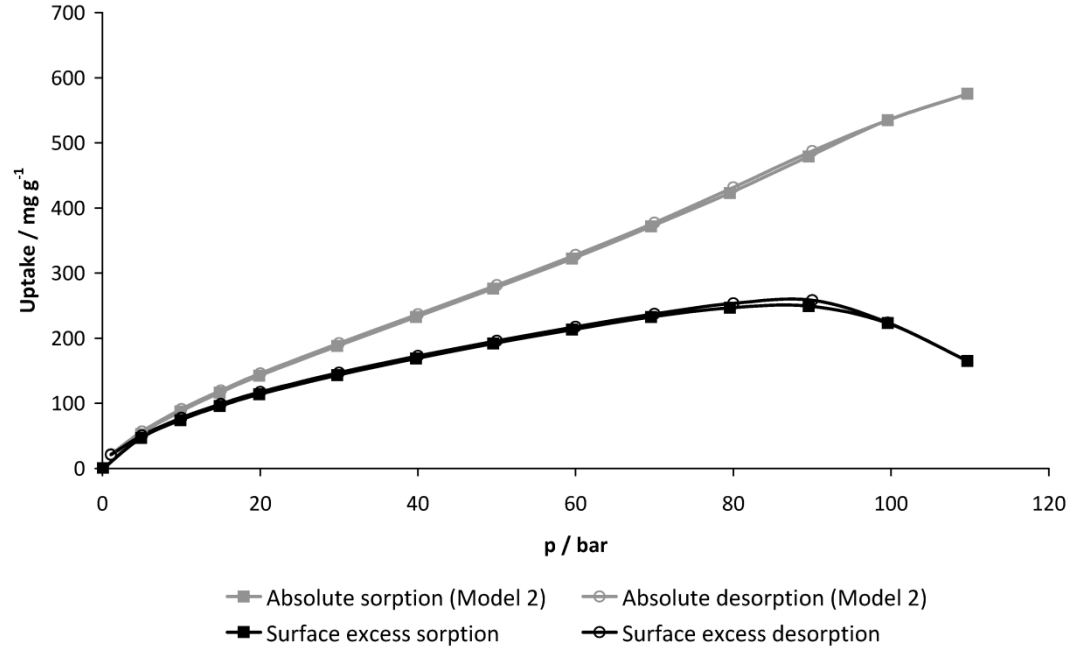

Figure 39: Isotherms for CO_2 sorption and desorption at 50 °C on AlO(OH) hollow spheres, surface excess (blank) *vs.* absolute amount (gray) using model 2, V^P/m^S = 0.826 cm^3 g^{-1}, V^P = 0.1125 cm^3.

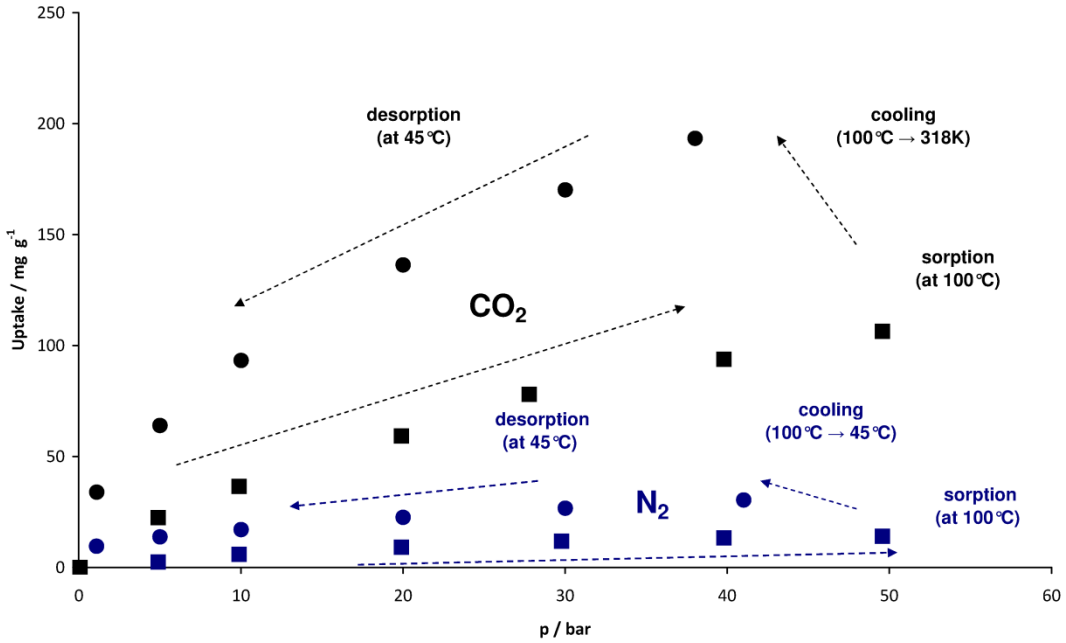

Figure 40: CO_2 (black) and N_2 (blue) sorption analysis of nanoscale AlO(OH) hollow spheres when reducing the temperature from 100 °C to 45 °C at a pressure of 50 bar.[98]

In order to verify the unique properties of the as-prepared nanoscale AlO(OH) hollow spheres, massive AlO(OH) nanoparticles of similar particle diameter and chemical composition but without an inner cavity were characterised and compared as a reference. Aiming at a reliable reference material that is commercially available, AlO(OH) nanoparticles with a diameter of 10 - 20 nm supplier by SkySpring Nanomaterials Inc., Houston, Texas were analysed. Electron microscopy and X-ray powder diffraction analysis confirmed the specifications as given by the supplier. Thus, the massive AlO(OH) nanoparticles exhibit an uniform size and shape with particle diameters ranging from 10 to 30 nm (Figure 41). Fourier-transform infrared spectra confirm the similarity of the hollow spheres and the massive AlO(OH) nanoparticles (3285 and 3099 cm^{-1} υ((Al)O–H), 1080 cm^{-1} δ(Al–O–H), 630 cm^{-1} υ(Al–O), 485 cm^{-1} δ(Al–O); the shoulder at 3490 cm^{-1} and the band at 1640 cm^{-1} can be assigned to the stretching and bending mode of water,[103] Figure 42). The reference sample was identified as crystalline boehmite *via* XRD (Figure 43). The more narrow shape of the vibrations in case of the massive nanoparticles is in line with the larger crystallite size as compared to the hollow spheres. Based on the similarity of size and composition of the as-prepared nanoscale AlO(OH) hollow spheres and the massive AlO(OH) nanoparticles, gas sorption and specific surface were compared. Nitrogen sorption of the reference material already turned out to be significantly different in comparison to the hollow spheres (Figure 44). Thus, only a minor hysteresis between N_2 adsorption and N_2 desorption is observed. Moreover, the specific surface area, as deduced *via* the BET formalism, results in 121(±5) m^2 g^{-1}, 4.5 times lower than the specific surface area measured for the hollow

spheres. This finding is in accordance with the absence of an inner cavity in case of the massive AlO(OH) nanoparticles. With regard to CO_2 sorption, massive AlO(OH) nanoparticles were pretreated at 150 °C under reduced pressure and analysed at 50 °C (Figure 45). The maximal CO_2 uptake of the reference material (80 mg g^{-1}) is again much lower as compared to the hollow spheres (260 mg g^{-1}). A CO_2 uptake being more than three-times as high as for massive AlO(OH) nanoparticles, again, points to the special properties of the as-prepared nanoscale AlO(OH) hollow spheres.

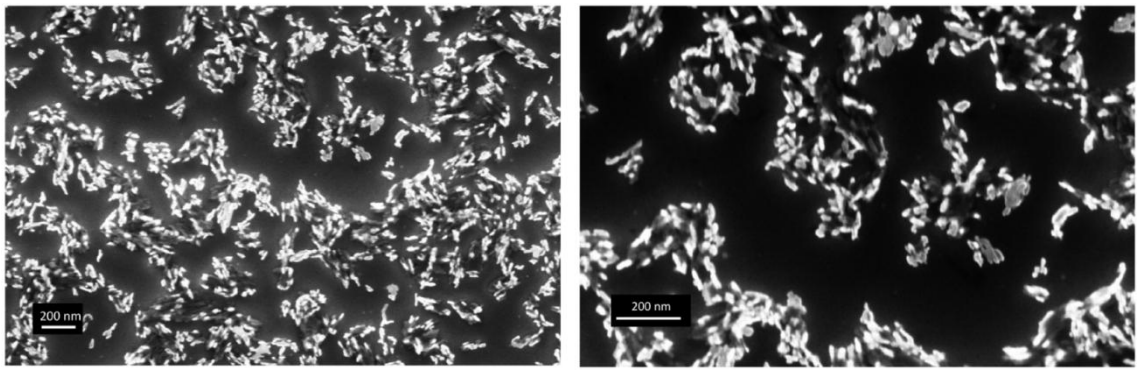

Figure 41: SEM pictures of massive AlO(OH) nanoparticles.[98]

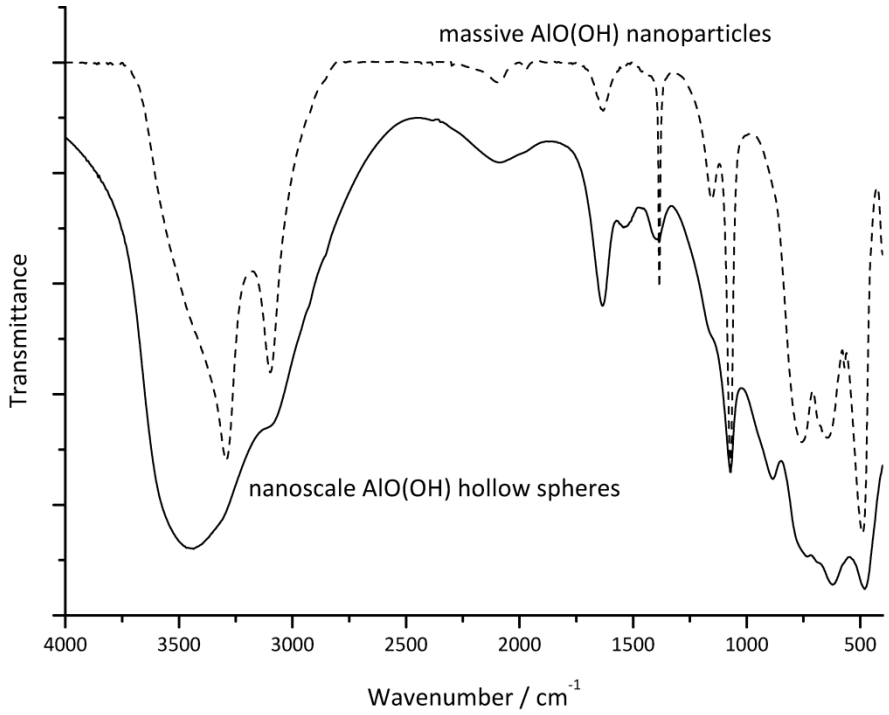

Figure 42: FT–IR spectra of nanoscale AlO(OH) hollow spheres and massive AlO(OH) nanoparticles (reference material: SkySpring Nanomaterials Inc.).[98]

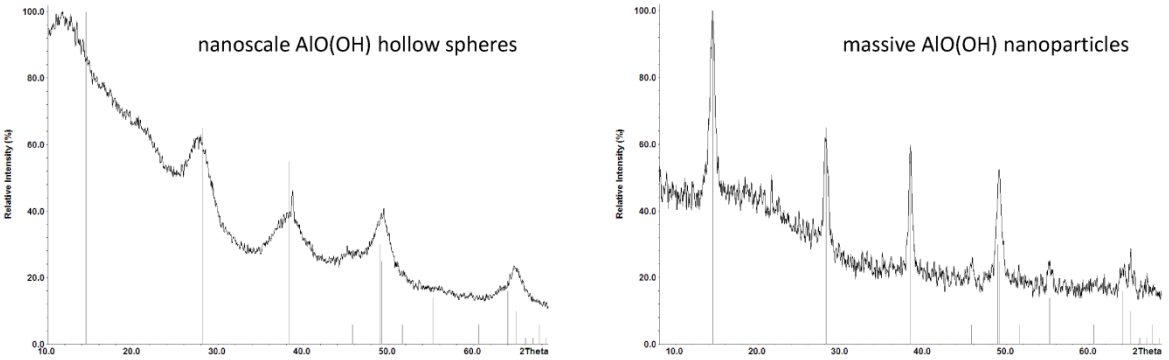

Figure 43: X-ray powder diffraction of nanoscale γ-AlO(OH) hollow spheres (left) and of massive AlO(OH) nanoparticles (right) (ICDD-No. 21-1307, γ-AlO(OH)-boehmite).[98]

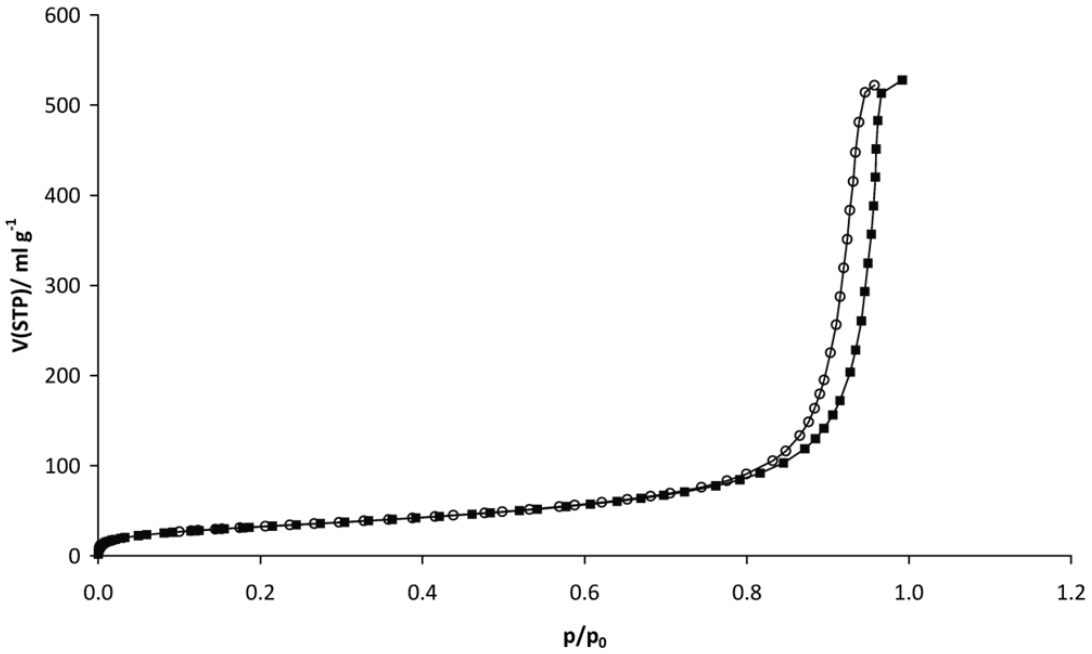

Figure 44: Volumetric analysis on massive AlO(OH) nanoparticles: N_2 sorption (squares) and desorption (circles) isotherms at -196°C.[98]

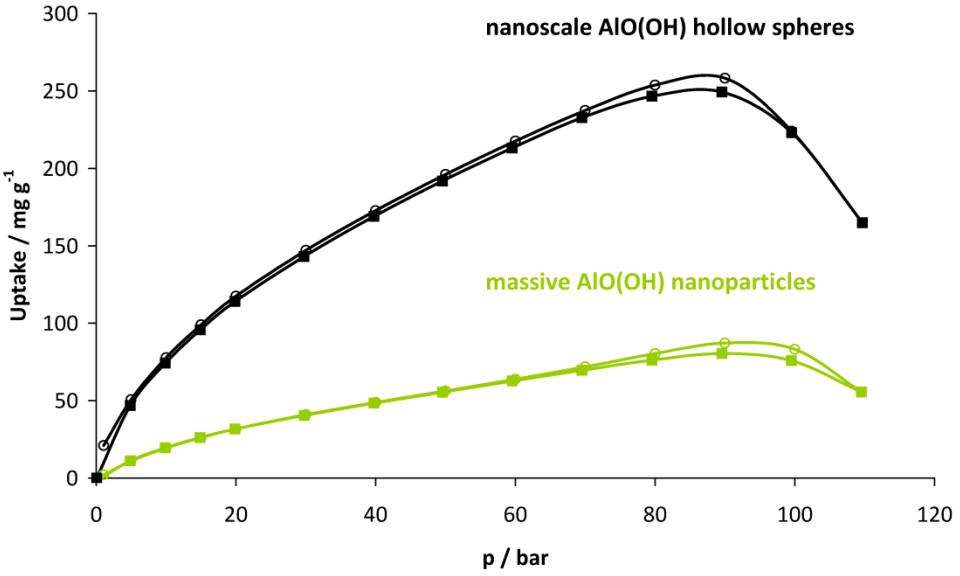

Figure 45: CO_2 isotherms on AlO(OH) hollow spheres (black) and massive AlO(OH) nanoparticles (green) at 50 °C. Both samples were pretreated in reduced pressure at 150 °C.[98]

In summary, the storage of CO_2 in AlO(OH) nanoscale hollow spheres were here shown for the first time, achieving a maximum of 260 mg of CO_2 sorbed per gram of AlO(OH) hollow spheres at 50 °C and 90 bar.

Modification of AlO(OH) hollow spheres with basic molecules

In order to improve the CO_2 capacity on AlO(OH) hollow spheres, the idea was to introduce a basic compound in the inner cavity of the nanocontainer directly during the synthesis. In this way, firstly, a higher uptake than 260 mg g^{-1} was addressed. Secondly, the theory of gas storage inside the cavity of the hollow spheres could be confirmed, after identification of the presence of basic compounds inside the nanocontainer. Due to the fact that the presence of an amino group should facilitate the sorption of the acidic gas CO_2, melamine, guanidine and urea were selected (Figure 46).

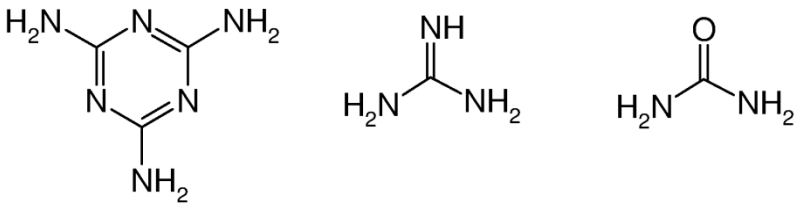

Figure 46: Basic molecules encapsulated on nanoscale AlO(OH) in order to increase CO_2 storage. Left: melamine, middle: guanidine, right: urea.

The CO_2 sorption measurements, performed under similar conditions as for the nanoscale pure AlO(OH), are shown in Figure 47.

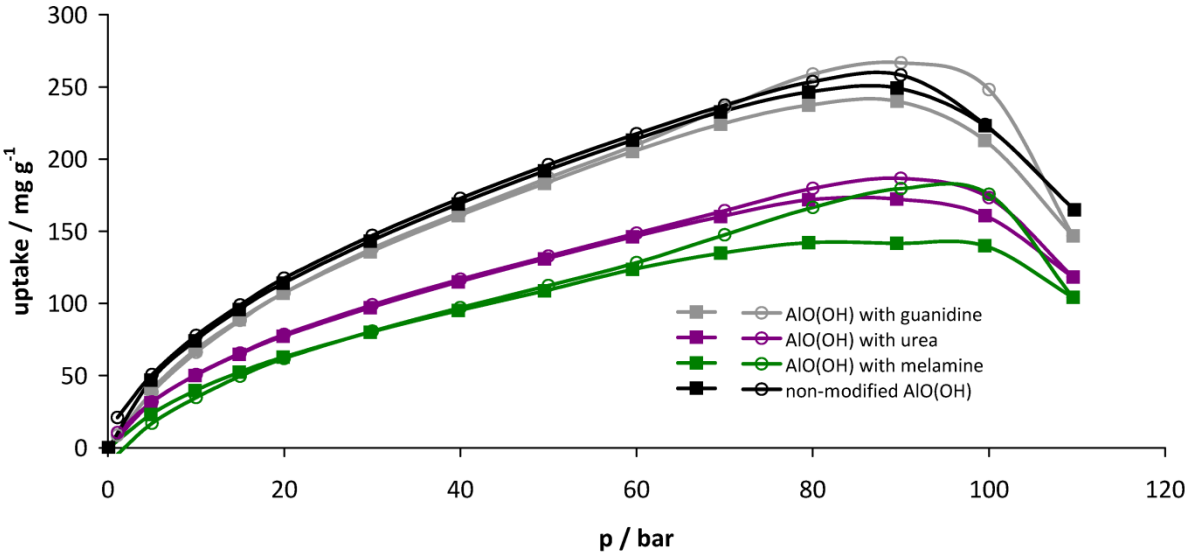

Figure 47: CO_2 sorption (squares) / desorption (circles) isotherms at 50 °C on nanoscale non-modified AlO(OH) (black) and AlO(OH) synthesized in the presence of guanidine (gray), urea (purple) and melamine (green). All materials were pretreated at 150 °C.

Only the material loaded with guanidine results in a similar uptake as the non-modified AlO(OH) (240 mg g^{-1} *vs.* 260 mg g^{-1}). The compounds containing urea and melamine show a reduced amount of CO_2, 170 mg g^{-1} and 142 mg g^{-1}, respectively.

The lower uptake of the urea-containing hollow spheres is easy explained: the high temperature used during the pretreatment of the sample on the MSB (T = 150°C) promote a decomposition of the amide, under evaporation of NH_3.[104] The ammonia reacts with the aluminium oxide hydroxide, generating aluminium hydroxide bayerite (Figure 48). The XRD patterns of the urea-modified AlO(OH) after CO_2 analysis appear sharper than the XRD reflections of the non-modified AlO(OH), which indicate a higher crystalline material, probably accompanied by the loss of the hollow structure. This results in the limited gas diffusion in the sample and, as a consequence, the reduction of the CO_2 capacity. According to XRD illustrated in Figure 49 and FT–IR spectroscopy[105] shown in Figure 50, the synthesis performed in the presence of melamine shows immediate formation of high crystalline $Al(OH)_3$ instead of AlO(OH) and, as well, a reduced CO_2 uptake.

The similar results in terms of CO_2 storage observed for the guanidine-modified and the non-modified AlO(OH) can be explained by analysis of the FT–IR spectrum (Figure 51): the typical vibrations (2100, 1070, 635, 480 cm^{-1})[103] identify the material as boehmite. Moreover, any

additional vibrations appear in the guanidine-modified AlO(OH) spectra. It is possible that the basic molecule was not encapsulated in the nanomaterial during the synthesis. On the other hand, the relevant vibrational bands of guanidine, due to the lower concentration of the basic molecule with respect to AlO(OH), are also low in intensity and are hidden by the strong bands of boehmite. The increase of the guanidine concentration during the synthesis would probably help its detection by FT–IR: unfortunately, the microemulsion system was destabilized upon addition of guanidine-concentrated polar phase, preventing any further steps. As an alternative, the colorimetric measurement of the adsorption produced by the purple reaction product between primary or secondary amines and ninhydrin[106], could be employed to test the presence of nitrogen in the final material. Since no improvement in the CO_2 capacity was observed, the guanidine-modified AlO(OH) system was not further investigated.

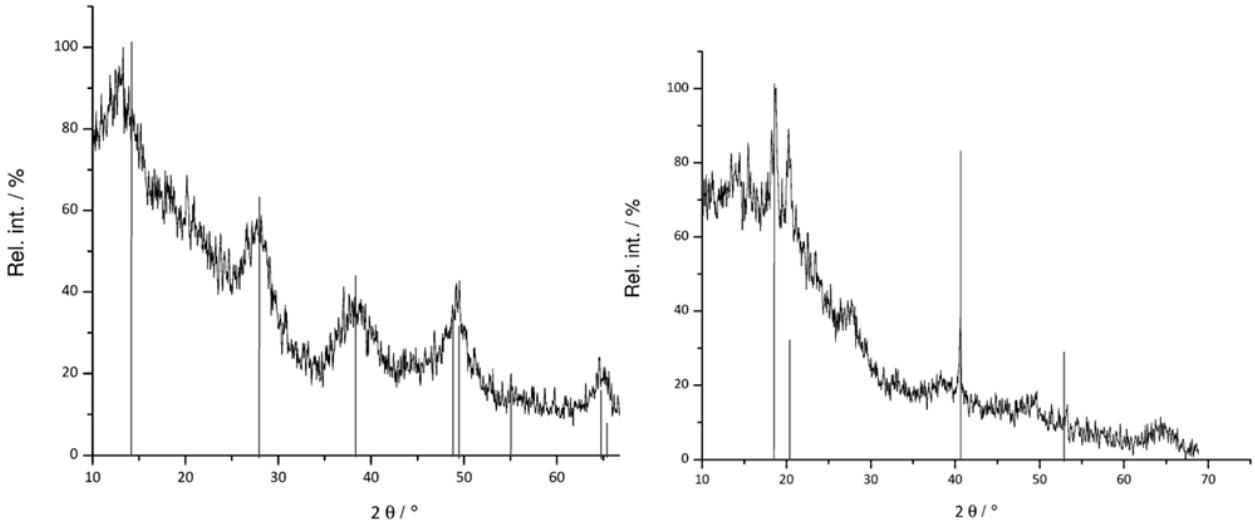

Figure 48: X-ray power diffraction patterns of the AlO(OH) modify with urea: left, as prepared (reference: ICDD-No.21-1307, aluminium oxide hydroxide, boehmite, syn). Right: after CO_2 sorption analysis at 50°C and pretreatment at 150°C (reference: ICDD-No. 1077-250, aluminium hydroxide, bayerite).

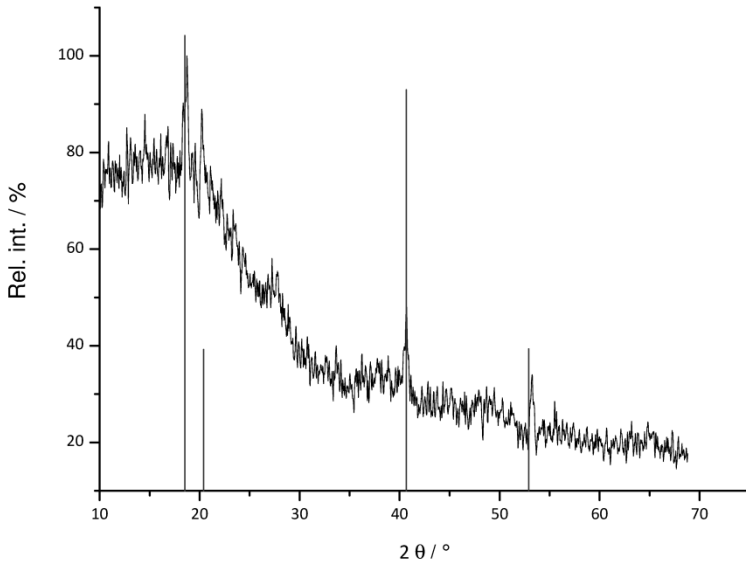

Figure 49: X-ray power diffraction patterns of the as prepared AlO(OH) modified with melamine (reference: ICDD-No.1077-250, aluminium hydroxide, bayerite).

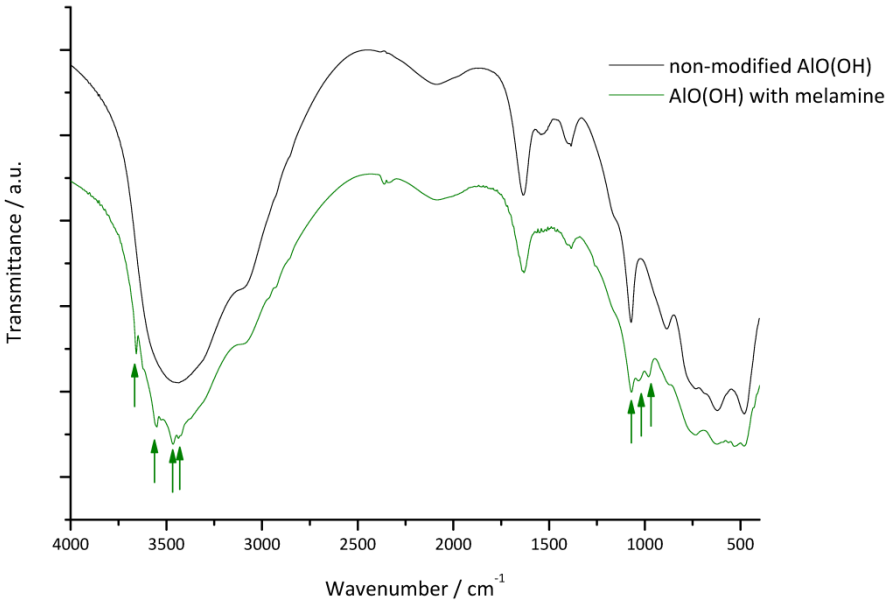

Figure 50: FT–IR spectra of non-modified AlO(OH) (black) and melamine modified AlO(OH) (green). The stretching and bending vibrations of the hydroxyl groups characteristic for bayerite (according to [105]), are indicated by arrows.

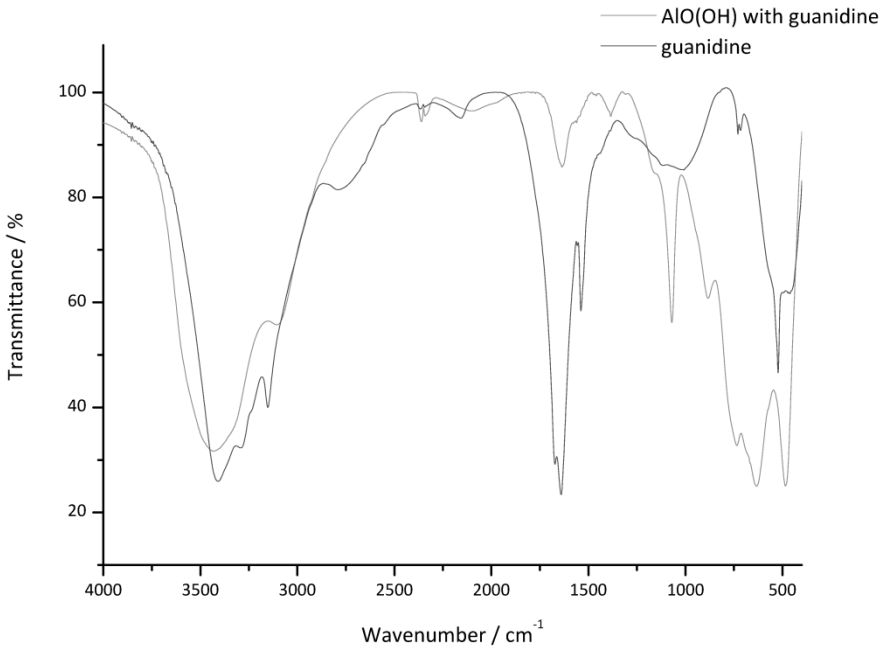

Figure 51: FT–IR spectrum of guanidine modified AlO(OH) (gray). The spectrum of pure guanidine (dark gray), very comparable to [107], is shown as a reference.

5.1.2 Nanoscale γ-AlO(OH)@doxorubicin for cancer therapy

Doxorubicin (DXR) is one of the most commonly used chemotherapeutic drugs to date, used to treat a range of tumours. Nevertheless, it has also some negative aspects: toxicity (cardiotoxicity first), low selectivity towards tumoral cells and fast metabolic decomposition before reaching cancer cells.[15] In order to improve the drug transport and, at the same time, to decrease the cytotoxicity of doxorubicin, different delivery systems were studied, including liposomes, hydrogel and nanoparticulate systems.[15] Even though drug-delivery systems based on nanoparticles have been extensively studied over the past decades, doxorubicin-filled AlO(OH) hollow spheres are proposed here, due to their easy, mild synthesis and low toxicity of the loading material. A deeper look into the literature clearly points out that different hollow sphere systems have already been proposed.[108] Jiao *et al.*[108a] suggest hollow mesoporous silica nanoparticles (average diameter larger than 200 nm) as a doxorubicin carrier. The drawback is the long process required to obtain the hollow silica nanomaterial. Firstly, the synthesis of the mesoporous silica nanoparticles has to be performed. Secondly the dissolution of the core template occurs; then the surface is modified with carbon-carbon double bonds and finally, the doxorubicin can be loaded. Wang *et al.*[108b] propose magnesium silicate hollow spheres (380 nm in diameter) with high storage capacity of guest molecules. The synthesis adopted here was a template-etching route, involving a heating step upwards to 160 °C for 12 hours. After cooling, drying and re-suspension, the doxorubicin was loaded. Zhu and co-

workers[108c] published the synthesis and characterisation of hollow zinc phosphate nanospheres for drug release prepared by biofriendly and template-free method at mild temperatures not more than 25 °C. The negative aspect is that they don't perform any *in vivo* analysis, leaving an open question: do hollow zinc phosphate nanospheres modified with doxorubicin show effects also on tumors progression in living organisms?

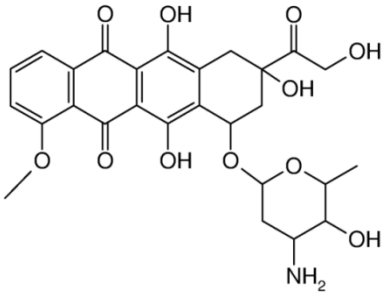

Figure 52: Chemical formula of doxorubicin. IUPAC name: (7S,9S)-7-[(2R,4S,5S,6S)-4-amino-5-hydroxy-6-methyloxan-2-yl]oxy-6,9,11-trihydroxy-9-(2-hydroxyacetyl)-4-methoxy-8,10-dihydro-7H-tetracene-5,12-dione.

Doxorubicin-filled AlO(OH) hollow spheres were gained by water-in-oil (*w/o*) microemulsion approach (see paragraph 8.2). After dissolution of the drug in the polar phase (water and methanol in the ratio 1:1), the formation of the sphere wall takes place at the phase boundary, between Al(*sec*-$OC_4H_9)_3$ dissolved in the non-polar-phase and water. The incorporation of the drug into the hollow spheres is easily validated by the colour as shows in Figure 53: the non-filled AlO(OH) hollow spheres are colourless, whereas the loaded ones appear pink. This change of physical property can be investigated *via* UV-Vis spectroscopy (Figure 54). Note the slight redshift of the AlO(OH)@doxorubicin band in comparison to the free doxorubicin: it originates from the fact that the free hydroxyl groups and carbonyl groups of doxorubicin (Figure 52) interact with the AlO(OH) container, varying the energetic levels of the molecular electrons, and, as consequence, the colour.

Figure 53: Nanoscale AlO(OH) hollow spheres (left) and DXR-filled AlO(OH) hollow spheres (right).

High resolution transmission electron microscopy (HRTEM) (Dr. R. Popescu, Laboratory for Electron Microscopy, LEM, KIT) proofs size, size distribution and shape of the as-prepared doxorubicin-filled AlO(OH) hollow spheres. The hollow spheres are characterized by an outer diameter of 10 - 40 nm, inner diameter of 5 - 10 nm and wall thickness of 3 - 7 nm (Figure 55). The chemical composition of the loaded hollow spheres was studied by infrared spectroscopy, illustrate in Figure 56. In addition to all the characteristic vibrations of aluminium oxide hydroxide, the loaded hollow spheres show supplementary bands in the $–CH_2–$ stretching region (2950 - 2880 cm^{-1}), confirming the presence of the organic molecule. For quantification purpose, elemental analysis and thermogravimetric analysis were used. EA of the as prepared sample shows a carbon weight percent between 2.5 and 4.3 (±1)%, whereas TGA, presented in Figure 57, results in 2.2% of drug present in the hollow spheres (13.7 – 11.5 = 2.2).

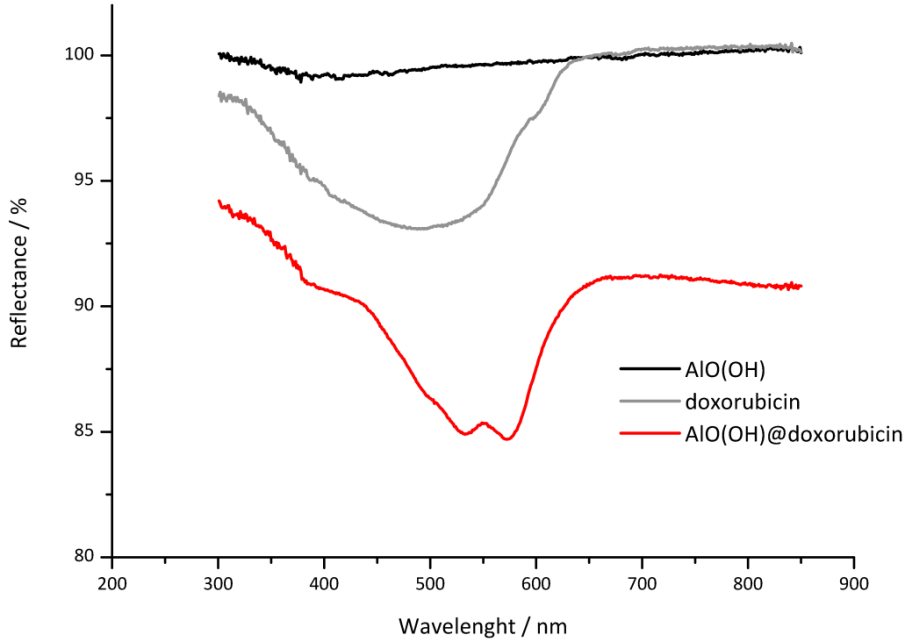

Figure 54: UV-Vis spectra of nanoscale AlO(OH) hollow spheres (black), free doxorubicin (gray) and doxorubicin-filled AlO(OH) hollow spheres.

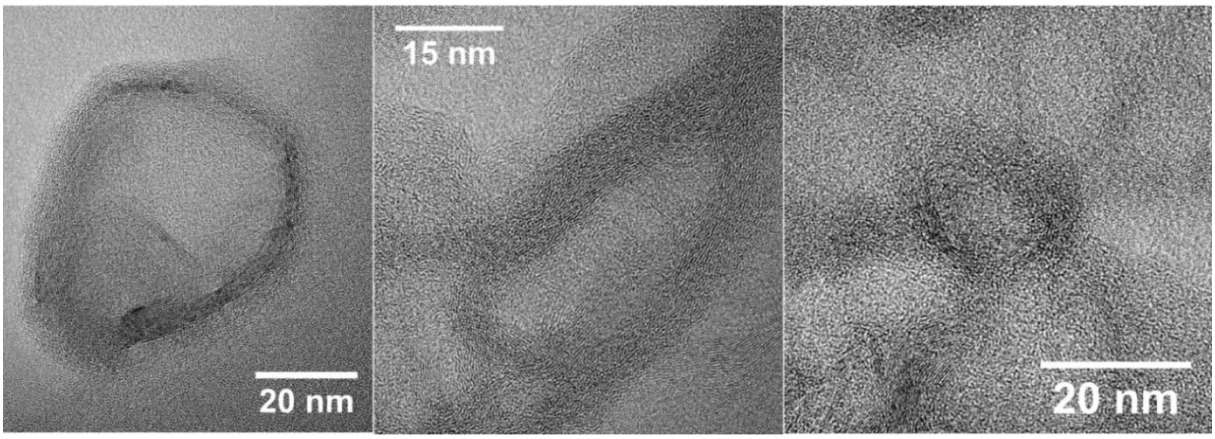

Figure 55: HRTEM of the as-prepared doxorubicin-filled AlO(OH) hollow spheres.[109]

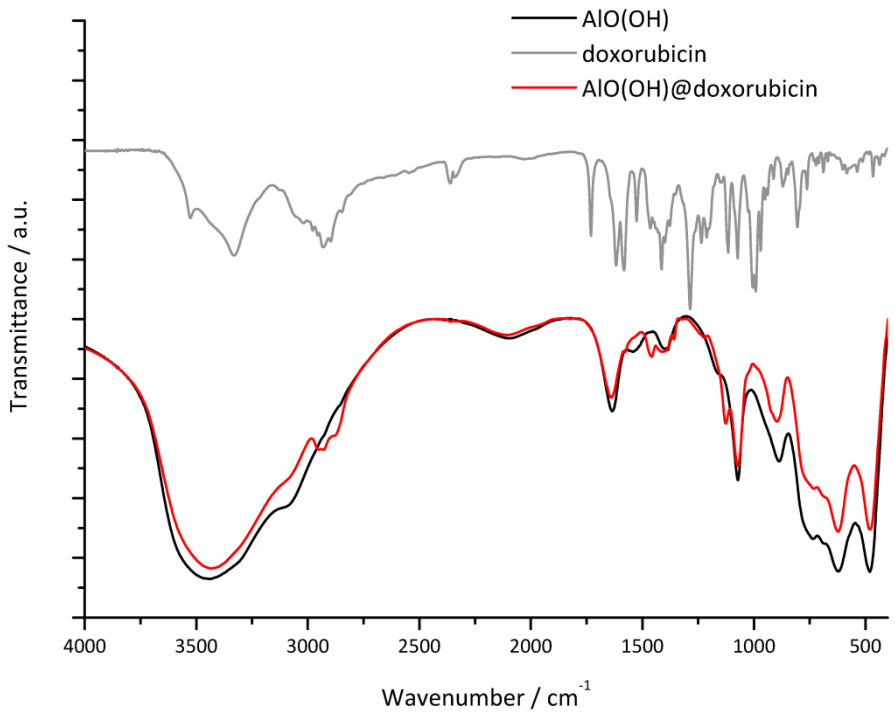

Figure 56: FT–IR spectra of nanoscale AlO(OH) hollow spheres (black), free doxorubicin (gray) and DXR-filled AlO(OH) hollow spheres.

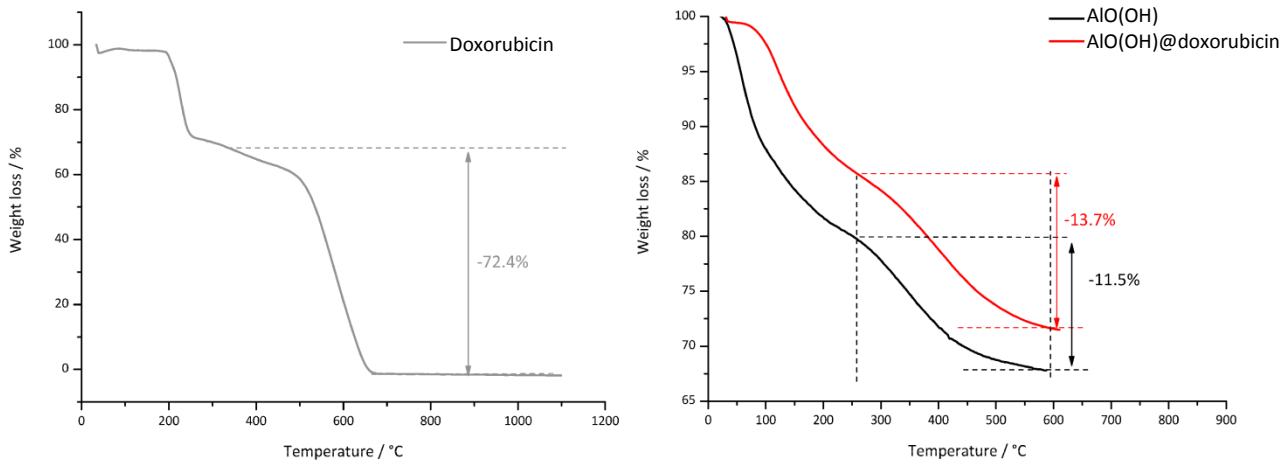

Figure 57: TGA of the free doxorubicin (gray), nanoscale AlO(OH) hollow spheres and DXR-filled AlO(OH) hollow spheres.

For biological tests, performed by C. Seidl in the group of Priv.-Doz. U. Schepers (Institute of Toxicology and Genetics, KIT) a suspension of the DXR-filled hollow spheres in a water solution of dextran (4 mg dextran per 1 ml of water) was prepared: more in detail, 0.75 mg of sample were suspended in 10 ml of water, giving a final doxorubicin concentration of 1.5 µg ml^{-1}.

Doxorubicin-filled AlO(OH) hollow spheres are taken up by the A459 lung adenocarcinoma cell line, as shown by confocal laser scanning microscopy (CLSM) (Figure 58a). The fluorescence of doxorubicin was excited with an argon laser at 488 nm to show red emission in the 590 nm range. However, the intracellular concentration of the DXR-filled AlO(OH) hollow spheres remained at a low level as compared to a cell treatment with non-encapsulated doxorubicin, as some spheres formed agglomerates which interact with the cell surface but were not internalized due to steric hindrance (Figure 58a).

Furthermore, doxorubicin-filled AlO(OH) hollow spheres showed no significant systemic cytotoxicity *in vitro* in MTT (3-(4,5-dimethylthiazol-2-yl)-2,5-diphenyltetrazolium bromide) assays. A459 cells were incubated for 72 h with different concentrations of doxorubicin-filled AlO(OH) hollow spheres. Cells were treated with 250 nM up to 1 µM of doxorubicin-filled AlO(OH) hollow spheres (concentrations related to doxorubicin content) and they show a survival rate of around 80% and an LD50 > 1 µM within the statistical error, indicating an excellent biocompatibility (Figure 58b). The same results were obtained for A459 cells treated with non-loaded AlO(OH) hollow spheres (Figure 58b). On the other hand, cells treated with non-encapsulated doxorubicin under the same conditions already began to undergo apoptosis and necrosis (Figure 58b).

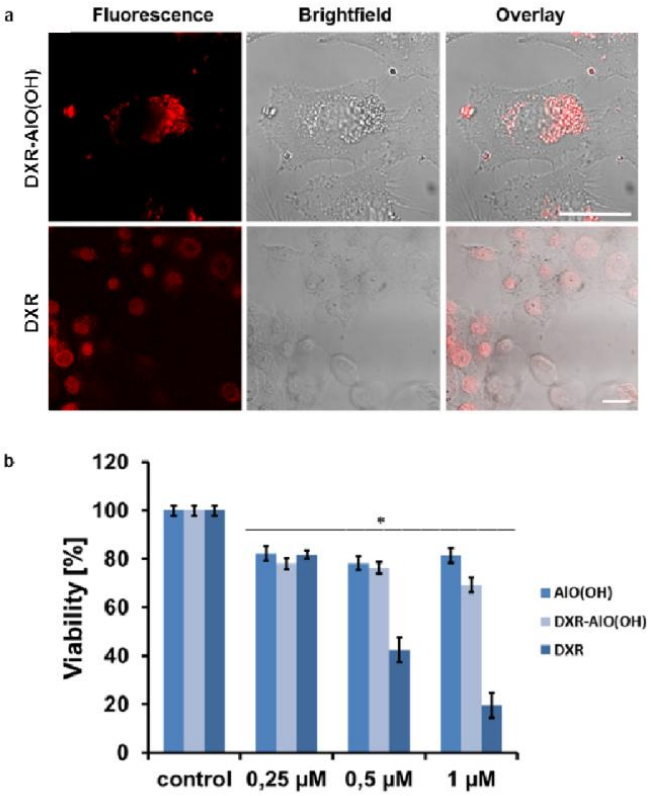

Figure 58: a) Visualization of DXR-filled AlO(OH) hollow spheres and non-encapsulated doxorubicin in cells *via* fluorescence CLSM using 488 nm excitation (emission at 590 nm) Scale bar is 50 µm for all images. b) Evaluation of the *in vitro* cytotoxicity of DXR-filled AlO(OH) hollow spheres in A459 cells using an MTT assay. Statistical errors bars were calculated from triplicates of n = 3. Significance was determined according to student's t-test.[109]

In vivo experiments were carried out to analyse the effects of doxorubicin-filled AlO(OH) hollow spheres on tumor progression. For this purpose, a breast cancer BALB/c mouse model was used.[110] Murine 4T1 breast-adenocarcinoma cells (1×10^6 cells per ml) were orthotopically implanted into the mammary fat pad of 8 - 12 weeks old female BALB/c-mice. The 4T1 cell line is an excellent system for investigation of human breast cancer, as it provides the opportunity to study the agent's impact not only on solid tumors but also on metastasis to organs affected in human breast cancer. 11 days after transplantation of the tumor cells, mice were intraperitoneally injected into the abdominal cavity with doxorubicin-filled AlO(OH) hollow spheres (0.15 mg doxorubicin per kg of body weight, in PBS buffer).

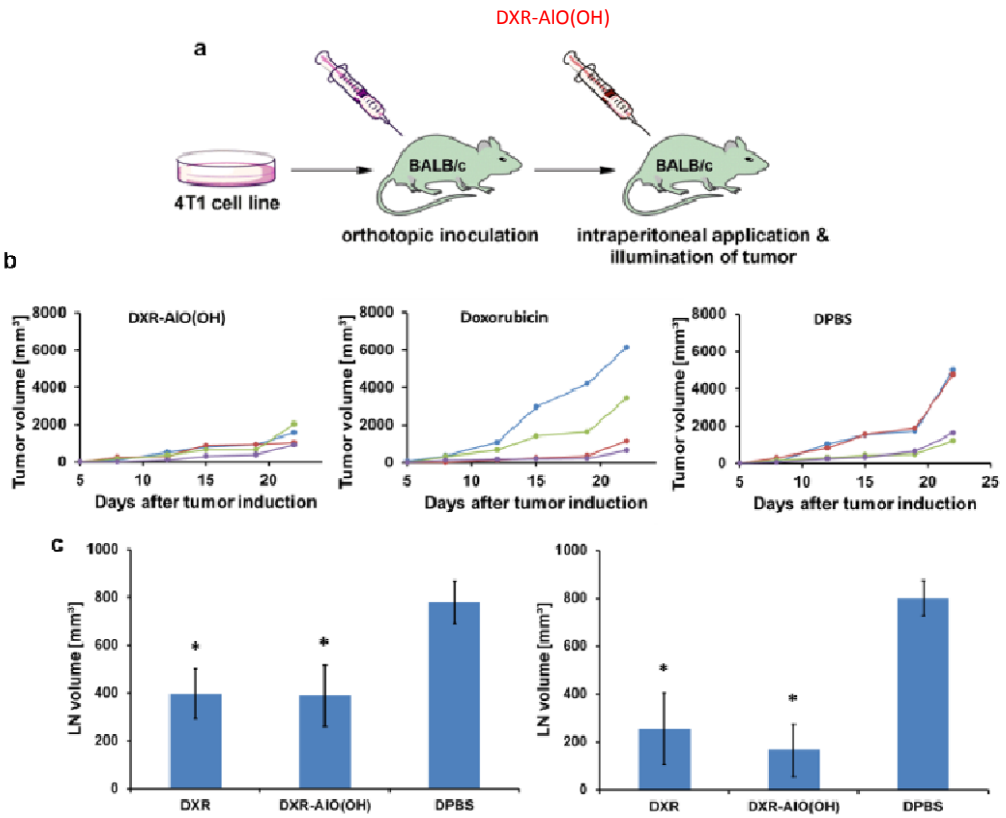

Figure 59: a) Schematic presentation of the animal treatments. Tumor bearing mice (n = 4) were treated with DXR-filled AlO(OH) hollow spheres (0.15 mg doxorubicin kg^{-1} of bodyweight). b) Measurement of the tumor volumes as a function of time (different colors of the curves represent different animals in the respective group of n = 4). c) Quantification of the lymph-node metastasis by measuring the lymph-node volume. Mean volumes of ipsilateral axillary (left) and inguinal (right) lymph nodes were measured. Error bars indicate the statistical error. Significance was tested according to student's t-test.[109]

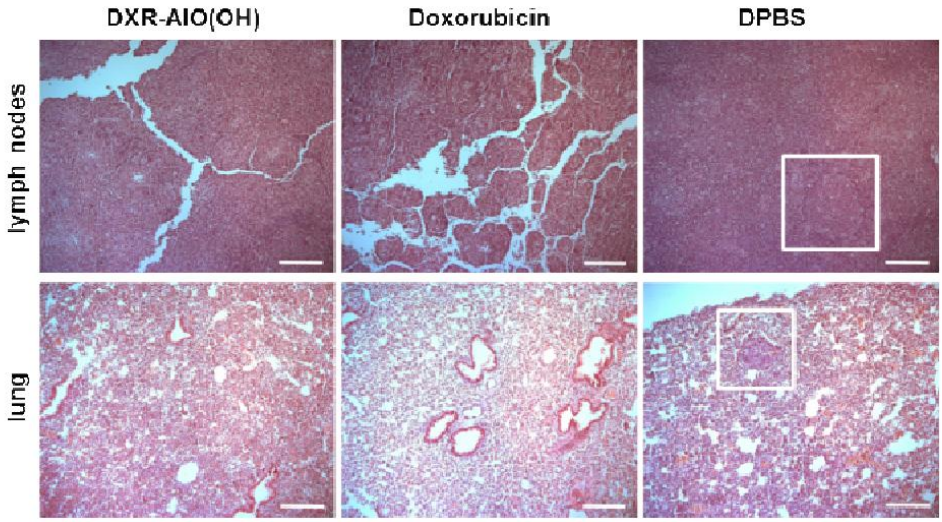

Figure 60: Qualitative histological analysis of lymph nodes and lungs. Pictures of haematoxylin- and eosin-stained histological sections confirm the presence of metastases in lymph nodes and lung of DPBS treated mice (see frame). Lung metastases were also macroscopically visible. Scale bar is 200 µm for all images.[109]

Injections of doxorubicin (2.5 mg kg^{-1} of body weight, in PBS buffer) or physiological saline (DPBS) served as positive and negative control. In literature, doxorubicin is also applied in higher doses of up to 20 mg kg^{-1} of bodyweight.[15, 111] However, the lowest dose of anti-tumor treatment which was found in the literature was employed in this study, in order to obtain doxorubicin concentrations similar to those present in the AlO(OH) hollow spheres. Seven injections were performed, three-times a week (Figure 59a). Throughout the experiment, body weight and the volume of tumors was assessed (Figure 59b).During the treatment, all animals showed no sign of abnormality or mortality as indicated by constant bodyweight (Figure 61). The tumor size of mice treated with physiological saline (DPBS) grew from day 1 to day 21, indicating that DPBS had no effect on the tumor increase. In contrast, mice treated with doxorubicin-filled AlO(OH) hollow spheres showed a greatly impaired tumor growth (Figure 59b): after 21 days, primary tumors treated with doxorubicin-filled AlO(OH) hollow spheres were significantly smaller (volumes up to 3 cm^3) as compared to the control groups treated with DPBS or doxorubicin (volumes up to 6 cm^3). Moreover, only the control group and the doxorubicin-treated group showed cortically visible, broken up tumors, whereas this was not the case for the doxorubicin-filled AlO(OH) hollow spheres-treated group. The tumoricidal efficacy of doxorubicin-filled AlO(OH) hollow spheres might be based on particle accumulation in tumor tissue *via* the enhanced permeability and retention (EPR) effect.[112]

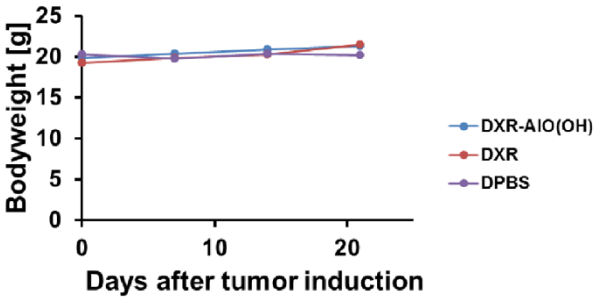

Figure 61: Body weight of BALB/c-mice. Tumor-bearing mice (n = 4) were treated with DXR-filled AlO(OH) hollow spheres (0.15 mg doxorubicin kg^{-1} of bodyweight). Treatments of mice with DPBS (n = 4) and DXR (2.5 mg kg^{-1} of bodyweight, n = 4) served as controls. During the whole study, the animals' bodyweight was documented as a function of time. Different colors of the curves represent the mean value of n = 4 animals.[109]

Just before sacrification of mice, blood was collected *via* cardiocentesis. Mice treated with doxorubicin-filled AlO(OH) hollow spheres show a similar blood count to control mice.[109] Only thrombocytes were rather low. In contrast to this, mice treated with doxorubicin show well-recognized side effects of chemotherapy, such as thrombozytopenia and injury of liver, kidney and other organs,[113] as indicated by elevated levels of lipase and triglycerids and low levels of globulins.[109] Thus, severe side-effects are already observed for doxorubicin, although applied in very

low concentration (2.5 mg kg^{-1}, 4.6 µmol kg^{-1} of bodyweight). In comparison, DXR-filled AlO(OH) hollow spheres (0.15 mg doxorubicin per kg^{-1} of bodyweight) show an even higher activity, but without any significant side-effect.

Histological evaluation was employed to qualitatively study the effect of the doxorubicin-filled AlO(OH) hollow spheres on the growth of 4T1 cells in lymph nodes and lungs (Figure 60). First hematoxylin/eosin (H/E) stainings of 7 µm sections were performed. Lungs of DPBS-treated mice contained multiple tumor nodules. Cells in metastatic regions appeared different in morphology and often had polyploid nuclei. In contrast to this, organs of mice treated with doxorubicin-filled AlO(OH) hollow spheres showed a significant reduction in metastatic foci and the morphology appeared quite normal. This observation confirms the anti-metastatic effect of DXR-filled AlO(OH) hollow spheres. For further analysis of metastasis, the volume of ipsilateral lymph nodes was evaluated. Contralateral lymph nodes served as a control. The doxorubicin-filled AlO(OH) hollow spheres seem to impede metastasis in lymph nodes draining the tumor, as the lymph-node volume is remarkably smaller than in animals treated with DPBS but comparable to the lymph-node volume of doxorubicin-treated mice (Figure 59c). Representative HE-stainings of histological sections confirm the presence of metastases mainly in DPBS-treated mice (Figure 60).[109]

In summary, the synthesis and characterization of doxorubicin-filled AlO(OH) is presented here for the first time. Although the here applied anticancer therapy, yet, relates to a conceptual study, the enormous potential is nevertheless demonstrated. The anticancer doxorubicin as model drug was used to study the encapsulation efficiency and load capacity of AlO(OH) hollow spheres: as further step, nanocarriers based on AlO(OH) hollow spheres could be evaluated as delivery system for other medicaments.

5.2 Inorganic–organic hybrid nanomaterials

5.2.1 Hybrid nanomaterials for CO_2 sorption and separation

As second class of materials for CO_2 capture, inorganic-organic hybrid nanomaterials were selected here: the organic part allows functionalization of the nanomaterial, whereas the inorganic cation is necessary to obtain an insoluble compound during the synthesis and to control particle nucleation. As a first inorganic metal cation Mg^{2+} was selected: in fact, the value for MOF Mg_2(dobdc) represents the highest low-pressure gravimetric and volumetric adsorption capacity for CO_2 in a MOF (see paragraph 2.4.1). The high CO_2 uptake is attributed to the higher ionic character of the Mg–O bonds in Mg_2(dobdc) as compared to, for instance, the Zn–O bonds on Zn_2(dobdc), leading to a higher partial positive charge on the Mg^{2+} metal centres. As a consequence, the metal cation supports higher degree of polarization of the adsorbed CO_2 molecules.[62] M_2(dobdc) (M = Mg, Mn, Fe, Co, Ni, Mn) series of metals-organic frameworks have recently been intensively studied: these compounds exhibit a honeycomb-type network topology featuring hexagonal one-dimensional channels with a high density of exposed M^{2+} adsorption sites. The specific metal employed has a dramatic effect on the adsorption capacity, binding strength, and material stability.[5] In this view, a study of the effect of changing metal ion in isostructural compounds is performed and described in paragraphs 5.2.1.2 and 5.2.1.3.

5.2.1.1 Magnesium aminoethyl phosphonate (Mg(2-AEP)) and its organic derivatives

In the following, magnesium aminoethyl phosphonate (Mg(2-AEP)) is proposed as an inorganic-organic hybrid nanomaterial for CO_2 sorption and separation. Mg(2-AEP) comprises several advantages: 1) a low specific weight due to Mg^{2+} as a light inorganic metal cation and $[2\text{-AEP}]^{2-}$ as a low-weight organic anion; 2) molar quantities of base amino groups to guarantee for high CO_2 uptake; 3) large specific surface area as a nanomaterial and wide pores between nanoparticles in a powder sample to facilitate fast diffusion of CO_2; 4) the presence of low-cost, non-toxic constituents.[13]

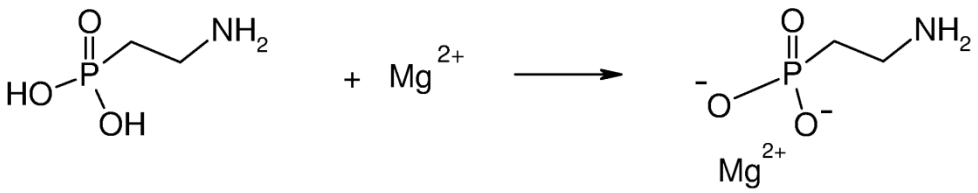

Figure 62: Reaction of aminoethyl phosphonic acid with Mg^{2+} to form magnesium aminoethyl phosphonate (Mg(2-AEP)).

To obtain nanoparticles of uniform size and size distribution, Mg(2-AEP) was prepared *via* a microemulsion approach. To this concern, a w/o microemulsion was established with toluene as the non-polar oil-phase, CTAB as the surfactant, *n*-hexanol as the co-surfactant and an aqueous solution of aminoethyl phosphonic acid (2-H_2AEP) as the polar phase. As the microemulsion was established, a solution of di-*n*-butyl magnesium in *n*-heptane was added to the nonpolar oil-phase. Immediate nucleation of Mg(2-AEP) was indicated by the formation of a light yellow precipitate (reaction scheme is illustrated in Figure 62). Subsequent to centrifugation, washing and drying, Mg(2-AEP) was obtained (for more details, see paragraph 8.3).

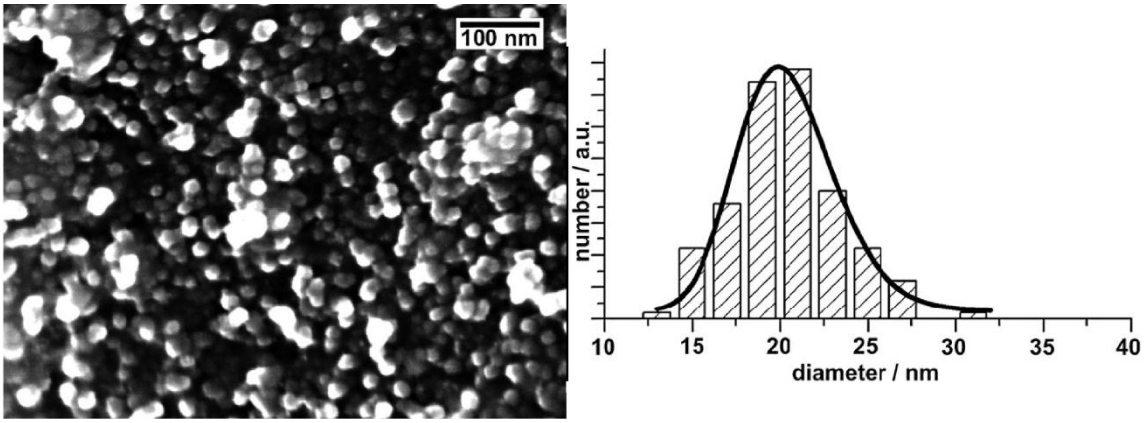

Figure 63: Particle size and size distribution of as-prepared Mg(2-AEP) nanoparticles according to electron microscopy.[13]

SEM analysis evidences a uniform, spherical shape with a mean diameter of 20 nm and a narrow size distribution of Mg(2-AEP) (Figure 63). According to X-ray powder diffraction, the as-prepared compound turned out to be non-crystalline. Therefore, FT–infrared spectroscopy (Figure 64), thermogravimetry, EDX analysis and elementary analysis were involved to describe the chemical composition. FT–IR spectra validate all characteristic vibrations as related to aminoethyl phosphonate: υ(O–H): 3300 - 2900 cm^{-1} (from H_2O intrinsically contained in the final sample), υ(C–H): 2950 - 2850 cm^{-1}, υ(C–N)/δ(C–H): 1600 - 1200 cm^{-1}, $\upsilon(PO_3)$: 1200 - 850 cm^{-1}, $\delta(PO_3)$: 750 - 400 cm^{-1}. The much sharper/splitted vibrations of 2-H_2AEP can be ascribed to the fact that the starting material

is highly crystalline whereas the as-prepared nanomaterial is amorphous. FT–IR spectra of Mg(2-AEP) are also very comparable to bulk-$Mg(HAEP)_2(H_2O)_5$ as reported by Menke *et al.*.[114]

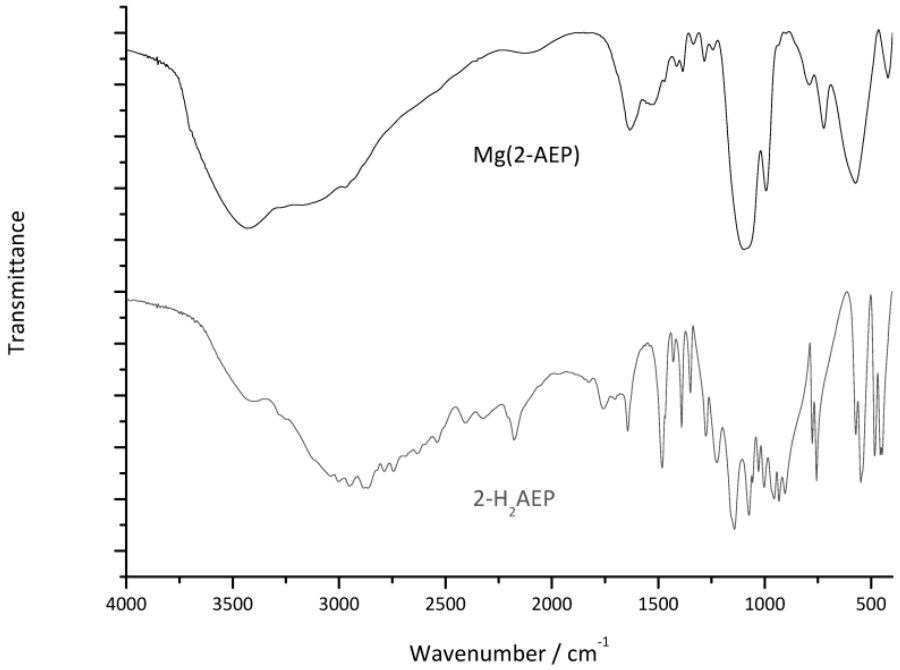

Figure 64: FT–IR spectra of as-prepared Mg(2-AEP) nanoparticles in comparison to aminoethyl phosphonic acid (2-H_2AEP) as the starting material.

Thermogravimetry of Mg(2-AEP) shows a four-step decomposition with a total weight loss of 43.5% (Figure 65, right). Hereof, the first step (11.0% at 100 - 250 °C) can be attributed to the loss of one equivalent of water (calc.: 10.9%). Next, the (2-AEP) linker decomposes, showing two overlapping weight losses (altogether 27.0% at 250 - 600°C; calc.: 27.2%). And finally, magnesiumphosphite ('$MgPO_3$') as a formal intermediate reacts with the atmospheric O_2 to magnesium orthophosphate (5.5% at 600 - 700 °C; calc.: 14.3%). P_4O_{10} as a decomposition product starts to react with the crucible material at temperatures of 600-700 °C and is therefore not evaporated completely. The thermal remnant was indeed identified as farringtonite ($Mg_3(PO_4)_2$) by XRD (Figure 65, left).

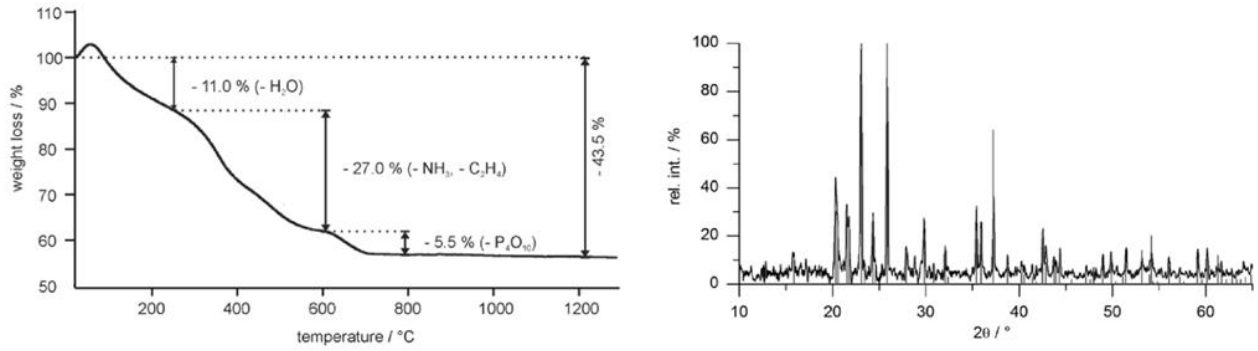

Figure 65: Right, TGA of as-prepared Mg(2-AEP) nanoparticles indicating the thermal decomposition (atmosphere: air; heating rate: 1 K min^{-1}). Left, X-ray powder diffraction pattern of the thermal remnant after the TGA with temperatures up to 1300 °C (reference: ICDD-No. 33-876, farringtonite syn, $Mg_3(PO_4)_2$).[13]

Thermogravimetry coupled with mass spectrometry (TG-MS) was performed up to a temperature of 600 °C to verify the above decomposition products (Figure 66). Accordingly, H_2O^+ at 90 - 200 °C (*m/z* = 18, indicating water), NH_2^+ at 320 - 600 °C (*m/z* = 16, indicating primary amines), and $C_2H_5^+$ 250 - 600 °C (*m/z* = 29, indicating ethyl derivatives) were observed. Note that the evaporation of H_2O is accompanied by minor amounts of OH^+ (*m/z* = 17, not shown) and O^{2+}(*m/z* = 16, similar to NH_2^+). In addition, evaporation of NH_3 is accompanied by minor amounts of NH_4^+ (*m/z* = 18, similar to H_2O^+) and NH_3^+ (*m/z* = 17, not shown). Moreover, evaporation of $C_2H_5^+$ is accompanied by additional fragments, too (*i.e.*, $C_2H_3^+$: *m/z* = 27, $C_2H_4^+$: *m/z* = 28). Based on mass spectrometry, the overlapping second and third decomposition steps of thermal decomposition can indeed be analysed as evaporation of NH_3 and C_2H_4.

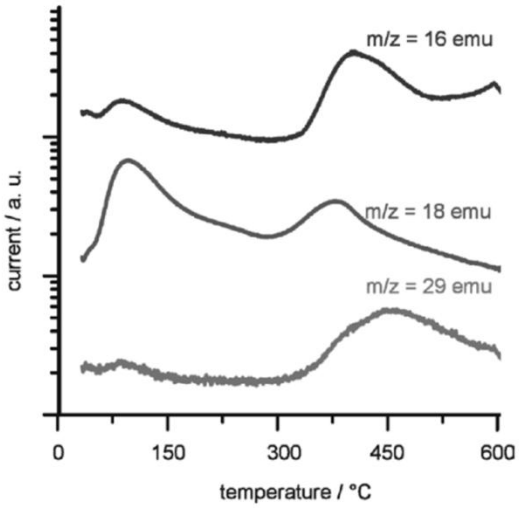

Figure 66: TG-MS of Mg(2-AEP) nanoparticles indicating NH_2^+ (m/z = 16), H_2O^+ (m/z = 18) and $C_2H_5^+$ (m/z = 29) as thermal decomposition products (atmosphere: helium; heating rate: 5 K min^{-1}).[13]

Elementary analysis (C, H, N) confirms the composition of Mg(2-AEP) with experimental values of $m(C)_{experimental}$= 14.2%, $m(H)_{experimental}$ =4.3% and $m(N)_{experimental}$ =6.0%.[13] These data are well in accordance with the calculated amounts $m(C)_{calculated}$= 14.5%, $m(H)_{calculated}$= 4.8% and $m(N)_{calculated}$ =8.5%. Finally, energy dispersive X-ray spectroscopy (Table 8) was performed. Qualitatively, the presence of the expected elements is verified. Nevertheless, it should be considered that EDX analysis, described in paragraph 3.9, presents some limits, first of all hydrogen can not be detected. Thus, only the ratio between the heaviest atoms in the molecule, magnesium and phosphorous, can be analysed and discussed. Accordingly, the experimental atomic ratio between Mg and P results in 2.0, exactly double the amount of the theoretical value. The alkyl chain is definitely present in the final sample, according to elemental analysis and infrared spectroscopy. The excess of the magnesium atomic percentage could be explained by the presence of impurities in the final compound: $Mg(OH)_2$ can be formed during the synthesis, as well MgO or $MgCO_3$. Nevertheless, the formation of large amounts of magnesium carbonate is reasonably discarded, due to the experimental amount of carbon detected by EA, which corresponds to the theoretical value. Magnesium hydroxide can be formed due to alkaline character of the molecule used as Mg^{2+} precursor, di-*n*-butyl magnesium. Based on the FT–IR spectra analysis, this theory can also be excluded, due to the absence of the strong vibrations characteristics of $Mg(OH)_2$.[115] The presence of magnesium oxide in the final sample can be proved by the analysis of the sortion-desorption of CO_2 isotherms and will be examined with the discussion of the sorption experimental results. Finally, the formation of another hybrid material can be rationalized to explain the experimental Mg/P ratio observed and its chemical formula is illustrated in Figure 67. Here, the amino group in the final compound is still present and the CO_2 capacity should be not affected.

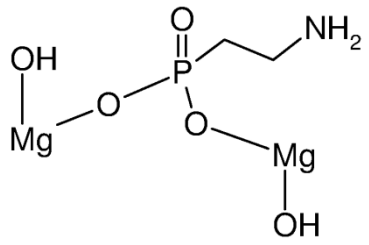

Figure 67: Chemical formula of the hybrid according to the ratio Mg/P = 2.0.

The presence of bromine in the sample is originated from the synthesis, which is performed in a microemulsion using CTAB as a surfactant: the high porosity of the final material contributes to the confinement of the only negative charged ion present in the solution.

Based on these analytical data (*i.e.* FT–IR, TG, qualitative EDX, elementary analysis) the chemical composition of Mg(2-AEP) is reliably validated.

Table 8: EDX analysis of Mg(2-AEP).

Mg(2-AEP)	Mg	P	C	H	N	O	Br	Total
Theory weight / % (with 1eq. H_2O)	14.7	18.7	14.5	4.8	8.5	38.7	-	100
EDX, weight / %	16.8	10.6	11.0	-	7.8	42.1	11.8	100
EDX, atomic / %	13.1	6.5	17.4	-	10.5	49.8	2.8	100

Aiming at gas sorption, first of all, standard nitrogen sorption analysis was performed (Figure 68). According to the BET formalism, a specific surface area of 358(±72) $m^2\ g^{-1}$ was obtained. Moreover, a pore volume of 0.7 - 0.9 $cm^3\ g^{-1}$ was calculated, in agreement with the BJH theory. In addition to the volumetric analysis, gravimetric sorption analysis was performed at 80 °C, up to 150 bar: Mg(2-AEP) powder samples were first dried until constant mass was reached (6 h, 60 °C, 10^{-3} mbar), then sorption and desorption isotherms were carried out. The result is shown in Figure 69: a certain hysteresis is observed and a maximal CO_2 uptake of 152 mg g^{-1} at 110 bar is determined.

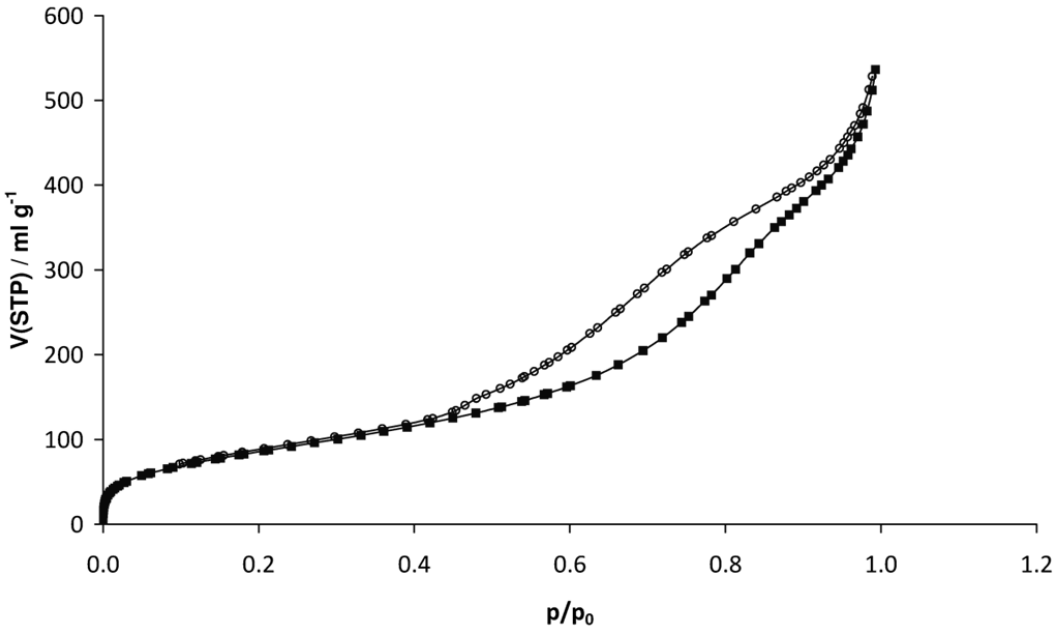

Figure 68: Nitrogen sorption obtained from volumetric analysis on Mg(2-AEP) nanoparticles.

CO_2 sorption on Mg(2-AEP) can be rationalized based on similar mechanisms as described for post-synthesis amine-functionalized MOFs and alkylamine-containing liquids. Accordingly, CO_2 reacts

as an acidic molecule with base primary amines (Equation (23)): taking ($H_4C_2PO_3$)Mg as R, the Mg(2-AEP) nanoparticles allow for adsorption of half an equivalent of CO_2 per equivalent of aminoethyl phosphonate:

$$2RNH_2 + CO_2 \leftrightarrows [RNHCOO]^- + [RNH_3]^+ \quad (23)$$

While considering the relevant molar mass (Mg(2-AEP) with 1 equivalent of H_2O: 165.4 g mol^{-1}; CO_2: 44.0 g mol^{-1}), the maximal CO_2 uptake on Mg(2-AEP) can be calculated to 133 mg g^{-1}. Hence, all expected amino groups are accessible to CO_2. With regard to Equation (23), Mg(2-AEP) adsorbs even more CO_2. In accordance with the literature and similar to what was discussed for amine-modified porous oxides and MOFs,[39, 47, 116] this additional uptake can be assigned to amino groups regenerated due to follow-up reaction of the carbamate and intrinsically available water (Equation (24)):

$$[RNHCOO]^- + H_2O \leftrightarrows [HCO_3]^- + RNH_2 \quad (24)$$

While most of the CO_2 is reversibly released during desorption (ca. 88%), a certain amount (ca. 20 mg g^{-1}) remains adsorbed even at a pressure of 1 bar (Figure 69). When performing the CO_2 sorption experiment once more (2nd cycle), adsorption starts at a value which corresponds to the final desorption value of the first cycle. Thereafter, the isotherms persist as obtained for the 1st cycle. Infrared spectra confirm the presence of CO_2 (υ(COO): 1650-1500 cm^{-1}) remaining on Mg(2-AEP) nanoparticles after the 1st sorption cycle (Figure 70). The spectra were normalized on the phosphonate valence vibration with its maximal absorption at 1099 cm^{-1}, since this intensity does not change upon interaction of Mg(2-AEP) nanoparticles with CO_2. This measure allows the comparison of the stretching vibrations of C=O, indicative for the amount of CO_2 sorbed on the nanoparticles, remaining on the nanoparticles subsequent to the first sorption cycle.

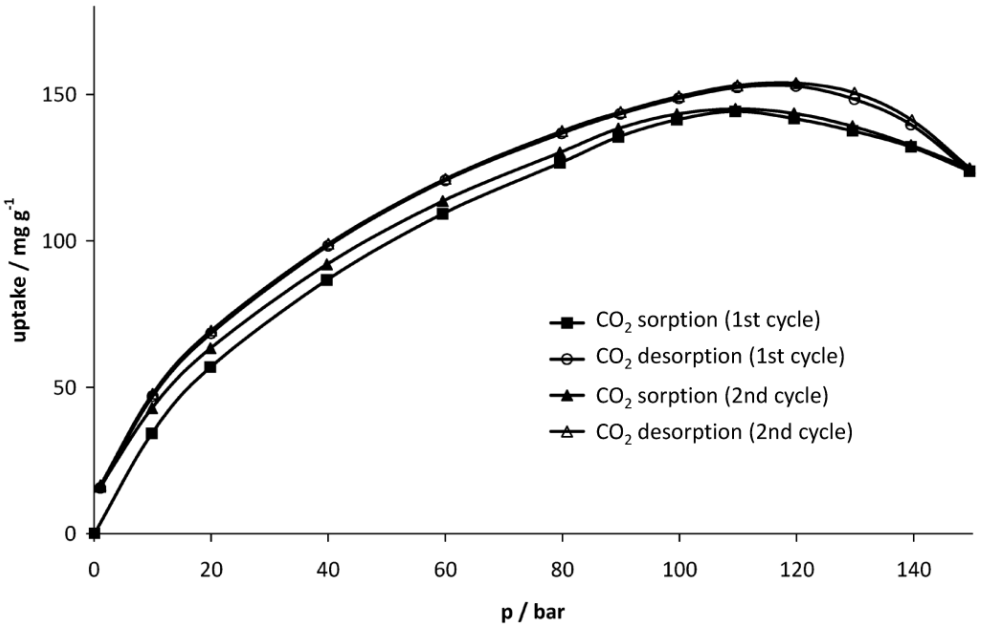

Figure 69: CO_2 sorption isotherms of Mg(2-AEP) nanoparticles at 80°C: 1st and 2nd cycles with 19mg g^{-1} remaining at 1 bar CO_2 pressure.

More-or-less all remaining CO_2 can be desorbed, however, by evacuation or by slightly heating in an atmosphere not containing CO_2. Accordingly, evacuation of the Mg(2-AEP) nanoparticles was performed at 60 °C for 6 hours subsequent to the sorption-desorption cycles (Figure 71, right). Note that the sample, after the first sorption-desorption cycle, was cooled at room temperature and, afterward, the pressure reduction to evacuation was conducted very slow, increasing simultaneously the temperature up to 60 °C. Alternatively, the Mg(2-AEP) sample was maintained after the first sorption-desorption cycle at the temperature of 80 °C and flushed with helium in order to remove the residual CO_2. The sample was then heated in helium atmosphere (1 bar) for 12 hours (Figure 71, left). With both these measurements, the remaining amount of CO_2 can be removed and the starting point of third sorption cycle is then again 0 mg g^{-1} (Figure 72). Altogether, the CO_2 sorbed on Mg(2-AEP) nanoparticles can be reversibly desorbed after an evacuation or heating step. At least nearly 90% of CO_2 can be reversibly desorbed just by pressure swing between 110 and 1 bar.

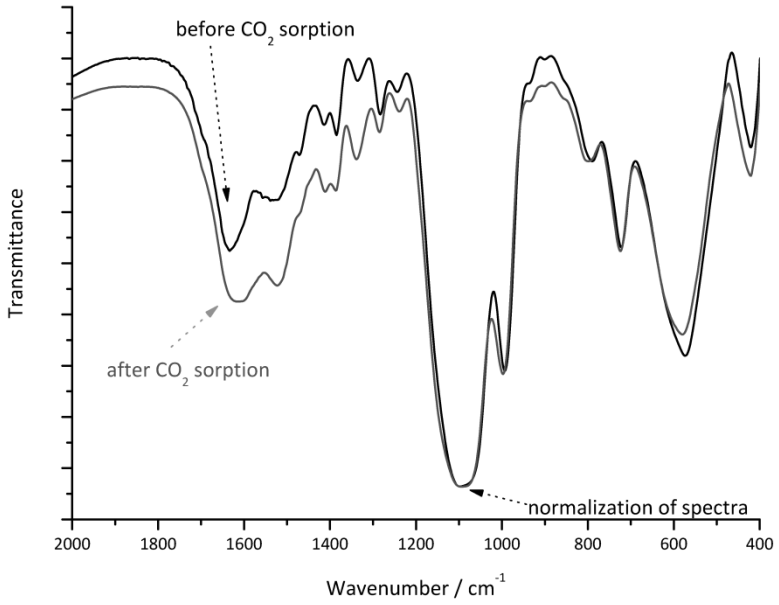

Figure 70: FT–IR spectra of Mg(2-AEP) nanoparticles before and after performing the CO_2 sorption experiments (spectra normalized on $\upsilon(PO_3)$ at 1099 cm^{-1}).

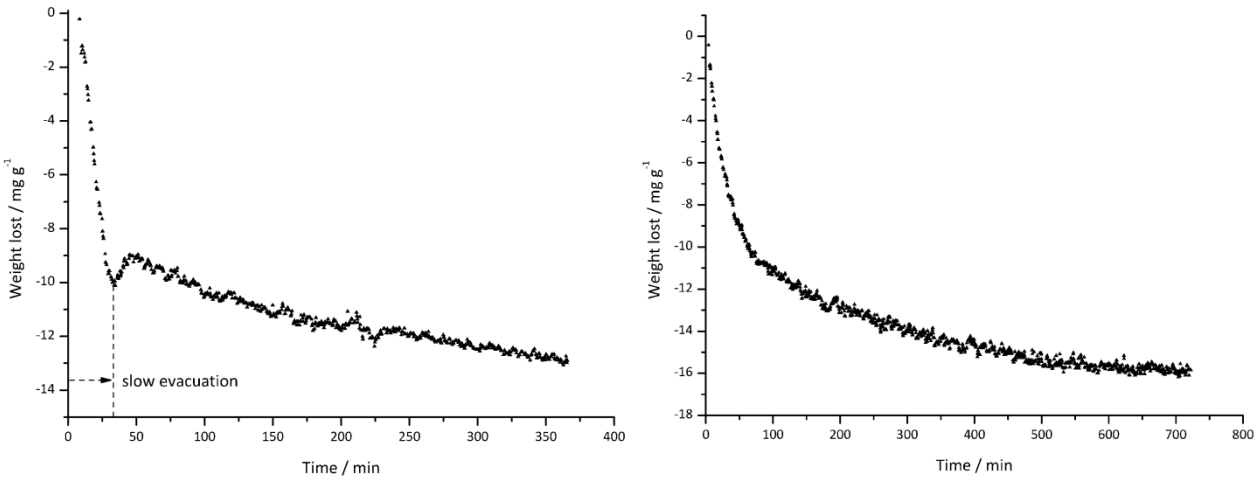

Figure 71: Right: release of CO_2 remaining after sorption-desorption cycle on Mg(2-AEP) nanoparticles *via* evacuation (*i.e.*, 10^{-3} mbar, 60 °C, 6 h, total sample weight: 92.4 mg). Left: release of CO_2 remaining after sorption-desorption cycle on Mg(2-AEP) nanoparticles *via* heating in atmosphere, not containing CO_2 (1 bar He , 80 °C, 12 h, total sample weight: 100.8 mg).

At this point, the presence of magnesium oxide and magnesium hydroxide (presumed according to EDX analysis) can be discussed. MgO and $Mg(OH)_2$ react irreversibly with CO_2 to $MgCO_3$ [117] and, due to the chemical transformation of the sorbent material, the desorption branch does not follow the sorption curve during the degassing. The desorption values maintain preferably a constant uptake, showing a significant hysteresis. Moreover, we can presume that the second sorption cycle will not show CO_2 uptake, which points out the irreversibility of the process. Neither of these

behaviours are observed for Mg(2-AEP) nanoparticles and, consequently, MgO and $Mg(OH)_2$, are not present in the final sample, or they are present as impurities and the CO_2 capacity is not affected.

In addition to CO_2, the uptake of N_2 was studied (Figure 72). Surprisingly, the N_2 uptake remains below 1.0 mg g^{-1} in the complete pressure range, up to 150 bar and at 80 °C. As a result, Mg(2-AEP) nanoparticles exhibit a selectivity of almost 100% for CO_2 as compared to N_2. This cannot be rationalized only based on the kinetic diameter of molecules, which is just slightly larger for N_2 as for CO_2 (see Table 2). This result is well in accordance with the above mechanism of CO_2 adsorbed by amino groups (Equation (23)), in which N_2 cannot be absorbed.

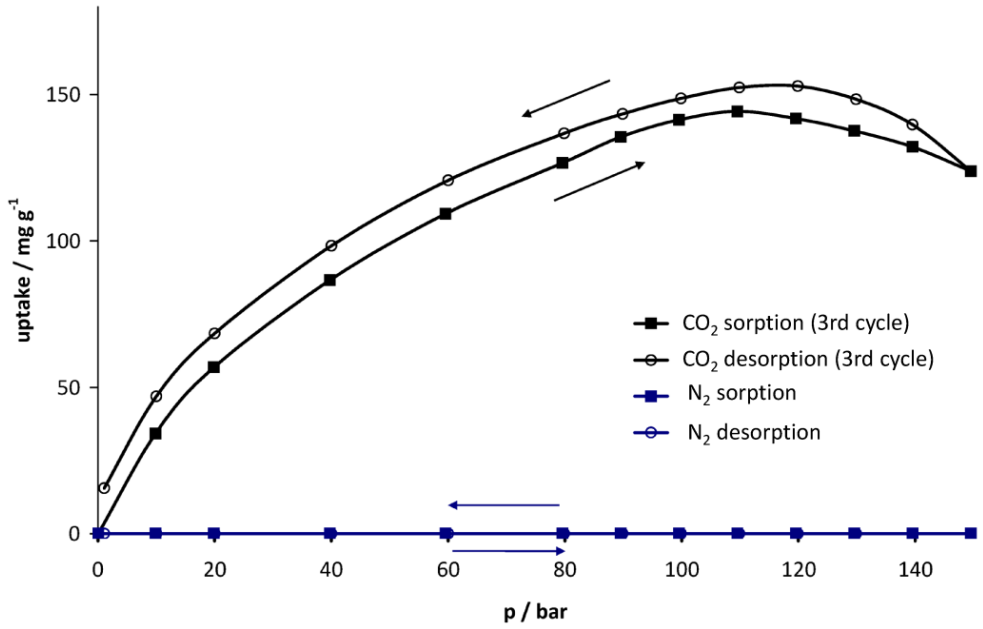

Figure 72: CO_2 and N_2 sorption isotherms of Mg(2-AEP) nanoparticles at 80 °C: 3rd CO_2 sorption/desorption cycle with additional evacuation (10^{-3} mbar) or heating (80 °C) as well as N_2 sorption isotherm at 80 °C.

Altogether, the selectivity for CO_2 over N_2 reported here is based on pure-component sorption isotherms and does not represent the true selectivity of the material in a real CO_2/N_2 mixture. In order to obtain a first impression of the Mg(2-AEP) nanoparticles behaviour on gas mixtures, gravimetric analysis was performed with 10% CO_2 / 90% N_2 mixture and the exhaust gas (the gas coming out from the device) was analysed by FT–IR spectroscopy. The results are reported in Table 9: the amount of CO_2 adsorbed on the material is the half of the original concentration (5.5% out of 10%). This finding was unexpected: if all the CO_2 is sorbed on the material, the exhausts gas has to be 100% N_2. What might have happened is that N_2, being in larger amount, would predominantly screen the amine binding sites, due to the high porosity of the sample, blocking the chemisorption of CO_2 on the $–NH_2$ functions. Moreover, it has to be underlined that this is a 'home-made method': the gas

was transferred from the MSB measurement cell to the IR gas cell controlling the pressure with the GDS and, successively, was analysed. A gas chromatograph technique for the exhaust gas could probably be a better analytical method.

Table 9: Gravimetric analysis and FT–IR of the exhaust gas of 10% CO_2/90% N_2 gas mixture sorption on Mg(2-AEP) nanoparticles.

Pressure / bar	MSB 100% CO_2 / mg g^{-1}	MSB 10% CO_2 / mg g^{-1}	IR exhaust gas / %	CO_2 sorbed / % 10% subtracted by IR exhaust gas
10	36.7	17.6	4.4(±2)	5.6(±2)
20	59.2	27.6	4.5(±2)	5.5(±2)
30	-	35.6	4.7(±2)	5.3(±2)
40	88.7	41.2	4.4(±2)	5.6(±2)
50	-	45.8	4.3(±2)	5.7(±2)

When evaluating the sorption properties of the Mg(2-AEP) nanoparticles, the CO_2 uptake is in the range of hydrotalcites, lithium zirconate and calcium oxide (5 - 300 mg g^{-1}).[39, 118] Moreover, the CO_2 uptake of Mg(2-AEP) is higher than for many amine-modified mesoporous silica (5 - 100 mg g^{-1}).[118] With 152 mg g^{-1} Mg(2-AEP) is also comparable to many MOFs, although its specific surface is much lower.[5, 9] While gas sorption on MOFs is most often driven by physisorption and, consequently, closely related to the specific surface area, a high CO_2 is often accompanied by a high uptake of other gases as well.[8-9] As a result, only few materials show a high CO_2/N_2 selectivity (> 90%), for example the MOF SNU-M10 shows 99% selectivity with a CO_2 uptake of 92 mg g^{-1} at room temperature.[119] Moreover, materials which show higher selectivity toward CO_2 normally are characterized by a low CO_2 uptake and studied only by the volumetric analysis and, consequently, only at low pressure and not with a high accurate device. In comparison with materials reported in the literature, Mg(2-AEP) has almost 100% selectivity in pure gases at high pressure and at temperatures higher than 25 °C, associated with an high CO_2 uptake (152 mg g^{-1}, at 80 °C). Additionally, the sorption equilibrium is reached in less than 30 minutes, which means that the adsorption rate is fast, a crucial characteristic for practical gas separation. Moreover, the material is stable not only toward air and water, but also toward high pressure of CO_2, since the isotherms collected at 80°C turn out to be completely reversible. In addition, Mg(2-AEP) can be regenerate only by using mild temperatures (80 °C), avoiding the use of high vacuum. As next steps, the long-term stability of Mg(2-AEP) and its behaviour in realistic flue gas mixtures in the presence of contaminants (H_2O, NO_x, CO, SO_2, CH_4) has

to be tested. In the following, the Mg(2-AEP) nanoparticles are analysed for the separation of CO_2/CH_4 mixtures.

CO_2 is present in flue gas emitted during the combustion of carbon-based fossil fuels, generated during stream reforming of natural gas, the major source of hydrogen. This process generates a gas mixture containing H_2, CO_2, CO and CH_4. Pure H_2 is recovered by pressure swing adsorption (PSA), whereas the remaining gas mixture containing CO_2-CH_4-CO is normally used as combustible for the stream reformer. In view of the current concerns about CO_2 emissions, CO_2 should be sequestrated, in order to recycle only CH_4 and CO as fuels to the stream reformer.[120] Moreover, CO_2 selective sorption is needed for the purification of biogas, which is essentially a mixture of CO_2 and CH_4. The CO_2/CH_4 adsorption data on Mg(2-AEP) nanoparticles presented here were performed by co-workers of Prof. Staudt, Institut für Nichtklassische Chemie, Lepizig. A volumetric chromatographic method was used to measure the partial loading of CO_2 and CH_4 in the gas mixture experiments. The description of the apparatus used can be found elsewhere.[121] The ideal adsorbed solution theory (IAST), developed by Myers and Prausnitz,[122] was used to predict binary adsorption equilibria from pure gas adsorption isotherms and used to compare experimental data of gas mixtures. Figure 73 shows the adsorption isotherms of CO_2 and CH_4 measured at 25 °C: at 25 bar the CO_2 uptake is 3.47 mmol g^{-1} (153.7 mg g^{-1}), whereas the CH_4 uptake at the same pressure results in 0.91 mmol g^{-1} (14.5 mg g^{-1}). The CH_4 isotherms were fitted using the Toth isotherm model,[26] whereas the Dual-Site Langmuir model[123] was used for the CO_2 isotherm (Figure 73). The two models were then used for the application of the IAST to predict CO_2/CH_4 mixtures sorption from the pure gas isotherms. In Figure 73 the calculation of three different CO_2/CH_4 mixtures are presented (CO_2:CH_4 = 75:25, CO_2:CH_4 = 25:75 and CO_2:CH_4 = 5:95).

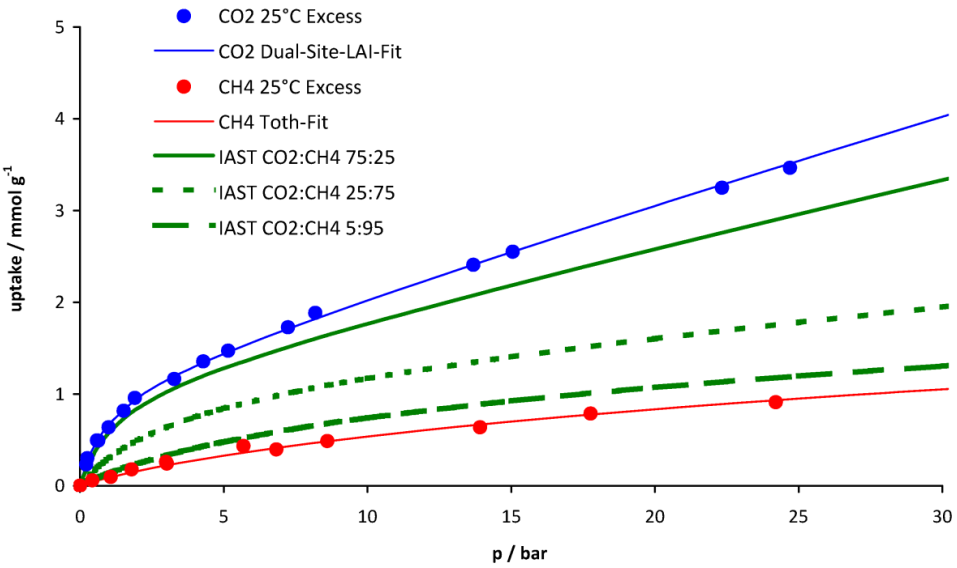

Figure 73: CO_2 (blue circles) and CH_4 (red circles) isotherms at 25 °C on Mg(2-AEP) nanoparticles. CO_2 experimental data are fitted using the Dual-Site Langmuir model (blue solid line), whereas CH_4 data are fitted the Toth isotherm model. Calculation of CO_2/CH_4 isotherms are performed according to IAST (green lines, solid line: $y_{CO2} = 0.75$; dotted line: $y_{CO2} = 0.25$; dashed line: $y_{CO2} = 0.05$).

Moreover, mixed CO_2/CH_4 isotherms were experimental determined at 25 °C and at constant pressures. The results are presented in Figure 74 in an *x*-*y* diagram (*x* and *y* are the molar fraction of the gas in the adsorbed and gas phases, respectively). Accordingly, the amount of CH_4 in the gas phase is higher that the CO_2 concentration, resulting in an increase of CO_2 in the adsorbate phase. Consequently, adsorption of CO_2 on Mg(2-AEP) nanoparticles is preferred over CH_4 confirming, once again, the mechanism of CO_2 sorbed by amino groups. The selectivity towards CO_2 (α) can be calculated according to the Equation (25):

$$\alpha = \frac{\left(\frac{x_{CO_2}}{y_{CO_2}}\right)}{\left(\frac{x_{CH_4}}{y_{CH_4}}\right)} \qquad (25)$$

α: selectivity towards CO_2, x_{CO_2}: molar fraction of CO_2 in the sorbate, y_{CO_2}: molar fraction of CO_2 in the gas phase, x_{CH_4}: molar fraction of CH_4 in the sorbate, y_{CH_4}: molar fraction of CH_4 in the gas phase

The experimental α results in the range between 8 and 20. The IAST gives α between 11 and 15, well in agreement with experimental data. When evaluating the selectivity of the Mg(2-AEP) nanoparticles, it results higher than for different MOFs and activated carbons, but, on the other hand, lower than for zeolites (see Table 10), confirming the big potential of Mg(2-AEP) nanoparticles as selective sorbent material for CO_2 sequestration.

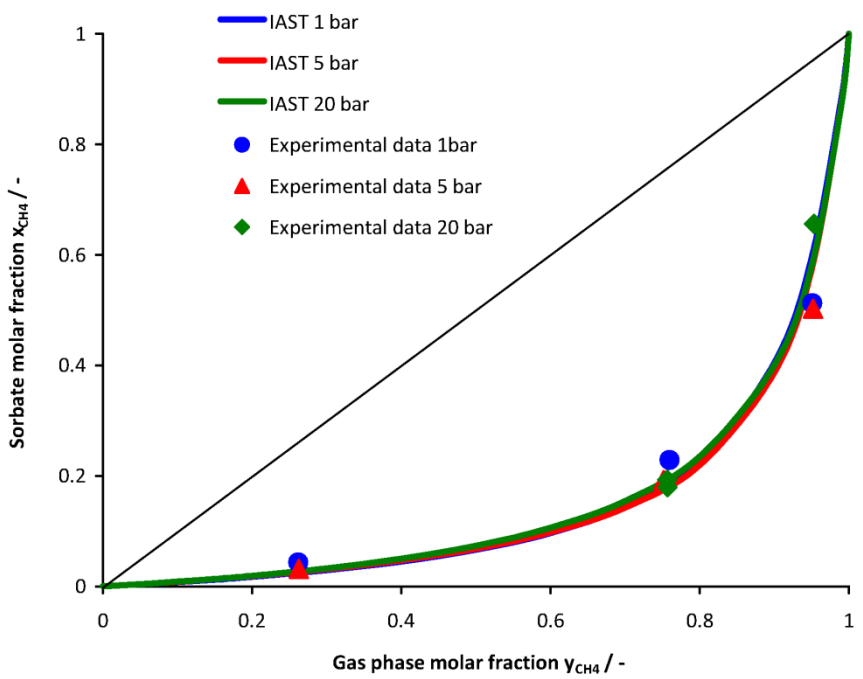

Figure 74: Experimental sorption of CO_2/CH_4 mixtures at 25 °C and at different pressures: 1 bar (blue circles), 5 bar (red triangles), 20 bar (green diamonds). IAST calculations of CO_2/CH_4 mixtures from pure gases isotherms are represented by lines.

Table 10: Selectivity CO_2/CH_4 in selected materials. [a] See list of abbreviations.

Material [a]	Temperature / °C	Selectivity $\alpha(CO_2/CH_4)$	Ref.
Mg(2-AEP)	25	8-20	this work
HKUST-1 $[Cu_3(BTC)_2]$	30	5-7	[120]
MIL-53-Al [Al(OH)(BDC)]	30	7	[124]
MIL-53-Cr [Cr(OH)(BDC)]	30	5-15	[125]
Amino functionalized MIL-101-Al $[Al_3O(H_2O)_2F(BDC)_3]$	25	30-50	[126]
Zeolite 13X	25	140-160	[127]
Zeolite 5A	25	250-300	[127]
Activated carbon CarboTech A35/A	25	3-5	[128]

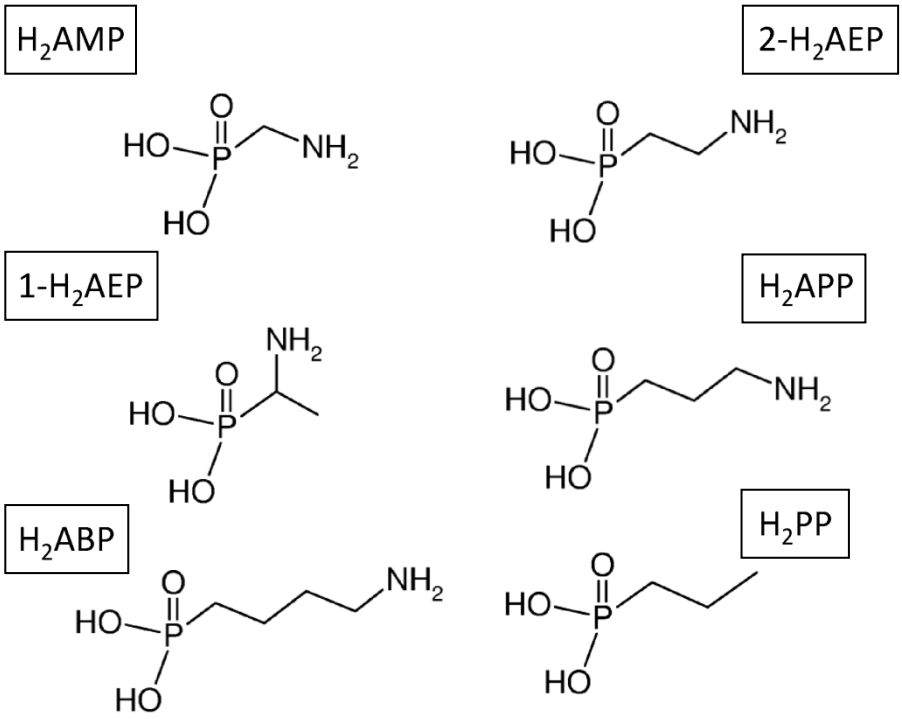

Figure 75: Chemical formulas of phosphonic acids used as precursors for the synthesis of inorganic-organic hybrid nanoparticles: H_2AMP, aminomethyl phosphonic acid; 2-H_2AEP, 2-aminoethyl phosphonic acid; 1-H_2AEP, DL-1-aminoethyl phosphonic acid; H_2APP, 3-aminopropyl phosphonic acid; H_2ABP, 4-aminobutyl phosphonic acid; H_2PP, propyl phosphonic acid.

Taking Mg(2-AEP) nanoparticles as starting point, modifications of the original materials were introduced in order to study the mechanism of interaction of the inorganic-organic hybrid with carbon dioxide and to improve the surface excess uptake. Not only was the influence of the organic linker investigated, but also the effect of magnesium as an inorganic cation (see paragraphs 5.2.1.2 and 5.2.1.3).

The organic linkers selected for this study are listed in Figure 75. The position of the amino group was changed, both with shorter (H_2AMP, aminomethyl phosphonic acid) and longer (H_2APP, aminopropyl phosphonic acid and H_2ABP, aminobutyl phosphonic acid) carbon chains. Moreover, the isomer structure of 2-H_2AEP was analysed: 1-H_2AEP (DL-1-aminoethyl phosphonic acid). In the latter, the amino group is the α-position, whereas in 2-H_2AEP is in the β-position. In order to prove the mechanism of the CO_2 sorption *via* reaction with the amino functionality, nanoparticles were synthesized with propyl phosphonic acid as precursor (H_2PP). All the syntheses were performed under similar conditions and following similar procedures (see paragraph 8.3).

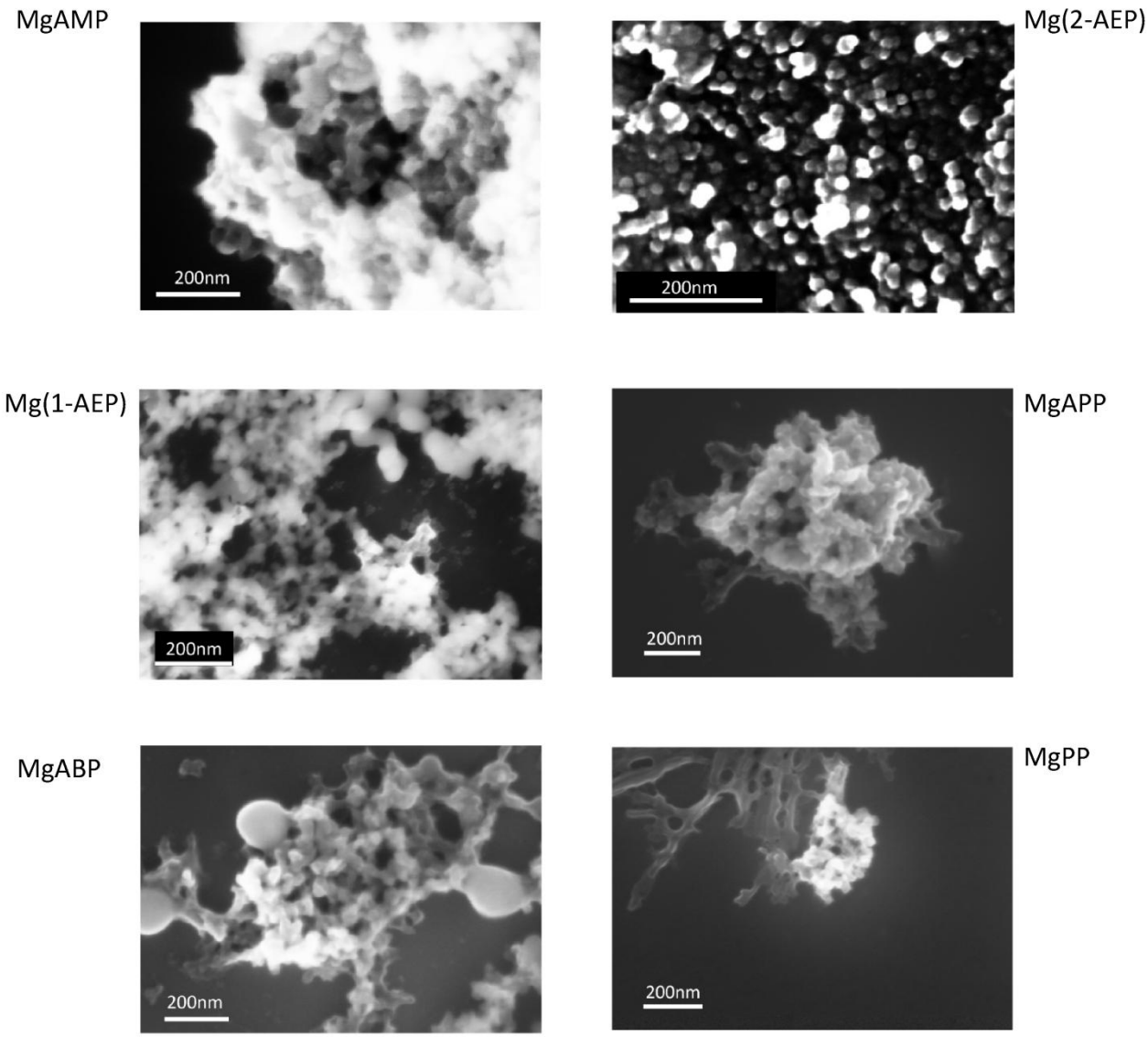

Figure 76: Particle size of as-prepared MgAMP, Mg(2-AEP), Mg(1-AEP), MgAPP, MgABP, Mg(PP) nanoparticles according to scanning electron microscopy.

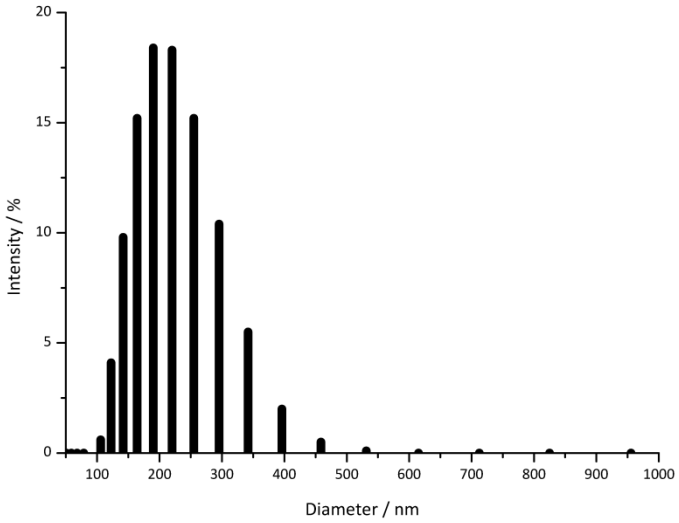

Figure 77: Dynamic light scattering of MgABP suspended in ethanol as representative DLS measurement for all the nanoscale magnesium phosphonate compounds presented.

All the compounds turned out to be nanomaterials, with an average diameter between 20 and 70 nm, according to SEM measurements (Figure 76). On the other hand, dynamic light scattering measurements show average diameters around 200 nm for all the compounds (Figure 77, example for MgABP): as reported in paragraph 3.6, the DLS technique has the disadvantage to detect agglomerates of nanoparticles in suspension and to record the hydrodynamic diameters of the samples.

In order to prove the chemical compositions, the resulting amorphous nanomaterials were characterized by FT–IR, EDX spectroscopy, thermogravimetric analysis and elemental analysis. The presence of the inorganic cation is confirmed by EDX analysis (Table 11), whereas the organic linker is detected *via* FT–IR spectra (Figure 78). Here, the increase of the number of carbon atoms in the alkyl chain results in the shift of the P=O and P–C stretching to lower wavenumbers (Figure 79, example for MgAMP and MgABP). The P–C stretching in MgAMP appears at 740 cm^{-1}, in Mg(2-AEP) at 722 cm^{-1}, in MgAPP at 717 cm^{-1} and for the MgABP compound it is at 716 cm^{-1}. These variations are due to the combination of the P–C and P=O stretching vibrations with adjacent C–C stretching or C–H vibrations.[129]

For quantification purposes, thermogravimetric analysis (Figure 80) EDX and EA (Table 11) are employed. The experimental elemental amounts are slightly deviated from the theoretical ones, and the discussion of this behaviour can be explained with similar arguments reported above for the compound Mg(2-AEP). As well, for the elemental analysis, the calculated amounts of the chemical components do not perfectly match the experimental results. This could be based on the fact that

during the burning of the sample, it is not completely decomposed and, as result, the weights collected are misleading. Nevertheless, an increase in the percentage of C (EA and EDX) and of H (EA) is observed, in line with the increase of the length of the organic chain.

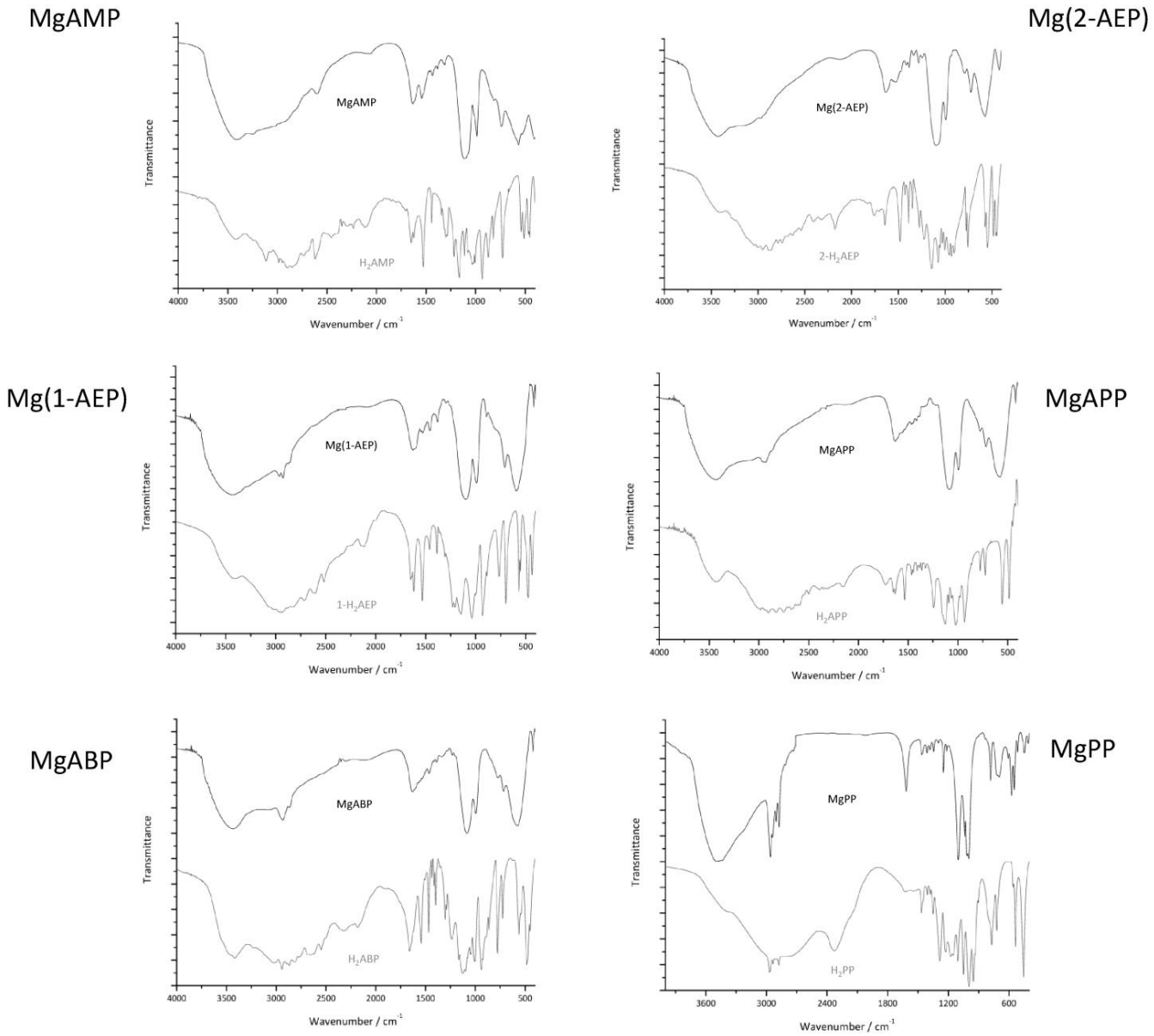

Figure 78: FT–IR spectra of as-prepared MgAMP, Mg(2-AEP), Mg(1-AEP), MgAPP, MgABP, Mg(PP) nanoparticles (black) in comparison to the corresponding phosphonic acids (gray) as starting material.

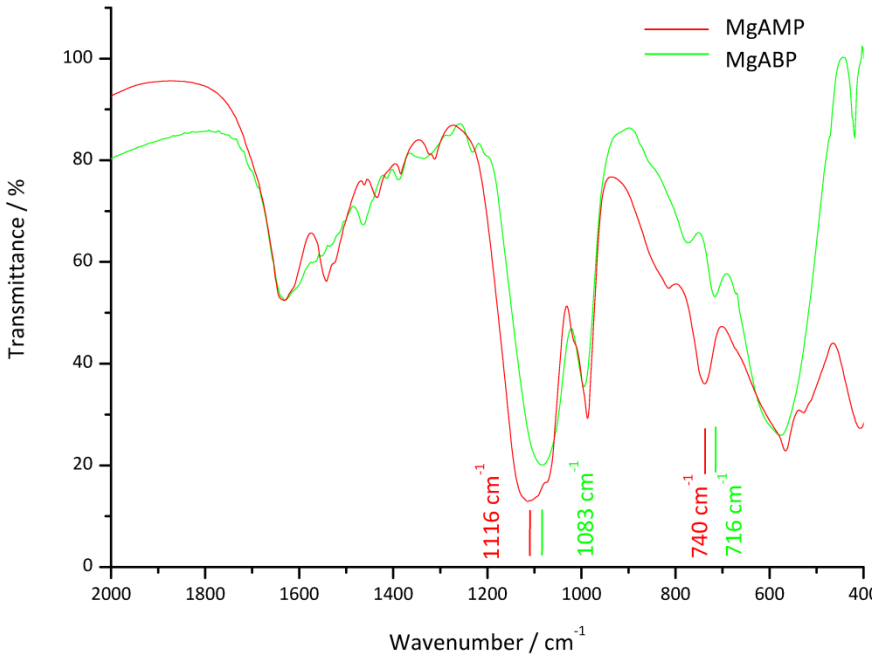

Figure 79: FT–IR spectra of MgAMP and MgABP: the P=O and P–C stretching modes are shifted to lower wavenumbers by increasing the weight of the organic chain.

Due to the limitations of the thermogravimetric analysis listed on page 47 (paragraph 3.10), the values of weight loss upon heating are not completely valid. However, all the TG curves show a similar profile: four steps of decomposition. Moreover, an increase of the weight loss can be observed by the increase of the length of the organic linker, for the TG measurements performed at 1 K min^{-1} and at 10 K min^{-1}, with the exception of MgAMP at rate heating of 1 K min^{-1}. In particular for this measurement, the theoretical decomposition result matches quite well with the experimental result. The weight change of -13.7% can be attributed to the loss of one equivalent of water (calc.: 11.9%). Next, the molecule decomposes losing the alkylic chain (experimental: 22.3%; calculated: 20.5%). And finally, magnesiumphosphite ('$MgPO_3$') as a formal intermediate decomposes to magnesium orthophosphate (experimental: 14.4%; calculated: 14.3%). Nevertheless, this explanation should not to be taken as the only possible one. Phosphorous pentaoxide (P_4O_{10}), produced *in situ* upon heating, reacts reasonably well with Al_2O_3 as the crucible material and does not evaporate completely. Moreover, surfactant or solvent residues could remnant in the final sample and decompose inside the TG device. The formal intermediates of the decomposition reaction containing Mg could also react with the crucible. Finally, the decomposition of the starting material is eventually incomplete. In summary, the experimental result of the TGA, being affected by different parameters, could be deceptive and should be analysed critically.

Table 11: Elemental compositions of MgAMP, Mg(1-AEP), MgAPP and MgABP according to EDX analysis (both weight percent and atomic percent) and EA. The theoretical amount is reported in the first rows of each compound.

	Mg	P	C	H	N	O	Br
MgAMP							
Theory weight / % (with 1eq. H_2O)	16.1	20.5	7.9	4.0	9.2	42.3	
EDX, weight / %	13.8	14.8	8.3	-	11.9	47.1	6.1
EDX, atomic / %	10.4	8.7	12.7	-	15.5	51.0	1.4
EA, weight / %	-	-	8.1	4.4	5.2	-	-
Mg(1-AEP)							
Theory weight / % (with 1eq. H_2O)	14.7	18.7	14.5	4.8	8.5	38.7	
EDX, weight / %	14.5	5.1	11.4	-	10.2	47.2	11.5
EDX, atomic / %	10.8	2.9	39.7	-	13.2	53.3	2.5
EA, weight / %	-	-	14.5	5.2	4.0	-	-
MgAPP							
Theory weight / % (no H_2O)	15.1	19.2	22.4	5.0	8.7	29.8	
EDX, weight / %	17.9	7.2	13.0	-	8.0	42.5	11.4
EDX, atomic / %	13.4	4.2	19.7	-	10.4	48.4	3.8
EA, weight / %	-	-	15.2	5.5	2.4	-	-
MgABP							
Theory weight / % (no H_2O)	13.8	17.7	27.4	5.7	8.0	27.4	
EDX, weight / %	20.6	7.4	14.6	-	6.2	40.9	8.2
EDX, atomic / %	15.1	4.3	21.6	-	7.8	45.4	5.3
EA, weight / %	-	-	17.2	5.6	3.1	-	-

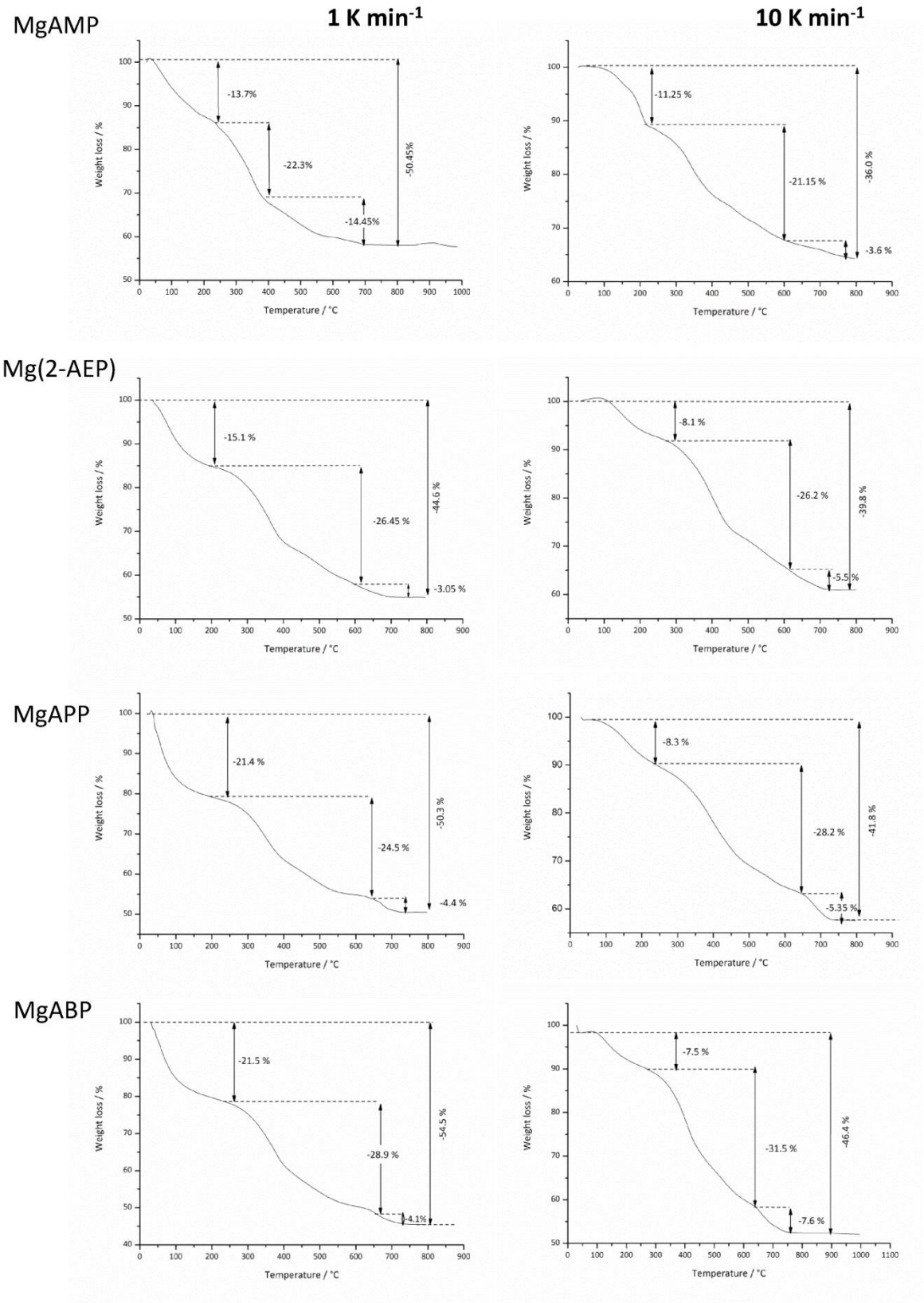

Figure 80: TGA of MgAMP, Mg(2-AEP), MgAPP and MgABP, both at 1 K min^{-1} and 10 K min^{-1} rate of heating (atmosphere: air).

Standard nitrogen sorption analysis was performed for all the compounds. The isotherms are shown in Figure 81, whereas gravimetric CO_2 sorption analyses, performed at 80 °C and up to 150 bar are illustrated in Figure 82. Table 12 summaries the specific surface areas according to the BET formalism, the experimental maximal CO_2 uptakes observed and the theoretical maximal uptakes, according to Equation (23).

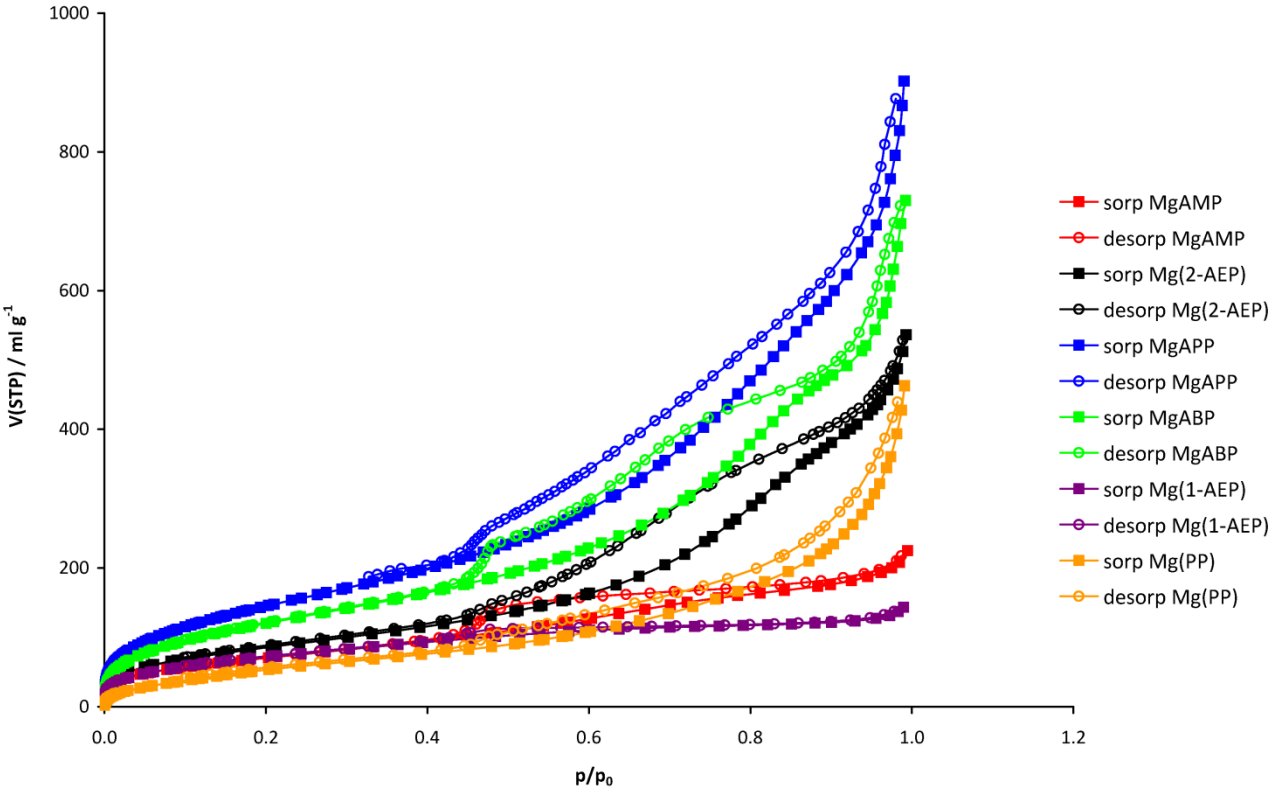

Figure 81: Nitrogen sorption obtained from volumetric analysis on MgAMP, Mg(2-AEP), MgAPP, MgABP, Mg(1-AEP), Mg(PP) nanoparticles.

The higher capacity, both in the volumetric and gravimetric analyses, is observed for the compound magnesium aminopropyl phosphonate, MgAPP. Mg(2-AEP) and MgABP have an almost similar behaviour, whereas MgAMP and Mg(1-AEP) appear to be the samples with the lower uptakes.

In the MOFs literature (see paragraph 2.4.1), it is well known that when expanding the length of an organic linker, an increase of the void volume is observed, followed by an enhance of the gas storage capacity per unit mass.[53] Here, the same idea could be employed to rationalize the experimental results: the CO_2 uptake increase from the methyl to the propyl derivates (CO_2 capacity: MgAMP < Mg(2-AEP) < MgAPP). The drastic reduction of gas stored on MgAMP could be also rationalized in terms of a steric effect: the amine functional group is much closer to the P=O group, causing repulsion after the formation of the carbamate species. Similar arguments can explain the

low capacity of Mg(1-AEP): in this case, the methyl group is in α-position and could interfere with the carbamate formed after interaction of CO_2 with the amino group. Contrary to this model, MgABP shows lower gravimetric and volumetric capacity: in this case, the increased weight of the sample could play the major role, lowering the excess values of gas sorbed, conventionally expressed per gram of solid sorbent. Moreover, the long organic chain is more flexible in comparison to the shorter organic chains: the increased mobility could promote an interaction between the carbamate, formed upon reaction with CO_2, and the partially positive charged Mg^{2+}, avoiding the re-activation (Equation (24)) and lowering the final CO_2 uptake.

Table 12: Specific surface areas, experimental CO_2 maximal uptakes and theoretical CO_2 maximal uptakes (according to Equation (23)) of MgAMP, Mg(1-AEP), Mg(2-AEP), MgAPP, MgABP and Mg(PP) nanoparticles.

	A_{BET} / $m^2\ g^{-1}$	Experimental CO_2 uptake / mg g^{-1}	Theoretical CO_2 uptake / mg g^{-1}
MgAMP	250(±12)	48	144
Mg(1-AEP)	258(±90)	98	133
Mg(2-AEP)	357(±72)	150	133
MgAPP	532(±69)	191	137
MgABP	436(±33)	147	126
Mg(PP)	222(±18)	54	-

With the study of the compound magnesium propyl phosphonate (Mg(PP)), the chemical interaction of CO_2 with the amino group is confirmed. Mg(PP) reveals a BET area of 222(±18) $m^2\ g^{-1}$, and a maximum uptake of 54 mg of CO_2 per gram of sample. This is 3.5 times lower than that for MgAPP at similar pressure. Even if Mg(PP) has no amine functionality, the low CO_2 sorption can be explained as a physisorption phenomenon, due to the large specific surface of the sorbent.

Unfortunately, the increased specific surface of the compound magnesium aminopropyl phosphonate (MgAPP: 532(±69) $m^2\ g^{-1}$ *vs.* Mg(2-AEP): 357(±72) $m^2\ g^{-1}$) is also combined with a nitrogen sorption at 80 °C, reducing the selectivity towards CO_2 from 100% of Mg(2-AEP) to 87% (Figure 83).

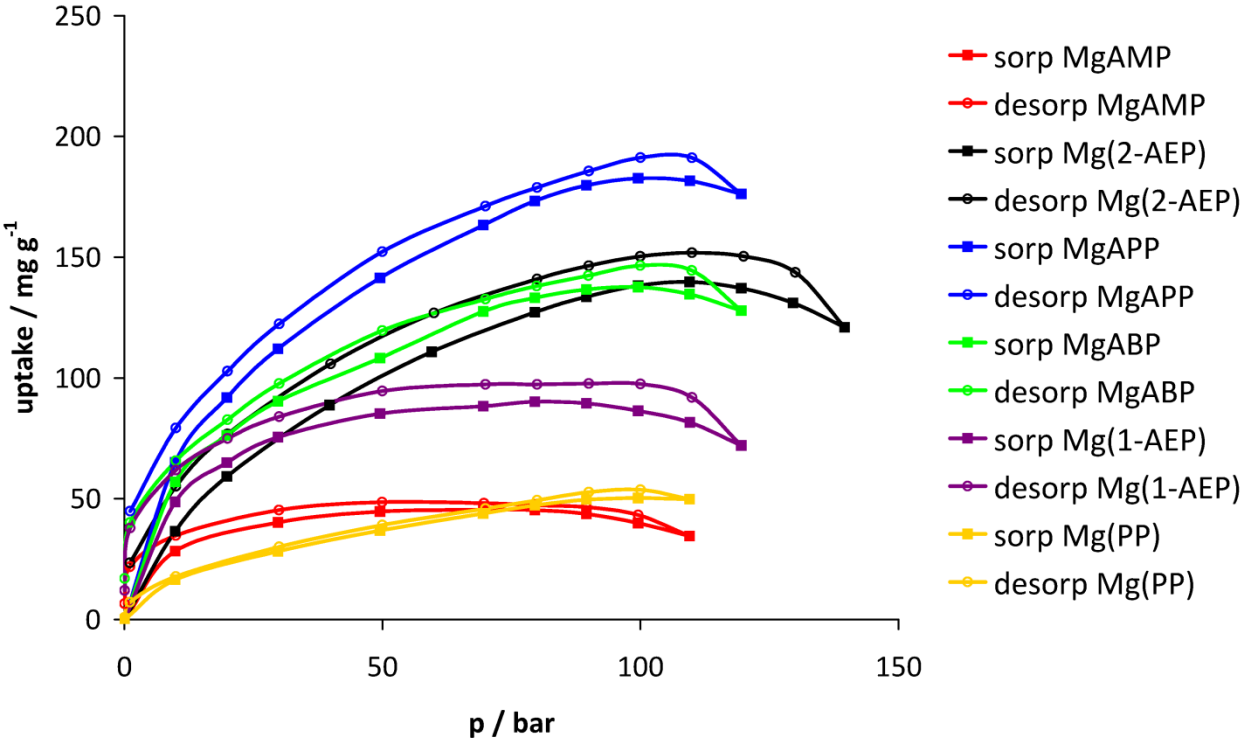

Figure 82: CO_2 sorption and desorption isotherms at 80°C obtained from gravimetric analysis on MgAMP, Mg(2-AEP), MgAPP, MgABP, Mg(1-AEP), Mg(PP) nanoparticles.

In summary, the study of the molecular derivatives of Mg(2-AEP) confirms this compound as the best selective sorbent with almost 100% selectivity toward CO_2. An increase of the specific surface, in fact, results in higher surface excess isotherms (maximum uptake of MgAPP is 191 mg g^{-1} at 100 bar and 80°C), but it is accompanied with a reduced selectivity, based on the pure gas isotherms (87%).

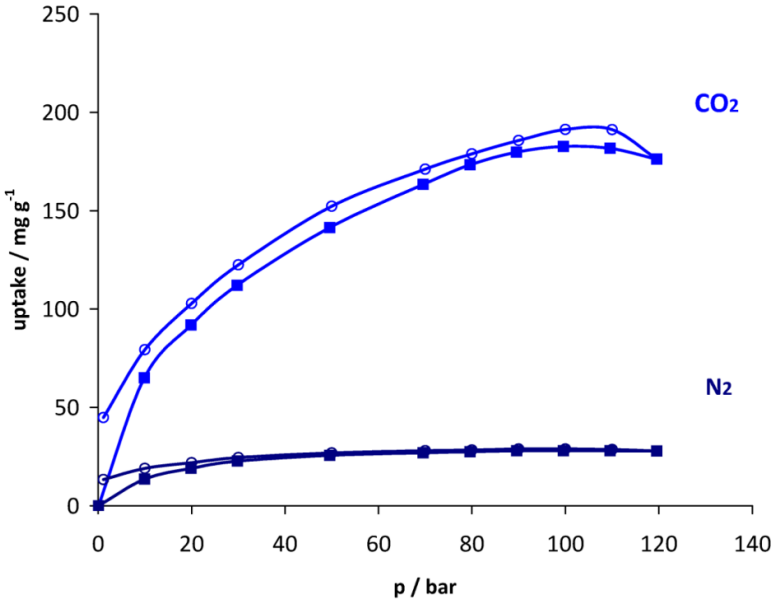

Figure 83: CO_2 and N_2 sorption isotherms of MgAPP nanoparticles at 80 °C.

5.2.1.2 Phosphonate hybrids with other alkaline earth metals

The first idea to study the effect of the Mg^{2+} cation on Mg(2-AEP) was to synthesize similar compounds with other alkaline earth metals. In this respect calcium and barium have been selected.

Following a similar synthesis strategy used for the compounds described above (the complete synthesis is reported in paragraph 8.4), the obtained products turned out to be amorphous nanomaterials with particle sizes between 30 and 80 nm. SEM analysis of calcium aminoethyl phosphonate (Ca(2-AEP)) and barium aminoethyl phosphonate (Ba(2-AEP)) are reported in Figure 84.

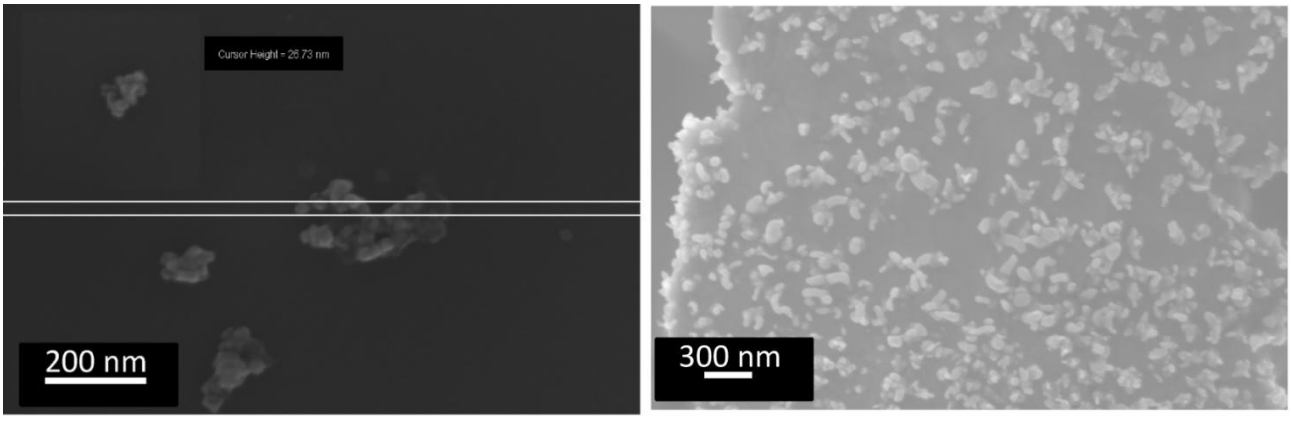

Figure 84: Particle sizes of the as-prepared Ca(2-AEP) nanoparticles (left) and Ba(2-AEP) nanoparticles (right) according to electron microscopy.

Chemical composition of the final nanomaterials were proven by EDX analysis, elemental analysis (both listed in Table 13) and infrared spectroscopy (Figure 85). Experimental amounts of C, H and N correspond with the theoretical values of Ca(2-AEP), as well the EDX ratio Ca/P, resulting in 0.7. The experimental values observed for the compound Ba(2-AEP) are slightly deviated according to elemental analysis, probably due to its incomplete decomposition. Nevertheless, the EDX ratio Ba/P is confirmed to be 0.9: based on these results, the chemical structures are reliably validated. According to FT–IR, it is evident that with the increase of the size of the cation, the characteristic vibrations of the P–C and P=O bonds are influenced differently by the adjacent O–M^{2+} bond (M: Ca or Ba): as result, P–C and P=O stretching vibrations appear shifted slightly.[129]

Table 13 Elemental compositions of Ca(2-AEP) and Ba(2-AEP) according to EDX analysis (both weight percent and atomic percent) and elemental analysis. The theoretical amount is reported in the first rows of each compound.

	Ca	P	C	H	N	O	Br
Ca(2-AEP)							
Theory weight / %	22.0	17.1	13.2	4.4	7.7	35.3	
EDX, weight / %	12.1	15.9	11.4	-	10.3	25.9	24.3
EDX, atomic / %	6.8	11.6	21.5	-	16.7	36.6	6.8
EA, weight / %	-	-	11.9	4.4	6.3	-	-
Ba(2-AEP)	Ba	P	C	H	N	O	Br
Theory weight / %	49.0	11.1	8.6	2.9	5.0	23.0	
EDX, weight / %	39.6	11.7	8.1	-	6.0	16.9	17.7
EDX, atomic / %	10.9	12.7	22	-	14.0	34.7	7.3
EA, weight / %	-	-	12.0	4.4	4.4	-	-

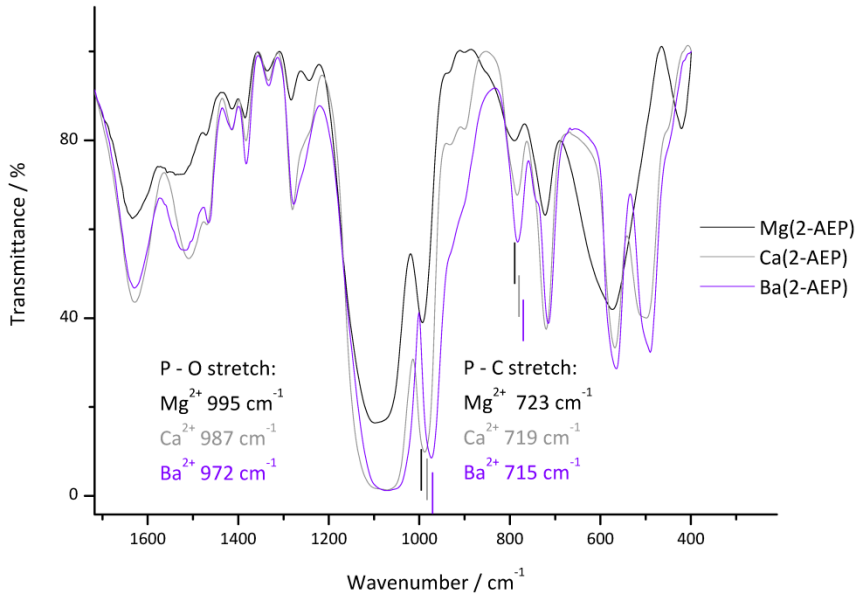

Figure 85: FT–IR spectra of Mg(2-AEP), Ca(2-AEP) and Ba(2-AEP): the stretching mode of the P–C bond and P–O is shifted to lower wavenumbers increasing the size of the cation.

Volumetric analysis under N_2 (Figure 86) as a result shows a drastically reduced specific surface area in comparison to Mg(2-AEP): 13.4(±0.7) $m^2\ g^{-1}$ for Ca(2-AEP) and 1.7(±0.3) $m^2\ g^{-1}$ for Ba(2-AEP). It is important to note that the specific surface is measured per gram of sample: calcium and even more barium are heavier than Mg (molecular weights of Mg, Ca and Ba are, respectively,

24.3 g mol^{-1}, 40.1 g mol^{-1}, 137.3 g mol^{-1}). Moreover, the porosity of the materials, according to BJH theory, resulted in 0.74 cm^3 g^{-1} for Mg(2-AEP), 0.13 cm^3 g^{-1} for Ca(2-AEP) and 0.02 cm^3 g^{-1} for Ba(2-AEP). Accordingly, the gravimetric CO_2 uptake, illustrated in Figure 87 for the calcium and magnesium compounds, is also decreased in comparison to Mg(2-AEP) nanoparticles: a maximal uptake of 5 mg g^{-1} is determined for Ca(2-AEP) in the complete pressure range, up to 110 bar and at 80 °C. Note that the CO_2 uptake on Ca(2-AEP) appears negative at pressure higher than 100 bar due to the imprecise buoyancy correction at high pressures. The Ba(2-AEP) isotherm is not shown here: the CO_2 uptake observed for this material is negative in the complete range of pressure. Due to the very low CO_2 uptake on the barium compound, after the application of the buoyancy correction, the excess isotherm results lower than 0 mg g^{-1}.

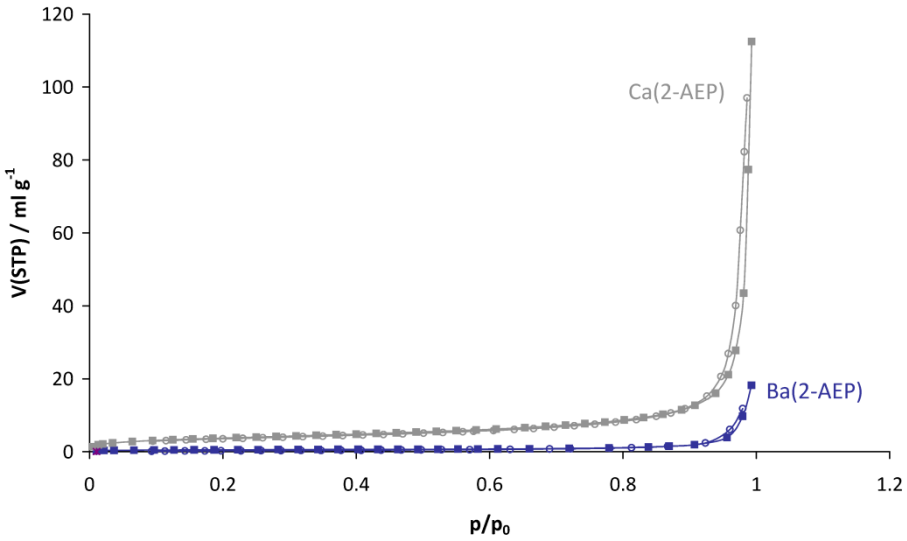

Figure 86: Nitrogen sorption obtained from volumetric analysis on Ca(2-AEP) and Ba(2-AEP) nanoparticles.

To summarise, a reduction of the porosity is observed in the materials Ca(2-AEP) and Ba(2-AEP): the decrease of the pore volume blocks the diffusion of the gas into the materials, resulting in a decrease of CO_2 uptake.

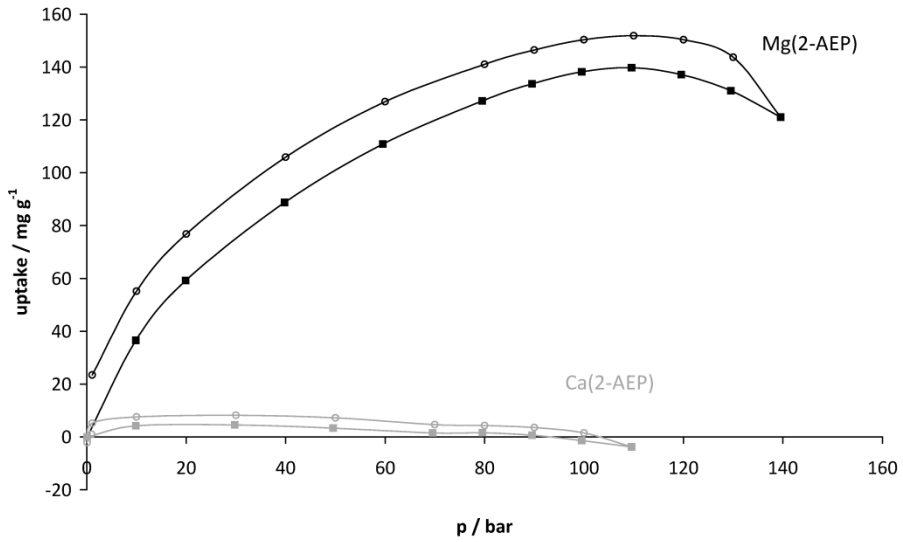

Figure 87: CO_2 sorption and desorption isotherms at 80°C obtained from gravimetric analysis on Mg(2-AEP) (black) and Ca(2-AEP) (gray) nanoparticles.

5.2.1.3 Phosphonate hybrids with transition cations

In the literature it is well known that, in the context of post-combustion CO_2 capture, the open coordination sites at metal serve as binding sites for CO_2. In comparison to N_2, CO_2 is adsorbed more strongly at these sites, owing to its greater quadrupole moment and polarizability (see paragraph 2.4.1 for references).

Figure 88: Picture of the final dried materials obtained combining aminoethyl phosphonic acid with different transition metal cations: Fe(2-AEP) yellow, Co(2-AEP) dark blue and Cu(2-AEP) light blue.

In order to study the effects of different open coordination sites on metal cation, three transition metal cations are selected and left to react with the organic ligand with the best selectivity towards CO_2: aminoethyl phosphonic acid. The syntheses were performed following similar procedures (see paragraph 8.5) *via* the microemulsion approach. Qualitatively, the presence of the cation in the three different compounds is proven by the colour of the final material: yellow for the iron aminoethyl

phosphonate (Fe(2-AEP)), dark blue for the cobalt aminoethyl phosphonate (Co(2-AEP)) and light blue for the copper aminoethyl phosphonate (Cu(2-AEP)) (see Figure 88). The presence of the organic linker was verified by elemental analysis (Table 14) and FT–IR spectroscopy (Figure 90). Here again, as explained in paragraph 5.2.1.2, the shift of the P=O and P–C stretching vibrations is evident. Note that the valance (+2) of the iron in the compound Fe(2-AEP) is only supposed and not experimental verified: due to the higher stability of Fe(III) compared to Fe(II), the precipitation of a hybrid material containing Fe^{3+} as cation is to take into account. Based on these results, the chemical compositions of Co(2-AEP) and Cu(2-AEP) are reliably confirmed.

Volumetric analysis (Figure 91) shows again a reduced specific surface area in comparison to Mg(2-AEP): 35 $m^2 g^{-1}$ for Fe(2-AEP), 35 $m^2 g^{-1}$ for Co(2-AEP) and 61 $m^2 g^{-1}$ for Cu(2-AEP). Surprisingly, the copper compound shows the higher A_{BET}, despite its heavier weight. As a consequence, it shows also the best CO_2 uptake in comparison to Fe(2-AEP) and Co(2-AEP) (see Figure 92). This can be explained by the analysis of the SEM images, illustrated in Figure 89: a lower degree of agglomeration of Cu(2-AEP) nanoparticles, with respect to the iron and cobalt aminoethyl phosphonates, is observed.

Table 14: Elemental compositions of Fe(2-AEP), Co(2-AEP) and Cu(2-AEP) according to EA. The theoretical amount is reported in the first rows of each compound.

	C	H	N
Fe(2-AEP)			
Theory, weight / %	13.4	3.3	7.8
Experimental, weight / %	10.9	4.1	5.9
Co(2-AEP)			
Theory weight / %	13.2	3.3	7.7
Experimental, weight / %	11.6	3.5	5.7
Cu(2-AEP)			
Theory weight / %	12.9	3.2	7.5
Experimental, weight / %	12.9	3.2	5.8

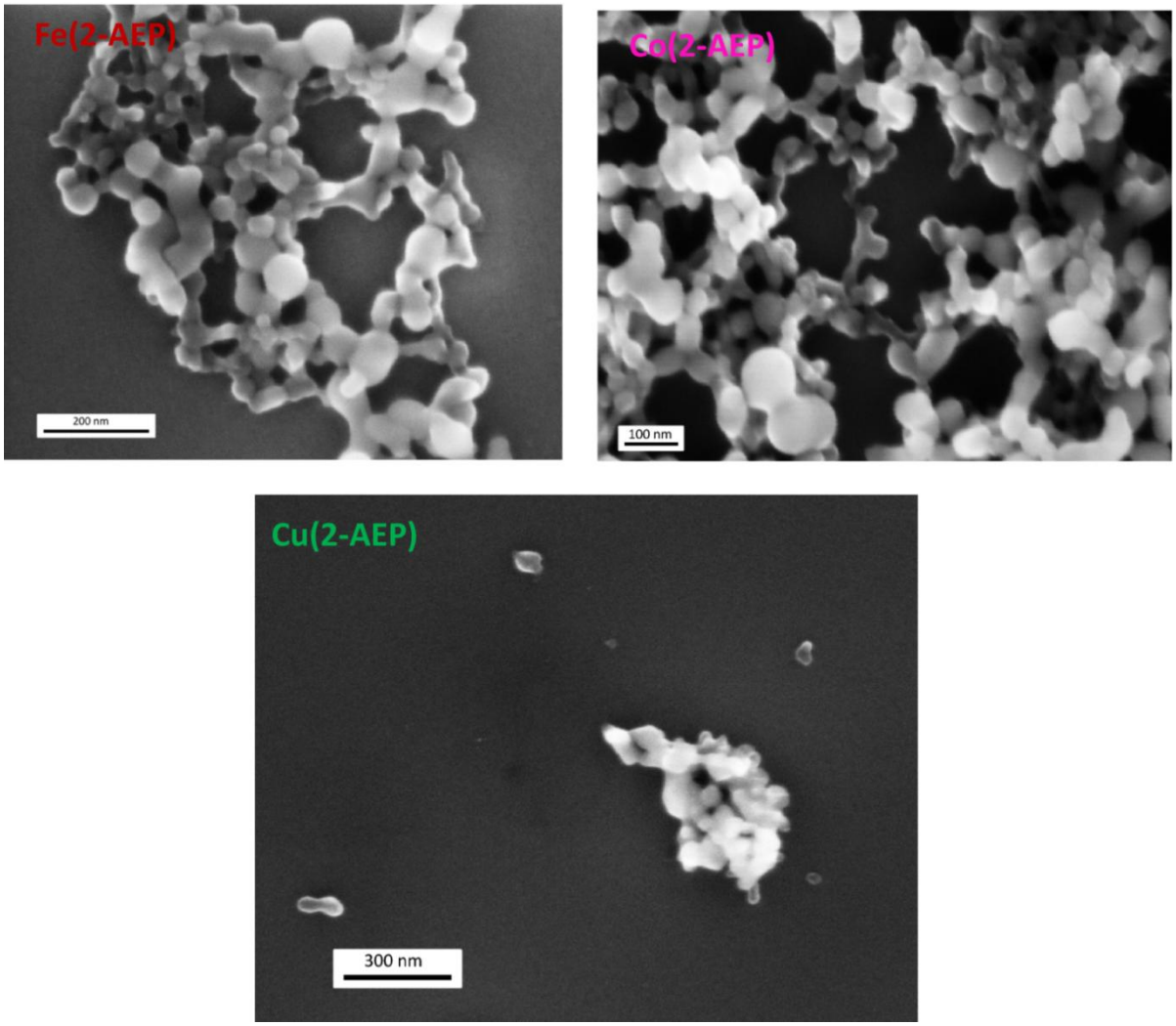

Figure 89: Representative SEM images of the as-prepared Fe(2-AEP), Co(2-AEP) and Cu(2-AEP) nanoparticles.

Another explanation of this behaviour can be found in the different charge density of cations. Fe, Co and Cu have valence (+2) and their atomic radii result in 156 pm for iron, 152 pm for cobalt and 145 pm for copper. As a consequence, Cu^{2+} shows the higher charge density and interacts more strongly with the quadrupole moment of CO_2.[5]

Interestingly, Fe(2-AEP) and Co(2-AEP) show the same specific surface according to the BET formalism, despite a clearly difference in the CO_2 gravimetric measurement: Co^{2+} obviously interacts more strongly with CO_2. This cannot be rationalized based on the diameter of the cations, which is just slightly larger for the cobalt. This finding could be attributed to a partial oxidation of Fe(II) to Fe(III) during the synthesis, giving as result $(Fe)_2(2\text{-}AEP)_3$. Accordingly, the theoretical CO_2 uptake on the iron compound is lower with respect to pure Fe(2-AEP), due to the heavier weight of the sorbent material.

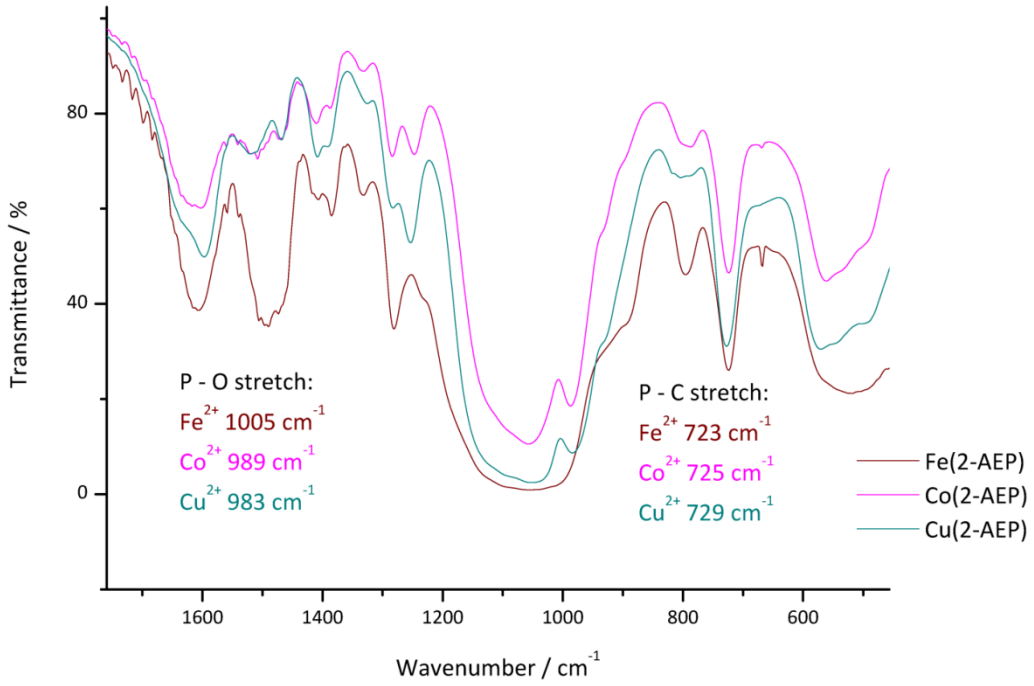

Figure 90: FT–IR spectra of Fe(2-AEP), Co(2-AEP) and Cu(2-AEP): the stretching mode of the P–C bond and P–O is shifted to different wavenumbers by changing the cation.

In summary, an intensive study of the cation influence on the aminoethyl phosponate compounds was performed. Mg(2-AEP) shows the highest gravimetric and volumetric sorption capacity. According to Zhang *et al.*,[9] the positive influence of magnesium as cation can been rationalized in this terms: the Mg–O bond has a strong ionic character, which leads to a higher partial positive charge on the Mg^{2+} metal centre, and consequently, facilitates a greater degree of polarization on the adsorbed CO_2 molecules.

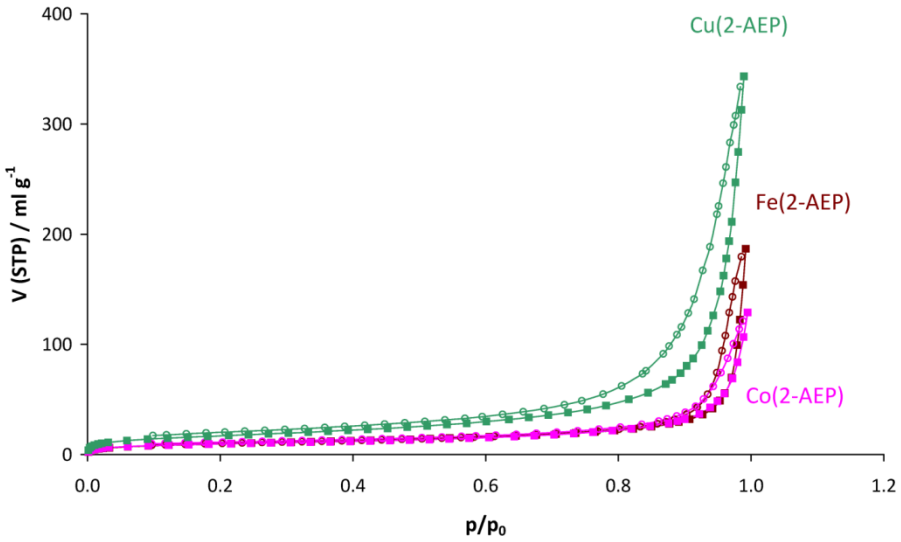

Figure 91: Nitrogen sorption obtained from volumetric analysis on Fe(2-AEP), Co(2-AEP) and Cu(2-AEP) nanoparticles.

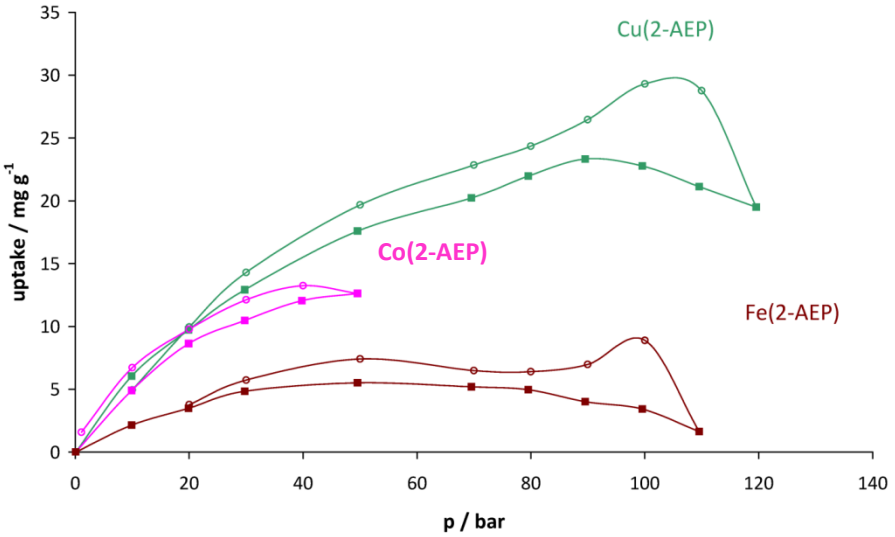

Figure 92: CO_2 sorption and desorption isotherms at 80°C obtained from gravimetric analysis on Fe(2-AEP), Co(2-AEP) and Cu(2-AEP) nanoparticles.

5.2.1.4 Mg(2-AEP)(FMN): a nanoscale phosphonate hybrid with luminescence response toward CO_2

There are needs for sensitive and selective gas detection for a range of applications including industrial process management, chemical threat detection, medical diagnostics, food quality control, occupational safety, and environmental monitoring.[130] In the context of CO_2 emission, the development of a CO_2 sensor that is able to detect the presence or absence of this gas can be extremely interesting, due to the fact that high concentrations of this gas are highly toxic for humans.[131]

Having an hybrid molecule that is able to selectively adsorb CO_2 (Mg(2-AEP)), the idea was to introduce another organic linker able to show luminescence upon excitation with UV light or a blue-light LED. In this way, CO_2 could interact with the 2-AEP ligand and, at the same time, influence the luminescent linker. Consequently, a variation of CO_2 concentration could be easily detected by the variation of wavelength and/or intensity of the emission spectrum of the excited material. The exploration of materials for guest-responsive luminescent sensors is still uncommon: in the literature, only few attempts can be found in the field of MOFs[132] and metal azolate frameworks.[133]

As the luminescent molecule, riboflavin-5'-monophosphate sodium (FMNHNa) salt was selected, according to the synthesis of the luminescent hybrid nanomaterial ZrO(FMN) published by Roming *et al.*.[134]

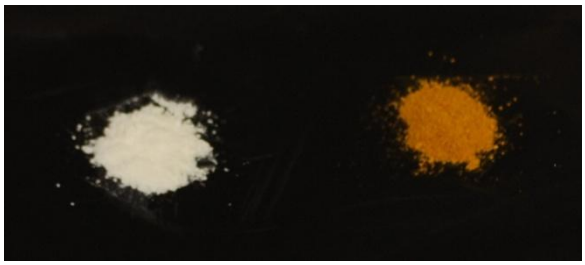

Figure 93: Picture of Mg(2-AEP) on the left and Mg(2-AEP)(FMN) nanoparticles on the right.

The synthesis of the new compound with the composition Mg(2-AEP)(FMN) can be found in paragraph 8.6. The incorporation of the fluorescent organic dye is proven by the change of the optical property compared to the material Mg(2-AEP) (Figure 93) and by the appearance of additional vibrations in FT–IR spectra (Figure 94) attributed to FMN (Figure 64, see IR spectrum of Mg(2-AEP) as reference). According to electron scanning microscopy, the final material has an average diameter of 20 - 30 nm as illustrated in Figure 95.

Fluorescence spectroscopy was performed with suspensions of the nanoparticles (0.5 mg ml^{-1}) in a 1:1 mixture of water and ethanol as solvents. Water has the advantage to dissolve CO_2 in high concentration, whereas ethanol supports the stabilization of the suspension. Carbon dioxide was qualitatively introduced as dry ice in a test tube containing the suspension. Suspensions were stirred during the spectroscopic analyses. All measurements were performed at room temperature.

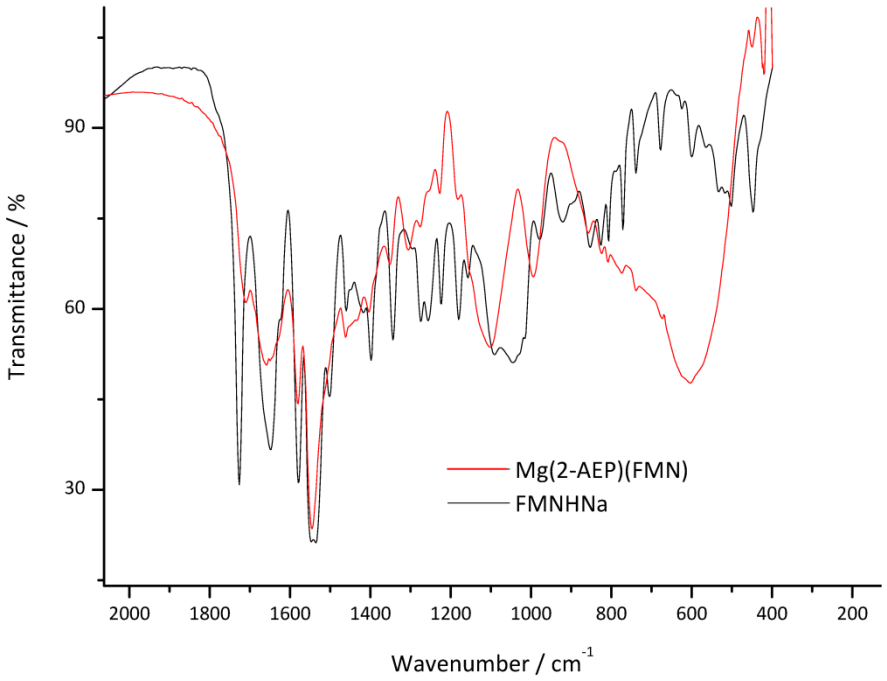

Figure 94: Infrared spectroscopy of the material Mg(2-AEP)(FMN) compared to the free linker FMNHNa.

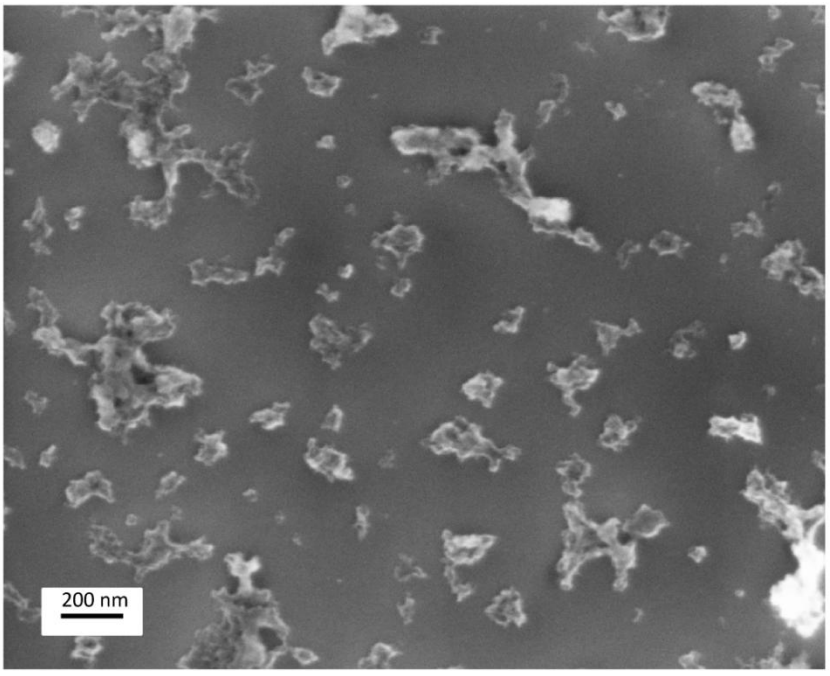

Figure 95: SEM image of the compound Mg(2-AEP)(FMN).

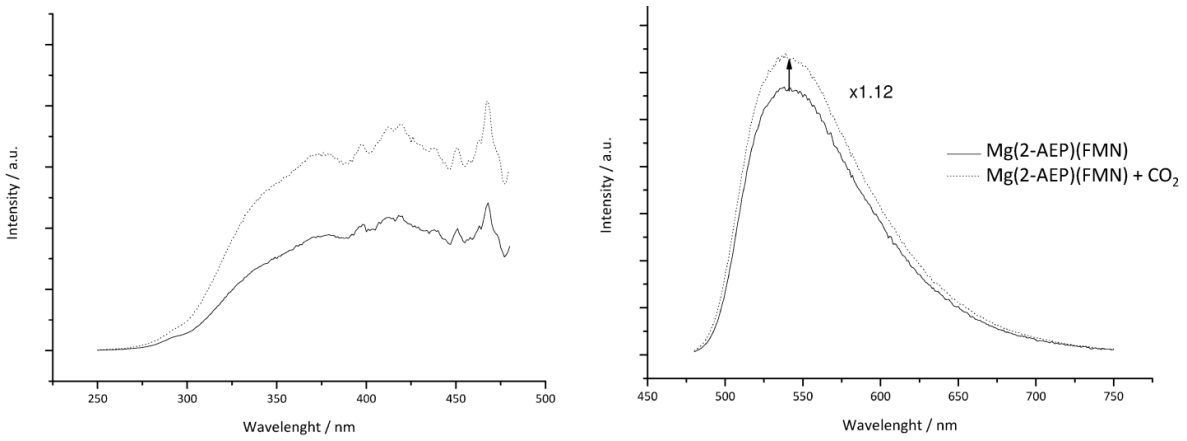

Figure 96: Excitation ($\lambda_{emission}$: 540 nm) and emission ($\lambda_{excitation}$: 465 nm) spectra of a Mg(2-AEP)(FMN) nanoparticle suspensions before (solid line) and after (dotted line) the introduction of CO_2 as dry ice (pH = 6.1). Suspensions were prepared in water-ethanol 1:1. Emission spectra were normalized on the excitation spectra in order to allow a facile comparison.

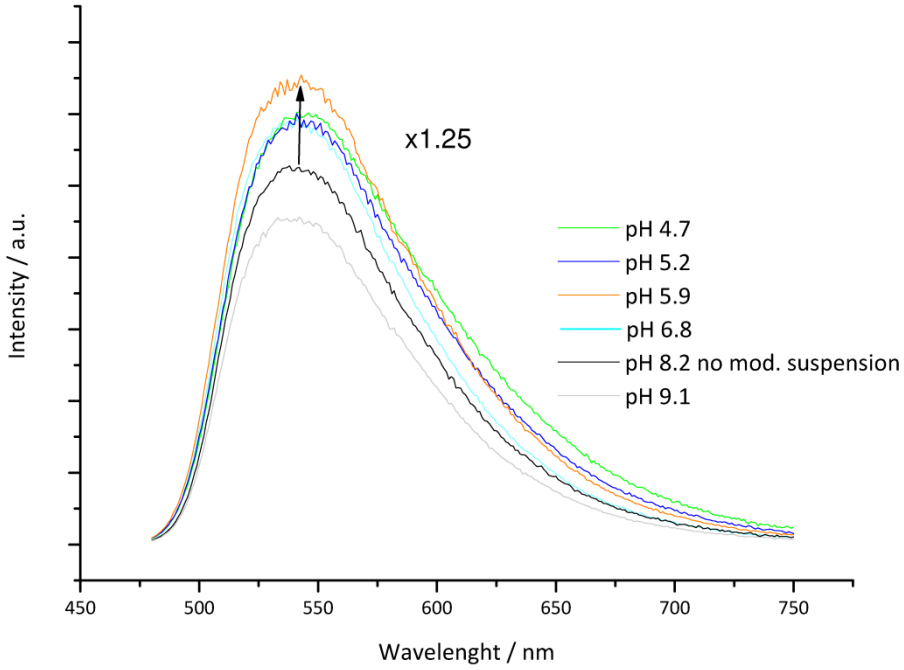

Figure 97: Emission ($\lambda_{excitation}$: 465 nm) spectra of a suspension of Mg(2-AEP)(FMN) nanoparticles at different pH. Suspensions were prepared in water-ethanol 1:1. Emission spectra were normalized on the excitation spectra in order to allow a facile comparison.

Excitation and emission spectra of the original suspension and of the suspension containing CO_2 are shown in Figure 96: after the introduction of CO_2, the intensity in the emission spectra is slightly increased, by a factor of 1.12. The explanation could be ascribed to the interaction of CO_2 with the free amino groups of the linker 2-AEP, in such a way that the energy level of the ground state of the molecule and its excited state are changed.

The intensified luminescence intensity upon introduction of CO_2 could be rationalized, otherwise, as a consequence of pH change, as carbon dioxide is an acidic gas ($pK_a(H_2CO_3)$: 3.9). For this purpose, the pH of the suspensions before and after introduction of CO_2 was tested with a pH meter: the original suspension of Mg(2-AEP)(FMN) in water:ethanol 1:1 had pH = 8.2, whereas after the introduction of dry ice, the pH decreased to 6.1. In order to verify the pH effect, the original suspension was divided into six test tubes and the pH modified upon introduction of acetic acid or a water solution of sodium acetate, controlling the pH with the pH meter. The spectra, collected under similar conditions, are illustrated in Figure 97. The luminescence intensity is only slightly changing upon acidification of the solution, showing a jump of 1.25 from the non-modified suspension (pH = 8.2) to pH = 5.9, very similar to the CO_2 containing suspension conditions.

In summary, after acidification of the starting suspension, an increase in the luminescence intensity is reported. The same result was obtained if CO_2 as dry ice was dissolved into the suspension. According to the CO_2 sorption reaction (Equation (23)), only one mole of carbon dioxide is sorbed every two moles of amine, giving as result one mole of protonated amino group and one carbamate. In the same way, the protonation of the amino group is the result of the acidification of the suspension upon introduction of acetic acid. Consequently, the increase of luminescence of the Mg(2-AEP)(FMN) suspension could be described as a pH effect, but the variation in intensity seems to be negligible for practical applications.

5.2.1.5 Non-phosphonate organic ligands

In order to increase the CO_2 uptake, the porous material should be lightweight. Consequently, a similar organic linker to H_2(2-AEP) was selected, just with carbon instead of phosphor: β-alanine (Figure 98, left). The reaction was performed *via* the microemulsion technique (see paragraph 8.7). Unfortunately, the synthesis gave only products which weren't easy to handle, highly hygroscopic or liquids. Consequently, no further analyses were performed, since the MSB cannot analyse liquid samples. As an alternative, barium could be used instead of magnesium: Ba^{2+} has solvatation energy of -1305 kJ mol^{-1}, whereas Mg^{2+} -1921 kJ mol^{-1}:[135] the Ba-compound is less hygroscopic that the Mg-compound and it should be solid under atmospheric conditions. Nevertheless, based on the result obtained for the compound Ba(2-AEP) in terms of specific surface area and CO_2 uptake, the study of this material was not performed.

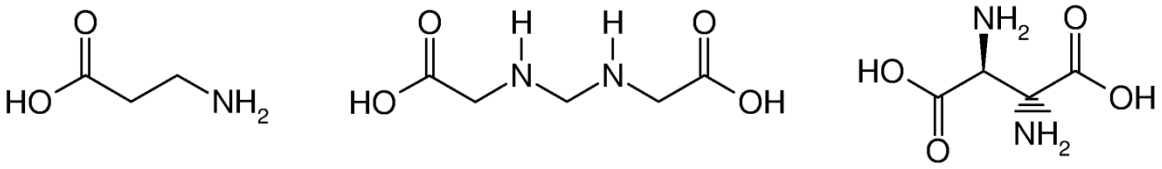

Figure 98: Chemical formulas of three non-containing phosphor organic linker. Left: β-alanine; middle: ethylenediamine-N,N'-diacetic acid; right: *meso*-2,3-diaminosuccinic acid.

The second option consisted in a chelating dicarbossilic acid, a derivate of succinic acid upon introduction of two secondary amine functional groups: ethylenediamine-N,N'-diacetic acid (Figure 98, middle). The molecule, that is soluble only in basic water, does not allow a synthesis *via* microemulsion due to the high alkalinity of the polar phase, which destabilizes the system. The synthesis was then performed *via* hot injection technique, but in this case, the high basicity of the solvent induces only the precipitation of hydroxides. Figure 99 illustrates the FT–IR spectra of the organic precursor (black) and of the product (red): the latter shows the typical vibrations of $Mg(OH)_2$.[115] Elemental analysis, moreover, gave as result 0.0% of N.

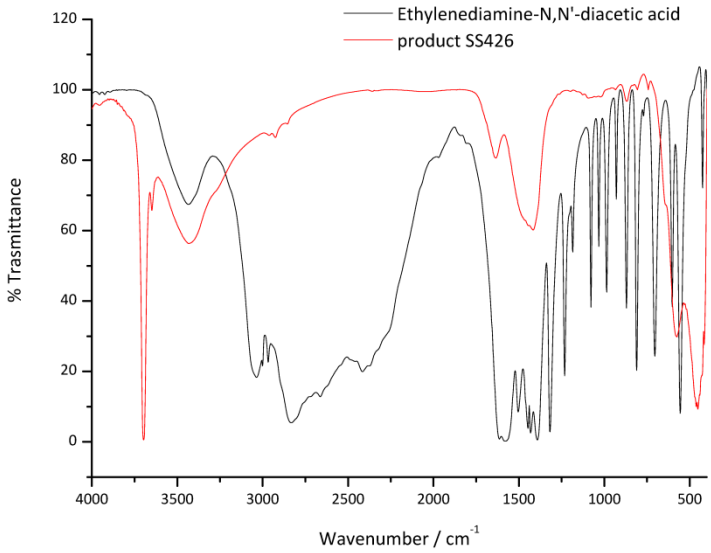

Figure 99: FT–IR spectrum of the precursor ethylenediamine-N, N'-diacetic acid compared to the product obtained *via* hot injection synthesis (cationic precursor was $MgCl_2$).

The third molecule under investigation was *meso*-2,3-diaminosuccinic acid (Figure 98, right). This chelating low-weight agent has two primary amino groups, one above and one below the plane of the paper. In this way, the formation of two carbamates upon interaction with CO_2 could occur without steric restrictions. Unfortunately, during the synthesis, performed *via* hot injection strategy, only the precipitation of magnesium hydroxide was preferred (Figure 100, FT–IR of the product indentifies it as $Mg(OH)_2$)[115] instead of an hybrid material.

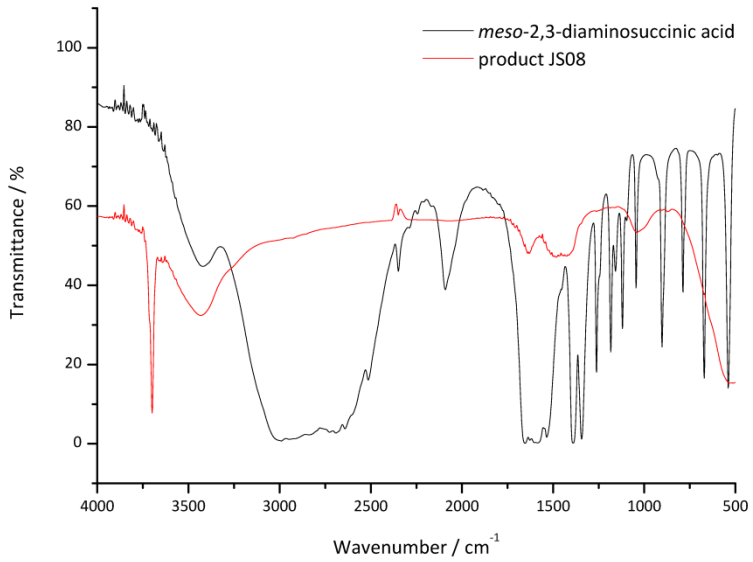

Figure 100: FT–IR spectrum of the precursor meso-2,3-diaminosuccinic acid compared to the product obtained *via* hot injection synthesis (cationic precursor was $MgCl_2$).

In summary, the synthesis of new Mg^{2+}-hybrids materials not containing phosphor in the organic precursor were unsuccessful results. As alternative three-valent (to stabilize the chelation process)[135] and low-weight cations (to assure high CO_2 uptake) can be proposed. For instance alluminium (valence (+3), molecular weight 27 g mol^{-1}) or scandium (valence (+3), molecular weight 45 g mol^{-1}) could result good candidates.

5.2.2 Hybrids for oxygen separation

The synthesis of porous magnetic materials for the O_2 sorption and separation was addressed. As reported in the paragraph 2.4.2, the paramagnetic property of O_2 can be used to separate O_2 from N_2 or, even more interestingly, O_2 from Ar, due to the similar adsorptive properties of these two gases.

As magnetic inorganic cations, cobalt(II) and gadolinium(III) were selected, as both contain unpaired electrons (Co(II): [Ar] $3d^7$; Gd(III): [Xe] $4f^6\,5d^1$). As organic anion, propyl phosphonic acid was used, since the presence of the amino group is not required for O_2 sorption and separation. The obtained materials were designed Co(PP) for cobalt(II) propyl phosphonate and $(Gd)_2(PP)_3$ for the gadolinium propyl phosphonate.

Both compounds were obtained *via* microemulsion synthesis, described in paragraph 8.8. The final materials showed magnetic properties, since they were tested and found attractive by a magnet (Figure 101).

Figure 101: Pictures of the dried Co(PP) (left) and $(Gd)_2(PP)_3$ (right) nanoparticles and their behavior in an external magnetic field.

The chemical composition is proven by FT–IR (Figure 104: Co(PP) compared to Mg(PP), Figure 105: $(Gd)_2(PP)_3$)). Infrared spectroscopy confirms the presence of the organic molecule: υ(C–H): 2950 - 2850 cm^{-1}; $\upsilon(PO_3)$: 1200 - 850 cm^{-1} and υ(O–H) from H_2O: 3300 - 2900 cm^{-1}. EDX analysis of Co(PP) nanoparticles, listed in Table 15, qualitatively proves the presence of the expected elements. Quantitatively, the atomic ratio Co/P results 2.3, more than twice bigger than the expected Co/P = 1.0. This finding however could be attributed to the formation of $Co_2(OH)_2(PO_3C_3H_7)$ instead of $Co(PO_3C_3H_7)$. (Figure 102). As an alternative to EDX, the inductively coupled plasma mass spectroscopy (ICP-MS) could be used for the determination of the cobalt amount in this sample and, as a consequence, employed to determine its chemical composition.

Elemental analysis of the Gd-compound confirms the composition of $(Gd)_2(PP)_3$ (Table 16 and Figure 103).

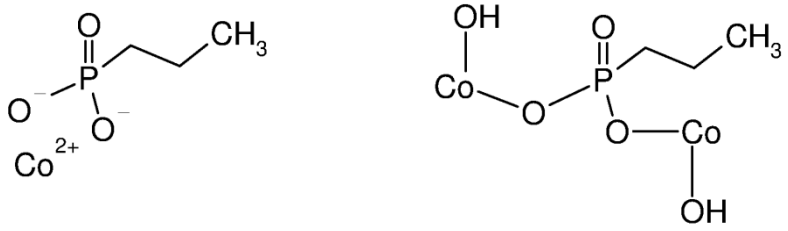

Figure 102: Chemical formulas of the Co-hybrid according to the ratio Co/P = 1.0. (Co(PP), $Co(PO_3C_3H_7)$ left) and to the ratio Co/P = 2.0 ($Co_2(OH)_2(PO_3C_3H_7)$, right).

Table 15: EDX analysis of Co(PP) nanoparticles.

	Co	P	C	H	N	O	Br	
Co(PP)								
Theory weight / %	32.6	17.1	19.9	3.9	0.0	26.5		100
EDX, weight / %	37.1	6.5	24.6	-	0.0	30.6	1.2	100
EDX, atomic / %	14.3	6.1	38.5	-	0.0	40.9	0.2	100

Table 16: Elemental analysis of $(Gd)_2(PP)_3$ nanoparticles.

	C	H	N
$(Gd)_2(PP)_3$			
Theory, weight / %	15.9	3.1	0.0
Experimental, weight / %	15.9	3.5	0.0

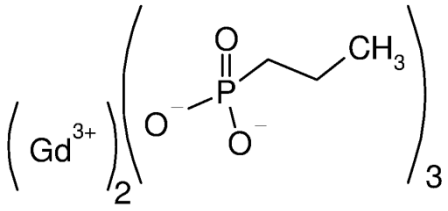

Figure 103: Chemical structure of $(Gd)_2(PP)_3$.

The resulting specific surfaces are 102 $m^2 g^{-1}$ for the Co-compound and 175 $m^2 g^{-1}$ for $Gd_2(PP)_3$ (Figure 106, volumetric analysis). The volumetric sorption analysis on $Gd_2(PP)_3$ nanoparticles shows an hysteresis, which is related to its larger specific surface area and suggests the presence of mesoporosity. A mesoporous structure, as well as a microporous structure, can be excluded for the hybrid Co(PP): the A_{BET} obtained for this compound could be related only to the spaces between the nanoparticles. SEM pictures give an additional hint: the Co-compound (Figure 107) seems to form preferably nanorods 200 nm in size instead of nanoparticles, whereas SEM images of $Gd_2(PP)_3$ show evidence of a uniform, spherical shape with an average diameter between 20 and 40 nm (Figure 108).

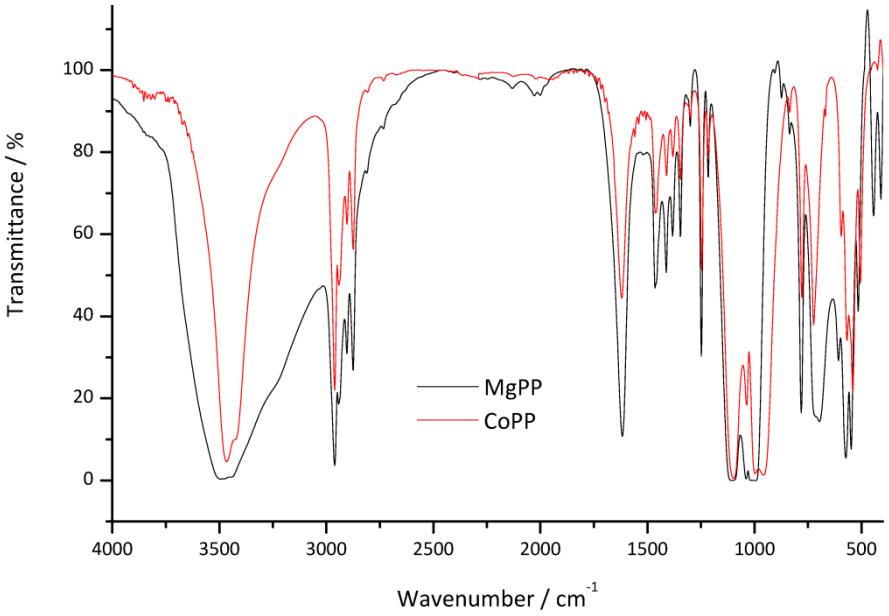

Figure 104: FT–IR spectrum of magnesium aminoethyl phosphonate nanoparticles (black) compared to the spectrum of cobalt aminoethyl phosphonate nanoparticles (red).

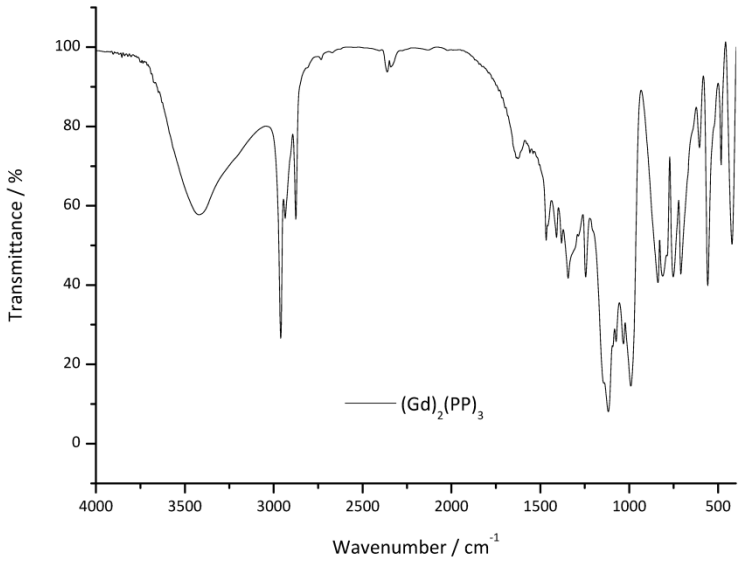

Figure 105: FT–IR spectrum of gadolinium aminoethyl phosphonate nanoparticles.

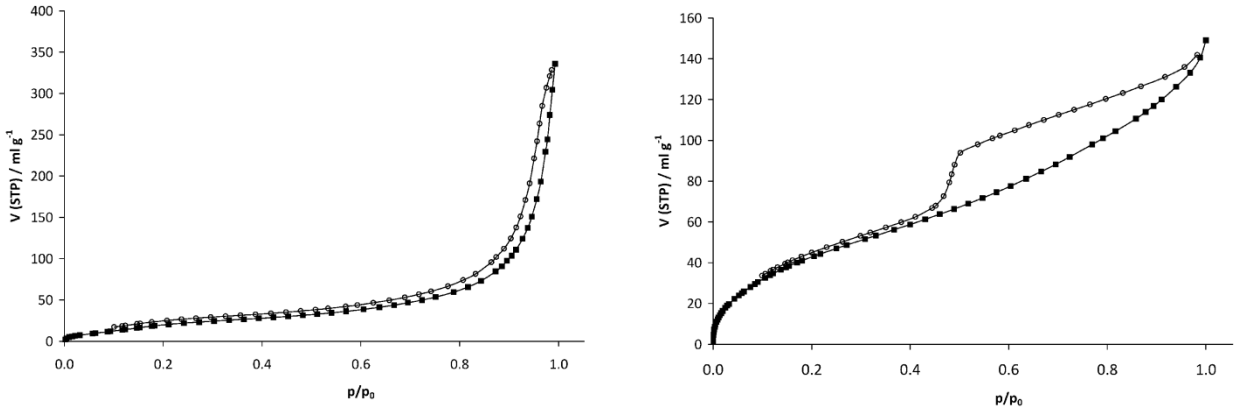

Figure 106: Volumetric N_2 sorption analysis performed on Co(PP) nanoparticles (left) and $Gd_2(PP)_3$ nanoparticles (right).

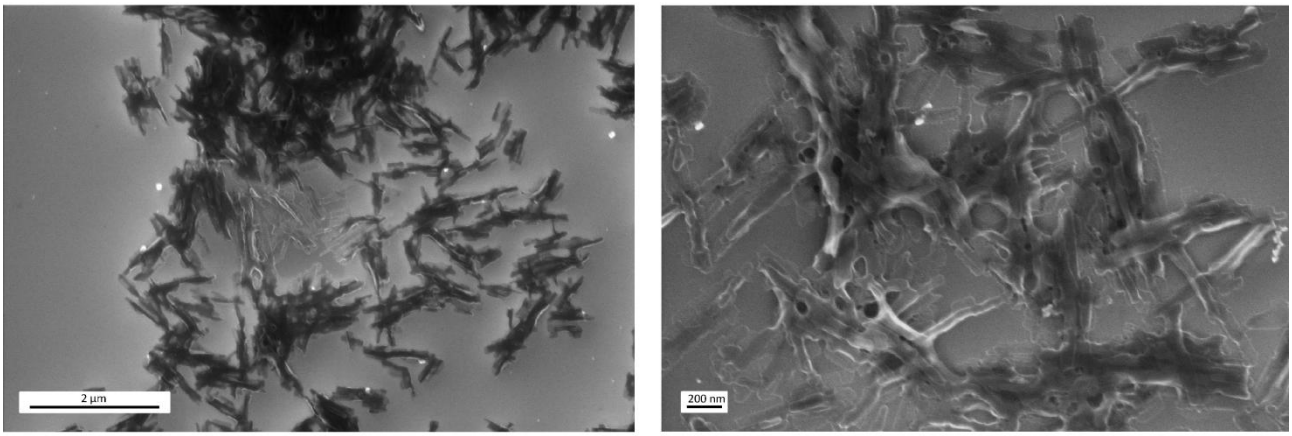

Figure 107: SEM pictures of the as prepared Co(PP) nanoparticles.

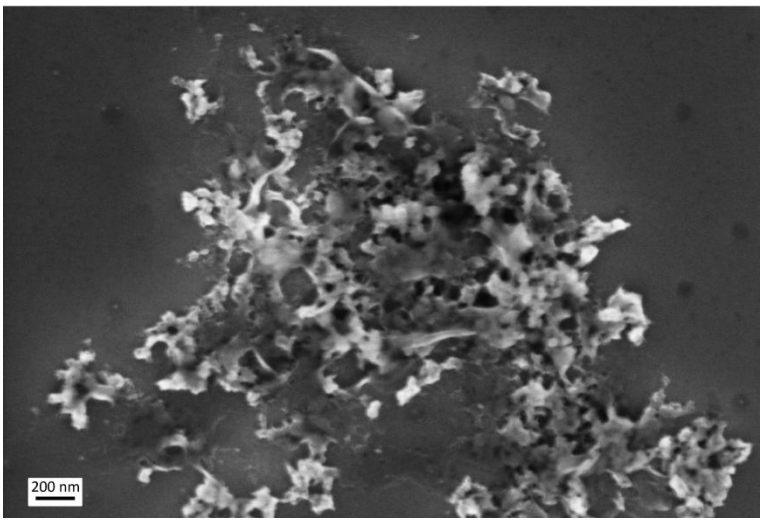

Figure 108: SEM picture of the as prepared $(Gd)_2(PP)_3$ nanoparticles.

The oxygen uptakes on the two materials, tested at 25 °C and at 50 °C up to 50 bar by MSB, were very low. A bigger reduction of the temperature would show a higher O_2 uptake, due to the exothermic properties of the adsorption process. For this purpose, O_2 pure gas sorption analyses at -196°C, as well as Ar and N_2 pure gas isotherms, on the two hybrids nanomaterials described above, were performed in the laboratories of Prof. Staudt, Institut für Nichtklassische Chemie (INC), Leipzig. The experimental results, measured by the volumetric method, are presented in Figure 109 for the Co(PP) and in Figure 110 for the $(Gd)_2(PP)_3$ nanoparticles. The capacities observed were not only low, but also very similar for the three gases: for Co(PP) the uptakes at p/p_0 = 0.5 resulted in 1.50 mmol g^{-1}, 1.55 mmol g^{-1}, 1.50 mmol g^{-1} for N_2, Ar and O_2, respectively. In the case of $(Gd)_2(PP)_3$ nanoparticles, the uptakes were 2.74 mmol g^{-1} for N_2, 3.13 mmol g^{-1} for Ar and 3.37 mmol g^{-1} for O_2. As a consequence, the separation of these gases is precluded in the proposed nanomaterials and further analyses with gas mixtures are not planned. One explanation of the experimental results obtained could be found in the relative low specific surface areas of these materials, smaller than 180 m^2 g^{-1}. As further step, in order to increase the contact surface between the gas and the sorbent material, the averaged diameter of the nanomarticles has to be reduced: the synthesis *via* hot injection, performed in a solvent in which the product has a low solubility, could represent an alternative pathway.

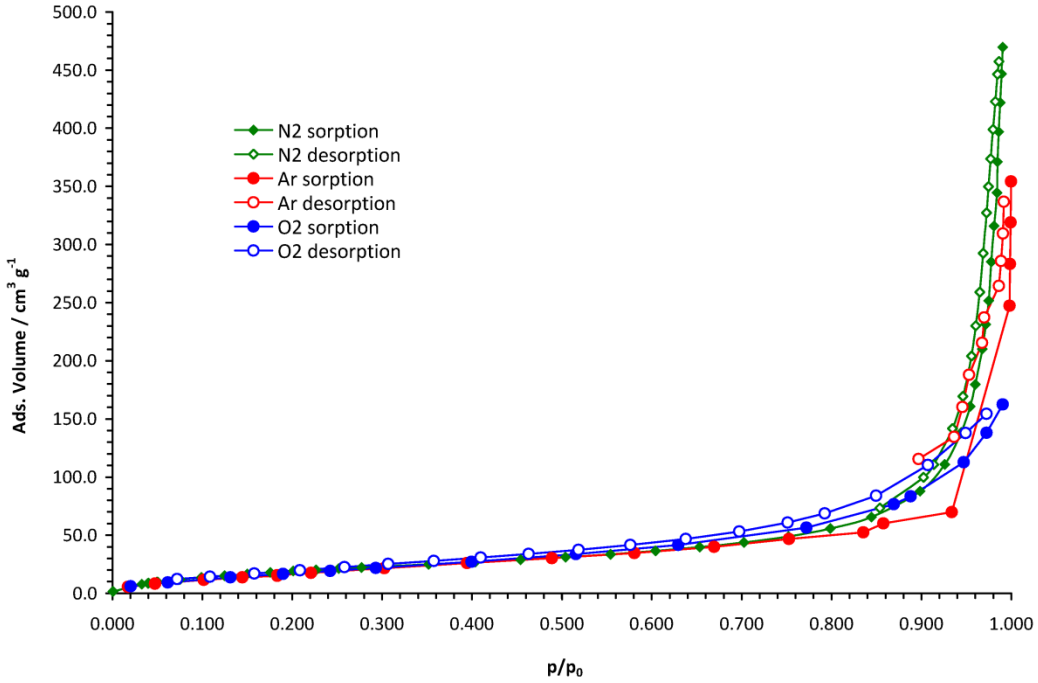

Figure 109: N_2 (green), Ar (red), O_2 (blue) isotherms at -196 °C on Co(PP) nanoparticles.

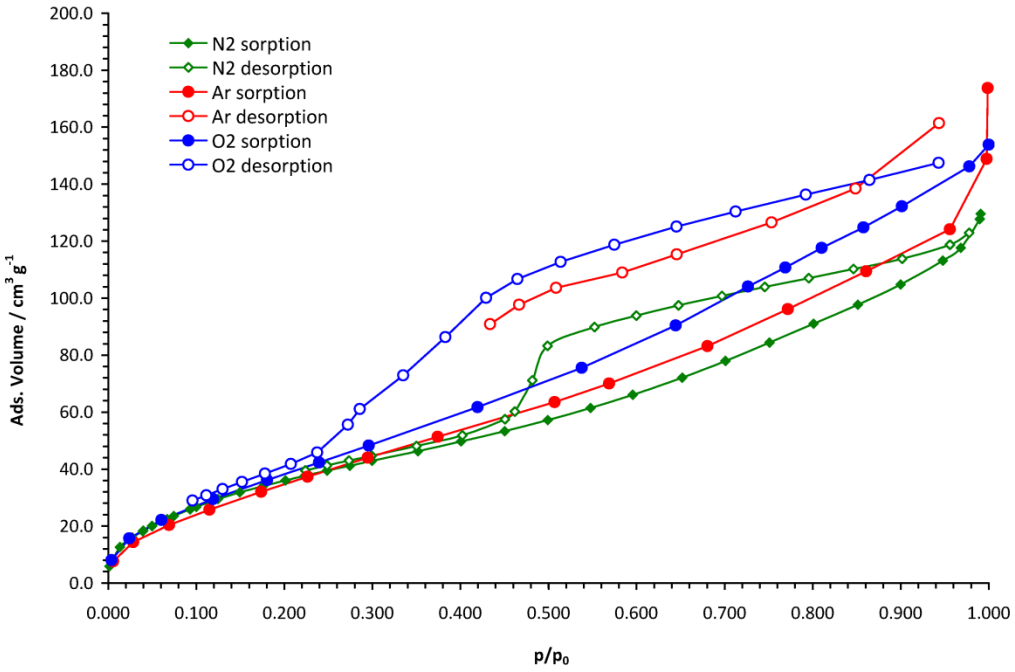

Figure 110: N_2 (green), Ar (red), O_2 (blue) isotherms at -196 °C on $(Gd)_2(PP)_3$ nanoparticles.

5.2.3 Hybrid for methane sorption

As reported in paragraph 2.4.3, the investigation of new materials for the sorption and separation of light hydrocarbons is a growing field. As an initial study, the material magnesium propyl phosphonate (Mg(PP)) as methane potential sorbent is proposed here. Mg(PP) is characterised by a relative high specific surface area (222(±18) $m^2 g^{-1}$) and an average particle size of 20 nm in diameter (SEM pictures are illustrated in Figure 111). The presence of the alkyl non-polar chain as an organic linker can interact by Van der Waals forces with methane, being itself a non-polar gas.

The synthesis of the compound Mg(PP) can be found in paragraph 8.3. Infrared spectroscopy, thermogravimetric analysis, as well as N_2 and CO_2 sorption analyses are described and discussed in paragraph 5.2.1.1. Here, the elemental analysis as well as EDX measurement are shown (Table 17), to prove its chemical composition. The experimental results match the theoretical values (EDX Mg/P ratio = 1.1): consequently, chemical composition of Mg(PP) is reliably validated. Moreover, SEM images are illustrated in Figure 111 (scale bar is 200 nm).

Table 17: Elemental composition of Mg(PP) according to EDX analysis and elemental analysis.

	Mg	P	C	H	N	O	Br
Mg(PP)							
Theory weight / %	14.8	18.9	22.0	5.5		39.9	
EDX, weight / %	19.6	22.3	14.8	-	0.0	38.3	5.0
EDX, atomic / %	15.4	13.8	23.7	-	0.0	45.9	1.1
EA, weight / %	-	-	17.5	5.2	0.0	-	-

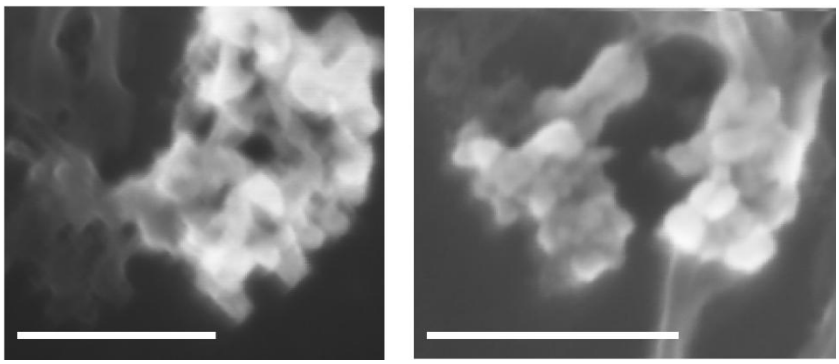

Figure 111: SEM images of the Mg(PP) nanoparticles. Scale bar is 200 nm for both images.

CH_4 gravimetric analysis at different temperatures will be performed in the near future in the laboratories of Prof. Staudt, Institut für Nichtklassische Chemie (INC), Leipzig.

5.2.4 Hybrids for (S/R) ibuprofen separation

The importance of the chirality on the activity and properties of many compounds is well known: enantiomers exhibit different biological, physiological and chemical behaviour and may show different pharmacodynamic effects.[136] Thus, obtaining chiral compounds with high enantiomeric excess have attracted increasing attention in the fields of pharmaceutical, fine chemicals and agroalimentary industries.[137]

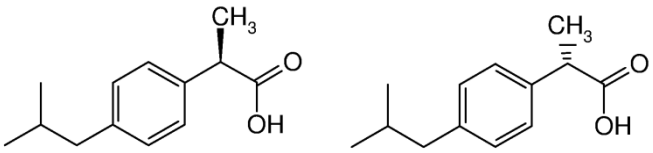

Figure 112: Chemical structure of (S)-(+)-Ibuprofen (left) and R-(-)-Ibuprofen (right).

Ibuprofen (isobutyl-propanoic-phenolic acid) is a chiral drug that is well-know for its analgesic, antipyretic and anti-inflammatory effects. It is characterised by a stereogenic centre adjacent to the carboxylic acid moiety (Figure 112). Ibuprofen is available as a racemic mixture although the (S)-enantiomer of this drug is 160 times more active than its (R)-enantiomer in the *in vitro* inhibition of prostaglandin synthesis.[138] Additionally, the latter contributes to increased side effects, affecting to the gastrointestinal tract, normal lipids metabolism and membrane function.[139]

In this view, the possibility to separate racemic ibuprofen using a chiral molecule as a resolving agent is reported in this work. This resolution involves interacting racemic ibuprofen with a single enantiomer of a resolving agent to form two different diastereometric salts. This reaction is performed in supercritical CO_2 (sc-CO_2) as solvent. A supercritical fluid is a physical-chemical state of a substance that occurs when temperature and pressure are elevated at or above its thermodynamic critical point. Supercritical fluids are characterised by densities very close to those of liquids and mass transfer properties (viscosities and diffusivities) ranging between those of gases and liquids. At the same temperature, the viscosity of a gas is typically less than one order of magnitude lower than the viscosity of supercritical fluid, but the density is liquid like. Thus, depending upon the fluid density, the fluid behaves as a solvent for a substance at one pressure, but as a non-solvent at another pressure.[140] Among the supercritical fluids, sc-CO_2 is particularly attractive since it is inexpensive, non-flammable and non-toxic. The diastereomeric salts are then analysed and separated by chiral supercritical fluid chromatography.[141]

In the following, two chiral inorganic-organic hybrid nanomaterials are proposed as resolving agents for (S/R)-ibuprofen. The organic linkers are chiral molecules commercially available as single enantiomers. The first hybrid described here was synthesized *via* hot injection technique, using (L)-cycteine as organic ligand (Figure 113) and Cu^{2+} as cation. The complete synthesis is reported on page 142, paragraph 8.9. The final compound is illustrate in Figure 114.

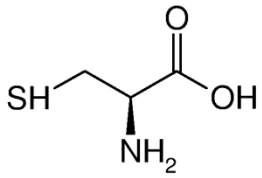

Figure 113: Chemical formula of (L)-cycteine.

The present of the organic linker in the final material was proven *via* infrared spectroscopy (Figure 115): accordingly, the characteristic vibrations of the free ligand are observed in the spectra of the hybrid material (υ(–NH_2): 3450 cm^{-1}; υ(C=O): 1630 - 1470 cm^{-1}; υ(C–S): 710 - 570 cm^{-1}). Elemental analysis (*i.e.*, C, H, N, S) confirms the composition of the final material with experimental values of $m(C)_{experimental}$ = 22.2%, $m(H)_{experimental}$ = 3.5%, $m(N)_{experimental}$ = 8.7% and $m(S)_{experimental}$ = 19.6%. These data are well in accordance to the calculated amounts $m(C)_{calculated}$ = 19.0%, $m(H)_{calculated}$ = 3.3%, $m(N)_{calculated}$ = 7.6% and $m(S)_{calculated}$ = 17.4%.

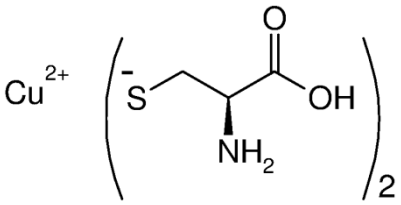

Figure 114: Chemical formula of the compound Cu (L)-cycteine.

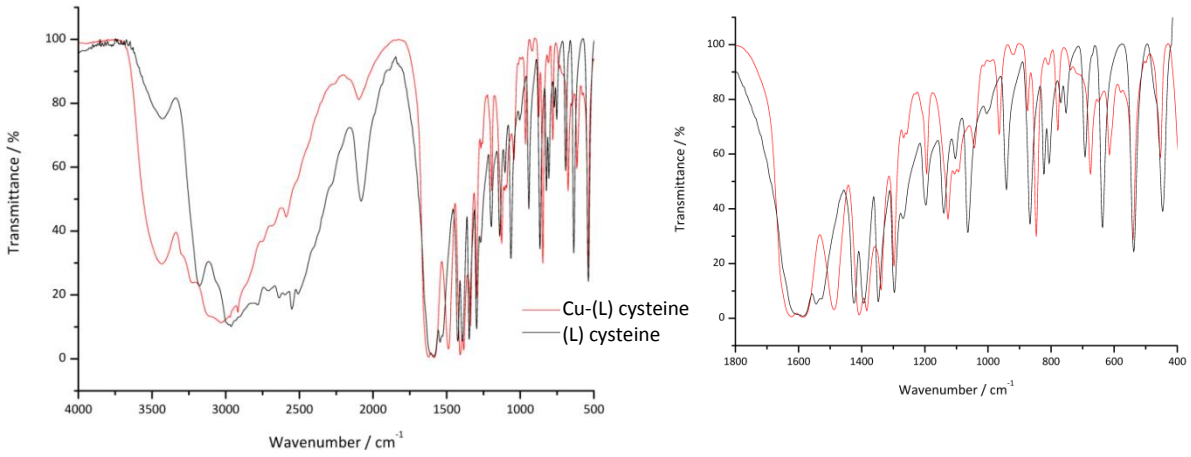

Figure 115: FT–IR spectra of Cu-(L) cysteine and (L) cycteine free as reference. Right: zoom in the region between 1800 and 400 cm^{-1}.

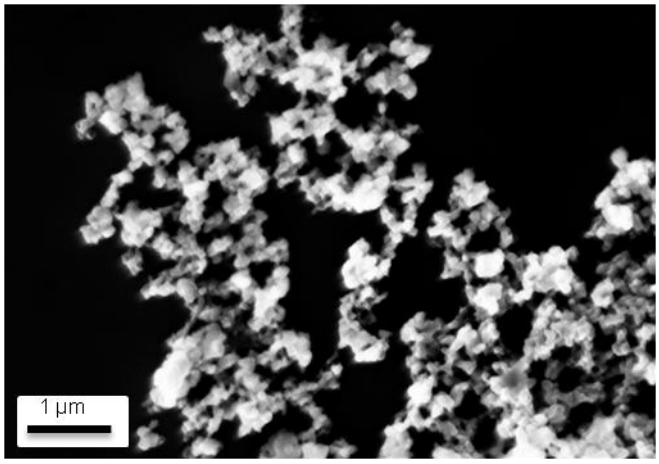

Figure 116: Scanning electron microscopy of the as prepared Cu-(L) cycteinen nanoparticle.

The material is characterised by an average particle dimension around 100 nm according to SEM analysis (one representative picture is shown in Figure 116). The specific surface area, calculated from the volumetric analysis shown in Figure 117, turns out to be 34.2(±0.6) m^2 g^{-1}, with a pore volume of 0.19(±0.06) cm^3 g^{-1}.

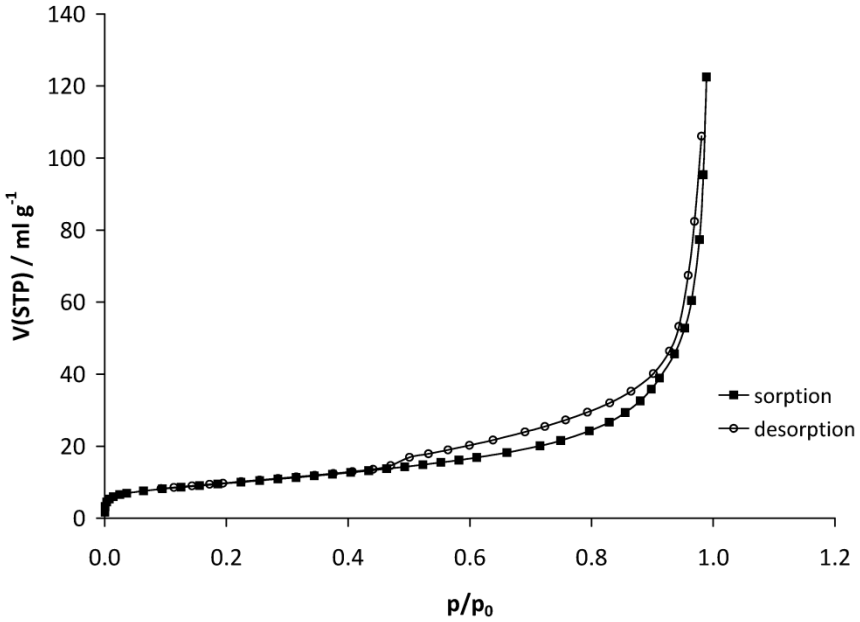

Figure 117: Nitrogen sorption and desorption isotherms at -196 °C on Cu-(L) cycteine nanoparticles.

The material was then tested for the sorption of racemic ibuprofen dissolved in sc-CO_2. These measurements, performed at 40 °C and 200 bar, in the laboratories of Prof. Türk (Institute for Technical Thermodynamics and Refrigeration, KIT) show no interaction between the nanomaterial and the racemic ibuprofen. The first idea to explain this behaviour was that the amine functional group present in the cycteine molecule interacts predominantly with the acidic sc-CO_2 used as the solvent, preventing any interaction with the acidic function of the ibuprofen. In order to avoid that, another organic ligand, not containing amino groups, was selected: (L)-malic acid (Figure 118).

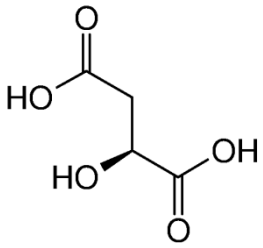

Figure 118: Chemical formula of the compound (L)-malic acid.

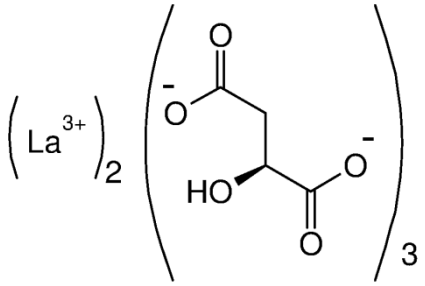

Figure 119: Chemical formula of the compound La (L)-malic acid.

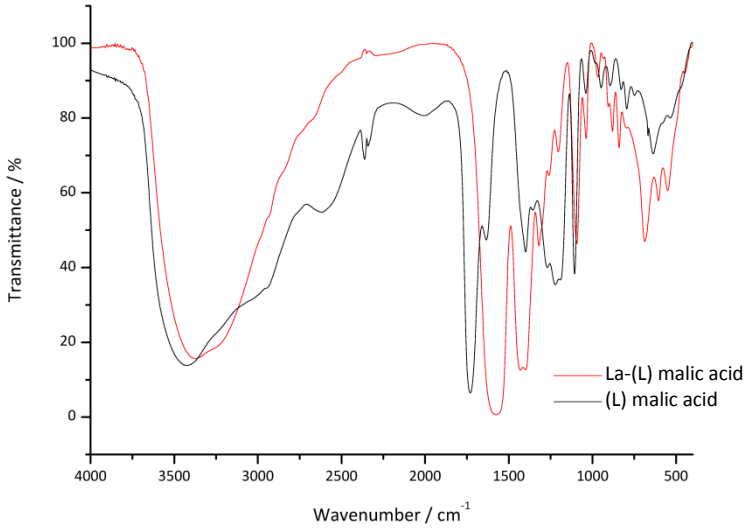

Figure 120: FT–IR spectra of La-(L) malic acid and the free (L) malic acid as reference.

The synthesis was performed *via* hot injection technique, using water as the solvent and lanthanum(III) as cation: the final material was analysed by infrared spectroscopy, which confirms the presence of the ligand. The broad signal between 3400 and 3000 cm^{-1} is identified as the O–H stretching vibration, whereas the narrow band at 1105 cm^{-1} is assigned to the C–OH stretching. Note the shift of C=O stretching vibration between the two spectra: it appears at 1733 cm^{-1} for the free ligand and at 1570 cm^{-1} for the material containing lanthanum. La is a heavy metal and its presence in the final molecule influence the stronger signal of the hybrid compound, changing its vibration energy. The specific surface area, according to the BET theory, was 19.5(±0.5) $m^2 g^{-1}$ (Figure 123). The sample was then tested by the cooperation partners in the group of Prof. Türk. The material was used as sorbent for the racemic mixture of ibuprofen dissolved in s-CO_2 (T: 40 °C, P: 200 bar). The result was 3.9×10^{-2} gram of (R/S)-ibuprofen sorbed per gram of sorbent material. In order to increase this last value, the specific surface of La-(L) malic acid had to be increased. For this purpose, the solvent used in the first synthesis (water) was substituted by ethanol. As shown in Figure 121, FT–IR

spectra of the material synthesised in water and of the compound obtained in ethanol show the same characteristic vibrations. Accordingly, it can be concluded that the two syntheses lead to materials with the same chemical composition. In order to study the particle size distributions of the two nanomaterials, dynamic light scattering were performed and the results can be seen in Figure 122: the average hydrodynamic diameter results in 295 nm for the synthesis performed in water and 220 nm for the material obtained in ethanol. The new synthesis gave as result a nanomaterial characterised by smaller average diameter of the particles. Accordingly, its specific surface area was improved: from the application of the BET theory on the N_2 isotherm (Figure 124), a value of 273(±50) $m^2 g^{-1}$ was obtained, with 0.79(±0.06) $cm^3 g^{-1}$ as pore volume.

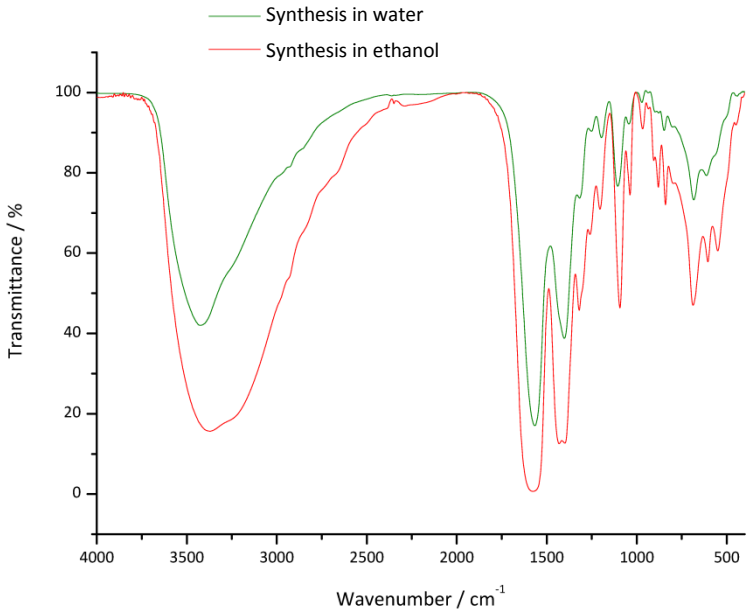

Figure 121: FT–IR spectra of La-(L) malic acid synthesised *via* hot injection in water and the same compound synthesised in ethanol.

The solubility of lanthanum chloride in ethanol is lower than its solubility in water (see paragraph 8.10): in line with this, it can be deduced that the La-malic acid hybrid material is more soluble in water than in ethanol. At the same concentration, the nanoparticles obtained in ethanol precipitate before than the nanoparticles synthesised in water. Consequently, the nanoparticles synthesised in water have a longer growth step than the nanoparticles synthesised in ethanol and the final nanomaterials have a bigger average diameter, resulting in a lower specific surface area.

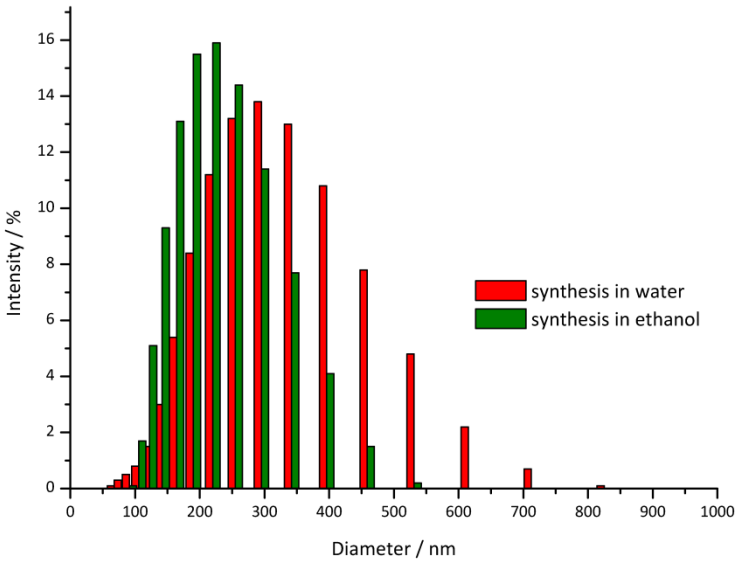

Figure 122: Particle size distribution according to DLS analysis. Red: La-(L) malic acid nanoparticles synthesized in water, suspended in ethanol; green: La-(L) malic acid nanoparticles synthesized in ethanol, suspended in ethanol.

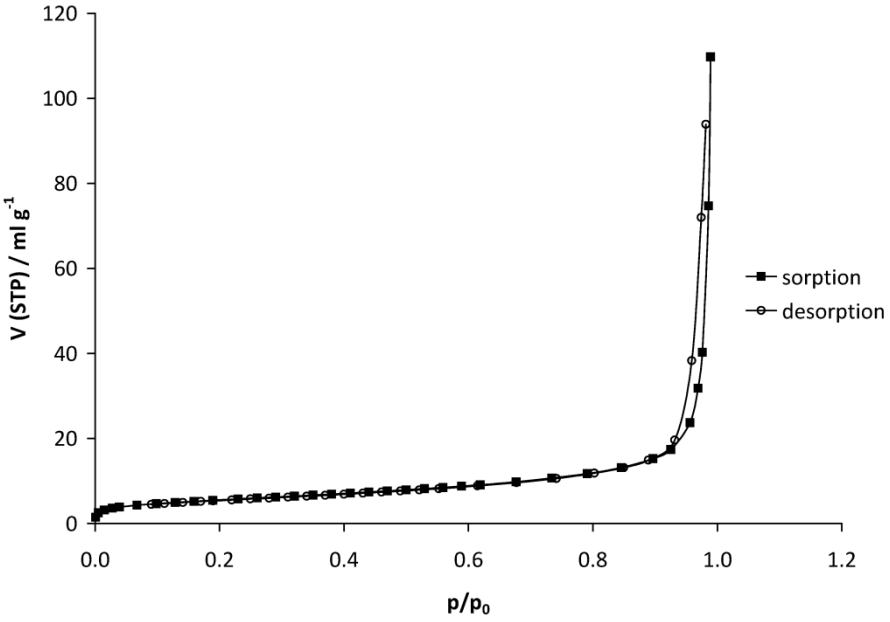

Figure 123: Nitrogen sorption obtained from volumetric analysis at -196 °C on La-(L) malic acid nanoparticles synthesised in water as solvent.

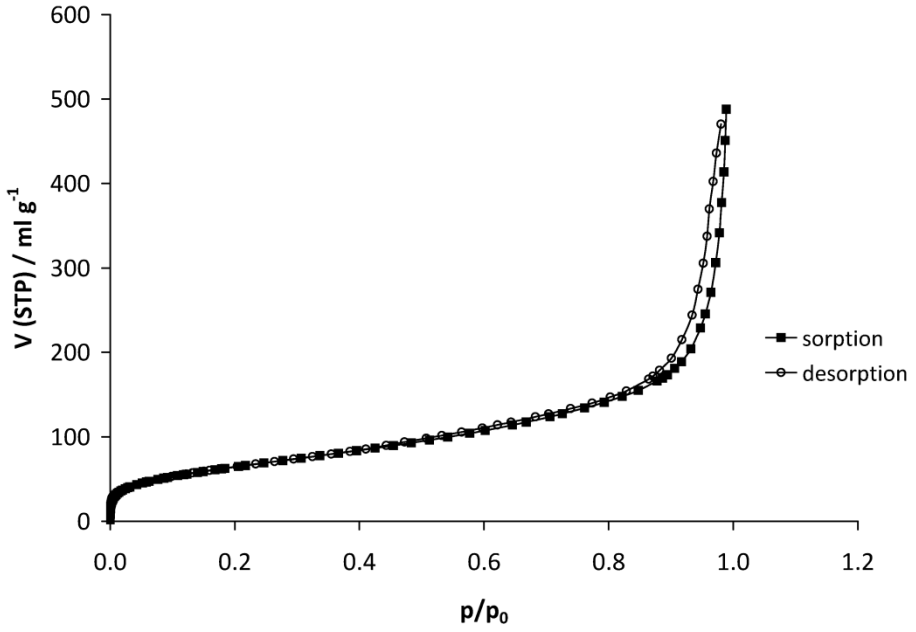

Figure 124: Nitrogen sorption obtained from volumetric analysis at -196 °C on La-(L) malic acid nanoparticles synthesised in ethanol as solvent.

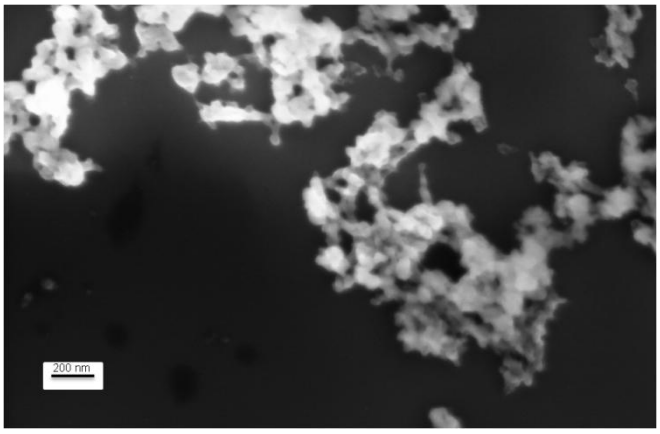

Figure 125: Scanning electron microscopy of the as prepared La-(L) malic acid nanoparticle in ethanol as solvent.

The new sample had an average particle diameter between 20 and 40 nm (Figure 125). The material was then used for the sorption of the mixture (S/R)-ibuprofen in s-CO_2. It results in 2.4×10^{-1} g sorbed per gram of hybrid nanomaterial, six-times more than the sorption observed on the nanoparticles synthesised in water. As next step, measurements have to be performed in order to know if the amount sorbed on the nanomaterial is the racemic mixture of the drug or only one enantiomer.

6 Summary

The aim of this work was to study the gas sorption behaviours of different nanomaterials. The nanomaterials were synthesized by the microemulsion approach or by hot injection technique. Gas adsorption capacities have been studied using the Rubotherm sorption apparatus (magnetic suspension balance) to obtain adsorption and desorption isotherms of the compounds.

As CO_2 sorbent material nanoscale AlO(OH) hollow spheres were proposed for the first time: the sorption of CO_2 shows an uptake of 260 mg g^{-1} at 50 °C and 90 bar, while the CO_2 uptake is 4.3-times higher in comparison to pure N_2. The attempt to increase the CO_2 capacity on this material upon encapsulation of basic molecules failed, due to the instability of AlO(OH) in strong alkaline conditions.

In order to increase the selectivity toward CO_2, new amine-functionalized nanoparticles are studied. Magnesium aminopropyl phosphonate (MgAPP) shows the best results in terms of specific surface area (532 m^2 g^{-1}) and CO_2 capacity: 191 milligram sorbed per gram of porous material, measured at 80°C and 100 bar. The nitrogen uptake, tested under similar conditions, results 8.7-times lower than CO_2, resulting in a selectivity of 87% (results based on single isotherms). The hybrid nanomaterial amino ethylphosphonate (Mg(2-AEP) shows the higher selectivity here reported: almost 100% at 80 °C and high pressure. This excellent selectivity is barely observed on MOFs, because, due to their higher specific surface areas, a high CO_2 uptake is often accompanied by a comparably high N_2 uptake, as well. The substitution of Mg^{2+} with other cations (Ca^{2+}, Ba^{2+}, Fe^{2+}, Co^{2+} and Cu^{2+}) introduces modification into the final material in such a way that the final CO_2 uptake is always reduced, highlighting the positive effect of magnesium in the CO_2 capture.

Oxygen, nitrogen and argon sorption analyses were tested at -196 °C on the nanomaterials cobalt propyl phosphonate and gadolinium propyl phosphonate. The uptakes observed were very similar, precluding the separation of these gases on the proposed hybrid materials.

The study on nanoscale hollow spheres and hybrid nanomaterials opened the investigation of the applications in the nanomedicine-field, previously unplanned at the beginning of the work. In this thesis, for medical purposes, nanoscale AlO(OH)@doxorubicin was produced and *in vitro* and *in vivo* results showed an efficacy of the product higher as compared to the free drug. Moreover, an initial study was conducted on nanomaterials for separation of the racemic mixture (S/R)-ibuprofen. The

material La(III)(L)-malic acid seems to have a positive interaction with the racemic mixture of the drug, but experiment to verify the enantiomeric adsorption are yet to be performed.

7 Outlook

This work is concerned to the synthesis and characterisation of nanomaterials for gas sorption and separation. As a strategy of synthesis, microemulsion was preferably selected. It is possible to affirm that the microemulsion approach is a good pathway to obtain nanoparticles in a laboratory scale, but it is not valid for a commercial scale. It requires large amounts of surfactant and solvents, which results in high costs for the chemicals and a long processing time for the purification of the final materials. In view of future industrial application, the synthesis has to be refined and improved.

In line with the principles of the green chemistry, the next goal could be the preparation of biocompatible/biodegradable adsorbents, which are able to reduce the emissions of greenhouse gases, while at the same time, being environmental compatible. With regard to this, derivate of amino acids could result interesting precursors for the synthesis of new hybrid nanomaterials.

Moreover, the CO_2 captured inside hybrid porous materials could then be employed to perform chemical reactions. The CO_2 could be transformed, for example, in methanol or methane upon interaction with hydrogen. The introduction of catalytic active metals could even improve the reaction.

The storage of CO_2 could be performed in a solid form, as a stable, environmentally benign mineral carbonate by chemical reaction of silicate into carbonates. Sequestration in the form of carbonate ensures long-term fixation of CO_2 rather than temporary storage. In addition, the risk of any accidental release of stored CO_2 is avoided. Silicate nanoparticles ($(Mg,Ca)_xSi_yO_{x+2y}$), with their huge specific surface areas in comparison to bulk materials, could represent an alternative pathway to the carbon sequestration.

8 Experimental Instructions

8.1 AlO(OH) hollow spheres

The micellar system was established in the following proportions: 50 ml *n*-hexane as the non-polar dispersant phase, a mixture of 1 ml of methanol and 1 ml of water as the polar phase, 1.82 g cetyltrimethylammonium bromide (CTAB) as surfactant and 5 ml *1*-hexanol as co-surfactant. At ambient temperature, Al(*sec*-$OC_4H_9)_3$ 0.1 molar in *n*-hexane was added to the dispersant phase of the equilibrated, transparent *w/o*-microemulsion and left to react for 12 hours. The as-prepared hollow spheres were collected as a colorless solid by centrifugation and purified by sequential re-suspension/centrifugation in/from isopropanol. Finally, the product was dried for 12 hours simultaneously increasing the temperature up to 60 °C and reducing the pressure up to 10^{-3} mbar.

Modification of AlO(OH) hollow spheres with basic molecules

The micellar system was established in the following proportions: 50 ml *n*-hexane as the non-polar dispersant phase, 1.82 g cetyltrimethylammonium bromide (CTAB) as surfactant, 5 ml *1*-hexanol as co-surfactant and 2 ml of water as polar phase (where 0.5 g of urea, 1 g guanidine or 4 mg melamine were dissolved, respectively). At ambient temperature, Al(*sec*-$OC_4H_9)_3$ 0.1 molar in *n*-hexane was added to the dispersant phase of the equilibrated, transparent *w/o*-microemulsion and left to react for 12 hours. The as-prepared hollow spheres were collected as a colourless solid by centrifugation and purified by sequential re-suspension/centrifugation in/from isopropanol. Finally, the product was dried for 12 hours while simultaneously increasing the temperature up to 60 °C and reducing the pressure up to 10^{-3} mbar.

8.2 AlO(OH) hollow spheres@doxorubicin

The micellar system was established in the following proportions: 50 ml *n*-hexane as the non-polar dispersant phase, a mixture of 2 ml methanol and water (1:1) as the polar phase where 1 mg of doxorubicin hydrochloride were dissolved, 1.82 g CTAB bromide as surfactant and 5 ml *1*-hexanol as co-surfactant. To the non-polar phase of the equilibrated, orange and clear *w/o*-microemulsion, a 0.1 molar solution in *n*-hexane of Al(*sec*-$OC_4H_9)_3$ was added and left to react for 12 hours. All the synthesis was performed in an ice-water bath in order to prevent decomposition of doxorubicin. The as-prepared filled hollow spheres were collected as a pink solid by centrifugation and purified by sequential re-suspension/centrifugation in/from isopropanol and water. Finally, an aqueous

suspension in dextran of the filled AlO(OH) hollow spheres was prepared (dextran concentration: 4 mg ml^{-1}; loaded hollow spheres concentration: 0.075 mg ml^{-1}). For spectroscopic measurements and thermogravimetric analysis, the product was carefully dried for 3 hours at 10^{-3} mbar and 60 °C.

8.3 Magnesium phosphonates (Mg(2-AEP) / MgAMP / Mg(1-AEP) / MgAPP/ MgABP / Mg(PP))

First off, a transparent microemulsion was prepared as follows: 70 ml of toluene as the non-polar phase, 0.8 mmol H_2(A)XP dissolved in 3 ml of water as the polar phase, 1.82 g of cetyltrimethylammonium bromide as the surfactant and 5 ml of *n*-hexanol as the co-surfactant. The mixture was stirred vigorously for 30 minutes at 35 °C (heating *via* oil bath). Subsequently, 1.6 mL of a 0.5 M Mg(*n*-C_4H_9)$_2$ solution in *n*-heptane (0.8 mmol) was injected. Immediately, the formation of product occurs and the mixture was left to react at room temperature for 12 hours while being continually stirred. The precipitate was washed three times with ethanol and carefully dried for 3 hours at 10^{-3} mbar and 60 °C.

8.4 Ca/Ba aminoehyl phosphonates

First off, a transparent microemulsion was prepared as follows: a mixture of 20 ml of toluene and 20ml *n*-hexane as the non-polar phase, 0.8 mmol (100 mg) 2-H_2AEP dissolved in 3ml water as the polar phase, 1.82 g of cetyltrimethylammonium bromide as the surfactant and 5 ml of *n*-hexanol as the co-surfactant. This mixture was stirred vigorously for 30 minutes at 35 °C (heating *via* oil bath). Separately, 0.8mmol of calcium (or barium) 2-ethylhexanoate (0.261 g or 0.330 g, respectively) were dissolved in 50 ml mixture of toluene and n-hexane in the ratio 1:1 and then injected to the previously prepared micromeulsion. The formation of product does not occur immediately, but after some hours. It was left to react at room temperature for 12 hours while being continually stirred. The precipitate was washed three times with ethanol and carefully dried for 3 hours at 10^{-3} mbar and 60 °C.

8.5 Fe/Co/Cu aminoethyl phosphonates

First off, a transparent microemulsion was prepared as follows: 70 ml of toluene as the non-polar phase, 0.8 mmol H_2AEP dissolved in 1.5 ml of water as the polar phase, 1.82 g of CTAB as the surfactant and 5 ml of *n*-hexanol as the co-surfactant were stirred vigorously for 30 minutes at 35 °C (heating *via* oil bath). Separately, 0.8 mmol of the respective cation precursor were diluted in 1.5 ml

of H_2O (Co(II) acetate: 0.1992 g, Cu(II) acetate: 0.1452 g, Fe(II) chloride: 0.159 g) and successively injected to the stable microemulsion. Immediately, the formation of product occurs and the mixture was left to react at room temperature for 8 hours while being continually stirred. The precipitate was washed three times with ethanol and carefully dried for 3 hours at 10^{-3} mbar and 60 °C.

8.6 Mg(2-AEP)(FMN)

The microemulsion was prepared as follows: 70 ml of toluene as the non-polar phase, 1.82 g of CTAB as the surfactant, 5 ml of *n*-hexanol as the co-surfactant. As polar phase, 0.56 mmol H_2(2-AEP) dissolved in 1.5 ml of water were added to a 1.5 ml water solution of 0.24 mmol of FMNHNa. All the chemicals were stirred vigorously for 30 minutes at 35 °C (heating *via* oil bath). The resulting microemulsion was isotropically transparent and orange coloured. Subsequently, 1.6 mL of a 0.5 M Mg(*n*-$C_4H_9)_2$ solution in *n*-heptane (0.8 mmol) was injected. Immediately, the formation of product occurs and the mixture was left to react at room temperature for 12 hours while being continually stirred. The precipitate was washed four times with ethanol, two times in a ratio 1:1 water-ethanol and twice in pure ethanol. For fluorescent spectroscopy, a 0.5 mg ml^{-1} suspension in mixture composed of 50% water - 50% ethanol was prepared. For infrared spectroscopy, the product was carefully dried for 3 hours at 10^{-3} mbar and 60 °C.

8.7 Not phosphonate organic ligands

β-alanine

First off, a transparent microemulsion was prepared as follows: 70 ml of toluene as the non-polar phase, 2.0 mmol β-alanine dissolved in 1.0 ml of water as the polar phase, 1.82 g of CTAB as the surfactant and 5 ml of *n*-hexanol as the co-surfactant. This mixture was stirred vigorously for 30 minutes at 35 °C (heating *via* oil bath). Separately, 1.0 mmol of $Mg(NO_3)_2$ were diluted in 1.5 ml of H_2O and successively injected to the stable microemulsion. The microemulsion turns completely white after ca. 10 minutes. The mixture was left to react at room temperature for 8 hours while being continually stirred. The precipitate was washed three times with ethanol and dried for 3 hours at 10^{-3} mbar at room temperature, or, alternatively, at atmospheric pressure at 60 °C.

Ethylenediamine-N,N'-diacetic acid

0.5 mmol of ethylenediamine-N,N'-diacetic acid (0.088 g) were dissolved in 5 ml of a solution NaOH 0.1M (pH = 7-8) and then heated at 60°C *via* oil bath. Separately, 0.5 mmol of $MgCl_2 \bullet 6H_2O$ (0.1015 g) were dissolved in 1 ml of H_2O. The Mg^{2+} solution was then injected at 60 °C into the first solution. No formation of the product was detected. Upon addition of ca. 0.2 ml of 3 M NaOH solution, the mixture started to turn turbid. The mixture was left to react overnight at room temperature. The precipitate was washed three times with a NaOH solution (0.5 M) and dried for 3 hours at 10^{-3} mbar and 70 °C.

Meso-2,3-diaminosuccinic acid

0.5 mmol of *meso*-2,3-diaminosuccinic acid (0.0747 g) were dissolved in 10 ml of a solution NaOH 0.1M (pH = 10) and the solution was then heated at 60°C *via* oil bath. Separately, 0.5 mmol of $MgCl_2 \bullet 6H_2O$ (0.1015 g) were dissolved in 1 ml of H_2O. The Mg^{2+} solution is then injected at 60 °C into the first solution. No formation of the product was detected (pH = 9). Upon addition of ca. 0.1 ml of 3 M NaOH solution, the mixture started to turn turbid (pH = 10). The mixture was left to react overnight at room temperature. The precipitate was washed three times with a NaOH solution (0.5 M) and dried for 3 hours at 10^{-3} mbar and 70 °C.

8.8 Gd/Co propyl phosphonates

First off, a transparent microemulsion was prepared as follows: 70 ml of toluene as the non-polar phase, 0.8 mmol H_2PP dissolved in 1.5 ml of water as the polar phase, 1.82 g of CTAB as the surfactant and 5 ml of *n*-hexanol as the co-surfactant. This mixture was stirred vigorously for 30 minutes at 35 °C (heating *via* oil bath). Separately, 0.8 mmol of Co(II) acetate (or 0.53 mmol of Gd(III) chloride: 0.2104 g) were diluted in 1.5 ml of H_2O and successively injected to the stable microemulsion. Immediately, the formation of product occurs and the mixture was left to react at room temperature for 8 hours while being continually stirred. The precipitate was washed three times with ethanol and carefully dried for 3 hours at 10^{-3} mbar and 60 °C.

8.9 Cu (L) - cysteine

3 mmol of (L)-cysteine (0.363 g) were dissolved in 10 ml of H_2O. The solution was then heated at 60°C *via* oil bath. Separately, 3mmol of $Cu(NO_3)_2 \bullet 3H_2O$ (0.723 g) were dissolved in 2 ml of H_2O. The Cu^{2+} solution is then injected at 60 °C into the first solution: immediately, the formation of the

product is indicated by the formation of a green precipitate. The mixture was left to react overnight at room temperature. The precipitate was washed three times with water and dried for 8 hours at 10^{-3} mbar and 70 °C.

8.10 La (L) - malic acid

3 mmol of (L)-malic acid (0.402 g) were dissolved in 10 ml of H_2O (or 10 ml ethanol) and heated at 60 °C *via* oil bath. Separately, 2 mmol of $LaCl_3 \cdot 7H_2O$ (0.734 g) were dissolved in 1 ml of H_2O (or 3 ml ethanol). The La^{3+} solution is then injected at 60 °C into the L-malic acid solution: no precipitation occur. The formation of the product was favourable upon alkalinisation of the mixture with a 3 M solution of NaOH. Precipitation started at pH 3. After reaching pH 7 (or pH=9 in case of ethanol as solvent), the mixture was left to react overnight at room temperature. The light-yellow precipitate was washed three times in water and dried for 3 hours at 10^{-3} mbar and 60 °C.

9 Appendix

List of Abbreviations

A_{BET}	specific surface area according to BET method
Ba(2-AEP)	barium(II) aminoethyl phosphonate
BET	Brunauer-Emmett-Teller
BBC	4,4',4"-(benzene-1,3,5-triyl-tris(benzene-4,1-diyl))-tribenzoate
BDC	1,4-benzenedicarboxylate
BJH	Barrett-Joyner-Halenda
BPDC	biphenyl-4,4'-dicarboxylate
BTB	4,4',4"-benzene-1,3,5-triyl-tribenzolate
BTE	4,4',4"-(benzene-1,3,5-triyl-tris(ethyne-2,1-diyl))-tribenzoate
BTC	1,3,5-benzenetriscarboxylate
Ca(2-AEP)	calcium(II) aminoethyl phosphonate
Co(2-AEP)	cobalt(II) aminoethyl phosphonate
Co(PP)	cobalt(II) propyl phosphonate
CLSM	confocal laser scanning microscopy
Cu(2-AEP)	copper(II) aminoethyl phosphonate
DLS	dynamic light scattering
dobdc	2,5-dioxido-1,4-benzenedicarboxylate
DPBS	dulbecco`s Phosphate Buffered Saline
DXR	doxorubicin
EA	elemental analysis
EDX	energy dispersive X-rays analysis
e.g.	(latin: exempli gratia) – for example
et al.	(latin: et alii) – and others

Fe(2-AEP)	iron(II) aminoethyl phosphonate
F^{EXP}	experimental force
FMNHNa	riboflavin 5'-monophosphate sodium salt
FT–IR	fourier transform – infrared spectroscopy
FMA	fumarate
g	gravitational force
$(Gd)_2(PP)_3$	gadolinium propyl phosphonate.
GDS	gas dosing system
H/E	enhanced permeability and retention
IAST	ideal adsorbed solution theory
i.e.	(latin: id est) – that is to say
IUPAC	international Union of Pure and Applied Chemistry
LD50	median lethal dose
M	molar – 1 mole per litre
m^A	mass of the sorbed phase
m^A_{GE}	gibbs excess mass
m^{BAL}	balance reading
Mg(1-AEP)	magnesium (DL-1-aminoethyl) phosphonate
Mg(2-AEP)	magnesium aminoethyl phosphonate
MgABP	magnesium aminobutyl phosphonate
MgAMP	magnesium aminomethyl phosphonate
MgAPP	magnesium aminopropyl phosphonate
Mg(PP)	magnesium propyl phosphonate
m^S	mass of the sorbent material
m^{SC}	weight of the sample container
MEA	monoethanolamine

MOFs	metal-organic frameworks
MTT	3-(4,5-dimethylthiazol-2-yl)-2,5-diphenyltetrazolium bromide
MSB	magnetic suspension balance
nm	nanometers, 10^{-9}m
o/w	oil-in-water
P	pressure
p	equilibrium pressure
p_0	saturation pressure
p/p_0	relative pressure
p_i	partial pressure of component i
PBS	phosphate buffered saline
pm	picometers, 10^{-12}m
r	radius of the pores
R_H	hydrodynamic radius
SEM	scanning electron microscopy
s-CO_2	supercritical carbon dioxide
T	temperature
TEA	triethanolamine
TEM	transmission electron microscopy
TCEPEB	1,3,5-tris[(1,3-carboxylic acid-5-(4-ethynyl)phenyl))-ethynyl]benzene
TGA	thermogravimetric analysis
Uv-Vis	ultraviolet-Visible
v_m	monolayer adsorbed gas quantity
V^A	volume of the sorbed phase
V^P	pore volume
vs.	versus

V^S	volume of the sample
V^{SC}	volume of the sample container
w/o	water-in-oil
wt	in weight
x	gas phase
XRD	X-ray diffraction
y	adsorbate phase
η	viscosity of the solvent
λ	wavelength
ρ	density
Ω	reduced mass

List of figures

List of tables

List of publications

[1] S. Simonato, H. Groger, J. Mollmer, R. Staudt, A. Puls, F. Dreisbach, C. Feldmann, *Chemical Communications* **2012**, *48*, 844-846.

[2] P. Leidinger, S. Simonato, C. Feldmann, *Chemical Communications* **2012**, *48*, 7046-7048.

[3] S. Simonato, R. Popescu, C. Seidl, U. Schepers, C. Feldmann, *in preparation*. (Doxorubicin-filled AlO(OH) Hollow Spheres for Tumor Therapy).

[4] J.Heck, S. Simonato, J. Napp, F. Alves, C. Feldmann, *in preparation*. (Inorganic-Organic Hybrid Nanoparticles with Multipurpose Function).

Attendance at international conferences

- 7th International Conference on Materials for Advance Technologies, Singapore, **2013** (Lecture)
- XI International Conference on Nanostructure Materials, Rhodes, **2012** (Poster)
- 1st International Symposium on Colloids and Materials, Amsterdam, **2011** (Poster)

Acknowledgements

My gratitude to Prof. Dr. C. Feldmann for the engaging subject assigned and for giving a notable contribution to this research with his support, interest and suggestions.

Many thanks to Dr. F. Dreisbach, Dr. A Puls and O. Zielinski (Rubotherm GmbH) for the prompt technical support with the MSB and the clarifications about the elaboration of the experimental data.

All the people in the workshop are thanked for quick assistance and the immediate order of new materials every time that I needed.

I would like to thank all the collaboration partners of this work: Dr. R Staudt, Dr. J. Möllmer, M. Lange for the experimental gas adsorption measurements with gas mixtures and at lower than room temperature. Thanks to Dr. R. Popescu for the TEM images, C. Seidl for biological tests, Dr. D. Bolten and Prof. Dr. M. Türk for the sorption experiments with (S/R)-Ibuprofen.

I am grateful to L. Sonntag and J. Steinmeyer, chemistry students, for their contributions to this work.

H. Gröger, thank you for your help in the last period of my PhD.

K. Pliester, thanks for your friendship and the peaceful atmosphere in the lab.

Many thanks to A. Kusmanoski for the fluorescence spectroscopy measurements, S. Stolz for the UV-Vis spectroscopy analyses, Dr. S. Wolf, Dr. R. Gomez and D. Hausmann for the thermogravimetric measurements and all supervisors of the devices for their help.

For the correction of this manuscript, I would like to thank: Dr. S. Wolf, Dr. F. Gyger, T. Quain, A. Steffani, H. Mansuri, L. Brütsch and A. Kusmanoski.

Grazie alla mia famiglia per il supporto durante gli anni di studio.

Grazie ad Alberto. Per tutto.

Sara

10 References

[1] R. P. Feynman, *Engineering and Science* **1960**, *23*, 22-29.
[2] H. Goesmann, C. Feldmann, *Angewandte Chemie-International Edition* **2010**, *49*, 1362-1395.
[3] R. K. Pachauri, A. Reisinger, *Fourth Assessment Report*, Intergovernmental Panel on Climate Change, **2007**.
[4] G. T. Rochelle, *Science* **2009**, *325*, 1652-1654.
[5] K. Sumida, D. L. Rogow, J. A. Mason, T. M. McDonald, E. D. Bloch, Z. R. Herm, T. H. Bae, J. R. Long, *Chemical Reviews* **2012**, *112*, 724-781.
[6] B. Arstad, H. Fjellvag, K. O. Kongshaug, O. Swang, R. Blom, *Adsorption-Journal of the International Adsorption Society* **2008**, *14*, 755-762.
[7] R. Vaidhyanathan, S. S. Iremonger, G. K. H. Shimizu, P. G. Boyd, S. Alavi, T. K. Woo, *Angewandte Chemie-International Edition* **2012**, *51*, 1826-1829.
[8] J. Liu, P. K. Thallapally, B. P. McGrail, D. R. Brown, J. Liu, *Chemical Society Reviews* **2012**, *41*, 2308-2322.
[9] Z. J. Zhang, Y. G. Zhao, Q. H. Gong, Z. Li, J. Li, *Chemical Communications* **2013**, *49*, 653-661.
[10] Z. H. Lee, K. T. Lee, S. Bhatia, A. R. Mohamed, *Renewable & Sustainable Energy Reviews* **2012**, *16*, 2599-2609.
[11] a) H. Gröger, C. Kind, P. Leidinger, M. Roming, C. Feldmann, *Materials* **2010**, *3*, 4355-4386; b) H. Gröger, F. Gyger, P. Leidinger, C. Zurmuhl, C. Feldmann, *Advanced Materials* **2009**, *21*, 1586-1590.
[12] D. H. M. Buchold, C. Feldmann, *Nano Letters* **2007**, *7*, 3489-3492.
[13] P. Leidinger, S. Simonato, C. Feldmann, *Chemical Communications* **2012**, *48*, 7046-7048.
[14] M. J. Kirschner, in *Ullmann's encyclopedia of industrial chemisty*, Wiley, **2000**.
[15] O. Tacar, P. Sriamornsak, C. R. Dass, *Journal of Pharmacy and Pharmacology* **2013**, *65*, 157-170.
[16] K. S. W. Sing, D. H. Everett, R. A. W. Haul, L. Moscou, R. A. Pierotti, J. Rouquerol, T. Siemieniewska, *Pure and Applied Chemistry* **1985**, *57*, 603-619.
[17] J. U. Keller, R. Staudt, *Gas Adsorption Equilibria*, Springer, **2005**.
[18] J. Rouquerol, D. Avnir, C. W. Fairbridge, D. H. Everett, J. H. Haynes, N. Pernicone, J. D. F. Ramsay, K. S. W. Sing, K. K. Unger, *Pure and Applied Chemistry* **1994**, *66*, 1739-1758.
[19] K. J. Laidler, *Chemical Kinetics*, Harper & Row, **2004**.
[20] I. Langmuir, *Physical Review* **1916**, *8*, 149.
[21] L. Chen, J. Mowat, D. Fairen-Jimenez, C. Morrison, S. Thompson, P. Wright, T. Düren, *Journal of American Chemical Society* **2013**, *135*, 15763-15773.
[22] R. Staudt, G. Saller, M. Tomalla, J. U. Keller, *Berichte Der Bunsen-Gesellschaft-Physical Chemistry Chemical Physics* **1993**, *97*, 98-105.
[23] S. Brunauer, P. H. Emmett, E. Teller, *Journal of American Chemical Society* **1938**, *60*, 309-319.
[24] C. Weidenthaler, *Nanoscale* **2011**, *3*, 792-810.
[25] I. Langmuir, *Journal of American Chemical Society* **1918**, *40*, 1361.
[26] J. Toth, *Advances in Colloid and Interface Science* **1995**, *55*, 1-239.
[27] M. M. Dubinin, L. V. Radushkevich, *Doklady Akademii nauk SSSR* **1947**, *55*, 331.
[28] M. G. Kaganer, *Russian Journal of Physical Chemistry* **1959**, *33*, 352.
[29] G. Jura, W. D. Harkins, *Journal of Chemical Physics* **1943**, *11*, 430.
[30] J. Adolphs, M. J. Setzer, *Journal of Colloid and Interface Science* **1998**, *207*, 349-354.
[31] E. P. Barrett, L. G. Joyner, P. P. Halenda, *Journal of the American Chemical Society* **1951**, *73*, 373-380.
[32] T. D. Oulton, *Journal of Physical and Colloid Chemistry* **1948**, *52*, 1296-1314.
[33] K. Kaneko, *Journal of Membrane Science* **1994**, *96*, 59-89.

[34] C. G. Shull, *Journal of the American Chemical Society* **1948**, *70*, 1405-1410.
[35] L. M. Skinner, J. R. Sambles, *Journal of Aerosol Science* **1972**, *3*, 199-210.
[36] S. Sircar, *Industrial & Engineering Chemistry Research* **1999**, *38*, 3670-3682.
[37] J. Moellmer, A. Moeller, F. Dreisbach, R. Glaeser, R. Staudt, *Microporous and Mesoporous Materials* **2011**, *138*, 140-148.
[38] R. Quadrelli, S. Peterson, *Energy Policy* **2007**, *35*, 5938-5952.
[39] D. M. D'Alessandro, B. Smit, J. R. Long, *Angewandte Chemie-International Edition* **2010**, *49*, 6058-6082.
[40] J. T. Litynski, S. M. Klara, H. G. McIlvried, R. D. Srivastava, *Environment International* **2006**, *32*, 128-138.
[41] J. D. Figueroa, T. Fout, S. Plasynski, H. McIlvried, R. D. Srivastava, *International Journal of Greenhouse Gas Control* **2008**, *2*, 9-20.
[42] T. Sakakura, J. Choi, H. Yasuda, *Chemical Reviews* **2007**, *107*, 2365-2387.
[43] I. I. E. Agency, http://www.iea.org, **2011**.
[44] J. Čejka, A. Corma, S. Zones, *Zeolites and Catalysis: Synthesis, Reactions and Applications*, Wiley, **2010**.
[45] J. S. Lee, J. H. Kim, J. T. Kim, J. K. Suh, J. M. Lee, C. H. Lee, *Journal of Chemical and Engineering Data* **2002**, *47*, 1237-1242.
[46] G. Li, P. Xiao, P. Webley, J. Zhang, R. Singh, *Energy Procedia* **2009**, *1*, 1123-1130.
[47] S. Choi, J. H. Drese, C. W. Jones, *ChemSusChem* **2009**, *2*, 796-854.
[48] M. G. Plaza, S. Garcia, F. Rubiera, J. J. Pis, C. Pevida, *Chemical Engineering Journal* **2010**, *163*, 41.
[49] Q. A. Wang, J. Z. Luo, Z. Y. Zhong, A. Borgna, *Energy & Environmental Science* **2011**, *4*, 42-55.
[50] K. B. Lee, M. G. Beaver, H. S. Caram, S. Sircar, *Industrial & Engineering Chemistry Research* **2008**, *47*, 8048-8062.
[51] D. J. Fauth, E. A. Frommell, J. S. Hoffman, R. P. Reasbeck, H. W. Pennline, *Fuel Processing Technology* **2005**, *86*, 1503-1521.
[52] N. L. Rosi, J. Kim, M. Eddaoudi, B. L. Chen, M. O'Keeffe, O. M. Yaghi, *Journal of the American Chemical Society* **2005**, *127*, 1504-1518.
[53] H. Furukawa, N. Ko, Y. B. Go, N. Aratani, S. B. Choi, E. Choi, A. O. Yazaydin, R. Q. Snurr, M. O'Keeffe, J. Kim, O. M. Yaghi, *Science* **2010**, *329*, 424-428.
[54] P. Atkins, J. De Paula, *Atkins' Physical Chemistry 8th edition*, Oxford, **2006**.
[55] O. K. Farha, A. O. Yazaydin, I. Eryazici, C. D. Malliakas, B. G. Hauser, M. G. Kanatzidis, S. T. Nguyen, R. Q. Snurr, J. T. Hupp, *Nature Chemistry* **2010**, *2*, 944-948.
[56] M. Xue, Y. Liu, R. M. Schaffino, S. C. Xiang, X. J. Zhao, G. S. Zhu, S. L. Qiu, B. L. Chen, *Inorganic Chemistry* **2009**, *48*, 4649-4651.
[57] P. D. C. Dietzel, V. Besikiotis, R. Blom, *Journal of Materials Chemistry* **2009**, *19*, 7362-7370.
[58] Z. R. Herm, J. A. Swisher, B. Smit, R. Krishna, J. R. Long, *Journal of the American Chemical Society* **2011**, *133*, 5664-5667.
[59] P. L. Llewellyn, S. Bourrelly, C. Serre, A. Vimont, M. Daturi, L. Hamon, G. De Weireld, J. S. Chang, D. Y. Hong, Y. K. Hwang, S. H. Jhung, G. Ferey, *Langmuir* **2008**, *24*, 7245-7250.
[60] J. A. Mason, K. Sumida, Z. R. Herm, R. Krishna, J. R. Long, *Energy & Environmental Science* **2011**, *4*, 3030-3040.
[61] A. O. Yazaydin, R. Q. Snurr, T. H. Park, K. Koh, J. Liu, M. D. LeVan, A. I. Benin, P. Jakubczak, M. Lanuza, D. B. Galloway, J. J. Low, R. R. Willis, *Journal of the American Chemical Society* **2009**, *131*, 18198-18199.
[62] S. R. Caskey, A. G. Wong-Foy, A. J. Matzger, *Journal of the American Chemical Society* **2008**, *130*, 10870-10871.
[63] P. Aprea, D. Caputo, N. Gargiulo, F. Iucolano, F. Pepe, *Journal of Chemical and Engineering Data* **2010**, *55*, 3655-3661.

[64] J. An, N. L. Rosi, *Journal of the American Chemical Society* **2010**, *132*, 5578-5579.
[65] J. Ermsley, *Oxygen, Nature's Building Blocks: An A-Z Guide to the Elements*, Oxford University Press, **2001**.
[66] E. D. Bloch, L. J. Murray, W. L. Queen, S. Chavan, S. N. Maximoff, J. P. Bigi, R. Krishna, V. K. Peterson, F. Grandjean, G. J. Long, B. Smit, S. Bordiga, C. M. Brown, J. R. Long, *Journal of the American Chemical Society* **2011**, *133*, 14814-14822.
[67] X. Jin, A. Malek, S. Farooq, *Industrial & Engineering Chemistry Research* **2006**, *45*, 5775-5787.
[68] R. S. Pillai, S. A. Peter, R. V. Jasra, *Microporous and Mesoporous Materials* **2008**, *113*, 268-276.
[69] J. W. Kovak, R. Agrawal, J. C. Peterson, U.S. Patent 5,159,816, **1992**.
[70] S. S. Madaeni, E. Enayati, V. Vatanpour, *Polymers for Advanced Technologies* **2011**, *22*, 2556-2563.
[71] R. B. Eldridge, *Industrial & Engineering Chemistry Research* **1993**, 2208-2212.
[72] E. D. Bloch, W. L. Queen, R. Krishna, J. M. Zadrozny, C. M. Brown, J. R. Long, *Science* **2012**, *335*, 1606-1610.
[73] Y. He, R. Krishna, B. Chen, *Energy & Environmental Science* **2012**, *5*, 9107-9120.
[74] *Sorption Measuring Instrument with Magnetic Suspension Balance-Manual*, Rubotherm, **2009**.
[75] F. Dreisbach, **2011**, personal communication.
[76] F. Dreisbach, H. W. Losch, P. Harting, *Adsorption-Journal of the International Adsorption Society* **2002**, *8*, 95-109.
[77] K. K. Mohindroo, *Basic Principles of Physics*, Pitambar, **1997**.
[78] *High Precision Adsorption measuring apparatus Operation manual*, Belsorp, **2004**.
[79] D. Dollimore, P. Spooner, A. Turner, *Surface Technology* **1976**, *4*, 121-160.
[80] a) E. M. W. Mackenzie, *Advances in applied Fourier transform infrared spectroscopy* Wiley, **1988**; b) B. Stuart, *Infrared spectroscopy : fundamentals and applications* Wiley, **2004**.
[81] M. Roming, **2011**, personal communication.
[82] a) J. C. Lindon, G. E. Tranter, D. W. Koppenaal, *Encyclopedia of spectroscopy and spectrometry*, Academic Press, **2000**; b) *Handbook of spectroscopy* (Eds.: G. Gauglitz, T. Vo-Dinh), Wiley, **2003**.
[83] a) G. Blasse, B. C. Grabmaier, *Luminescent Materials*, Springer, **1994**; b) C. Ronda, *Luminescence*, Wiley, **2008**.
[84] a) S. Wolfgang, *Light Scattering from Polymer Solutions and Nanoparticle Dispersions*, Springer, **2007**; b) *Zetasizer nano series user manual*, **2003**; c) B. J. Berne, R. Pecora, *Dynamic Light Scattering with applications to chemistry, biology and physics*, Dover Publications, Inc., **2000**.
[85] a) *Manual for the SUPRA (VP) and ULTRA Scanning Electron Microscopes*, Zeiss, **2005**; b) *In situ Scanning Electron Microscopy in Materials Research* (Eds.: K. Wetzig, D. Schulze), Akademie Verlag, **1995**; c) P. J. Goodhew, J. Humphreys, R. Beanland, *Electron Microscopy and Analysis, third edition*, Taylor & Francis, **2001**; d) Z. L. N. Yao, *Wang Handbook of Microscopy for Nanotechnology*, Springer, **2005**.
[86] a) *X-Ray Spectrometry: Recent Technological Advances* (Eds.: K. Tsuji, J. Injuk, R. Van Grieken), Wiley, **2004**; b) A. J. Garnett-Reed, *Energy-dispersive X-ray analysis in the electron microscope*, Oxford, **2003**.
[87] a) *Thermal analysis* (Ed.: J. F. Tyson), Van Nostrand Reinhold Company, Ltd, **1973**; b) E. L. Charsley, S. B. Warrington, *Thermal Analysis - Tecniques and Applications*, The Royal Society of Chemistry, **1992**.
[88] a) W. Borchardt-Ott, *Kristallographie*, Springer, **2009**; b) Y. Waseda, E. Matsubara, K. Shinoda, *X-Ray Diffraction Crystallography, Introduction, Examples and Solved Problems*, Springer, **2011**.

[89] P. Scherrer, *Nachr. Ges. Wiss. Goettingen, Math.-Phys. Kl.* **1918**, *2*, 96.
[90] V. K. Lamer, R. H. Dinegar, *Journal of the American Chemical Society* **1950**, *72*, 4847-4854.
[91] M. A. Lopez-Quintela, J. Rivas, M. C. Blanco, C. Tojo, *Synthesis of Nanoparticles in Microemulsions in Nanoscale Materials*, Kluwer, **2003**.
[92] R. G. Alany, T. Rades, S. Agatonovic-Kustrin, N. M. Davies, I. G. Tucker, *International Journal of Pharmaceutics* **2000**, *196*, 141-145.
[93] M. M. Husein, N. N. Nassar, *Current Nanoscience* **2008**, *4*, 370-380.
[94] X. W. Lou, L. A. Archer, Z. C. Yang, *Advanced Materials* **2008**, *20*, 3987-4019.
[95] M. P. Pileni, *Nature Materials* **2003**, *2*, 145-150.
[96] D. H. M. Buchold, C. Feldmann, *Advanced Functional Materials* **2008**, *18*, 1002-1011.
[97] C. D. Donega, P. Liljeroth, D. Vanmaekelbergh, *Small* **2005**, *1*, 1152-1162.
[98] S. Simonato, H. Gröger, J. Mollmer, R. Staudt, A. Puls, F. Dreisbach, C. Feldmann, *Chemical Communications* **2012**, *48*, 844-846.
[99] J. H. Jiang, Q. M. Gao, Z. J. Zheng, K. S. Xia, J. Hu, *International Journal of Hydrogen Energy* **2010**, *35*, 210-216.
[100] T. Miyao, K. Minoshima, Y. Kurokawa, K. Shinohara, W. H. Shen, S. Naito, *Catalysis Today* **2008**, *132*, 132-137.
[101] M. G. Frere, G. F. De Weireld, *Journal of Chemical and Engineering Data* **2002**, *47*, 823-829.
[102] http://webbook.nist.gov/chemistry/fluid/.
[103] H. Hongwei, X. Yi, Y. Qing, G. Qixun, T. Chenrong, *Nanotechnology* **2005**, *16*, 741-745.
[104] a) L. Stradella, M. Argentero, *Thermochimica Acta* **1993**, *219*, 315-323; b) A. N. Alexandrova, W. L. Jorgensen, *Journal of Physical Chemistry B* **2007**, *111*, 720-730.
[105] E. Wolska, W. Szajda, *Journal of Applied Spectroscopy* **1983**, *38*, 137-140.
[106] H. Meyer, *Biochemical journal* **1957**, *67*, 333-340.
[107] O. D. Bonner, C. F. Jordan, *Spectrochimica Acta* **1976**, *12A*, 1243-1246.
[108] a) Y. Jiao, Y. Sun, B. Chang, D. Lu, W. Yang, *Chemistry-a European Journal* **2013**, *19*, 15410-15420; b) B. Wang, W. Meng, M. Bi, Y. Ni, Q. Caib, J. Wang, *Dalton Transactions* **2013**, *42*, 8918-8925; c) X. Yuan, B. Zhu, X. Ma, G. Tong, Y. Su, X. Zhu, *Langmuir* **2013**, *29*, 12275-12283; d) R. J. Xing, A. A. Bhirde, S. J. Wang, X. L. Sun, G. Liu, Y. L. Hou, X. Y. Chen, *Nano Research* **2013**, *6*, 1-9; e) J. You, R. Zhang, G. D. Zhang, M. Zhong, Y. Liu, C. S. Van Pelt, D. Liang, W. Wei, A. K. Sood, C. Li, *Journal of Controlled Release* **2012**, *158*, 319-328; f) S. Tan, Q. X. Wu, J. Wang, Y. L. Wang, X. L. Liu, K. K. Sui, X. Y. Deng, H. F. Wang, M. H. Wu, *Microporous and Mesoporous Materials* **2011**, *142*, 601-608; g) S. H. Tang, X. Q. Huang, X. L. Chen, N. F. Zheng, *Advanced Functional Materials* **2010**, *20*, 2442-2447; h) W. Wei, G. H. Ma, G. Hu, D. Yu, T. McLeish, Z. G. Su, Z. Y. Shen, *Journal of the American Chemical Society* **2008**, *130*, 15808-15810; i) Q. H. Zhao, B. S. Han, Z. H. Wang, C. Y. Gao, C. H. Peng, J. C. Shen, *Nanomedicine-Nanotechnology Biology and Medicine* **2007**, *3*, 63-74.
[109] S. Simonato, R. Popescu, C. Seidl, U. Schepers, C. Feldmann, *in preparation*.
[110] J. Ungelenk, C. Seidl, E. Zittel, S. Roming, U. Schepers, C. Feldmann, *submittet*.
[111] a) A. Gabizon, D. Tzemach, L. Mak, M. Bronstein, A. T. Horowitz, *Journal of Drug Targeting* **2002**, *10*, 539-548; b) E. J. Kim, K. M. Lim, K. Y. Kim, O. N. Bae, J. Y. Noh, S. M. Chung, S. Shin, Y. P. Yun, J. H. Chung, *Journal of Thrombosis and Haemostasis* **2009**, *7*, 1172-1183.
[112] H. Maeda, J. Wu, T. Sawa, Y. Matsumura, K. Hori, *Journal of Controlled Release* **2000**, *65*, 271-284.
[113] M. J. Kim, H. K. Kim, *Acta Biologica Hungarica* **2011**, *62*, 244-254.
[114] A. G. Menke, F. Walmsley, *Inorganica Chimica Acta* **1976**, *17*, 193-197.
[115] H. C. Pang, G. L. Ning, W. T. Gong, J. W. Ye, Y. Lin, *Chemical Communications* **2011**, *47*, 6317-6319.
[116] S. Q. Ma, H. C. Zhou, *Chemical Communications* **2010**, *46*, 44-53.
[117] S. M. Ward, J. Braslaw, R. L. Gealer, *Thermochimica Acta* **1983**, *64*, 107-114.

[118] N. Hedin, L. J. Chen, A. Laaksonen, *Nanoscale* **2010**, *2*, 1819-1841.
[119] H. S. Choi, M. P. Suh, *Angewandte Chemie-International Edition* **2009**, *48*, 6865-6869.
[120] L. Hamon, E. Jolimaitre, G. D. Pirngruber, *Industrial & Engineering Chemistry Research* **2010**, *49*, 7497-7503.
[121] J. Mollmer, M. Lange, A. Moller, C. Patzschke, K. Stein, D. Lassig, J. Lincke, R. Glaser, H. Krautscheid, R. Staudt, *Journal of Materials Chemistry* **2012**, *22*, 10274-10286.
[122] A. L. Myers, J. M. Prausnitz, *Aiche Journal* **1965**, *11*, 121-127.
[123] P. M. Mathias, R. Kumar, J. D. Moyer, J. M. Schork, S. R. Srinivasan, S. R. Auvil, O. Talu, *Industrial & Engineering Chemistry Research* **1996**, *35*, 2477-2483.
[124] V. Finsy, L. Ma, L. Alaerts, D. E. De Vos, G. V. Baron, J. F. M. Denayer, *Microporous and Mesoporous Materials* **2009**, *120*, 221-227.
[125] L. Hamon, C. Serre, T. Devic, T. Loiseau, F. Millange, G. Ferey, G. De Weireld, *Journal of the American Chemical Society* **2009**, *131*, 8775-8777.
[126] P. Serra-Crespo, E. V. Ramos-Fernandez, J. Gascon, F. Kapteijn, *Chemistry of Materials* **2011**, *23*, 2565-2572.
[127] P. D. Rolniak, R. Kobayashi, *Aiche Journal* **1980**, *26*, 616-625.
[128] M. Heuchel, G. M. Davies, E. Buss, N. A. Seaton, *Langmuir* **1999**, *15*, 8695-8705.
[129] D. A. Skoog, J. J. Leary, *Chimica analitica strumentale*, Edises, **2000**.
[130] L. E. Kreno, K. Leong, O. K. Farha, M. Allendorf, R. P. Van Duyne, J. T. Hupp, *Chemical Reviews* **2012**, *112*, 1105-1125.
[131] A. Guais, G. Brand, L. Jacquot, M. Karrer, S. Dukan, G. Grevillot, T. J. Molina, J. Bonte, M. Regnier, L. Schwartz, *Chemical Research in Toxicology* **2011**, *24*, 2061-2070.
[132] J. Xiao, Y. Wu, M. Li, B. Y. Liu, X. C. Huang, D. Li, *Chemistry-a European Journal* **2013**, *19*, 1891-1895.
[133] X. L. Qi, R. B. Lin, Q. Chen, J. B. Lin, J. P. Zhang, X. M. Chen, *Chemical Science* **2011**, *2*, 2214-2218.
[134] M. Roming, H. Lunsdorf, K. E. J. Dittmar, C. Feldmann, *Angewandte Chemie-International Edition* **2010**, *49*, 632-637.
[135] D. J. Lee, *Chimica Inorganca*, Piccin, **2000**.
[136] R. Bhushan, J. Martens, *Biomedical Chromatography* **1998**, *12*, 309-316.
[137] D. M. Solano, P. Hoyos, M. J. Hernaiz, A. R. Alcantara, J. M. Sanchez-Montero, *Bioresource Technology* **2012**, *115*, 196-207.
[138] T. Siódmiaka, M. Ziegler-Borowska, M. Piotr Marszałł, *Journal of Molecular Catalysis B: Enzymatic* **2013**, *94*, 7-14.
[139] Y. Liu, F. Wang, T. Tan, *Journal of Molecular Catalysis B: Enzymatic* **2009**, *56*, 126-130.
[140] M. Türk, D. Bolten, *The Journal of Supercritical Fluids* **2010**, *55*, 778-785.
[141] K. De Klerck, D. Mangelings, Y. V. Heyden, *Journal of Pharmaceutical and Biomedical Analysis* **2012**, *69*, 77-92.